transactions of the ASME

Published Quarterly by
The American Society of
Mechanical Engineers

Volume 92 • Series C • Number 2
MAY 1970

journal of heat transfer

EDITORIAL OFFICES are at ASME Headquarters, United Engineering Center, 345 East 47th Street, New York, N. Y. 10017. Cable address, "Mechaneer," New York.
PUBLISHED QUARTERLY at 20th and Northampton Streets, Easton, Pa. 18042. Second-class postage paid at Easton.
CHANGES OF ADDRESS must be received at Society headquarters seven weeks before they are to be effective. Please send old label and new address.
PRICES: to members, $2.25 a copy, $7.50 annually; to nonmembers, $4.50 a copy, $15.00 annually.
Add 50 cents for postage to countries outside the U. S. and Canada.
STATEMENT from By-Laws. The Society shall not be responsible for statements or opinions advanced in papers or . . . printed in its publications (B13, Par. 4).

INDEXED by the Engineering Index, Inc.

J. W. ACKERMAN
Research Engineer,
Research and Development Division,
The Babcock & Wilcox Co.,
Alliance, Ohio. Mem. ASME

A. R. BRUNSVOLD
Research Assistant,
University of Michigan,
Ann Arbor, Mich.

Heat Transfer and Draft Loss Performance of Extended Surface Tube Banks

New heat transfer and draft loss data are presented for one extended surface geometry which was investigated in five staggered and one in-line bank arrangements. In these tests, $1^7/_8$-inch OD tubes with 1-in. long elliptical studs were investigated. The tube banks, which were in a clean condition, were either 8 or 10 rows deep and covered ratios of transverse spacing to diameter $\left(\frac{S_T}{D}\right)$ from 2.1 to 3.2 and longitudinal spacing to diameter $\left(\frac{S_L}{D}\right)$ from 1.7 to 2.4. Heat transfer was from air to the tube banks, with Reynolds numbers ranging from 13,700 to 46,400. Correlations with suitable arrangement factors are shown to adequately describe the performance of the surface investigated. The relative heat transfer, draft loss performance of all arrangements is shown to depend upon the basis of comparison used.

Introduction

During the past years there has been an increased use of extended surface in heat transfer equipment. In oil heaters in the petroleum industry and steam generator economizers in the electric utility industry, extended surface has in many cases taken the form of studded tubes. Operating in cross flow, the heat transferred from hot combustion gases to the studded surface.

For one application of particular interest to The Babcock & Wilcox Company—steam generator economizers—the use of extended surface offered several potential advantages. However, little heat transfer-draft loss information was available on which to base economizer designs using the relatively small diameter studded tubing contemplated. Therefore, in 1964, the company initiated an experimental program to obtain information on both staggered and in-line tube banks for one studded tube geometry. Clean heat transfer surface was used in all cases. Because an existing test facility was available at B&W Limited's research facilities in Renfrew, Scotland, actual testing was conducted there.

The objective of this paper is to present the results of the first series of tests conducted on one in-line and five staggered tube bank arrangements, and to compare their heat transfer-draft loss performance using several bases of comparison.

Contributed by the Heat Transfer Division and presented at the Winter Annual Meeting, Los Angeles, Calif., November 16–20, 1969, of The American Society of Mechanical Engineers. Manuscript received by the Heat Transfer Division, May 22, 1968. Paper No. 69-WA/HT-5.

Range of Variables

Studded Tube Geometry:

$1^7/_8$-in. OD tube with elliptical studs ($^1/_2$-in. wide × $^1/_8$-in. thick × 1-in. long on $^1/_4$-in. staggered pitch with 6 studs per row).

A photograph of the surface appears in Fig. 1.

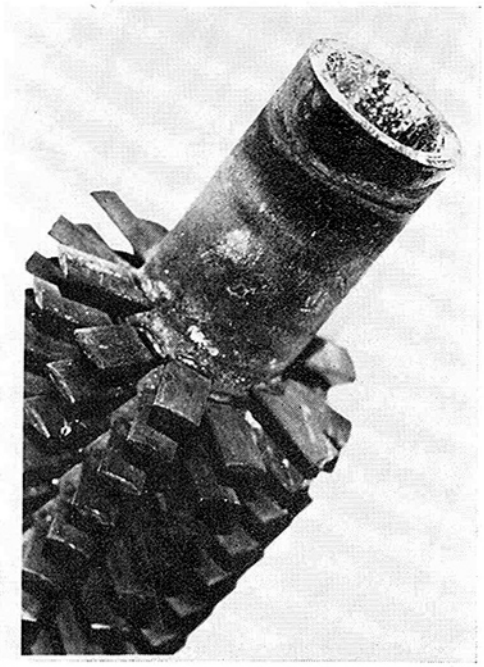

Fig. 1 Photograph of extended surface tubing used

Tube Bank Geometry:

Tube bank number	S_T	$\frac{S_T}{D}$	S_L	$\frac{S_L}{D}$	Arrangement
1	5 in.	2.7	3.5 in.	1.9	Staggered
2	6 in.	3.2	3.25 in.	1.7	Staggered
3	5 in.	2.7	4.5 in.	2.4	Staggered
4	5 in.	2.7	4.5 in.	2.4	In-Line
5	5 in.	2.7	3.25 in.	1.7	Staggered
6	4 in.	2.1	3.5 in.	1.9	Staggered (Reference Arrg't)

Gas inlet temperature: 195 to 422 F
Gas flow: 25,000 to 66,600 lb/hr
Cooling water temperature inside tubes: 60 to 160 F
Water flow: 22,000 to 29,000 lb/hr
Gas Reynolds number: 13,700 to 46,400

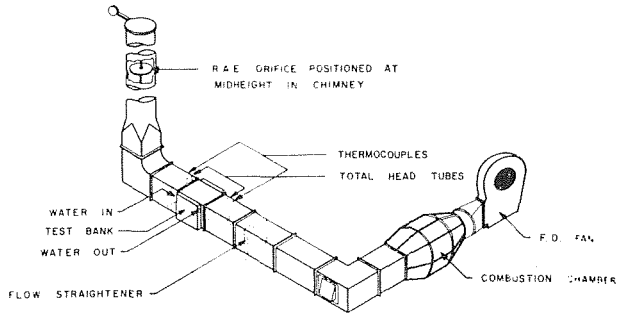

Fig. 2 Isometric view of apparatus

Test Apparatus

The apparatus has already been described in detail in reference [1],[1] and, therefore, a description of only the major components will be repeated here.

An isometric view of the atmospheric-pressure heat transfer facility is shown in Fig. 2. The main air flow is supplied by a forced-draft centrifugal fan to a direct-fired preheater. Air flow is controlled by radial vane dampers arranged at the inlet to the combustion chamber. The air is heated while passing through a double conical, refractory-lined chamber in which light distillate oil is burned. Secondary air for the burner is supplied by a small forced-draft fan.

The heated air passes along the horizontal duct and through an expanded metal flow straightening grid to the test section. The gases are exhausted to the atmosphere through a circular stack containing a calibrated orifice assembly.

Gas temperature was measured with grids of chromel-alumel thermocouples located before and after the test bank in 3-ft × 3-ft square ducts. Each thermocouple was connected through a cold junction and selector switch to a manually operated potentiometer.

In all tests the studded tubes were connected by 180-degree bends external to the test bank to give two parallel water circuits running counter-flow to the gas stream. Cooling water for the cross-flow test bank was supplied from a mixing tank through two calibrated flowrators in parallel to the two circuits forming each test bank. Water temperatures were measured with calibrated, immersion-type mercury thermometers at the inlet and outlet of each flow circuit.

The extended surface tubing used is shown in Fig. 1. (This photograph was supplied by B&W Limited.) The tube banks were built into a 3-ft × 3-ft frontal area by 4-ft long section. As large a bank as possible was fitted centrally into the test section with baffle plates at the top and bottom containing uncooled half-tubes to prevent gas by-passing.

In order to determine the relative performance of each tube bank tested, tube bank Number 6 (S_T = 4.0 in., S_L = 3.5 in.) was designated as a "reference" arrangement and subsequently used as a standard against which the performance of the other tube banks was compared.

[1] Numbers in brackets designate References at end of paper.

Nomenclature

C_p = specific heat of gas at mean gas bulk temperature, Btu/lb-F
d = tube ID, in.
D = tube OD, in.
E_{STD} = friction power lost per sq ft of heat transfer surface, where all gas properties are evaluated at 500 F, fhp/ft²
E'_{STD} = friction power lost per cubic foot of heat transfer surface, where all gas properties are evaluated at 500 F, fhp/ft³
F = draft loss coefficient expressed in velocity heads lost per tube row crossed
F_D = draft loss arrangement factor, as used in Fig. 7
F_H = heat transfer arrangement factor, as used in Fig. 5
g = acceleration due to gravity, ft/sec²
G = gas mass velocity through empty approach duct, lb/hr-ft²
G_g = gas mass velocity through minimum free flow area in tube bank, lb/hr-ft²
h = mean, local gas side heat transfer coefficient (corrected for fin efficiency), Btu/hr-ft²-F
h_{STD} = mean, local gas side heat transfer coefficient based on area of heat transfer surface, at standardized conditions where all properties are evaluated at 500 F, Btu/hr-ft²-F
h'_{STD} = mean, local gas side heat transfer coefficient based on volume of heat transfer surface, at standardized condition where all properties are evaluated at 500 F, Btu/hr-ft³-F
k = gas thermal conductivity at mean gas bulk temperature, Btu/hr-ft-F
k' = tube metal thermal conductivity, Btu/hr-ft-F
N = numbers of tube rows in tube bank
Nu = Nusselt number, $hD/12k$
ΔP = static pressure loss across tube bank, psf
Pr = gas Prandtl number, $C_p\mu/k$
Q_W = heat absorbed by water flowing inside tubes, Btu/hr
Re = gas Reynolds number, $DG_g/12\mu$
Re′ = modified gas Reynolds number, G/μ, ft^{-1}
S_T = transverse tube pitch, in.
S_L = longitudinal tube pitch, in.
S = total outside surface area of tubes, including studs and stud ends, ft²
t_1 = water temperature entering tube bank, F
t_2 = water temperature leaving tube bank, F
ΔT_m = log mean temperature difference between gas and water, F
U = overall heat transfer coefficient between gas and water, Btu hr-ft²-F
U_g = average gas-side heat transfer coefficient, Btu/hr-ft²-F
U_m = tube metal conductance, x/k', Btu/hr-ft²-F
U_W = water-side heat transfer coefficient, Btu/hr-ft²-F
V = velocity of gas, ft/sec
x = equivalent tube wall thickness, ft
ρ = density of gas at mean gas bulk temperature, lb/ft³
μ = viscosity of gas at mean gas bulk temperature, lb/ft-hr

Procedure

Before each test series the tube bank was chemically cleaned to remove scale from the internal surface of the tubes. During each test, the pH level of the water was maintained at 10 by the addition of sodium hydroxide. The water flow rate through both circuits was equalized at a chosen value and the gas flow rate and temperature allowed to stabilize for approximately 30 minutes before the test data were recorded. This same procedure was then repeated over a range of gas flow rates. Isothermal pressure drop tests were also conducted to supplement that data obtained with heat transfer.

The criterion for acceptance of a particular test was that the measured heat loss from the gas agreed with the heat absorbed by the water to within ±5 percent.

The basic steps used to correlate the heat transfer data were as follows:

1 Calculation of an overall heat transfer coefficient (U):

$$U = \frac{Q_W}{S\Delta T_m} \tag{1}$$

where Q_W is the heat absorbed by the water, S is the total outside surface area including the studs, and ΔT_m is the log mean temperature difference between the gas and water.

2 Calculation of the average gas side coefficient(U_g):

$$U_g = \frac{1}{\frac{1}{U} - \frac{1}{U_m} - \frac{1}{U_W}} \tag{2}$$

where $\frac{1}{U_m}$ is the tube metal resistance (equals x/k'; x being the equivalent tube wall thickness and k' the metal conductivity) and $1/U_W$ is the water film resistance.

3 Correction of gas side coefficient for fin efficiency. This correction, based on Gardner's paper [2], gives the mean local gas side heat transfer coefficient (h). The curves shown in Fig. 3 show the fin efficiency and the resulting correction.

4 The mean *local* gas side coefficient (h) was then correlated in the form of (Nusselt no.)(Prandtl no.)$^{-1/3}$ against Reynolds number. The characteristic dimension in the Nusselt and Reynolds numbers was taken as the tube outside diameter, the mass velocity in the Reynolds number is that at the minimum free flow area, and the gas properties are all at reference temperature, T_f, where

$$T_f = \frac{t_1 + t_2}{2} + \frac{\Delta T_m}{2} \tag{3}$$

where $t_1 + t_2/2$ is the average bulk water temperature and ΔT_m is the log mean temperature difference between gas and water.

The basic steps in correlating the draft loss data were as follows:

1 Calculation of draft loss coefficient, F, defined as the number of velocity heads lost per tube row crossed:

$$F = \Delta P \Big/ \frac{\rho V^2}{2g} N \tag{4}$$

where ΔP is the *static* pressure loss from the total head grid upstream of the bank to the total head grid downstream of the bank; where $\frac{\rho V^2}{2g}$ is the velocity head based on the minimum free flow area and the average bulk gas temperature; and where N is the number of tube rows crossed by the gas.

2 Correlation of the draft loss coefficient as a function of gas Reynolds number. Note that only the data obtained during the heat transfer tests were used in these correlations. The isothermal data were used only for comparison purposes.

The properties of air, as contained in NBS circular 564, were used in computing test results and other correlation work.

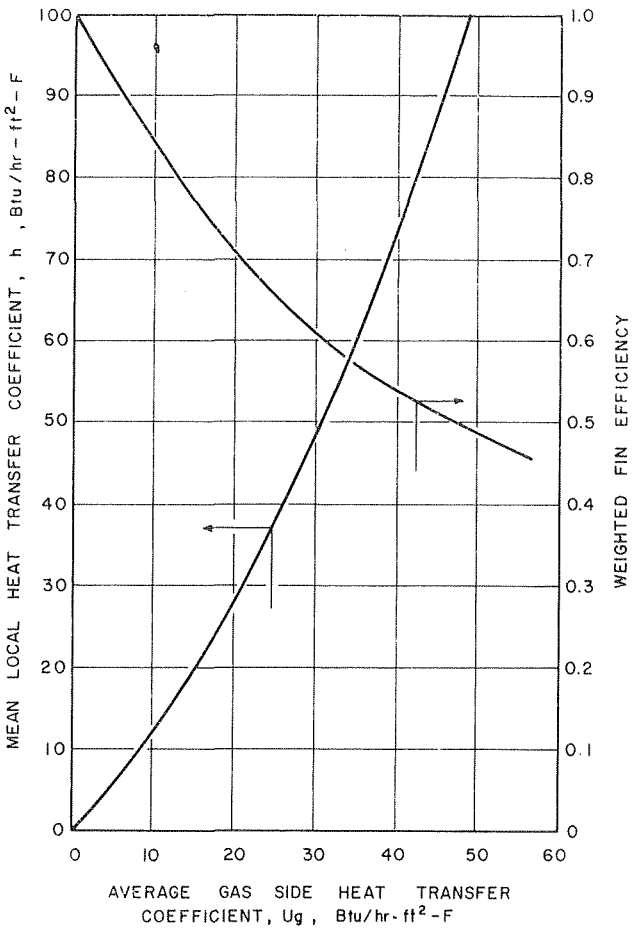

Fig. 3 Fin efficiency correction

Heat Transfer Correlations. Fig. 4 shows plots of $\mathrm{Nu(Pr)}^{-1/3}$ versus Re for the tube banks tested. It can be seen that the in-line tube bank (Curve 4) provided the lowest heat transfer performance of all arrangements, whereas the "reference" arrangement (Curve 6) provided the lowest performance of all staggered arrangements.

Further inspection of the data indicates that for the staggered arrangements the most important factor affecting the heat transfer performance is transverse pitch. The performance is best

SYM.	TUBE BANK	S_T	S_L	ARRG'T	HEAT TRANSFER CORRELATION	STD. DEVIATION
□	1	5.0	3.5	STAG	$Nu\,Pr^{-1/3} = 0.684\,Re^{0.547}$	1.4%
△	2	6.0	3.25	STAG	$Nu\,Pr^{-1/3} = 0.737\,Re^{0.547}$	0.69%
◊	3	5.0	4.5	STAG	$Nu\,Pr^{-1/3} = 0.698\,Re^{0.547}$	0.45%
◇	4	5.0	4.5	IN-LINE	$Nu\,Pr^{-1/3} = 0.575\,Re^{0.547}$	1.5%
○	5	5.0	3.25	STAG	$Nu\,Pr^{-1/3} = 0.698\,Re^{0.547}$	1.2%
△	6	4.0	3.5	STAG	$Nu\,Pr^{-1/3} = 0.639\,Re^{0.547}$	2.7%

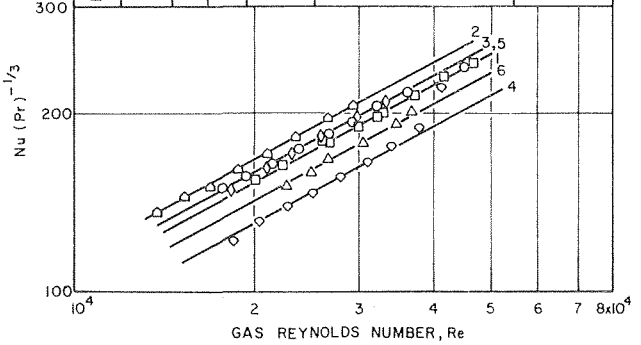

Fig. 4 Heat transfer results

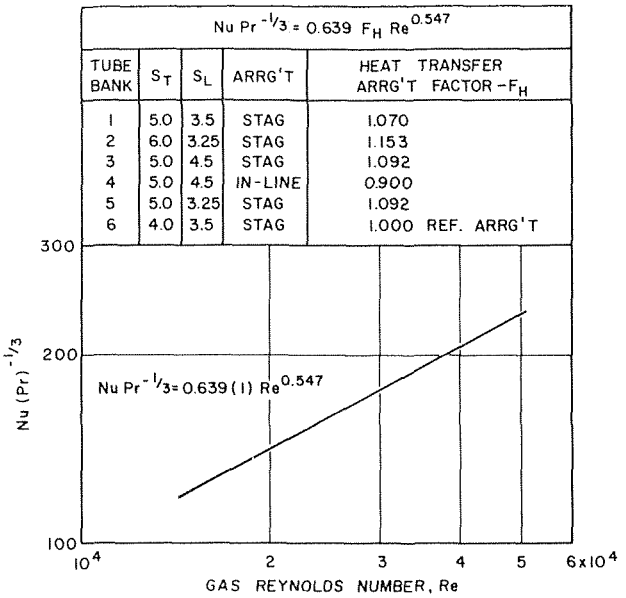

Fig. 5 Heat transfer correlations

with the widest transverse pitch (Curve 2) and progressively decreases as transverse pitch decreases.

To facilitate the use of the information in Fig. 4, our objective was to correlate the experimental data in such a way that a single equation, together with suitable multiplying arrangement factors, would describe the heat transfer performance of all six arrangements tested.

Visual inspection of the data showed that all six tube arrangements gave correlation lines approximately parallel. Accordingly, best lines were fitted to the data by the method of least squares on the assumption that the lines were, in fact, parallel. It is realized that the procedure does not give the best fit for all arrangements. In particular, arrangement 6 (S_T = 4.0 in., S_L = 3.5 in.) would best be correlated by a Reynolds number exponent of 0.680 instead of 0.547. However, the error introduced when using the correlations in the range of Reynolds number covered is small.

Fig. 5 presents the results of the correlation work and shows that the heat transfer performance of each of the six tube banks tested can be described by the equation:

$$\mathrm{Nu} = 0.639 F_H \mathrm{Re}^{0.547} \mathrm{Pr}^{1/3} \tag{5}$$

where F_H is an arrangement factor (tabulated in Fig. 5) based on the relative heat transfer performance of the "reference" arrangement. These factors were determined by dividing the Reynolds number coefficients for each correlating equation given in Fig. 4 by the coefficient for the "reference" arrangement. The standard deviation of the data for each tube bank from equation (5) is, therefore, the same as given in Fig. 4.

Draft Loss Correlation. Fig. 6 shows plots of F versus Re for the tube banks tested. It can be seen that the in-line tube bank provided the lowest draft loss performance (Curve 4), whereas all of the staggered arrangements exhibit similar performance which does not reveal a general trend directly attributable to transverse or longitudinal pitch only.

As was observed with the heat transfer data, all staggered tube arrangements appeared to give correlation lines approximately parallel. Therefore best lines were fitted to the staggered tube draft loss data on the assumption that the lines were parallel. The data for the in-line arrangement were correlated separately since the slope of the line was obviously different.

Fig. 7 presents the results of the correlation work and shows that the draft loss performance of each of the five staggered arrangements can be described by the equation:

$$F = 3.51 F_D \mathrm{Re}^{-0.202} \tag{6}$$

where F_D is an arrangement factor based on the relative draft loss performance of the "reference" arrangement. The same procedure used for determining the heat transfer factor (F_H) was used to determine F_D. The performance of the in-line arrangement can be described by:

$$F = 0.551 \mathrm{Re}^{-0.069} \tag{7}$$

It should be noted that the isothermal pressure drop data obtained provided results nearly identical with the above results obtained with heat transfer.

Relative Heat Transfer-Draft Loss Performance. By using Figs. 5 and 7, the heat transfer and draft loss performance of any of the six arrangements tested can be determined. However, these plots deal only with heat transfer or only with draft loss, but not the two together.

The overall performance of a tube bank is dependent upon the consideration of both heat transfer and draft loss together. Therefore, since the designer of a heat exchanger must judge the relative performance of various tube banks considering both heat transfer and draft loss, a convenient method for doing this is desirable.

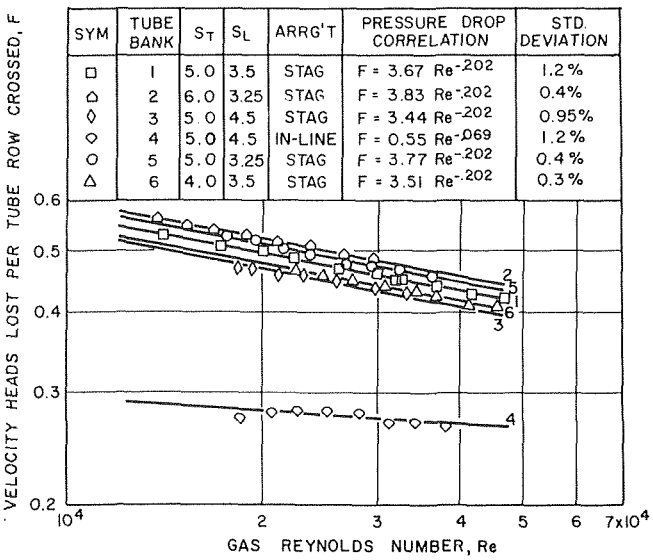

Fig. 6 Draft loss results

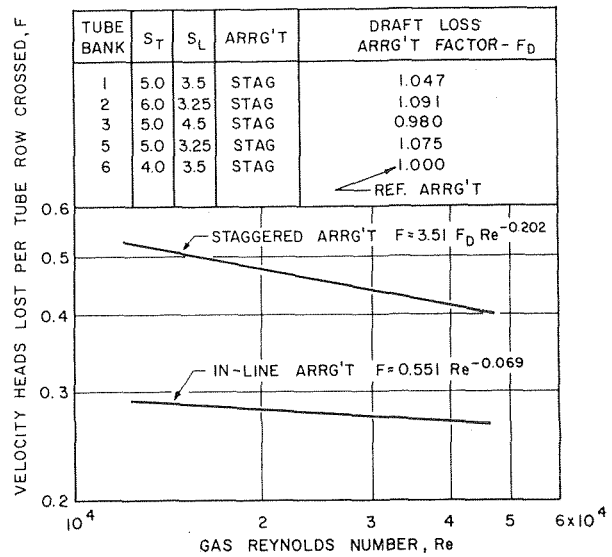

Fig. 7 Draft loss correlations

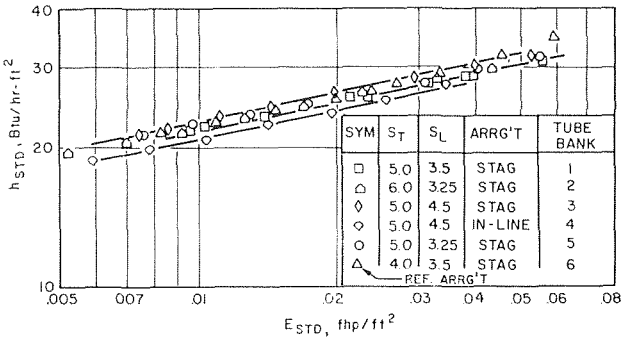

Fig. 8 Relative performance, area basis, h_{STD} versus E_{STD}

One method used in the past (3, 4) has employed plots of a standardized heat transfer coefficient (which is a measure of a tube bank's heat transfer performance) versus a standardized power expenditure (which is a measure of the tube bank's draft loss performance). The term "standardized" means that all gas properties are evaluated at a constant temperature, usually 500 F. (References [3] and [4] provide a complete description and sample calculation for this technique.) With this method, one can determine which tube bank exhibits the best heat transfer performance for a given power expenditure. This comparison can be based on either the heat transfer surface area in the heat exchanger (i.e., Btu/hr-*sq ft*-F, transferred for a given friction horsepower loss *per sq ft*) or the heat exchanger volume (i.e., Btu/hr-*cu ft*-F transferred for a given friction horsepower loss *per cu ft*).

For example, Fig. 8 is a plot of h_{STD} versus E_{STD} on an area basis for all of the data from the six tube banks tested. Standard conditions are based on gas properties at 500 F. This plot shows that the staggered tube bank Number 3 (S_T = 5.0 in., S_L = 4.5 in.) transfers more heat per square foot of heat transfer surface for a given friction horsepower expended than any of the other arrangements tested. However, the relative performance of all staggered arrangements including the "reference" arrangement is quite close, whereas the performance of the in-line arrangement is the worst on this particular basis.

Fig. 9 is a plot of h'_{STD} versus E'_{STD} on a *volume* basis for representative data from all tube banks. This plot shows that for a given friction power expended, the "reference" arrangement transfers more heat per cubic foot of heat exchanger volume than any other arrangement. The in-line arrangement is again the worst on this basis.

A second method that can be used to determine the relative performance of various tube banks employs plots of the ratio h_{STD}/E_{STD} (that is, the ratio of energy transferred to energy lost) versus Reynolds number. The Reynolds number in this case is based on the mass velocity in a given size empty flow channel into which the heat transfer surface is to be installed. This concept is useful when heat transfer surface has to be installed in a fixed size flow passage in which the gas flow rate is also fixed, and

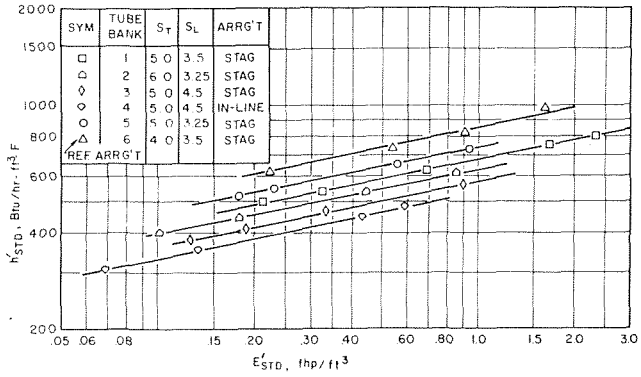

Fig. 9 Relative performance, volume basis, h'_{STD} versus E'_{STD}

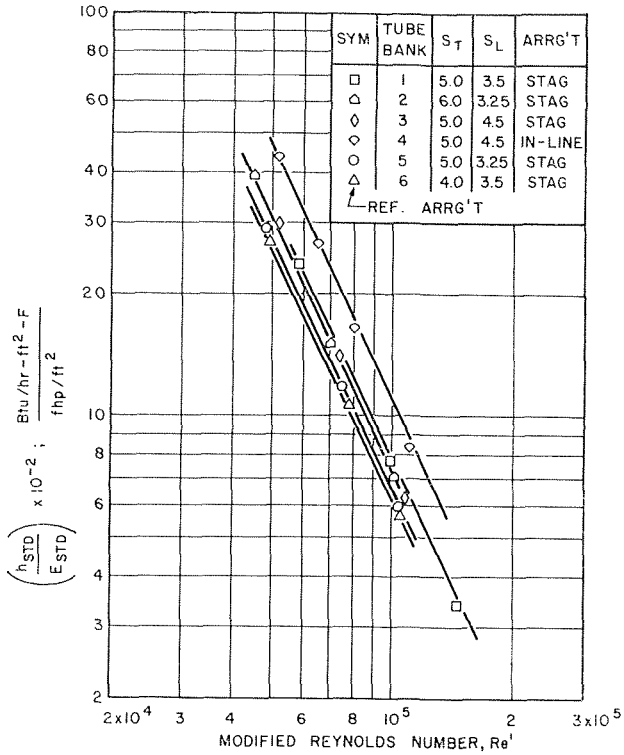

Fig. 10 Performance index based on h_{STD}/E_{STD} versus modified Reynolds number

when the optimum surface configuration for these fixed conditions is desired. One example of this type of use is in gas-cooled reactor design, where certain flow passage dimensions may have been set by space limitations and where gas flow rates may have been set by load requirements.

For example, Fig. 10 is a plot of the ratio h_{STD}/E_{STD} versus a

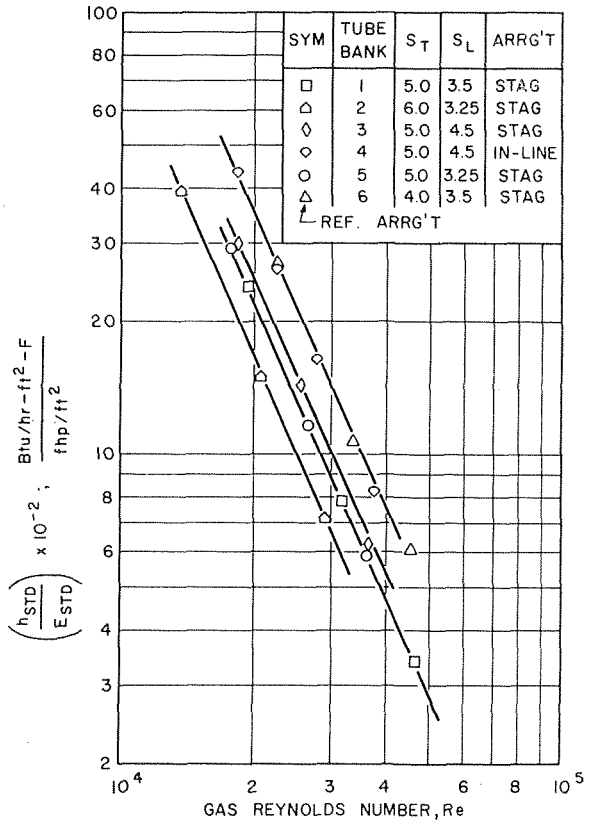

Fig. 11 Performance index based on h_{STD}/E_{STD} versus gas Reynolds number

modified Reynolds number for representative data from all tube banks. A modified Reynolds number (which does not include diameter) is used for this comparison since the empty duct size for all tube banks was approximately the same size, and since we are primarily interested in determining the relative performance of the various surfaces *in the same empty duct.*

This plot shows that for a given Reynolds number in a fixed size empty duct, the in-line arrangement provides the highest ratio of energy transferred to energy lost. The in-line arrangement would, therefore, be considered the optimum surface for these fixed conditions. Note, however, that this method gives no indication of the amount of surface required by any arrangement to transfer a given amount of heat from the gas to the water.

For comparison purposes, the "reference" arrangement is seen to provide the lowest ratio of energy transferred to energy lost.

To emphasize the importance of knowing what criterion has been used in a given relative performance study, we selected a variation of this second method which might be of some interest to a designer. This method employs plots of the ratio h_{STD}/E_{STD} (as was used above) versus the Reynolds number in the minimum free flow area of the tube bank.

As shown on Fig. 11, the comparative performance of the various tube banks has once more been changed and now both the in-line arrangement and the "reference" arrangement provide the highest ratios of energy transferred to energy lost. But again, there is no indication of the amount of surface required to do a given job.

Summary of Relative Performance

To summarize the discussion on the different methods of comparing extended surface tube bank performance, the designer should keep in mind the information each method conveys:

Method 1

(*a*) h_{STD} versus E_{STD}, on an *area* basis, determines the arrangement that, for a given friction horsepower loss, will transfer the most heat per square foot of heat transfer surface.

(*b*) h'_{STD} versus E'_{STD}, on a *volume* basis, determines the arrangement that, for a given friction horsepower loss, will transfer the most heat per cubic foot of heat exchanger volume.

Method 2

(*a*) h_{STD}/E_{STD} versus empty-duct Reynolds number determines the arrangement that, for a given Reynolds number in a fixed empty flow passage, will provide the highest ratio of energy transferred to energy lost.

(*b*) h_{STD}/E_{STD} versus minimum-flow-area Reynolds number determines the arrangement that, for a given Reynolds number in the tube bank being considered, will provide the highest ratio of energy transferred to energy lost.

Since the designer of heat exchangers which might use the type of extended surface investigated here is seldom faced with designing under the conditions imposed under Method 2, we consider this method of less value than Method 1. However, use of the various methods of determining the relative performance of different surface arrangements shown here may be of some value in certain cases.

References

1 Miller, J. M., and Reising, G. F. S., "Gas Flow Across Banks of Tubes," *Engineering*, Vol. 186, Dec. 5, 1959, pp. 737–740.

2 Gardner, K. A., "Efficiency of Extended Surface," TRANS. ASME, Vol. 67, 1945, pp. 621–631.

3 Kays, W. M., and London, A. L., *Compact Heat Exchangers*, National Press, Palo Alto, Calif., 1955.

4 Fairchild, H. N., and Welch, C. P., "Convection Heat Transfer and Pressure Drop of Air Flow Across In-Line Tube Bank at Close Back Spacings." ASME Paper 61-WA-250, Dec. 1961.

Heat Transfer by Thermal Radiation and Laminar Forced Convection to an Absorbing Fluid in the Entry Region of a Pipe

B. E. PEARCE
Graduate Student;
Presently,
Member of the Technical Staff,
The Aerospace Corp.,
El Segundo, Calif.

A. F. EMERY
Professor.

Department of Mechanical Engineering,
University of Washington,
Seattle, Wash.

The heat transferred to an absorbing fluid by coupled thermal radiation and laminar forced convection is computed for the entrance region of a tube with circular cross section. The tube wall is black and isothermal and the fluid enters with either a fully developed (parabolic) or uniform axial velocity distribution. Both gray and approximately nongray absorption are considered with the nongray absorption specified by the "box model" which approximates the spectral absorption of a vibration-rotation band in a molecular gas by an absorption coefficient which is a constant within an effective bandwidth and zero elsewhere. The box model is applied to carbon monoxide and to carbon dioxide and the calculations additionally include the effects of variable transport properties and variable density. It is shown that for the range of parameters considered in this paper, the effect of the absorbed radiation is to increase the heat transfer near the entrance by as much as a factor of four and to decrease the thermal entry length by a factor of ten. The effects of radiation are shown to be more important when the fluid is heated than when it is cooled. By comparing the solutions for a gray fluid with constant properties with those using the box model of the absorption it is demonstrated that the gray approximation is not quantitatively accurate. Approximate solutions are investigated and it is shown that when the radiation-convection interaction is weak the radiation heat flux can be computed approximately by ignoring the interaction and using the known forced convection temperature solution. When the interaction is intense, both the coupling of the radiation and convection and also the spectral absorption must be accounted for in calculating the heat transfer. The box model is shown to be an acceptable method for specifying the approximate spectral absorption coefficient in nonisothermal gases.

Introduction

The thermal analysis of modern engineering systems must often include the effects of thermal radiation and forced convection. When the radiation is either very weak or very intense one mode of heat transfer may be clearly predominant. However, in some cases both can be of equal importance and the interaction of radiation with forced convection must be considered in establishing the overall heat transfer in the system. The description of this coupling effect in a manner suitable for engineering analysis is not well established, primarily because of the difficulty of accounting for the heat transfer by thermal radiation from nonisothermal gases.

Heat transfer from isothermal gases can be adequately determined in terms of the total band absorptance and transmittance for homogeneous optical paths. In contrast, a nonisothermal gas requires a knowledge of the spectral absorption coefficient, which is a function of the local thermodynamic state. That energy which is absorbed in gases with temperatures below 5000 deg R is due to vibrational-rotational energy transitions in the near-infrared and is strongly spectrally dependent. This precludes the use of a single mean absorption coefficient. A practical specification of the absorption is offered by those approximate absorption coefficients which ignore the complicated spectral fluctuations but yet maintain the gross properties of the true absorption. An example of such an approximation is given by the "box model" described by Penner [1][1] and recently examined by Cess, et al. [2], in which the absorption is constant over an effective bandwidth. An improved model has been given by Edwards and Menard [3] as an extension of early work by Schaak [4] which makes an additional correction for the distribution of line intensities within the band. This is the "exponential wide-band" model. Both models are most accurate at large pressure-path lengths or high temperatures where the individual lines in a band are overlapped.

Contributed by the Heat Transfer Division and presented at the Winter Annual Meeting, Los Angeles, Calif., November 16–20, 1969, of The American Society of Mechanical Engineers. Manuscript received by Heat Transfer Division, April 15, 1969. Paper No. 69-WA/HT-16.

[1] Numbers in brackets designate References at end of paper.

The purpose of this paper is to apply approximate specifications of the absorption to study the heat transfer in an absorbing fluid in laminar flow at the entrance to a black isothermal tube with circular cross section. The fluid is initially isothermal and enters with either a uniform or parabolic axial velocity distribution. A solution consists of specifying the temperature within the fluid at arbitrary axial and radial locations and the heat transfer rate downstream from the entrance when the wall temperature is different from the initial temperature. This problem was chosen in order to minimize the complications in a coupled radiation-convection problem while displaying the essential features of the interaction. The problem is particularly convenient because the thermal and hydrodynamic development are of the "boundary layer" type. The types of absorption to be considered are the gray approximation, in which the absorption coefficient is spectrally uniform, and the box model, or effective bandwidth approximation. In the gray case the fluid properties and the absorption coefficient are independent of temperature while both the density and the transport properties are taken to be temperature dependent in the nongray case.

Previous studies of this type are those of Einstein [5], de Soto and Edwards [6], and de Soto [7]. Einstein considered the flow of a constant property gray fluid with a parabolic velocity distribution. He reported only the total heat transfer to the fluid in a tube with a length of five diameters for a single ratio of wall to initial temperature. de Soto and Edwards, and de Soto also considered constant property flow with a parabolic velocity distribution but use the more accurate wide-band model for the absorption in carbon dioxide. The solution [6] is approximate in that the radiation heat flux is computed from the known forced convection temperature distribution. de Soto's solution [7] is exact within the restriction to constant properties in that the temperature is established by the coupled radiation-convection effects. All these solutions predict that the total heat transfer is significantly augmented by the radiation, with de Soto [7] showing an increase at the entrance by a factor of two for temperatures below 2500 deg R.

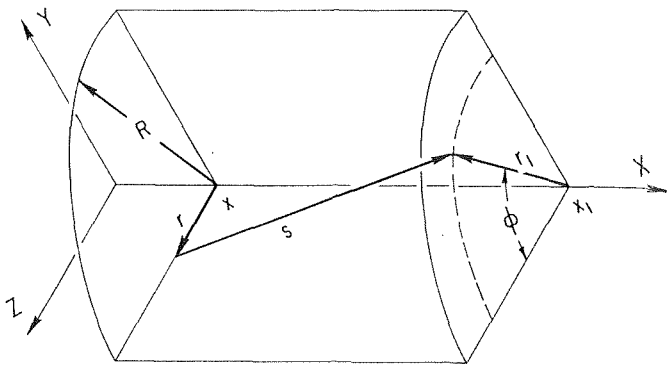

Fig. 1 Cylindrical coordinate system

Formulation of the Problem

Consider the cylindrical coordinate system in Fig. 1 where an arbitrary point is denoted by (x, r) and a variable point by (x_1, r_1, ϕ). The distance s is then given by

$$s = \{(x - x_1)^2 + r^2 + r_1^2 - 2rr_1 \cos \phi\}^{1/2} \quad (1)$$

and s_w denotes the value of s when $r_1 = R$, the tube radius.

Following [8], the monochromatic intensity at the point (x, r) in a direction opposite to that of increasing s is given by the integrated equation of transfer

$$I_\omega = J_\omega e^{-\tau(s_w)} + \int_0^{s_w} \rho\kappa_\omega B_\omega e^{-\tau(s)} ds \quad (2)$$

where J_ω is the intensity at the wall, B_ω is the Planck function, and $\tau(s)$ is the optical path length defined by

Nomenclature

A = total band absorption, cm^{-1}
a, b, c = exponents for the temperature dependence of the specific heat, viscosity, and conductivity, respectively
B_ω = Planck function Btu/ft²-hr-cm^{-1}-steradian
c_p = specific heat at constant pressure Btu/lb_m-deg R
c = speed of light in equation (28a)
$F(\tau_0)$ and $F(\bar{\tau})$ = integrals defined by equations (17) and (25)
H = nondimensional enthalpy, $(h - h_0)/c_{p0}T_0 = (\theta^{1+a} - 1)/(1 + a)$
h = enthalpy, Btu/lb_m (or Planck's constant in equation (28a))
$H(\tau_0\eta)$ and $H(\bar{\tau}\eta)$ = integrals defined by equations (15a) and (23)
I_ω = specific intensity of radiation. Btu/hr-ft²-cm^{-1}-steradian
J_ω = intensity from the wall. Btu/hr-ft²-cm^{-1}-steradian
$K(\bar{\tau}_0\eta, \tau_0\eta_1)$ and $K(\bar{\tau}\eta, \bar{\tau}\eta_1)$ = integrals defined by equations (15b) and (24)
k = thermal conductivity, Btu/hr-ft-deg R (or Boltzmann's constant in equation (28a))
N = conduction-radiation parameter $\rho\kappa k/4\sigma T_0^3$
Nu = Nusselt number, $2Rq_w/k(T_m - T_w)$
P = nondimensional pressure, $(p - p_0)/{}^1/_2\rho_0 u_m^2$
p = pressure, atm
Pr = Prandt lnumber, $\mu_0 c_{p0}/k_0$
q = heat flux, Btu/hr-ft²
R = tube radius, ft or cm
Re = Reynolds number, $2R\rho_0 u_m/\mu_0$
r = radial coordinate
s = distance along optical path, ft or cm
$S(T)$ = integrated band intensity, cm^{-2}-atm^{-1}
T = absolute temperature, deg R or deg K
u, v = axial and radial velocity, ft/sec
U = nondimensional axial velocity, u/u_m
V = nondimensional radial velocity, v Re$/u_m$
x = axial coordinate
σ = Stefan-Boltzmann constant, 0.1718×10^{-8} Btu/hr-ft²-deg R⁴
κ = mass absorption coefficient, ft²/lb_m
τ = optical distance
ϕ = angle defined in Fig. 1
μ = viscosity, lb_m/sec-ft
θ = nondimensional temperature, T/T_0
ω = wave number, cm^{-1}
ξ = nondimensional axial coordinate, $x/R/$RePr
η = nondimensional radial coordinate, r/R
ρ = fluid density, lb_m/ft^3
Ω = solid angle, steradian

Subscripts

ω = monochromatic value
0 = evaluated at initial conditions or reference conditions
m = mean values
w = evaluated at the wall
1 = dummy variable of integration
R = radiation component (also used as a superscript)

$$\tau(s) = \int_0^s \rho(s')\kappa_\omega(s')ds'. \tag{3}$$

It is assumed that the fluid is in local thermodynamic equilibrium and scattering is not considered. The divergence of the radiation heat flux vector

$$-div\ \mathbf{q}^R = -div\left(\int_0^\infty \int_0^{4\pi} I_\omega d\Omega d\omega\right) = \int_0^\infty \int_0^{4\pi} \frac{dI_\omega}{ds} d\Omega d\omega \tag{4}$$

is the additional source term in the energy equation

$$\rho u \frac{\partial h}{\partial x} + \rho v \frac{\partial h}{\partial r} = \frac{1}{r}\frac{\partial}{\partial r}\left(\frac{rk}{c_p}\frac{\partial h}{\partial r}\right) - div\ \mathbf{q}^R. \tag{5}$$

Using the equation of transfer and its integral (2), the radiation contribution is

$$\begin{aligned} -div\ \mathbf{q}^R &= \rho \int_0^\infty \kappa_\omega \int_0^{4\pi} (I_\omega - B_\omega) d\Omega d\omega \\ &= \rho \int_0^\infty \left\{ \kappa_\omega \int_0^{4\pi} J_\omega e^{-\tau(s_w)} d\Omega \right. \\ &\left. + \kappa_\omega \int_0^{4\pi} \int_0^{s_w} \rho \kappa_\omega B_\omega e^{-\tau(s)} ds d\Omega - 4\pi\kappa_\omega B_\omega \right\} d\omega. \end{aligned} \tag{6}$$

When specialized to the cylindrical coordinate system, equation (6) becomes

$$\begin{aligned} -div\ \mathbf{q}^R = \rho \int_0^\infty \left\{ \kappa_\omega \int_{-\infty}^\infty J_\omega(x_1) \int_0^{2\pi} e^{-\tau(s_w)} (R - r\cos\phi) \right. \\ \times R \frac{d\phi dx_1}{s_w^3} + \kappa_\omega \int_{-\infty}^\infty \int_0^R \rho\kappa_\omega B_\omega r_1 \int_0^{2\pi} e^{-\tau(s)} \\ \left. \times d\phi dr_1 \frac{dx_1}{s^2} - 4\pi\kappa_\omega B_\omega \right\} d\omega. \end{aligned} \tag{7}$$

In equation (7) and the subsequent work the temperature distribution and the wall intensity are circumferentially uniform.

At the wall, the heat flux is in the radial direction and the radial component of the flux due to radiation is

$$q^R = \int_0^\infty \int_0^{4\pi} I_\omega \cos(r, s) d\Omega d\omega.^2 \tag{8}$$

Following Heaslet and Warming [9], the flux is conveniently split into inwardly and outwardly directed components according to

$$q^R = q_+^R - q_-^R$$

where

$$\begin{aligned} q_+^R &= q^R \text{ if } \cos(r, s) \geq 0 \text{ (outward)} \\ q_-^R &= q^R \text{ if } \cos(r, s) < 0 \text{ (inward)} \end{aligned} \tag{9}$$

At the wall, $r = R$, the two components are

$$\begin{aligned} q_+^R = \int_0^\infty \left\{ \int_{-\infty}^\infty J_\omega \int_0^{2\pi} e^{-\tau(s_w)} (R - R\cos\phi)^2 R d\phi \frac{dx_1}{s_w^4} \right. \\ \left. + \int_{-\infty}^\infty \int_0^R \rho\kappa_\omega B_\omega r_1 \int_0^{2\pi} e^{-\tau(s)} (R - r_1\cos\phi) d\phi \frac{dr_1}{s^3} dx_1 \right\} d\omega \end{aligned} \tag{10a}$$

$$q_-^R = \pi \int_0^\infty J_\omega d\omega \tag{10b}$$

and for a black wall

$$q_-^R = \sigma T_w^4. \tag{10c}$$

[2] Henceforth q^R is used to denote only the radial component.

Equation (7) for the divergence and equations (10) for the heat flux are valid for arbitrary absorption and a temperature distribution dependent upon both x and r. The wall intensity can have an arbitrary dependence upon x. However, specifying the spatial variation of J_ω or κ_ω in any generality significantly complicates the solution. Even numerical solutions for the coupled problem are generally prohibitive because of the excessive number of quadratures which must be performed. According to Einstein [5] the integral terms constitute the most significant difficulty due to the addition of radiation even when the absorption coefficient and wall intensity are spatially uniform.

For the laminar flow of a gas in a tube the effects due to radiation pressure and radiation energy density are negligible and are not included in the present problem. The momentum and continuity equations are then expressed as

$$\rho u \frac{\partial u}{\partial x} + \rho v \frac{\partial u}{\partial r} = \frac{1}{r}\frac{\partial}{\partial r}\left(r\mu \frac{\partial u}{\partial r}\right) - \frac{dp}{dx} \tag{11a}$$

$$\frac{\partial}{\partial x}(\rho u r) + \frac{\partial}{\partial r}(\rho v r) = 0. \tag{11b}$$

The energy equation (5) and the momentum equation (11a) are in boundary layer form and it has been demonstrated [10], in the absence of radiation, that they adequately describe laminar flow in a tube. Moreover, according to de Soto and Edwards [6], the true radiative heat flux is accurately approximated by that which is calculated for an infinite cylinder with a radial temperature distribution the same as that at the axial position at which the flux is to be evaluated. Consequently, the axial temperature variation is neglected for the purpose of determining the radiation contribution, which is consistent with the boundary layer approximations in equations (5) and (11a). Extending the criterion given by Sparrow and Cess [11] for flow between infinite parallel planes, the boundary layer solution will be accurate for axial positions away from the entrance such that

$$N\ \mathrm{RePr}\left(\frac{x}{R}\right) \gg 1$$

where N is the conduction-radiation parameter, $N = \rho\kappa k/4\sigma T_0^3$. This hypothesis was tested in [6] and [7] and found to be valid except very near the entrance, where the boundary layer approximations themselves are least accurate.

An additional approximation which is made in evaluating the radiation contribution to the energy equation and heat flux is to neglect the change in wall temperature at the entrance. The wall is treated as an infinite tube at the uniform temperature T_w. Because of the rapidly diminishing shape factor from the entrance disk to any point on the wall more than a few radii from the entrance (more rapid than $\exp -(x/R)$) this approximation is consistent with the boundary layer approximations. For the solutions presented in this paper the error in the total heat flux at the position closest to the entrance is less than ten percent.

In the conservation equations the density and transport properties are taken to be variable since the large temperature difference will preclude the use of constant properties. For a thermally perfect gas, the nondimensional enthalpy and density are given by

$$H = \frac{1}{1+a}(\theta^{1+a} - 1) \text{ and } \rho/\rho_0 = \frac{p}{\theta p_0}. \tag{12}$$

Transport properties are taken to be power law functions of the temperature and independent of pressure.

The solutions require the simultaneous satisfaction of equations (5) and (11) with the radiation terms specified by equation (7). Because of the coupling between the equations and the nonlinear dependence of the radiation source terms on the temperature, the solutions are numerical and of an iterative type. In performing the iterations, equations (5), (11a), and (11b) are solved sequentially. Further discussion of the numerical solutions is given in the Appendix.

Solutions for a Gray Fluid

Because of the simplicity of the gray fluid and because solutions for such a fluid are essentially the most general which can be obtained, a series of computations was performed to provide some quantitative insight into the effects of radiation. Furthermore, since the gray approximation is so unrealistic a model for the absorption of real fluids, the calculations are additionally restricted to constant density and transport properties.

The momentum and continuity equations in nondimensional form for this case are

$$U\frac{\partial U}{\partial \xi} + V\frac{\partial U}{\partial \eta} = \frac{2}{\eta}\,\mathrm{Pr}\,\frac{\partial}{\partial \eta}\left(\eta\frac{\partial U}{\partial \eta}\right) - \frac{dP}{d\xi} \tag{13a}$$

$$\frac{\partial}{\partial \xi}(U\eta) + \frac{\partial}{\partial \eta}(V\eta) = 0. \tag{13b}$$

These equations apply only when the initial axial velocity is uniform since a parabolic initial velocity distribution represents the entire solution when the fluid properties are constant.

Using the work of Heaslet and Warming [9], the energy equation with the approximate radiation contribution can be written as

$$U\frac{\partial \theta}{\partial \xi} + V\frac{\partial \theta}{\partial \eta} = \frac{2}{\eta}\frac{\partial}{\partial \eta}\left(\eta\frac{\partial \theta}{\partial \eta}\right) + 2\frac{\tau_0^3}{N}H(\tau_0\eta)\theta_w^4 + 2\frac{\tau_0^4}{N}\int_0^1 \theta^4(\eta_1)\eta_1 K(\tau_0\eta_1, \tau_0\eta)d\eta_1 - 2\frac{\tau_0^2}{N}\theta^4(\eta) \tag{14}$$

where

$$H(\tau_0\eta) = \int_1^\infty K_1(\tau_0 y)I_0(\tau_0\eta y)\frac{dy}{y} \tag{15a}$$

$$\left.\begin{aligned} K(\tau_0\eta, \tau_0\eta_1) &= \int_1^\infty K_0(\tau_0\eta y)I_0(\tau_0\eta_1 y)dy \quad \eta > \eta_1 \\ &= \int_1^\infty K_0(\tau_0\eta_1 y)I_0(\tau_0\eta y)dy \quad \eta < \eta_1 \end{aligned}\right\} \tag{15b}$$

At the wall, the nondimensional heat flux is

$$\frac{Rq_w}{k_0T_0} = -\left.\frac{\partial \theta}{\partial \eta}\right|_{\eta=1} - \frac{\tau_0^2}{N}F(\tau_0)\theta_w^4 + \frac{\tau_0^3}{N}\int_0^1 \theta^4(\eta_1)\eta_1 H(\tau_0\eta_1)d\eta_1 \tag{16}$$

where

$$F(\tau_0) = \int_1^\infty K_1(\tau_0 y)I_1(\tau_0 y)\frac{dy}{y^2} \tag{17}$$

(K_0, K_1, I_0, and I_1 are modified Bessel functions of the first and second kind of order zero and one, respectively [12]). Since the absorption coefficient is uniform, the integrals H, K, and F need be evaluated only once as functions of radial position in the tube.

Solutions for this problem are given as functions of the conduction-radiation parameter N, the ratio of wall to inlet temperature θ_w, and the optical radius $\tau_0 = \rho\kappa R$. For the particular case of $\theta_w = 2.5$ and a parabolic velocity distribution the solutions presented here can be compared with those of Einstein [5], who considered the contributions to the radiation terms from both the axial temperature gradient and the wall upstream from the entrance. This comparison is therefore a check of the validity of the approximations made in this work. Einstein reports only the mean temperature at the exit of a tube with a length of five diameters. These are compared with the present solutions in Fig. 2 for three values of the optical radius and for the solution without radiation. The agreement is excellent, particularly at the larger Peclet numbers, for which the boundary layer approximations were explicitly derived.

The solution without radiation, $\tau_0 = 0$, is given to illustrate the effect of radiation, which is shown to be of increasing importance with increasing Peclet number. For small RePr, implying either small velocity or a large thermal diffusivity, molecular diffusion acts nearly uniformly over the tube cross section and radiation is relatively less important. In contrast, for larger RePr, molecular diffusion is confined to a region near the tube wall while the radiation contribution, acting across the entire cross section, becomes relatively more important.

Solutions for a gray fluid with constant density and transport properties are illustrated in Fig. 3 in terms of the Nusselt number based on the total heat flux. These few cases are shown in order to illustrate the relative effect of each of the three independent variables N, τ_0, and θ_w. The solution without radiation, ob-

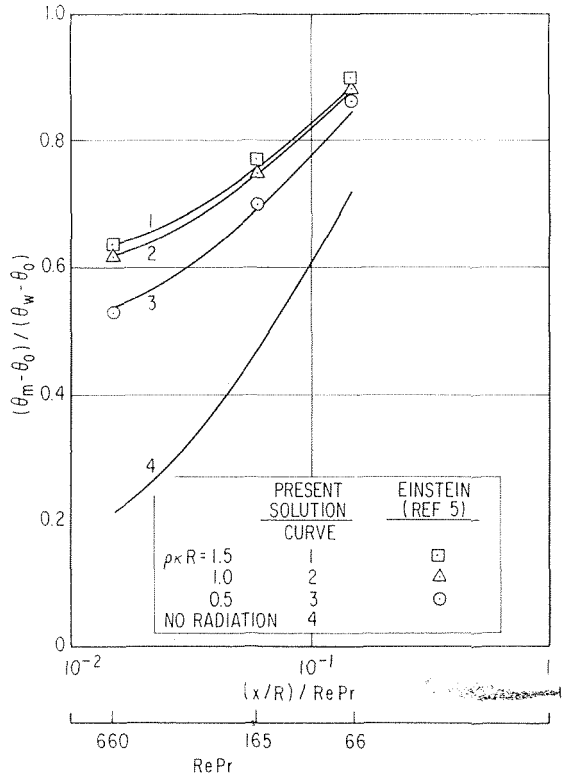

Fig. 2 Mean temperature at the exit to a tube five diameters long with a gray, constant property fluid and a parabolic velocity distribution, $\theta_w = 2.5$

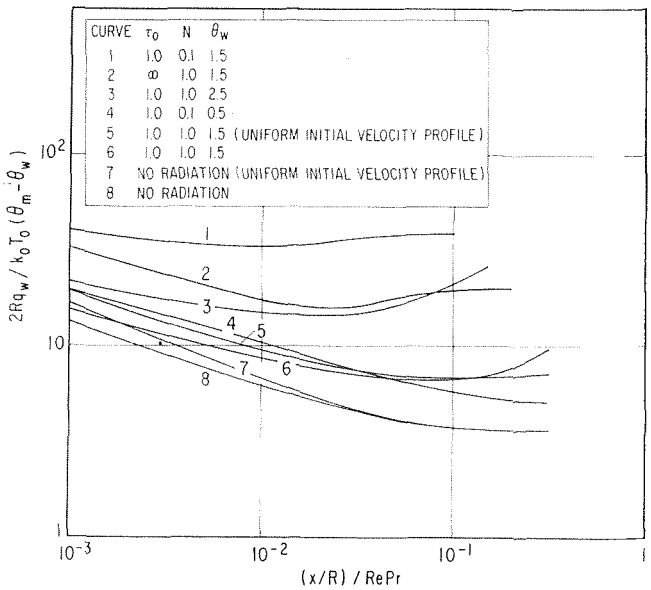

Fig. 3 Nusselt numbers for a gray, constant property fluid with a parabolic velocity distribution

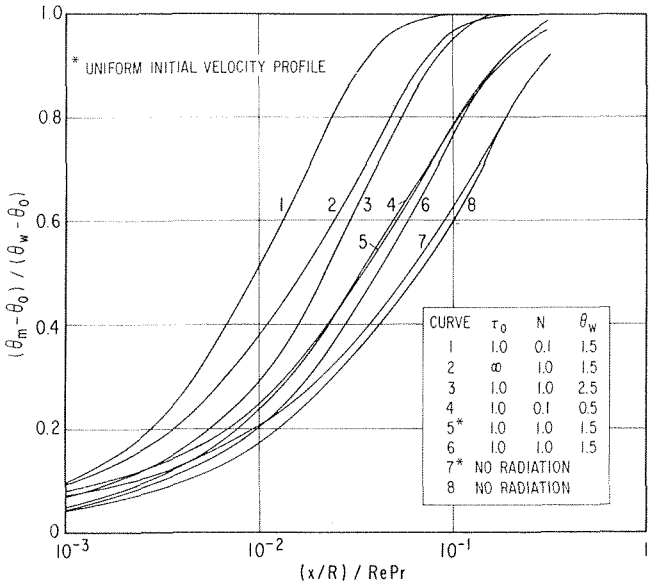

Fig. 4 Mean temperatures for a gray, constant property fluid with a parabolic velocity distribution

tained from the present numerical solutions by deleting the radiation terms, is also shown for comparison. In all cases the Nusselt number with radiation is larger than that without radiation. This is due to two effects. The first is that radiation is an additional mechanism for heat transfer through the fluid resulting in an increased heat flux. Secondly, the radiation source term augments the rate of thermal development so that the mean temperature approaches the wall temperature at a more rapid rate. This rapid thermal development is shown in Fig. 4 for the same combinations of N, τ_0, and θ_w used in Fig. 3. Both effects act to increase the local Nusselt number, although the effects are not equally important in all regions of the flow. Initially, the Nusselt number is augmented only by the additional heat flux, while further downstream, the more rapid thermal development contributes when the mean temperature approaches the wall temperature. In fact, far from the entrance, the increased Nusselt number can be due entirely to the accelerated thermal development because the total heat flux for an absorbing fluid can be less than that from a nonabsorbing fluid for certain combinations of the three independent parameters.

It can be seen from the solutions shown in Fig. 3 that the Nusselt number for a heated fluid is different from that for a cooled fluid. This effect is due to the contribution from the region near the wall to the radiation heat flux. When the wall temperature is greater than the inlet temperature the radiation heat flux is much larger than when the wall temperature is less than the inlet temperature. The Nusselt number for $\theta_w > 1$ is therefore greater than that for $\theta_w < 1$ for equal N and τ_0. Also, the axial dependence of the Nusselt number is different, with the case for $\theta_w > 1$ having a minimum value. The radiation component of the Nusselt number can be shown to be essentially an increasing function of the axial distance when $\theta_w > 1$ while it is a decreasing function for $\theta_w < 1$. When added to the conduction contribution, which decreases with axial distance, the result is a minimum value when $\theta_w > 1$ and a monotone decreasing Nusselt number when $\theta_w < 1$.

By a heuristic argument it can be shown that the radiation component of the Nusselt number approaches a definite value far from the entrance which is given by

$$\mathrm{Nu}_{R\infty} = \lim_{\xi\to\infty} \frac{2Rq^R}{k_0T_0(\theta_m - \theta_w)} = 8\,\frac{\tau_0^2}{N}\,F(\tau_0)\theta_w^3. \qquad (18)$$

The approach to this value is from below for $\theta_w > 1$ and from above for $\theta_w < 1$. The numerical solutions could not be continued to this limit because of the errors involved when θ_m is very near θ_w. Values of $\tau_0F(\tau_0)$ are given in Table 1 which can be used to calculate this limiting Nusselt number and provide some estimate of the importance of radiation. No limiting value was obtained for the conduction component.

Table 1 Values of the integral $F(\tau_0)$

τ_0	0.01	0.05	0.1	0.5	1	5	10
$\tau_0F(\tau_0)$	0.005	0.0237	0.0395	0.149	0.154	0.225	0.25

The Nusselt numbers in Fig. 3 and mean temperatures in Fig. 4 illustrate the effect of changing the conduction-radiation parameter, N, while maintaining a constant optical thickness. Decreasing N increases the relative effect of radiation and this is reflected by the increased Nusselt number and the rapid thermal development shown for the cases with $N = 0.1$.

Of particular interest is the effect of the optical radius τ_0. If τ_0 is increased with N held constant the effect is to increase the tube radius. This effect is shown by comparing the solutions for $\tau_0 = 1$ with that for $\tau_0 \to \infty$ (optically dense) which shows that there is an upper limit to the effect of tube size. For all practical purposes, the flow becomes optically dense when $\tau_0 \cong 10$. If the optical radius is changed with τ_0/N held constant the effect is to change only the absorption coefficient. It was found that there is a value of τ_0, approximately 1.5 in this case, such that the effect of a radiation is a maximum. This is in agreement with the results given by Einstein [5] and also the work by Viskanta [13] who found the maximum to occur at $\rho\kappa L = 1.85$, where L is the distance between parallel planes. This effect is explained by appealing to the limiting forms taken by the radiation contribution for very weak and very intense absorption. We have, from Sparrow and Cess [11] that

$$\lim_{\rho\kappa\to 0} \operatorname{div} \mathbf{q}^R = 0(\rho\kappa);\ \lim_{\rho\kappa\to\infty} \operatorname{div} \mathbf{q}^R = 0\left(\frac{1}{\rho\kappa}\right).$$

Consequently, the effect of radiation vanishes when the fluid is transparent or opaque and there is an intermediate value of the absorption coefficient such that the effect is a maximum.

A solution with a uniform initial velocity distribution was obtained in one case and is shown in Fig. 3. The effect of the developing velocity is essentially the same as that without radiation, giving an increased Nusselt number at the entrance and coinciding with the solution for a fully developed velocity distribution far from the entrance.

The temperature distributions obtained from the present solutions were found to be essentially the same as those without radiation when the radiation-convection interaction is weak. However, when the interaction is intense, such as for the curves 1, 2, and 3 in Fig. 3, there is an essential difference. In contrast to the case with no radiation, there is no axial length beyond which the nondimensional temperature distribution $(\theta - \theta_0)/(\theta_m - \theta_0)$ becomes independent of axial position, or "fully developed." Moreover, for those cases studied which did reach a state of full thermal development, it did not occur until the centerline temperature was very near the wall temperature. Viskanta [13] presents solutions for a thermally fully developed flow between parallel plates. The center line temperature was an independent parameter and solutions were presented for $0.1 < \theta(\text{℄})/\theta_w < 10$. However, the results for a developing flow with radiation in a tube suggest that flows for which $(\theta(\text{℄}) - \theta_w)/\theta_w$ exceeds 20 or 30 per cent may not be representative of full thermal development.

Nongray Gases

The type of abosrption which is of interest is due to vibrational-rotational energy transitions in molecular gases which occur in the infrared region of the spectrum ($1 < \lambda < 15$ microns) and which contributes to heat transfer in gases whose temperatures are in the range $500 < T < 5000$ deg R. Two models of the absorption coefficient which have been used are the box model [2] and the exponential wide-band model [7]. The former treats the absorption as constant over an effective band-

width and requires a specification of the integrated band intensity and the bandwidth. The latter model likewise deals with the gross absorption but allows the absorption to vary within a band to account for line structure in an approximate manner. For numerical calculations, in which the integral terms are evaluated directly, the box model yields the most economical algorithim, although the wide-band model is recognized to be the more accurate of the two. Accordingly, one of the purposes of this study is to assess the applicability of the box model.

An appropriate gas for the application of the box model is carbon monoxide, a diatomic gas with a single fundamental band for which the overtones contribute little to the absorption. Following Penner [1] and Cess, et al. [2], the model is constructed to maintain the proper integrated band intensity

$$\frac{\overline{\rho\kappa}}{p}\,\Delta\omega = S(T) = \frac{\rho}{p}\int_{\Delta\omega}\kappa_\omega\,d\omega = S(T_0)\,\frac{T_0}{T} \tag{19}$$

where $S(T_0) = 237\ \text{cm}^{-2} - \text{atm}^{-1}$ and $T_0 = 540$ deg R. Defining the effective bandwidth to be that interval centered at the band center for which the intensity is at least 0.001 times the maximum intensity gives [2]

$$\Delta\omega(T) = \Delta\omega_0\left(\frac{T}{T_0}\right)^{1/2} = 214\left(\frac{T}{T_0}\right)^{1/2}\text{cm}^{-1} \tag{20}$$

which yields

$$\frac{\overline{\rho\kappa}}{p} = 1.11\left(\frac{T_0}{T}\right)^{3/2}\text{cm}^{-1} - \text{atm}^{-1} \tag{21}$$

where ω_0, the band center, is at 2143 cm^{-1}. The effective absorption coefficient, equation (21), is that used by Cess, et al. [2]. A comparison of the total band absorption

$$A(pL) = \int_{\Delta\omega}\left\{1 - \exp - \frac{\overline{\rho\kappa}}{p}\,(pL)\right\}d\omega \tag{22}$$

predicted by the box model and wide-band model is shown in Fig. 5 for the fundamental band of CO. Experimental data from Abu-Romia and Tien [14] is also shown. The two models are in acceptable agreement with the experimental data at moderate pressure-path lengths. Using the box model, the integrals expressing the radiation contribution to the divergence and heat flux terms become

$$H(\bar{\tau}\eta) = \int_0^\infty\int_0^\pi e^{-\tau}(1 - \eta\cos\phi)d\phi\,\frac{dx_1}{s_w^3} \tag{23}$$

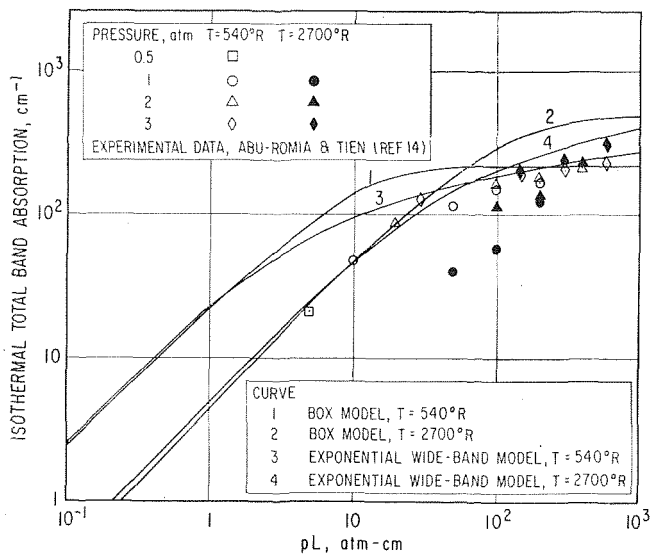

Fig. 5 The isothermal total band absorption at 540 and 2700 deg R for the fundamental band of CO using the box model and exponential wide-band models

$$K(\bar{\tau}\eta,\bar{\tau}\eta_1) = \int_0^\infty\int_0^\pi e^{-\tau}d\phi\,\frac{dx_1}{s^2} \tag{24}$$

$$F(\bar{\tau}) = \int_0^\infty\int_0^\pi e^{-\tau}(1 - \cos\phi)^2 d\phi\,\frac{dx_1}{s_w^4}. \tag{25}$$

The total contribution of radiation to the energy equation and the heat flux then becomes

$$\frac{-R^2}{k_0T_0}\,\text{div}\,\mathbf{q}^R = \frac{\bar{\tau}^2}{N}\,\frac{p}{p_0}\,\theta^{-1}\Delta\omega_0\left\{\frac{\pi B_{\omega_0}}{\sigma T_0^4}\,H(\bar{\tau}\eta) + \bar{\tau}\,\frac{p}{p_0}\int_0^1\theta^{-3/2}\eta_1\,\frac{\pi B_{\omega_0}}{\sigma T_0^4}\,K(\bar{\tau}\eta,\bar{\tau}\eta_1)d\eta_1 - \frac{\pi B_{\omega_0}}{\sigma T_0^4}\right\} \tag{26}$$

$$\frac{Rq^R}{k_0T_0} = \frac{\bar{\tau}\theta_w^{1/2}}{N}\,\Delta\omega_0\left\{\frac{\pi B_{\omega_0}}{\sigma T_0^4}\left[F(\bar{\tau}) - \frac{1}{4}\right] + \bar{\tau}\,\frac{p}{p_0}\int_0^1\theta^{-3/2}\frac{\pi B_{\omega_0}}{\sigma T_0^4}\,\eta_1 H(\bar{\tau}\eta_1)d\eta_1\right\} \tag{27}$$

where

$$\frac{\pi B_{\omega_0}}{\sigma T_0^4} = 15\left(\frac{hc}{\pi kT_0}\right)^4\omega_0^3\left\{\exp\left(\frac{hc\omega_0}{kT_0\theta}\right) - 1\right\}^{-1} \tag{28a}$$

and

$$N = \frac{k\bar{\tau}/R}{4\sigma T_0^3};\ \bar{\tau} = 1.11\,\theta_0^{-3/2}p_0R \tag{28b}$$

and

$$\tau = \int_0^s\rho\bar{\kappa}ds = \bar{\tau}\int_0^s\theta^{-3/2}(s')\,\frac{p}{p_0}\,ds'. \tag{28c}$$

It is additionally assumed that

$$\int_{\Delta\omega}B_\omega d\omega = B_{\omega_0}\Delta\omega$$

for which the error was computed to be less than one percent.

In solving for the temperatures, the temperature dependence of the properties was accounted for by power laws as

$$c_p/c_{p_0} = \theta^{0.147};\ \mu/\mu_0 = \theta^{0.642};\ k/k_0 = \theta^{0.85}. \tag{29}$$

Because of the temperature dependence of the density and viscosity, the velocity distribution changes with the axial position giving a hydrodynamic entrance region problem even when the velocity profile is initially developed. The numerical solution in the present work was verified, without the radiation terms, by comparing the solution for air with those given by Worsøe-Schmidt and Leppert [10]. The Nusselt numbers for the two solutions differed by less than 2 percent and since the solutions from [10] were obtained with a very small grid spacing, the agreement is taken as verification of the present finite difference approximations. The algorithms for the integral terms were checked against those computed for a uniform absorption coefficient.

Nusselt numbers for CO with the absorption specified by the box model were computed for four cases and are shown in Fig. 6. For three, the initial temperature is 1000 deg R and the wall temperatures are 1500 and 500 deg R with a parabolic initial velocity distribution and 1500 deg R with a uniform initial velocity distribution. The additional case is for an initial temperature of 530 deg R and a wall temperature of 2500 deg R with a parabolic velocity distribution. Since the transport properties, density, and absorption coefficient now depend upon the temperature, the optical radius and conduction-radiation parameter are not independent. The values used in these solutions are based on the initial temperature and the initial pressure, which is always one atmosphere. The Nusselt number is based on the thermal conductivity evaluated at the mean temperature.

The Nusselt numbers in Fig. 6 and the corresponding mean temperatures in Fig. 7 do not differ qualitatively from those of

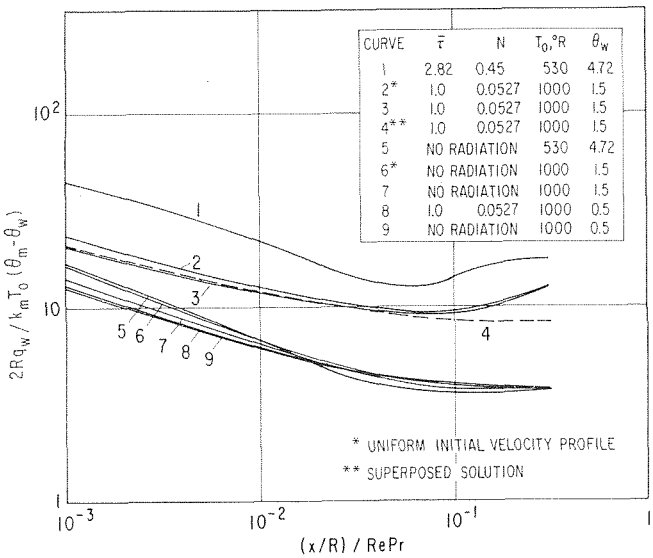

Fig. 6 Nusselt numbers for CO using the box model absorption coefficient with temperature dependent properties and a parabolic initial velocity distribution

a gray fluid and constant properties, although the effect of radiation is quantitatively less for equal optical radii and conduction-radiation parameters because the absorption takes place in a narrow band. The minimum value of the Nusselt number and the much larger heat transfer and rate of thermal development for $\theta_w > 1$ are found as for the gray fluid. Moreover, it is expected that there exists an optical radius for which the fluid can be considered optically dense and for which the effect of radiation will be maximum. However, these values would now be dependent upon the temperature and pressure. Also, the observations about the occurrence of a fully developed temperature profile carry over to the nongray fluid. The solutions for $\theta_w = 1.5$ and 0.5 appeared to reach a fully developed temperature distribution while that for $\theta_w = 4.72$ showed no indication of this condition within the axial length for which the solution was obtained. The relationship between the solutions with a uniform and parabolic initial velocity is also the same as that for the gray fluid. Since the net heat transfer and bulk thermal development are integrated effects there is no particular feature which distinguishes the nongray from the gray absorption. However, since the absorption occurs only in a narrow band, the effect of radiation depends strongly on the relative position of this band and the spectral distribution of the radiation intensity. Even when presented in nondimensional form, the overall effects of the radiation are therefore, in contrast to a gray fluid, strongly dependent upon the absolute temperature of the fluid and the walls.

The Nusselt numbers and mean temperatures given in Figs. 6 and 7 are presented as accurate estimates of the effect of radiation on forced convection in a tube with black walls. They can also serve to assess the accuracy of more approximate solutions. Approximate solutions which estimate the heat transfer and thermal development in nongray gases are of particular value since exact solutions are difficult to formulate and calculate. Even the solutions which use a uniform absorption coefficient are of value even though moderately difficult to obtain, especially for complex geometries, because they are much simpler than the accurate nongray solutions.

In the present paper two approximations are examined and compared to the solutions using the box model for CO. One uses an equivalent gray fluid with constant properties and the other is a "superposed" solution, which calculates the radiation heat flux for a nongray fluid from the temperature distribution of the solution without radiation. Both these approximations are used when the wall temperature is not substantially different from the initial temperature (i.e., $\theta_w = 1.5, 0.5$). The Nusselt numbers and mean temperatures are compared in Figs. 6 and 7,

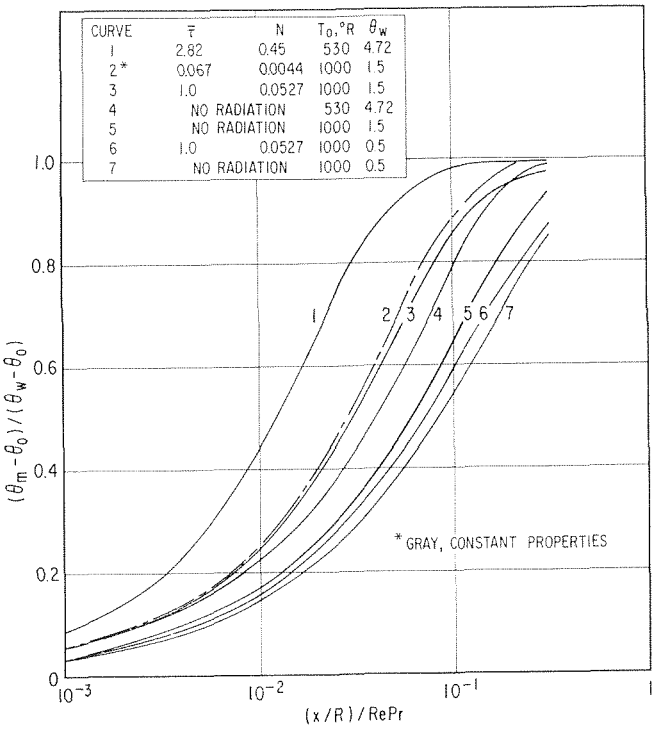

Fig. 7 Mean temperatures for CO using the box model absorption coefficient with temperature dependent properties and a parabolic initial velocity distribution

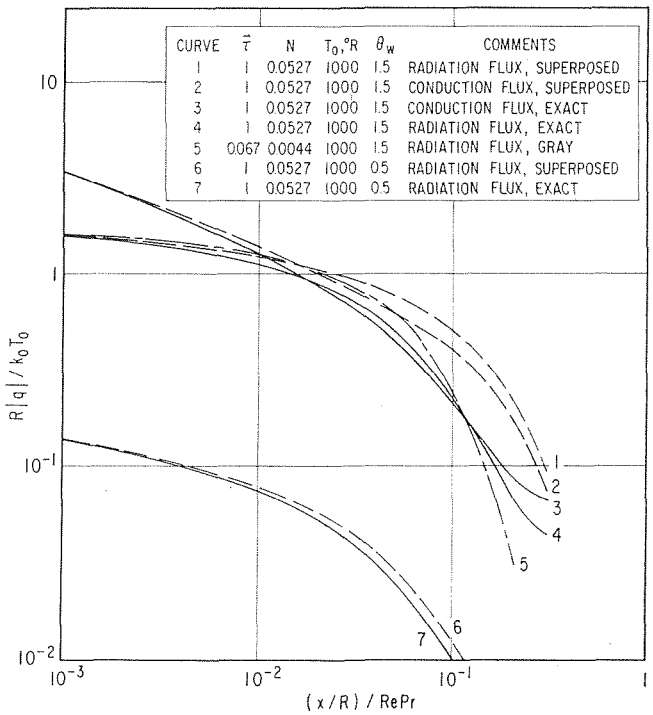

Fig. 8 The radiation and conduction heat flux in CO for $T_0 = 1000$ deg R and $T_w = 1500$ and 500 deg R with a parabolic initial velocity distribution

respectively. However, a more precise comparison is made in Fig. 8 by showing the conduction and radiation components of the heat flux. For these two cases the equivalent gray fluid is based on the wall temperature according to

$$(\rho\kappa)_e = \frac{\int_{\Delta\omega} \overline{\rho\kappa_\omega} B_\omega(T_w) d\omega}{\int_0^\infty B_\omega(T_w) d\omega} = \frac{\pi}{\sigma T_w^4} \overline{\rho\kappa_\omega(T_w)} B_\omega(T_w) \quad (30)$$

Table 2 Parameters for a gray fluid equivalent to the nongray fluid with T_0 = 1000 deg R, $\bar{\tau}$ = 1, and N = 0.0527

θ_w	τ_0	N
1.5	0.0668	0.0044
0.5	0.01	0.0044

while the conduction-radiation parameter is based on the initial temperature. The equivalent parameters are given in Table 2. The superposition approximation to the cold wall heat flux is good and is due to the fact that radiation has little effect on this solution and therefore the temperature distributions with and without radiation are essentially the same. The gray approximation for this case is poor, and is not shown. When the fluid is heated, both the superposed and gray approximations are very good near the entrance. However, far from the entrance, where radiation has affected the temperature distribution, these approximations are inaccurate. In addition to the heat flux, the equivalent gray fluid permits an estimate of the mean temperature. The comparison in Fig. 7 shows that the gray approximation gives too rapid a thermal development. The choice of matching conditions for the gray approximation used here is not unique and there may be others which could improve the approximation at specific points. However, for the case where θ_w = 1.5, the radiation interaction is sufficiently important so that there is probably no single value of the equivalent absorption which applies uniformly over the entire axial length.

For the case where θ_w = 4.72, the temperature variation is so large that no attempt was made to approximate the solution by an equivalent gray fluid. Only the superposed solution is compared with the exact solution in Fig. 9. It is obvious that the radiation interaction in this case is very important and that the superposed solution, and likewise the equivalent gray fluid, are grossly inadequate. It is precisely for problems like this that the effect of the coupling between convection and radiation and the spectral dependence of the absorption must be accurately specified.

A solution which is complementary to that of de Soto and Edwards [6] can be obtained by applying the box model to the flow of carbon dioxide. Since the solution in [6] is of the superposed type and because the interest is primarily with the radiation contribution, it is only necessary to perform the computations by using the box model with the nonradiation temperature distribution. The box model requires an effective bandwidth and integrated intensity for each vibration-rotation band. Unlike CO, which is a diatomic gas with a single band which contributes essentially all the absorption, CO_2 is a polyatomic gas for which several bands are important. Following de Soto and Edwards, only the three bands centered at 2.7, 4.3, and 15 microns are considered. The integrated intensity and effective bandwidth for the 4.3μ band are given by Penner [1]. However, no effective bandwidth estimates were found for the other two bands. Lacking this information, the box model for the remaining bands was constructed in the following manner. The total absorption for the 4.3μ band was computed using the box model and was found to match that of the wide-band model at pL = 1 cm-atm at 540 deg R. If the other bands are also matched at the same conditions, it is possible to infer their effective bandwidths for the box model when the integrated intensities are known. Using the integrated intensities for the 2.7 and 15μ bands listed by Tien [15], the box model for CO_2 is defined in Table 3. The temperature dependence of the integrated intensity and bandwidths are the same as those assigned to CO.

Table 3 Parameters for the box model of CO_2 at 540 deg R

Band microns	Band center cm^{-1}	Integrated absorption cm^{-2}-atm^{-1}	Effective bandwidth cm^{-1}
15	667	330	77
4.3	2410	2700	108
2.7	3750	61	350

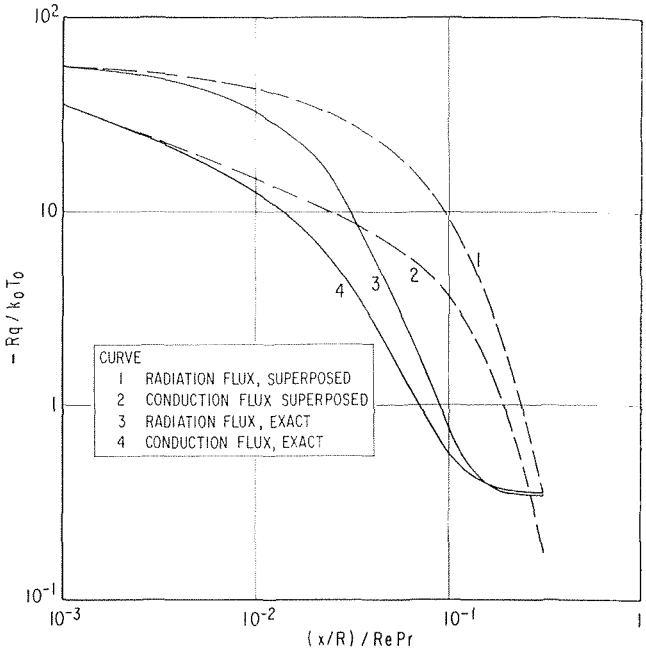

Fig. 9 The radiation and conduction heat flux in CO for T_0 = 530 deg R and T_w = 2500 deg R with $\bar{\tau}$ = 2.82, N = 0.45 (2 in. diameter tube) and a parabolic initial velocity distribution

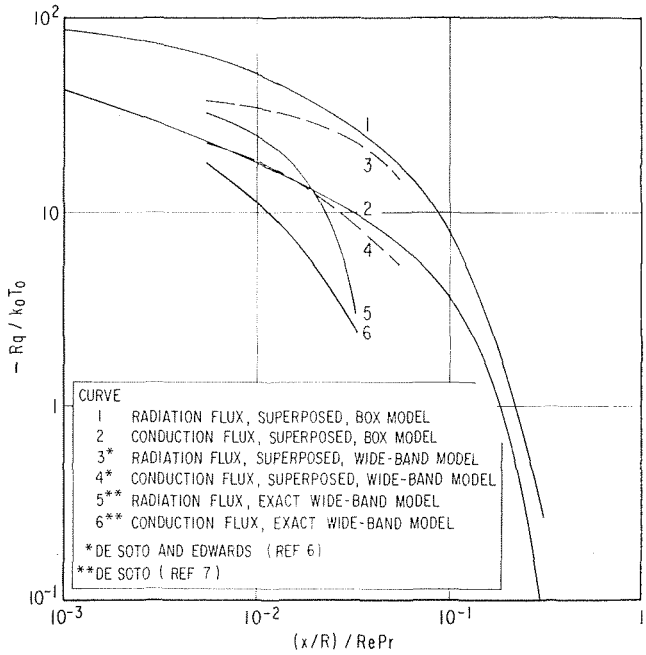

Fig. 10 Comparison of the radiation and conduction heat fluxes in CO_2 predicted by the box model and wide-band model for T_0 = 530 deg R and T_w = 2500 deg R (2-in.-dia tube) with a parabolic initial velocity distribution

A comparison of the superposed solutions using the above parameters for the box model and the solution given by de Soto and Edwards [6] is given in Fig. 10. In addition to the models for the absorption, the solutions differ in that the present calculations include variable density and transport properties with the exponents a = 0.194, b = 0.685, c = 0.943, while the properties used in [6] were evaluated at the mean temperature of 1500 deg R. The comparison shows that the box model does not give the same radiation heat flux as that obtained for the wide-band model. Some of the difference can be attributed to the difference between the solutions with variable and constant properties. However, most is due to the different absorption predicted by the two models. Of course, the two models are not expected to give the same results. The wide-band model accounts for the

line structure, which will be an important factor when temperature differences are large. The important feature which is illustrated by this comparison is that the box model gives what can be regarded as an acceptable estimate of the radiation heat flux. The box model represents an improvement over the gray approximation by accounting in an approximate manner for the spectral dependence of the absorption. The exponential wide band model is a further improvement which accounts for the effect of the distribution of line intensities within a band.

The coupled solution for CO_2 using the wide-model given by de Soto [7] is also shown in Fig. 10 and can be compared with the superposed solution given by de Soto and Edwards [6]. It is interesting to note that the relationship between the superposed and coupled solution for CO_2 is essentially the same as that for CO, as shown in Fig. 9. The thermal development is actually more rapid for CO_2 and is due to the additional absorption of the three-band system. However, the absorption of CO_2 is due primarily to the 4.3μ band in these temperature ranges.

The box model of the absorption due to vibration-rotation bands cannot be applied without modification to every gas or to arbitrarily large path lengths or pressures. Penner [1] discusses the limits of effective bandwidth calculations. For instance, he argues that for some gases, including CO_2, intense rotational lines can make a contribution to the absorption outside the effective bandwidth for high pressures and large optical densities. He indicates that the box model is most appropriately applied to hydrogen chloride and water vapor in addition to carbon monoxide.

Conclusions

An extension of the boundary layer approximation to the radiation contribution to the energy equation and the heat flux is achieved by observing that the radiation contributions are determined essentially by the radial temperature distribution. This permits an efficient solution which proceeds in a manner similar to that used in ordinary forced convection flows. In the present work this approximation is verified by the agreement with Einstein's solutions, which do not make this assumption. The additional simplification of neglecting the contribution of the tube wall upstream from the entrance permits the use of simplified integral expressions for the radiation terms which are strictly valid for an infinite cylinder. Error estimates show that this is acceptable for the set of parameters used in the present work. It should be noted that this approximation permits the solutions to be obtained for a nondimensional axial coordinate without specifying the absolute axial location.

Solutions which account for both a gray and an approximate nongray absorption coefficient are given for several sets of values of the wall and initial temperatures, a characteristic optical radius and the conduction-radiation parameter. The range of these parameters is sufficient to include both very intense and very weak radiation-convection interactions. The gray case provides the most simple solutions which are independent of the absolute temperature level and contain the essential features of the radiation interaction. The nongray solutions, which use the box model approximation to the band absorption of CO and CO_2 provide more accurate estimates of the effect of radiation from real gases and provide a basis for assessing the validity of approximate solutions.

The primary effects due to absorbed radiation in this entrance region problem are an increase in the heat flux at the wall during the initial thermal development and an acceleration of the adjustment of the fluid temperature to that at the wall. There is an essential difference in the heat transfer when the fluid is heated or cooled. The Nusselt number or heat transfer coefficient for a heated fluid has a minimum value upstream from the point at which the flow approaches full thermal development. When the fluid is cooled this minimum value is not found and the effect of the radiation is proportionally smaller than for a heated fluid. In all cases the Nusselt number is increased due to the effect of radiation. In agreement with the findings in [5] and [13] a value for the absorption coefficient exists for which the effect of radiation is a maximum. The value $\tau_0 = 1.5$ agrees with that found in [5] for a gray, constant property fluid.

Temperature distributions in the fluid are affected by the absorbed radiation. The effect is small when the radiation interaction is small, such as that for a cooled fluid. For more intense interactions, such as for a heated fluid, the effect is to delay the onset of full thermal development until the mean temperature is very nearly equal to the wall temperature. If the radiation interaction is very intense, it is doubtful that full thermal development will occur.

Use of the box model to approximate the absorption coefficient of CO was found to yield an approximation to the spectral absorption of real gases which provides heat transfer solutions by directly extending the methods used for a gray fluid. The heat transfer and bulk thermal development are qualitatively the same as those for a gray fluid but due to the narrow spectral region of the absorption, the gross effects are less pronounced. These solutions account for variable properties and density and when the effect of radiation is large, the effect of variable transport properties is of secondary importance.

Two approximate solutions are compared with the more exact coupled solutions with the box model of the absorption. A gray fluid with a properly chosen effective absorption coefficient can be used to estimate the thermal development in a real fluid when the effect of radiation is small. The predictions of the nongray radiation heat flux given by an equivalent gray fluid are not satisfactory. When the effect of radiation is small the radiation heat flux can be better approximated by a superposition technique which uses the temperature distribution without radiation to calculate the radiation heat flux. This method can be used with any specification of the absorption. For intense radiation, neither approximation is satisfactory and the coupled solution with nongray absorption is required.

The box model is applied to CO_2 and compared with a solution using the more exact exponential wide-band model. It is indicated that the box model can be used as an alternative specification to the wide-band model for polyatomic gases.

The present solution method in which the integrals are evaluated directly by quadratures is an alternative to Hottel's zone method [5]. Unlike the zone method, which is most easily applied to equal volume and surface zones, the direct integration method permits the accuracy and flexibility of Gaussian quadratures to be utilized. The present method is probably most useful when the surface geometry is regular so that the limits of integration are uncomplicated and the integrals need not be split (i.e., the boundary is a natural surface of the coordinate system).

It has been demonstrated by a sequence of specific solutions that thermal radiation can have a significant effect on the heat transfer in laminar flow when the fluid absorbs thermal radiation. For the moderate range of parameters used in this study the heat flux was increased by a factor of as much as three to four and the effective entry length decreased by a factor of ten relative to that due to molecular conduction alone. By using a relatively simple specification of the spectral absorption which uses a constant absorption coefficient acting over an effective bandwidth, solutions were obtained which give a better approximation to the absorption of real gases than that obtained from a gray fluid.

Acknowledgments

The authors wish to acknowledge a grant of computer time from the Research Computer Center of the University of Washington. The first author also acknowledges the financial support of the Graduate School and the College of Engineering of the University of Washington, and an NDEA Title IV Fellowship.

References

1 Penner, S. S., *Quantitative Molecular Spectroscopy and Gas Emmissivities*, Addison-Wesley, Reading, Mass. Chapt. 11, 1959.

2 Cess, R. D., Mighdoll, R., and Tiwari, S. M., "Infrared Radiative Heat Transfer, in Nongray Gases," *International Journal of Heat Mass Transfer*, Vol. 10, 1967, pp. 1521–32.

3 Edwards, D. K., and Menard, W. A., "Correlations for Absorption by Methane and Carbon Dioxide Gases," *Applied Optics*, Vol. 7, 1964, pp. 847–52.

4 Schaak, A., *Industrial Heat Transfer*, Wiley, New York, 1965.

5 Einstein, T. H., "Radiant Heat Transfer to Absorbing Gases Enclosed in a Circular Pipe with Conduction, Gas Flow, and Internal Heat Generation," NASA TR R-156, 1963.

6 de Soto, S., and Edwards, D. K., "Radiative Emission and Absorption in Nonisothermal Nongray Gases in Tubes," Heat Transfer and Fluid Mech. Institute, *Proceedings*, 1965, pp. 358–72.

7 de Soto, S., "Coupled Radiation, Conduction and Convection in Entrance Region Flow," *Internal Journal of Heat Mass Transfer*, Vol. 11, 1968, pp. 39–53, (1968).

8 Vincenti, W. G., and Kruger, C. H., *Introduction to Physical Gas Dynamics*, Wiley, New York, Chapt. 11, 1965.

9 Heaslet, M. A., and Warming, R. F., "Theoretical Prediction of Radiative Transfer in a Homogeneous Cylindrical Medium," *J. Quant. Spectrosc. Radiative Transfer*, Vol. 6, 1966, pp. 751–74.

10 Worsøe-Schmidt, P. M., and Leppert, G., "Heat Transfer and Friction for Laminar Flow of Gas in a Circular Tube at High Heating Rate," *International Journal of Heat Mass Transfer*, Vol. 8, 1965, pp. 1281–1301.

11 Sparrow, E. M., and Cess, R. D., *Radiation Heat Transfer*, Brooks/Cole, Belmont, Calif., 1966, p. 267.

12 Watson, G. N., *A Treatise on the Theory of Bessel Functions*, Cambridge Univ. Press, New York, 1966, p. 79.

13 Viskanta, R., "Interaction of Heat Transfer by Conduction, Convection, and Radiation in a Radiating Fluid," JOURNAL OF HEAT TRANSFER, TRANS. ASME, Series C, Vol. 85, 1963, pp. 318–328.

14 Abu-Romia, M., and Tien, C. L., "Measurements and Correlations of Infrared Radiation of Carbon Monoxide at Elevated Temperatures," *Journal of Quantitative Spectros Radiative Transfer*, Vol. 6, 1966, pp. 143–67.

15 Tien, C. L., "Thermal Radiation Properties of Gases," to appear in *Advances in Heat Transfer*, Vol. 5, Academic Press, New York.

16 Pearce, B. E., "Heat Transfer by Thermal Radiation and Forced Convection to a Laminar Flow of an Absorbing Fluid in the Entrance Region of a Tube," PhD thesis, Dept. of Mechanical Engineering, University of Washington, 1968.

APPENDIX

Numerical Solution

The partial derivatives in equations (5) and (11) were approximated by finite differences for a rectangular mesh with varying Δr and Δx. The energy equation (5) has the additional term accounting for radiation which is defined by definite integrals. The integral terms are evaluated numerically and it is necessary that the nodal points for the radial finite differences correspond to the quadrature points of the numerical integration. To achieve satisfactory accuracy and good resolution near the wall, where gradients are the largest, a nonuniform radial grid spacing was used. By experimenting with the order of the quadrature and checking the finite difference solutions with known solutions, it was found that a 15-point Gaussian quadrature using the positive roots of a 30th order Legendre polynomial gave satisfactory results. The energy equation (5), with the radial derivatives in implicit form and the addition of the radiation terms, becomes a set of simultaneous nonlinear algebraic equations for the temperature or enthalpy at the radial grid points.

Use of the approximation that the radiation contribution is determined by the local radial temperature distribution reduces the energy equation to a parabolic type which can be solved in essentially the same manner as the problem without radiation. That is, the solution proceeds downstream from the entrance by solving for the radial temperature distribution at each axial position. The energy equation is solved by considering the radiation term as a known source which is evaluated from the temperatures of the previous iterate. The initial values for the radiation terms at a new axial position are taken from the final solution for the temperatures at the preceeding axial station. Final values for the temperatures and velocities at an axial position were established when the respective changes per iteration were less than 0.01 and 0.1 percent. The technique of over-relaxation was used to speed convergence. The treatment of the radiation terms as a source and the over-relaxation technique were found to be very satisfactory and are believed to yield an efficient and accurate way of obtaining numerical solutions for problems of this type. A more detailed discussion of the numerical considerations along with a complete discussion of the over-relaxation technique and the numerical experiments used to evaluate the best value of the overrelaxation factor are given in [16].

JOHN W. McCULLOCH[1]
J. EDWARD SUNDERLAND
Department of Mechanical and Aerospace Engineering, North Carolina State University, Raleigh, N. C.

Measurement of Monochromatic Emittance of Nonconductors at Moderate Temperatures[2]

The measurement of the monochromatic emittance of thermal insulators at temperatures near room temperature is discussed. Results for the spectral emittance of freeze-dried beef are presented. For temperatures between 115 F and 125 deg F, the emittance is between 0.7 and 0.85. These values compare favorably with existing total emittance data. A discussion of the error involved in making such measurements is discussed in detail.

Introduction

THE accurate measurement of monochromatic emittance of surfaces at temperatures near room temperature is exceedingly difficult. At these temperatures, the energy emitted is low and the effects of electrical noise and background radiation can be significant. For nonconductors, the problem is further complicated by the difficulty experienced in attempting to make accurate surface temperature measurements. Several papers have been written on methods of obtaining this type of data.

Gier, et al., [1][3] measured the monochromatic reflectance of metals in the wavelength range from 1.0 to 15.0 microns. The basic components of the system consisted of a heated hohlraum, a water-cooled sample, and a monochromator. The hohlraum, which was heated to 1400 deg F by electrical heaters, had two openings. The water-cooled sample was inserted in one opening and was arranged so that energy from the sample or the hohlraum wall could be alternately viewed by the monochromator. At a particular wavelength, the ratio of the energy leaving the sample to that from the ideal radiator is the reflectance. If the surface temperature had been measured, the monochromatic emittance could have been calculated from the monochromatic reflectance data. The method presented in this paper is not applicable to measuring the monochromatic reflectance of nonconductors near room temperature. Due to the inherently low thermal conductivity of nonconductors, it would be extremely difficult to cool the sample sufficiently while it is radiated by a high temperature source in an enclosure and also permit a constant surface temperature.

Dunkle, et al., [2] used the same general apparatus described in the foregoing to measure the monochromatic reflectance of fabrics from 1.0 to 23.0 microns. The sample was cooled by allowing an inert cooling gas, which was transparent to thermal radiation, to flow through the cloth samples. The data presented for cotton, linen, wool, silk, acetate, Arnel, rayon, orlon, dacron, and nylon showed that for most of these fabrics the use of dyes does not materially affect the infrared spectrum past three microns. Since data was not presented for the transmittance, this reflection data should not be used in the calculation of the absorptance or emittance.

Stierwalt [3] developed a technique for measuring the spectral emittance of both opaque and transparent materials from 40 C to 200 deg C in the 2.0 to 25.0 micron spectral region. The energy emitted by a sample was compared to the energy emitted by a blackbody at the same temperature. The spectrophotometer was evacuable and the temperature of the instrument was controlled by circulating water through copper tubing lining the instrument. By controlling the temperature of the background, samples could be run at temperatures lower than room temperature. Since the sample compartment was evacuable, atmospheric absorptions were eliminated and the instrument could be operated on single beam.

Stierwalt, et al., [4] used the procedure and apparatus outlined above to measure the spectral absorptance of magnesium fluoride, zinc sulfide, calcium fluoride, zinc selenide, crystalline quartz, silicon, and several blackening materials such as flat black paint.

White [5] introduced a new method of measuring the diffuse reflectance of samples in the infrared region. The sample was irradiated from all directions by chopped light. The sample and source were placed at conjugate foci of a hemispherical mirror with the chopper between the source and the mirror. This made the component reflected by the sample distinguishable from the one emitted by it. The main advantages of this method were

---

[1] Presently, Bell Telephone Laboratories, Greensboro, N. C.

[2] This research was supported by Public Health Service Research Grants FD-00156-02 and FD-00156-03 from the Food and Drug Administration.

[3] Numbers in brackets designate References at end of paper.

Contributed by the Heat Transfer Division for publication (without presentation) in the JOURNAL OF HEAT TRANSFER. Manuscript received by the Heat Transfer Division, July 10, 1969; revised manuscript received November 1, 1969. Paper No. 70-HT-D.

that the reflectance of diffuse samples could be measured over a wide range of sample temperatures and that heating of the sample by the source of energy was small. Another chopper was added after the sample so that the emitted component could be recorded as an indication of the sample temperature. The sample was illuminated from all directions and observed through a peephole as in the hohlraum of Gier, et al. [1].

Aronson and McLinden [6] presented a technique for studying the far infrared radiation of solids at temperatures down to 6.5 deg K. Materials studied in this work include sapphire, quartz, strontium fluoride, silicon, germanium, stainless steel, and an aluminum alloy.

An excellent reference of spectral as well as total reflectance, emittance, absorptance, and transmittance data was written by Gubareff, et al. [7]. This report presented an extensive survey and tabulation of radiation property data from over three hundred references. Another report written by Edwards, et al. [8] presented a comprehensive study of solar absorptance. Two important sources concerning radiation measurements were published in NASA publications which were edited by Richmond [9] and Katzoff [10].

The purpose of the current investigation is to present a method for measuring the spectral emittance of nonconductors near room temperature, and then to demonstrate this method by measuring the spectral emittance of freeze-dried beef. The only previous data for beef, or any food substance, was reported by Sevcik and Sunderland [11]. They measured the total normal emissivity of beef in the temperature range, 66 F to 94 deg F. A thermopile detector was used to measure the emf generated due to the difference in the energy emitted from the sample and that of a blackbody. The emissivity of beef was found to vary from 0.73 to 0.78 over the temperature range investigated.

Apparatus

The apparatus used to measure the monochromatic emittance is shown schematically in Fig. 1 and a pictorial drawing of the entire system is given in Fig. 2. The apparatus consists of a spectrophotometer, hohlraums, sample holder, and temperature control and measurement equipment.

Spectrophotometer. Depending on the specific mode of operation utilized, the role of the spectrophotometer is to collect, focus, disperse, detect, and record either differences in the intensity of energy from a sample and reference, or the intensity of energy from the sample alone. The spectrophotometer used in the current investigation, the Beckman IR-4, is a double beam, recording, infrared spectrophotometer that can also be used in single beam operation.

In the double beam mode, the thermocouple detector alternately views the sample and reference beams, and any difference in the intensity of the alternating beams appears as an alternating signal having a strength proportional to this difference. When the sample and reference components of the beam are equal in intensity, no signal is observed. However, when there is an unbalanced signal, an optical attenuator placed in the reference beam responds to this signal from the detector and moves to restore the system to optical null. The signal is transmitted electrically to the recorder which prints the difference between the intensity of the two beams. Since double beam operation involves a comparison of the radiation from the sample and reference, the absorption due to carbon dioxide and water vapor in the atmosphere should not influence the results if the optical paths of both beams are equal in length and contain the same gaseous composition. This can be checked by placing sources of equal intensity in the sample and reference beams. The chart should record a constant value throughout the scan if the optical paths are equivalent. This is especially difficult to achieve, however, when external optics are used.

In the single beam mode, the reference beam is blocked and

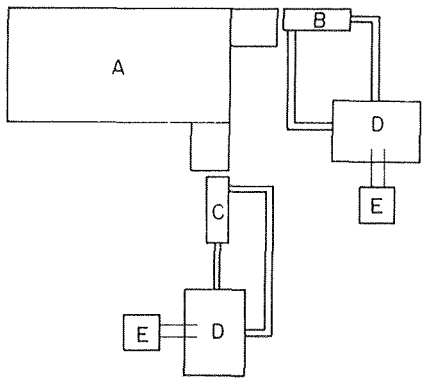

A. BECKMAN IR4 SPECTROPHOTOMETER
B. REFERENCE HOHLRAUM # 1
C. SAMPLE HOLDER AND REFERENCE HOHLRAUM # 2
D. HEATER
E. TEMPERATURE CONTROLLER

Fig. 1 Schematic drawing of the apparatus

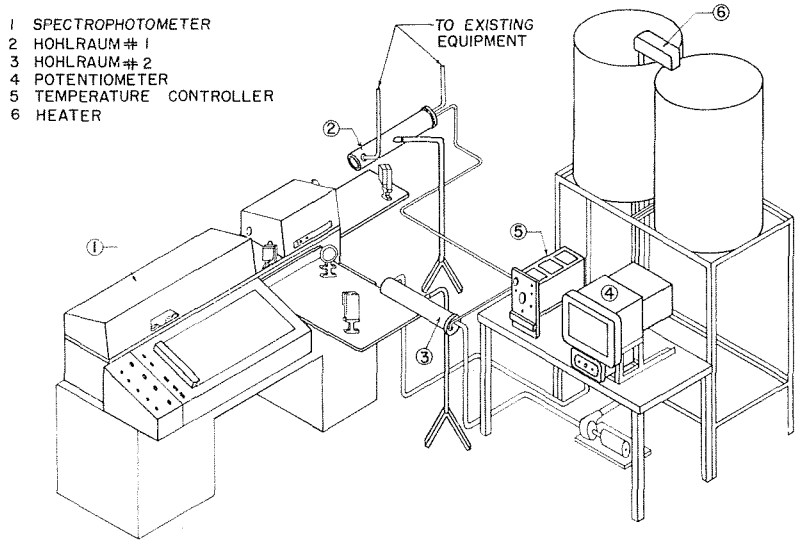

Fig. 2 Pictorial drawing of the apparatus

the thermocouple detects only the energy in the sample beam. In order to obtain quantitative results, a known reference must be scanned over the same wavelength range at the same instrument settings and the results compared. If only qualitative results are required, care must be taken to scan only in wavelength regions where atmospheric absorption is negligible.

In both modes of operation, energy is collected and focused by mirrors before being chopped by a rotating half mirror to form the alternating signal. Front surface mirrors are used throughout the system since glass is opaque to infrared energy beyond approximately four microns. The alternating energy enters through the entrance slit of the double monochromator and passes through two prisms which disperse the energy into narrow wavebands. Then one narrow band of wavelengths passes through the monochrometer exit slit to the thermocouple. The IR-4 instrument used in this work had two sets of prisms and optics required to scan from one to thirty-five microns. The basic interchange contains two high-resolution sodium chloride prisms which are nearly transparent to thermal radiation in the 1.0 to 16.0 micron range. An accessory interchange consisting of two cesium bromide prisms and related optics is used for the 11.0 to 35.0 micron range. These interchanges are prealigned and adjusted, and while one is not in use it is stored in a thermostatically controlled heated box to protect the hydroscopic prism materials. The internal temperature of the spectrophotometer is controlled to protect the hydroscopic prisms from excess moisture and to minimize temperature influences on the calibration of the instrument.

The IR-4 is equipped with a drive mechanism which rotates certain optical components so that the infrared spectrum can be continuously scanned in the wavelength range of the prism materials. The wavelength drive mechanism is coupled to the chart drive mechanism to facilitate direct readings on standard chart paper.

A set of external optics are supplied to optically connect the basic spectrophotometer with both the reference and sample hohlraums. The optical paths between the respective front surface mirrors comprising the external optics are equal in the reference and sample beams.

Hohlraums and Sample Holder. In order to measure monochromatic emittance, the amount of energy emitted by a sample is compared with the energy emitted by a blackbody at the same temperature and wavelength. The two hohlraums shown in Fig. 1 serve as the required blackbody references used in this work.

For double beam operation, two blackbodies are required. Hohlraum #1 is the reference while hohlraum #2 serves two functions. First, it is used for calibration purposes. As stated earlier, two sources of equal intensity are needed to determine if the absorption bands due to water vapor and carbon dioxide are equally compensated for in the wavelength range being considered. The resulting scan is often denoted as the "100 percent line." This reference line on the chart can be set at any location. Since the apparent emittance of the blackbody is nearly one, the reference line corresponds to the least upper bound of all possible values for the emittance of the sample. Second, hohlraum #2 serves as a heater and mount for the sample holder.

In single beam studies, the reference path is blocked and hohlraum #2 serves as the mount and heater for the sample holder and as the blackbody reference. A detailed description of the construction of the hohlraums and sample holder is given in the following.

Hohlraum. Two identical hohlraums are used in the investigation. A blackbody can be approximated to a high degree of accuracy by a deep cylindrical cavity open on one end. According to Buckley [12] and Sparrow, et al. [13], if the cylinder walls are diffuse and have an emittance above 0.75 and if the length-to-diameter ratio is greater than four, the resulting apparent emittance of the cavity will be greater than 0.99.

The hohlraums used in this apparatus were constructed so

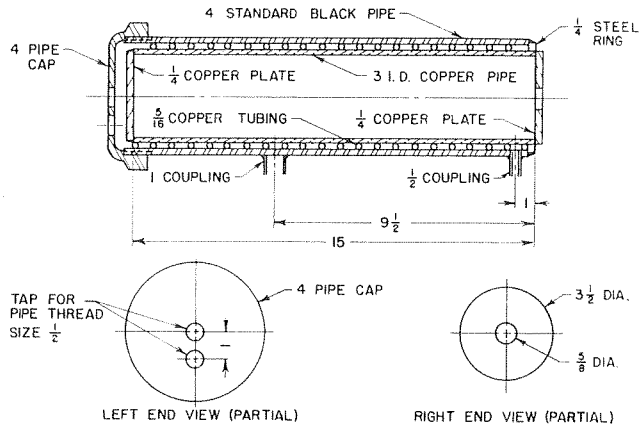

Fig. 3 Hohlraum

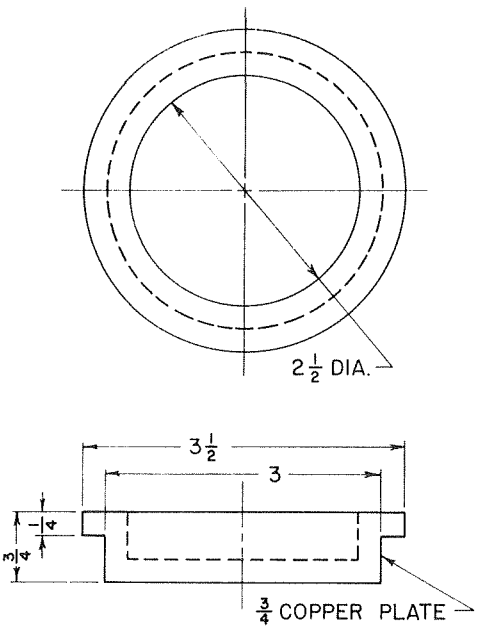

Fig. 4 Sample holder

that the apparent emittance would be greater than 0.99 (see Fig. 3). The inside surface of the hohlraum was sandblasted and smoked with acetylene soot, which has an emittance above 0.95. Copper tubing was wrapped in a spiral around the outside of the copper cavity to provide a continuous path for the thermal fluid circulated around the cavity. This entire assembly was then slipped into a section of four-in. iron pipe. Thermocouple wires leading from five junctions distributed along the cavity exited through a port drilled in the pipe cap shown in the figure. A hole was drilled in the lateral face of the outside pipe near the start of the spiral to serve as an entrance port for the circulating fluid. A similar hole was drilled in the pipe cap to serve as an exit port.

When the hohlraum is used as a mount and heater for the sample holder, the disk is removed and the sample holder is inserted (see Fig. 4). It was constructed so that it would fit into the copper cavity to such a depth as to provide ample thermal contact area for heating of the sample holder.

Temperature Control and Measurement Equipment. In order to accurately measure the monochromatic emittance of a sample, the surface temperature must be known and remain constant during each run. Due to the low thermal conductivities of the samples considered, the temperature of the sample holder must be held at a sufficiently high value to make sure that the surface of the sample and the reference hohlraum have the same tempera-

ture. A recording potentiometer is used to continuously monitor various temperatures throughout the system. Proportional temperature controllers were used to control the temperature of the fluids circulating through both hohlraums. In order to measure the temperature in the two hohlraums and in the sample, thermocouples are used in conjunction with a recording potentiometer. In the two hohlraums, 24-gauge copper constantan thermocouple wire is used. Thermocouples made from 36-gauge copper constantan wire are used to measure the surface temperature of the sample.

Procedure

Double Beam Operation. In the double beam studies hohlraum #1 serves as the blackbody reference, while hohlraum #2 serves the dual role of being the mount and heater for the sample holder as well as serving as the calibrating blackbody used in determining the "100 percent line." The following procedure is used to measure the monochromatic emittance of a sample at a specified temperature:

1 Blackbodies are positioned in both the reference and sample paths, and the temperature controllers in both systems are set for the desired temperature.

2 The system is allowed to operate for several hours until thermal equilibrium conditions exist. Minor adjustments are made during this period to insure that both hohlraums are at the same temperature.

3 Gain, period, slit, and comb adjustments are made in order to position the chart pen at approximately 90 percent full scale. At this position the "100 percent line" is run several times.

4 The sample is placed in the sample path and the temperature of the circulating fluid is raised until the temperature of the sample surface becomes equal to that of the reference hohlraum. Several hours are required for the system to reach equilibrium.

5 The sample is scanned several times throughout the wavelength range of the optics in the spectrophotometer. The necessary information needed to calculate the monochromatic emittance is provided.

6 The process discussed in the foregoing is repeated for the wavelength range covered by the other set of optics.

Single Beam Operation. In single beam studies, the reference beam is blocked and hohlraum #2 serves as the mount and heater for the sample holder and as the blackbody reference. In using the single beam method to measure the monochromatic emittance of a sample, the following procedure is followed:

1 With the hohlraum serving as a blackbody, the desired temperature is set on the controller.

2 After equilibrium is reached throughout the hohlraum, the maximum energy is set to read 90 percent on the chart.

3 The blackbody energy spectrum is scanned in regions of negligible atmospheric absorption for the particular set of optics in the spectrophotometer.

4 The sample is next placed in the path and the temperature of the circulating fluid is raised until the sample surface temperature is identical to that of the blackbody reference. Several hours are required for this step.

5 The sample is scanned over the same wavelength range as the blackbody.

6 The process is repeated for the other set of optics.

Monochromatic Emittance of Freeze-Dried Beef

Experimental Measurements. The monochromatic emittance of several samples of freeze-dried beef was measured at 115 F and 125 deg F. The accuracy and repeatability of the measurements was checked by making several runs over the same wavelength range and at the same temperature and instrument settings. Since the variation in the measurements appear to be random, the arithmetic mean of the emittance is calculated every 0.2 microns and plotted as a function of wavelength.

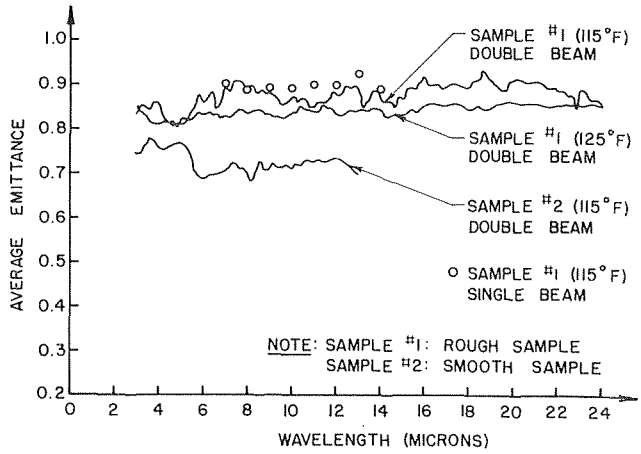

Fig. 5 Average emittance versus wavelength

Fig. 5 presents data for a rough specimen, sample #1, for temperatures of 115 F and 125 deg F. The rough sample is pitted with small holes and cracks in the viewing area of the spectrophotometer. Since these imperfections radiate as miniature cavities, the emittance of the rough sample is higher than that of sample #2 which is comparatively smooth. By examining the data, it is apparent that the variation in sample surface conditions has a pronounced effect upon the monochromatic emittance. In addition, it is seen that the monochromatic emittance does not vary appreciably with temperature. It is apparent that, for all practical purposes, freeze-dried beef emits energy as a gray body.

Since freeze-dried beef is essentially gray, total emittance values can be used in heat transfer analyses. Using a method described by Giedt [14], the total emittance of a sample can be calculated from monochromatic data. The total emittance of sample #1 is 0.84 at 125 deg F and 0.88 at 115 deg F. Note that the emittance decreases with increasing temperatures. This variation of emittance with temperature also occurs with wood and most nonconducting solids. The total emittance of sample #2 at 115 deg F is 0.72. Assuming that the monochromatic emittance of sample #2 at 100 deg F is approximately the same as at 115 deg F and using blackbody data at 100 deg F, the total emittance is estimated to be 0.72 at 100 deg F also. Since the total emittance is not strongly dependent upon temperature, it seems advisable not to construct elaborate equipment needed to measure emittances at room temperature, but to use values determined at 115 deg F. The value of 0.72 at 100 deg F compares to a value of 0.73 determined by Sevcik and Sunderland [11].

Data is also presented in Fig. 5 for sample #2 at 115 deg F using single beam methods outlined earlier. Since this is essentially an independent method, it is important to note that the results compare favorably with those taken by double beam methods.

Discussion of Error. The energy radiated by the sample is actually the sum of the energy emitted by the sample and the energy reflected by the sample. Since the monochromatic emittance is defined as the ratio of the energy emitted by the sample to that emitted by a blackbody at the same temperature, it is important to determine if the reflected component is indeed negligible. In order to check this experimentally, the energy radiated by a sample at room temperature was compared to the energy emitted by a blackbody at 115 deg F. It was found that the energy in the sample beam was negligible in comparison to the blackbody emission. Hence, if the reflectance does not vary radically with temperature, the reflected component will be negligible at 115 deg F also.

As discussed earlier, several runs were made at identical conditions to facilitate checking the repeatability of the results and

to serve as a basis for arriving at a confidence level for use of the data in heat transfer calculations. As an example, sample #1 was run five times at a temperature of 125 deg F. Using a method discussed by Hoel [15], the standard deviation, $\bar{\sigma}$, was calculated for this case. As shown in Fig. 6, a band of width $4\bar{\sigma}$ is plotted about the arithmetic mean. If the variability is not a function of wavelengths, this band should include 95 percent of the experimental points.

The scatter of the data can be partly attributed to small variations in sample surface temperature resulting from changes in room temperature or oscillations of the fluid temperature circulating in the hohlraum. The oxidation of the sample surface may also affect the emittance. The effect of these errors was checked by allowing the chart to continue running for several hours while holding the wavelength constant. The resulting plot varied from a straight line by less than 5 percent.

Fig. 7 is included to show the variation in the "100 percent line" due to unequal optical paths in the reference and sample beam during double beam operation. The large dip near 6.5 microns is attributed to the absorption of more energy in the sample path than in the reference path. It was impossible to align the hohlraums to a degree of accuracy that would eliminate this effect. A similar dip occurs in the sample run so that when the ratio of the two is calculated to determine the emittance, the effect is minimized.

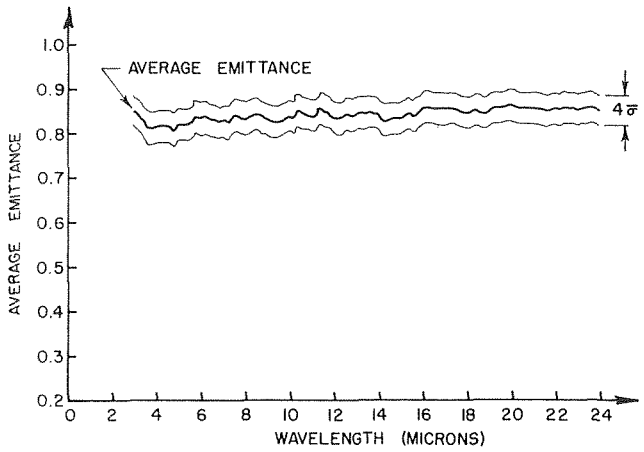

Fig. 6 Confidence band for sample #1 (125 deg F)

Recommendations. In order to take meaningful data below three microns and above 24 microns where the energy is extremely low, it is necessary to operate in the single beam mode. The following method is outlined for this type of sensitive measurement.

Instead of scanning the reference first and then the sample, a swival mechanism should be provided, with the sample holder on one end and the reference hohlraum on the other. Depending on the position of the swival mechanism, either the sample or reference could be viewed by the spectrophotometer. The procedure would be to alternately view the reference and then the sample at each desired wavelength. At each wavelength, the gain should be adjusted to have the reference read 100 percent on the scale. In this manner, the emittance could be read from the chart directly. The entire system should be purged with dry nitrogen to eliminate the carbon dioxide and water vapor absorption bands.

If in the future studies the monochromatic emittance is needed at room temperatures, the method discussed by Stierwalt [3] could be used. A brief discussion of this method is included in the introduction.

References

1 Gier, J. T., Dunkle, R. V., and Bevens, J. T., "Measurement of Absolute Spectral Reflectivity From 1.0 to 15 Microns," *Journal of the Optical Society of America*, Vol. 44, No. 7, 1954, pp. 558–562.

2 Dunkle, R. V., Ehrenburg, F., and Gier, J. T., "Spectral Characteristics of Fabrics From 1 to 23 Microns," JOURNAL OF HEAT TRANSFER, TRANS. ASME, Series C, Vol. 82, No. 1, Feb. 1960, pp. 64–70.

3 Stierwalt, D. L., "Spectral Emittance Measurements From 40°C to 200°C," Richmond, J. C., ed., *Measurement of Thermal Radiation Properties of Solids*, NASA Sp-31, National Aeronautics and Space Administration, Washington, D. C., 1963, pp. 231–236.

4 Stierwalt, D. L., Berstein, J. B., and Kirk, D. D., "Measurement of the Infrared Spectral Absorptance of Optical Materials," *Applied Optics*, Vol. 2, No. 11, 1963, pp. 1169–1173.

5 White, J. U., "New Method for Measuring Diffuse Reflec-

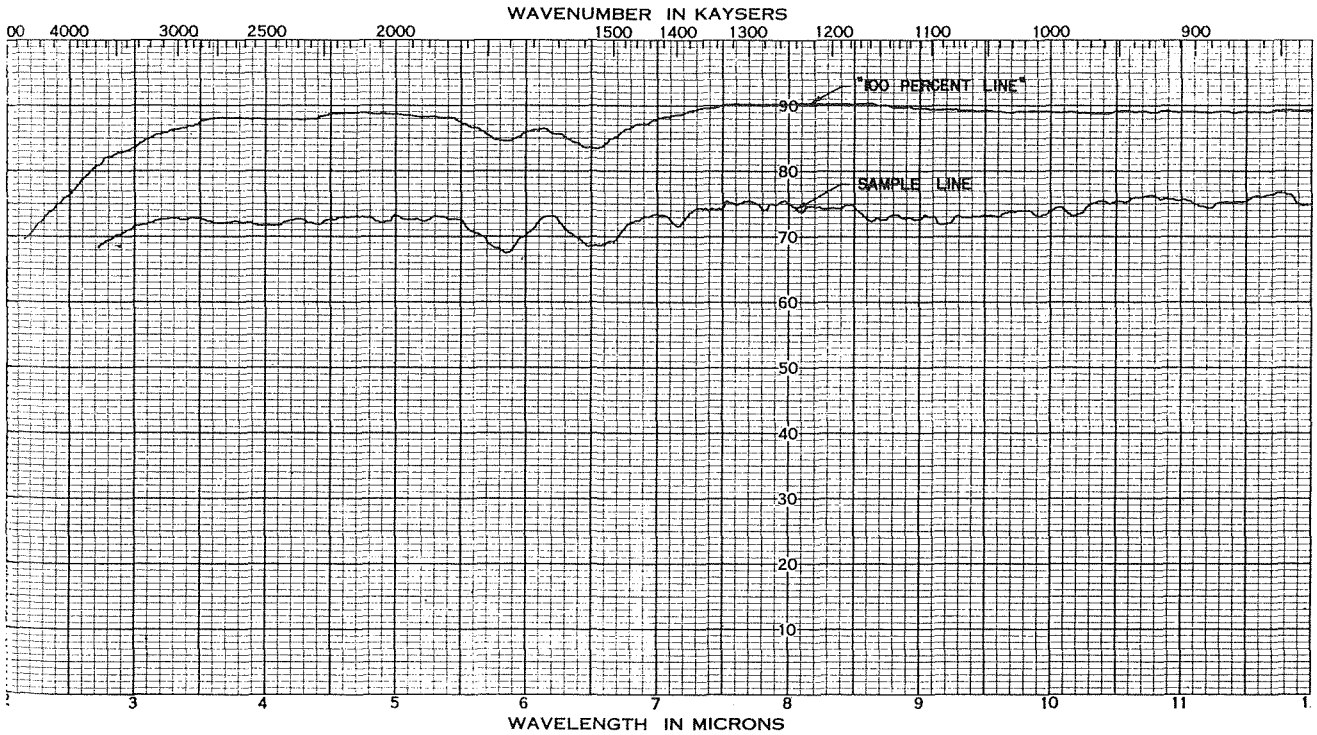

Fig. 7 Raw data showing variation of "100 percent line"

tance in the Infrared," *Journal of the Optical Society of America*, Vol. 54, No. 11, 1964, pp. 1332–1337.

6 Aronson, J. R., and McLinden, H. G., "Far-infrared Spectra of Solids," Katzoff, S., ed., *Symposium on Thermal Radiation of Solids*, NASA Sp-55, National Aeronautics and Space Administration, Washington, D. C., 1965, pp. 29–38.

7 Gubareff, G. G., Janssen, J. E., and Torborg, R. H., "Thermal Radiation Properties Survey," Honeywell Research Center, Minneapolis-Honeywell Regulator Company, Minneapolis, Minn., 1969.

8 Edwards, D. K., Nelson, K. E., Roddick, R. D., and Gier, J. T., "Basic Studies on the Use and Control of Solar Energy," Report No. 60–93, Department of Engineering, University of California, Los Angeles, Calif., 1960.

9 Richmond, J. C., ed., *Measurement of Thermal Radiation Properties of Solids*, NASA Sp-31, National Aeronautics and Space Administration, Washington, D. C., 1963.

10 Katzoff, S., ed., *Symposium on Thermal Radiation of Solids*, NASA Sp-55, National Aeronautics and Space Administration, Washington, D. C., 1965.

11 Sevcik, V. J., and Sunderland, J. E., "Emissivity of Beef," *Food Technology*, Vol. 16, 1962, pp. 124–126.

12 Buckley, H., "On the Radiation From the Inside of a Circular Cylinder—Part III," *Philosophical Magazine*, Vol. 17, 1934, pp. 576–581.

13 Sparrow, E. M., Albers, L. V., and Eckert, E. R. G., "Thermal Radiation Characteristics of Cylindrical Enclosures," JOURNAL OF HEAT TRANSFER, TRANS. ASME, Series C, Vol. 84, No. 1, Feb., 1962, 73–81.

14 Giedt, W. H., *Principles of Engineering Heat Transfer*, D. Van Nostrand Company, Inc., Princeton, N. J., 1957.

15 Hoel, P. G., *Elementary Statistics*, 2nd ed., Wiley, New York, N. Y., 1966.

M. IQBAL
Associate Professor.

S. A. ANSARI
Graduate Student.

Department of Mechanical Engineering,
University of British Columbia,
Vancouver, Canada

B. D. AGGARWALA
Associate Professor, Department of
Mathematics, University of Calgary,
Calgary, Canada

Effect of Buoyancy on Forced Convection in Vertical Regular Polygonal Ducts

Laminar combined free and forced convection through vertical regular polygonal ducts has been studied. All fluid properties are considered constant, except variation of density in the buoyancy term. Heat flux is considered uniform in the flow direction while in the transverse direction two wall conditions have been considered; Case 1—uniform circumferential wall temperature, and Case 2—uniform circumferential heat flux. A solution by point matching method in terms of a series containing Bessel functions has been obtained. Nusselt numbers, local heat flux, local shear stress, and pressure drop have been investigated. The condition of Case 1 results in higher Nusselt number values compared to the condition of Case 2. However, these differences in Nusselt number diminish as the number of sides of the polygon are increased. In each case, at higher values of the Rayleigh number, the Nusselt number is less sensitive to the number of sides. When Nusselt numbers against number of sides are considered, in Case 1, the Nusselt numbers reach asymptotic value at lower number of duct sides compared to Case 2. At low values of buoyancy effect, in Case 1, the maximum circumferential heat flux results at the centre of the wall, while at higher values of the same, the local heat flux becomes uniform over a substantial portion of the wall. Under Case 1 buoyancy effect increases the heat flux ratio at the duct corners. In three-sided polygon at higher values of the buoyancy parameter the maximum shear stress is no longer incident at the wall center. As the number of sides is increased, however, the maximum shear stress again takes place at the wall center. The Case 1 produces higher shear stress values near the wall center, while the Case 2 produces higher shear stress values near the duct corner. When the buoyancy parameter is high and the number of sides is not large, Case 2 results in higher values of pressure drop parameter compared to Case 1.

Introduction

In convective heat transfer processes, free convection effects result under the influence of a gravitational force field. The free convection effects are due to density differences arising out of temperature differences. In a convective process, theoretically there is never a pure forced convection case. When the effects of forced convection are dominant, the natural convection effects are usually ignored. On the other hand, when the buoyancy forces arising from density differences are relatively large, the forced convection effects may be ignored. In many practical situations both the effects of free convection and forced convection are present. Elenbaas [1][1] has analyzed the case of pure free convection through vertical ducts. It is known the effects of buoyancy on a forced convection process can considerably alter the heat transfer rate. Most previous studies in this area have been documented in a literature survey by Bhattacharyya [2].

For flow through circular ducts when the wall temperature varies linearly or is uniform in the flow direction, the peripheral wall temperature at any section remains constant. For flow through noncircular ducts, however, the fluid slows down near the corners, thereby transmitting less heat in these areas. This may result in nonuniform peripheral wall temperature and nonuniform peripheral wall heat flux. The extent of this rotational assymetry depends upon the duct configuration, thermal conductivity, and thickness of duct wall. This circumferential assymmetry is also present in combined free and forced convection through vertical noncircular ducts.

It is known [3, 4] that for fully developed laminar flow through ducts under uniform axial heat flux, the equation describing temperature distribution through the ducts is mathematically similar to that describing deflection of thin plates. As such, one can borrow the available solutions from the plate theory (whenever possible) to solve the duct flow problem. However, this poses one restriction, namely, the usual boundary condition from the plate theory is equivalent to that of uniform peripheral wall

[1] Numbers in brackets designate References at end of paper.

Contributed by the Heat Transfer Division and presented at the Winter Annual Meeting, Los Angeles, Calif., November 16–20, 1969, of THE AMERICAN SOCIETY OF MECHANICAL ENGINEERS. Manuscript received by the Heat Transfer Division, January 6, 1969. Paper No. 69-WA/HT-10.

temperature. The case of uniform peripheral heat flux in duct flow will, however, give rise to a set of boundary conditions which is normally not encountered in the plate theory.

Some studies of laminar pure forced convection through noncircular and regular polygonal ducts under uniform axial heat flux and uniform peripheral wall temperature are available in references [5–10]. Yen [11] has presented an exact solution of pure forced convection through wedge-shaped passages under uniform peripheral heat flux, while Tao [12] presented an exact solution by conformal mapping for the same boundary conditions, but for a cardioid duct. Combined free and forced convection solution for vertical noncircular and circular sector ducts under the conditions of uniform axial heat flux and uniform peripheral wall temperature have been presented by Lu [4], Tao [13, 14], and Han [15]. For noncircular ducts, solutions of combined free and forced convection with uniform peripheral heat flux do not appear to be available in the literature.

The present study treats the case of fully developed laminar combined free and forced convection through vertical regular polygonal ducts under uniform axial heat flux. The boundary conditions considered are (i) uniform peripheral wall temperature and (ii) uniform peripheral wall heat flux. Solutions have been presented which satisfy exactly the differential equations and satisfy the boundary conditions only at a number of points on the walls. As will be shown in the following sections, the results obtained are very accurate.

Formulation of the Problem

Consider a vertical straight regular polygonal duct, Fig. 1. Consider fully developed laminar flow through the duct in the vertical upward direction along the positive z-axis. Uniform heat flux in the axial direction is assumed. Viscous dissipation, pressure work, and axial conduction terms in the energy equation are considered identically zero. All fluid properties are assumed constant except for variation of density in the buoyancy term of the equation of motion. The fluid may contain uniform volume heat sources. Under these conditions, the governing equations can be written as:

$$0 = -\frac{\partial p}{\partial z} + \mu\nabla^2 u - \rho g, \tag{1}$$

$$\rho C_p u \frac{\partial T}{\partial z} = k\nabla^2 T + Q, \tag{2}$$

where

$$\nabla^2 \equiv \frac{\partial^2}{\partial r^2} + \frac{1}{r}\frac{\partial}{\partial r} + \frac{1}{r^2}\frac{\partial^2}{\partial \theta^2}.$$

The wall and fluid temperature gradients are $\frac{\partial T}{\partial z} = C_1$, C_1 being a constant.

The equation of state can be written as

$$\rho = \rho_w[1 - \beta(T - T_w)]. \tag{3}$$

where T_w can be replaced by T_{apex} for the case of uniform peripheral heat flux. The wall temperature is defined as

$$T_w = T_0 + z\frac{\partial T}{\partial z},$$

where T_0 is the reference temperature at $z = 0$. Inserting equation (3) in (1) and (2) and nondimensionalizing, we obtain

$$\nabla^2 V + N_{Ra}\phi = -L, \tag{4}$$

$$\nabla^2\phi - V = -F, \tag{5}$$

where

$$\nabla^2 \equiv \frac{\partial^2}{\partial R^2} + \frac{1}{R}\frac{\partial}{\partial R} + \frac{1}{R^2}\frac{\partial^2}{\partial \theta^2}. \tag{6}$$

In equations (4) and (5), the Rayleigh number N_{Ra} and the heat generation parameter F are prescribed quantities, while V, ϕ, and L are the three unknowns. We therefore need a third equation which is provided by the continuity considerations in the duct,

$$\iint V dA = \iint dA. \tag{7}$$

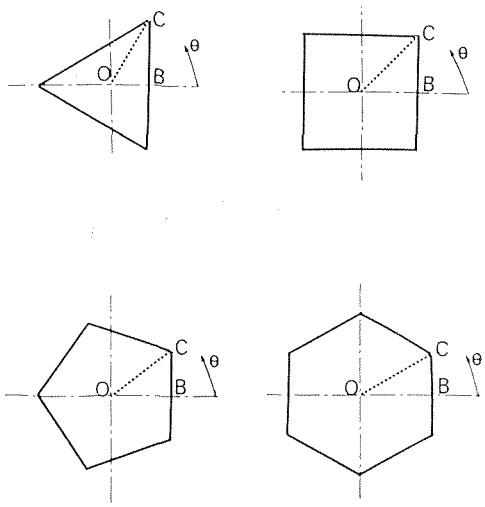

Fig. 1 Coordinate system

Nomenclature

A = area of cross section
C_p = specific heat of the fluid at constant pressure
C_1 = temperature gradient in flow direction
D_h = hydraulic diameter = (4 cross-sectional area)/(heat transfer perimeter)
F = $Q/\rho C_p C_1 U$, heat generation parameter, dimensionless
$\bar{F}$ = F/L, dimensionless
g = gravitational acceleration
h_{avg} = average peripheral heat transfer coefficient
L = pressure drop parameter, dimensionless
N_{Nu} = hD_h/κ, Nusselt number, dimensionless
N_{Ra} = $(\rho^2 g C_p C_1 \beta D_h^4)/\kappa\mu$, Rayleigh number, dimensionless
Q = heat generation rate
R = r/D_h, dimensionless radius
s = number of sides of a regular polygon
q_{avg} = average surface heat flux
T = temperature
u = axial velocity
U = average axial velocity
V = u/U, dimensionless axial velocity
$\bar{V}$ = V/L, dimensionless
R, θ = coordinates
z = axial coordinate in flow direction
λ = $(T - T_w)$ or $(T - T_{apex})$
ϕ = $\lambda/\left[\frac{\rho U C_p C_1 D_h^2}{\kappa}\right]$, dimensionless temperature function
$\bar{\phi}$ = ϕ/L, dimensionless
β, ρ, κ, μ = fluid properties in standard notation
η = $(N_{Ra})^{1/4}$
τ = local wall shear stress
τ_{avg} = average wall shear stress

In the assumptions stated above nothing has been said about the conditions of peripheral wall temperature or the peripheral wall heat flux. We wish to solve equations (4) to (7) under the following two cases:

Case 1: Uniform peripheral wall temperature,

$$V = \phi = 0 \qquad \text{at the wall.} \tag{8}$$

Case 2: Uniform peripheral wall heat flux,

$$\left.\begin{aligned} \frac{\partial \phi}{\partial N} &= \text{Constant} \\ V &= 0 \end{aligned}\right] \quad \text{at the wall,} \tag{9}$$

$$\phi = 0 \qquad \text{at the apex of the duct.} \tag{10}$$

Solution

In equations (4) and (5) the pressure drop parameter L is an unknown constant. We therefore can divide (4) and (5) by L and obtain the following two equations

$$\nabla^2 \bar{V} + N_{Ra}\bar{\phi} = -1, \tag{11}$$

$$\nabla^2 \bar{\phi} - \bar{V} = 0. \tag{12}$$

where $\bar{V} = V/L$, $\bar{\phi} = \phi/L$. $\bar{F} = F/L$ has been dropped for the time being. Solutions for finite nonzero values of F will be explained later in the analysis. Elimination of L in (11) and (12) simplifies the problem, considering the fact that we now have only two equations in two unknowns, $\bar{V}$ and $\bar{\phi}$. The method by which L is obtained will be explained later when we deal with the particular boundary conditions.

We first of all present a general solution of equations (11) and (12). These two equations can be combined together to give

$$\nabla^4 \bar{V} + N_{\mathrm{Ra}}\bar{V} = 0. \tag{13}$$

Let

$$N_{\mathrm{Ra}} = \eta^4 \tag{14}$$

so that (13) can be rewritten as

$$\nabla^4 \bar{V} + \eta^4 \bar{V} = 0, \tag{15}$$

or

$$(\nabla^2 + i\eta^2)(\nabla^2 - i\eta^2)\bar{V} = 0. \tag{16}$$

General solution of equation (16) can be obtained by combining solutions of

$$(\nabla^2 + i\eta^2)\bar{V} = 0, \tag{17}$$

and

$$(\nabla^2 - i\eta^2)\bar{V} = 0. \tag{18}$$

This solution will contain the terms [16],

$$\begin{aligned} &ber_n(\eta R)\cos n\theta,\ bei_n(\eta R)\cos n\theta, \\ &ber_n(\eta R)\sin n\theta,\ bei_n(\eta R)\sin n\theta, \\ &Ker_n(\eta R)\cos n\theta,\ Kei_n(\eta R)\cos n\theta, \\ &Ker_n(\eta R)\sin n\theta,\ Kei_n(\eta R)\sin n\theta. \end{aligned} \tag{19}$$

Since the problem is even in θ, the terms containing sin $n\theta$ will drop out. In addition, as the velocity is finite at the center, the *ker* and *kei* terms will not exist in the present case.

Because of the symmetry of the regular polygons, only the region OBC, Fig. 1, need be considered. For this region the general expression for velocity can be written as

$$\bar{V} = \sum_{n=0}^{\infty} C_{ns} ber_{ns}(\eta R)\cos ns\theta + \sum_{n=0}^{\infty} D_{ns} bei_{ns}(\eta R)\cos ns\theta. \tag{20}$$

From equation (20) we can write

$$\nabla^2 \bar{V} = \eta^2 \left[-\sum_{n=0}^{\infty} C_{ns} bei_{ns}(\eta R)\cos ns\theta + \sum_{n=0}^{\infty} D_{ns} ber_{ns}(\eta R)\cos ns\theta \right]. \tag{20a}$$

From (11), the temperature function can be written as

$$\bar{\phi} = -\frac{1}{N_{\mathrm{Ra}}}[1 + \nabla^2 \bar{V}]. \tag{21}$$

Equations (20) and (21) give a general solution of the equations (11) and (12). However, we have still to evaluate the constants, C_{ns}, D_{ns}, and the pressure-drop parameter L. These quantities are obtained by point-matching at the walls with respect to each boundary condition.

Case 1: This boundary condition states that

$$\bar{V} = \bar{\phi} = 0 \quad \text{at the wall.}$$

which is the same as $V = \phi = 0$ at the wall. To satisfy the condition of no-slip at the wall, equation (20) gives

$$0 = \sum_{n=0}^{\infty} C_{ns} ber_{ns}(\eta R)\cos ns\theta + \sum_{n=0}^{\infty} D_{ns} bei_{ns}(\eta R)\cos ns\theta, \tag{22}$$

while the second condition gives, from (11),

$$\nabla^2 \bar{V} = -1 \quad \text{at the wall.} \tag{23}$$

Introducing (20*a*) in (23), one obtains

$$-1 = \eta^2 \left[-\sum_{n=0}^{\infty} C_{ns} bei_{ns}(\eta R)\cos ns\theta + \sum_{n=0}^{\infty} D_{ns} ber_{ns}(\eta R)\cos ns\theta \right]. \tag{24}$$

The coefficients C_{ns} and D_{ns} are obtained from (22) and (24) by point matching at the wall BC.

For n number of points on the boundary, (22) and (24) will give $2n$ number of equations in $2n$ unknowns. These equations will be of linear algebraic type and can be readily solved, except that each term of these equations is an infinite series.

Determination of the coefficients C_{ns} and D_{ns} completely solves the problems for $\bar{V}$ and $\bar{\phi}$. The pressure-drop parameter L can now be evaluated from the continuity equation as

$$L = \frac{\int\int dA}{\int\int \bar{V} dA}, \tag{25}$$

where the integration is performed over the area OBC. Determination of L now gives the required quantities V and ϕ.

The reason for originally eliminating L from (11) and (12) is now obvious. This simplification is good, however, as long as $F = 0$, a situation which is most common. In the event results are required for finite values of F other than zero, $\bar{F}$ then becomes an unknown constant. For this situation the point-matching procedure described above can be followed except that now n number of points on the boundary will result in $2n$ number of equations in $(2n + 1)$ number of unknowns. The $(2n + 1)^{th}$ equation will now be provided by the continuity equation (7).

Case 2. For the case of uniform peripheral heat flux, the condition $\bar{V} = 0$ at the wall remains the same as in Case 1. Accordingly, as before, the condition $\bar{V} = 0$ at the wall will give equation (22). However, the condition $\partial\phi/\partial N$ = constant at the wall gives

$$\frac{\partial \bar{\phi}}{\partial N} = 0.25\left(\frac{1}{L} - \bar{F}\right) \tag{26}$$

For the system of coordinates, Fig. 1

$$\frac{\partial}{\partial N} = \cos\theta \frac{\partial}{\partial R} - \frac{\sin\theta}{R}\frac{\partial}{\partial \theta}. \tag{27}$$

From (21) and (26), one obtains

$$-\frac{1}{N_{Ra}}\left[\frac{\partial}{\partial N}(\nabla^2 \bar{V})\right] = \frac{0.25}{L}(1 - F). \tag{28}$$

where $\nabla^2 \bar{V}$ is given in equation (20*a*).

The coefficients C_{ns} and D_{ns} can now be evaluated from (22) and (28), but for the parameter L. We therefore need an additional equation. This equation is provided by the condition $\bar{\phi} = 0$ at the apex, which from (21) gives

$$\nabla^2 \bar{V} = -1. \tag{29}$$

The coefficients C_{ns}, D_{ns} and the pressure-drop parameter L can now be obtained by point matching (22) and (28) at the wall BC and (29) at the apex C.

It may be noted here that the continuity equation is not explicitly required to evaluate L in Case 2. The reason for this is that the continuity requirement has been utilized in deriving (26).

This completes the solution of the problem for the two cases. The method described in the foregoing can be extended to a prescribed circumferential temperature distribution as well. Having obtained the solution for velocity and temperature profiles, we can now evaluate Nusselt number, local heat flux, and local shear stress distribution.

Nusselt Numbers. Nusselt number signifies the energy convected from a surface.

$$N_{\mathrm{Nu}} = \frac{D_h h_{\mathrm{avg}}}{k} = \frac{D_h}{k}\frac{q_{\mathrm{avg}}}{\bar{T}_w - T_b}, \tag{30}$$

where $\bar{T}_W$ is the average wall temperature. For the Case 1, Nusselt number in the nondimensional form can be written as

$$N_{\mathrm{Nu}} = -\frac{1 - F}{4\phi_{mx}}, \tag{31}$$

where

$$\phi_{mx} = \frac{\int\int \phi V dA}{\int\int V dA}. \tag{32}$$

For the Case 2, the expression for Nusselt number reduces to

$$N_{\mathrm{Nu}} = \frac{1 - F}{4\left[\frac{1}{\pi/s}\int_0^{\pi/s} (\phi)_{\mathrm{wall}} d\theta - \phi_{mx}\right]}. \tag{33}$$

In equations (32) and (33) the area integrals are performed over the region OBC while the line integrals are performed over the wall BC.

Local Heat Flux. For the boundary conditions of Case 1, the local wall heat flux will vary over the circumference. In nondimensional terms, the ratio of the local to the average wall heat flux can be written as

$$\frac{q}{q_{\mathrm{avg}}} = \frac{\left(\frac{\partial \phi}{\partial N}\right)_{\mathrm{wall}}}{\frac{1}{\pi/s}\int_0^{\pi/s}\left(\frac{\partial \phi}{\partial N}\right)_{\mathrm{wall}} d\theta}. \tag{34}$$

Local Shear Stress. In a manner similar to the local heat flux, the ratio of the local to the average shear stress can be written as

$$\frac{\tau}{\tau_{\mathrm{avg}}} = \frac{\left(\frac{\partial V}{\partial N}\right)_{\mathrm{wall}}}{\frac{1}{\pi/s}\int_0^{\pi/s}\left(\frac{\partial V}{\partial N}\right)_{\mathrm{wall}} d\theta}. \tag{35}$$

Table 1 Improvement of Nusselt numbers with number of points on the wall for a square duct and comparison with an exact solution, for uniform circumferential wall temperatures

N_{Ra}	NUSSELT NUMBERS			
	Number of Points on the Wall BC, Present Analysis			Exact Solution [15]
	2	3	4	
π^4	3.7702	3.7092	3.7004	3.6962
$10\pi^4$	4.5891	4.4722	4.4492	4.4372
$100\pi^4$	7.4134	8.3815	8.3342	8.2716

Table 2 Improvement of Nusselt numbers with number of points on the wall for an equilateral triangular duct and comparison with an exact solution, for the case of uniform circumferential wall temperature

N_{Ra}	NUSSELT NUMBERS			
	Number of Points on the Wall BC, Present Analysis			Exact Solution [17]
	2	3	4	
10	3.1250	3.1248	3.1248	3.1249
100	3.2390	3.2472	3.2475	3.2475
500	3.5547	3.7489	3.7537	3.7537
1000	3.6921	4.2846	4.3029	4.3029
5000	1.6686	6.4505	6.7896	6.7971
10000		7.3051	8.2678	8.2944

Discussions

Before we discuss the various results of the present analysis, it is worthwhile to point out some of the computational details. First, the actual location of the points on the wall BC had little effect on the final results as long as the points were evenly distributed. Secondly, in the evaluation of the infinite series $ber_{ns}(\eta R)$ and $bei_{ns}(\eta R)$, etc., it is known that their convergence depends on the values of their argument and suffix, as such extreme care was taken to insure their convergence.

We now present the results of Nusselt numbers, local heat flux, local shear stress, and pressure-drop parameter and compare them with those of published work.

Nusselt Numbers Under Constant Circumferential Wall Temperature. Table 1 presents the Nusselt numbers obtained by the present analysis as compared to those of an exact solution by Han [15] for square ducts. This table also shows the effect of number of points (on the wall BC, Fig. 1) on the Nusselt number values. This table shows that with only four points, the results are very close to those of the exact solution.[2]

A similar comparison is given in Table 2 for the case of an

[2] In Table 3 of Han these Nusselt numbers are given as 3.69, 4.27, and 9.46, respectively. A recalculation of Han's expressions shows that some of the values in his Table 3 were somewhat in error.

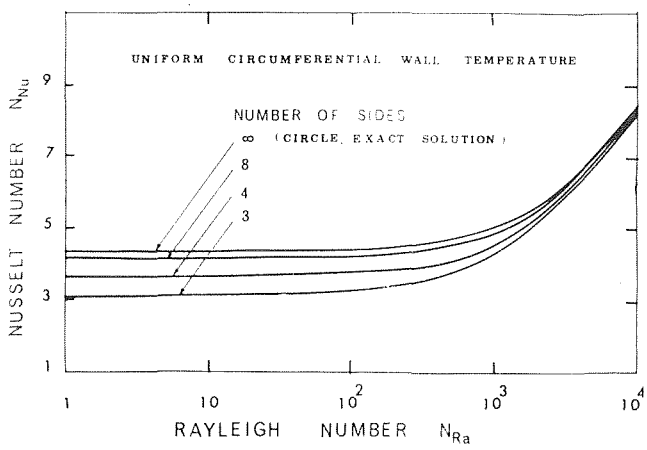

Fig. 2 Nusselt number against Rayleigh number for various polygons under uniform circumferential wall temperature

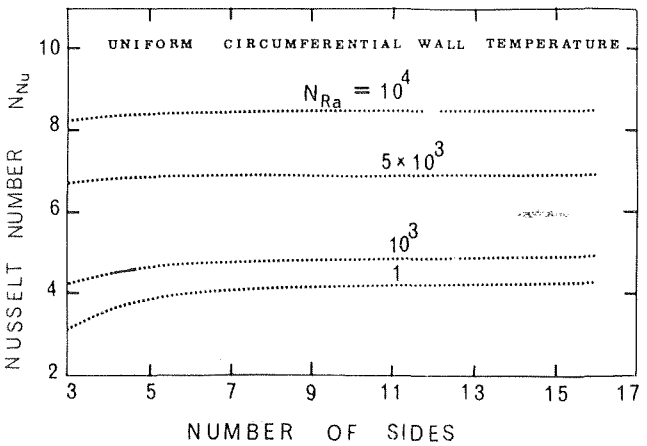

Fig. 3 Nusselt number against number of sides for various Rayleigh numbers under uniform circumferential wall temperature

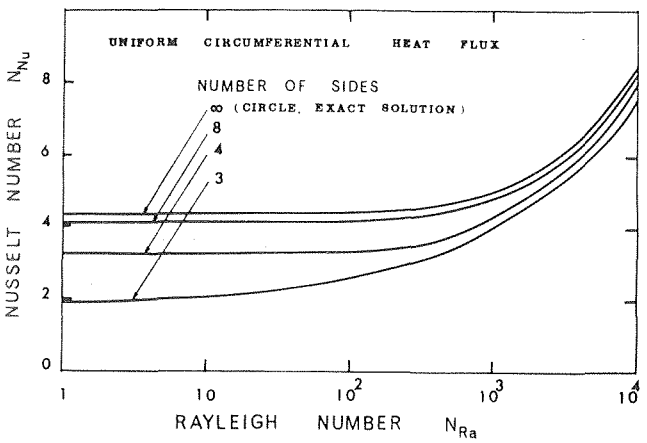

Fig. 4 Nusselt number against Rayleigh number for various polygons under uniform circumferential heat flux

equilateral triangle. The exact solution for this case is given in [17]. This table gives additional evidence that the present point-matching method is quite accurate.

Fig. 2 presents the variation of Nusselt number against Rayleigh number for different number of sides. This figure shows that as the Rayleigh number increases, the effect of number of sides on the Nusselt number diminishes. Fig. 3 gives the plots of variation of Nusselt number against number of sides for some values of the Rayleigh number. From this figure one can clearly note how the Nusselt numbers attain asymptotic values for various amounts of buoyancy effects.

Table 3 Nusselt numbers against Rayleigh numbers for various polygons for uniform circumferential wall temperature

N_{Ra}	NUSSELT NUMBERS							
	Number of Sides of Polygon							
	3	4	5	6	7	8	12	Circle (Exact Solution)
1	3.11	3.61	3.87	4.01	4.10	4.16	4.27	4.36
100	3.25	3.70	3.95	4.08	4.17	4.23	4.34	4.43
500	3.75	4.06	4.26	4.37	4.45	4.51	4.60	4.69
1000	4.30	4.47	4.63	4.72	4.78	4.85	4.92	4.99
2000	5.18	5.20	5.30	5.35	5.38	5.46	5.50	5.56
5000	6.79	6.80	6.88	6.89	6.90	6.91	6.91	6.94
10000	8.27	8.40	8.43	8.46	8.47	8.48	8.48	8.49

Table 4 Nusselt numbers against Rayleigh numbers for various polygons for uniform circumferential heat flux

N_{Ra}	NUSSELT NUMBERS							
	Number of Sides of Polygon							
	3	4	5	6	7	8	12	Circle (Exact Solution)
1	1.90	3.23	3.65	3.88	4.02	4.13	4.28	4.36
100	2.53	3.32	3.72	3.96	4.09	4.17	4.34	4.43
500	3.35	3.69	4.02	4.24	4.36	4.44	4.61	4.69
1000	3.61	4.14	4.37	4.57	4.69	4.77	4.93	4.99
2000	4.69	4.95	5.00	5.18	5.28	5.34	5.52	5.56
5000	6.01	6.34	6.47	6.61	6.70	6.73	6.93	6.94
10000	7.84	8.10	8.17	8.17	8.26	8.31	8.48	8.49

Table 3 lists Nusselt number values. It may be added here that in this table the values of Nusselt number at $N_{Ra} = 1$ should closely correspond to the results of pure forced convection through regular polygonal ducts. Comparison with Cheng's [10] values indicates that this indeed is the case.

Nusselt Numbers Under Constant Circumferential Wall Heat Flux. As indicated earlier, for combined free and forced convection through vertical noncircular ducts, there does not appear to be available any study corresponding to the case of uniform peripheral wall heat flux. As such, the accuracy of the present results is difficult to estimate. However, at $N_{Ra} = 1$, the Nusselt number values given in Table 4 agree closely with the corresponding values given by references [18] and [19] for pure forced convection case.

We present the Nusselt number of plots in Fig. 4 as function of Rayleigh number for various number of sides. The variation of Nusselt number against number of sides for various values of the Rayleigh number are given in Fig. 5. Table 4 lists the Nusselt number values.

We now compare the Nusselt numbers for the two cases of uniform peripheral wall temperature and the uniform peripheral wall heat flux.

When Figs. 4 and 5 are compared to the corresponding Figs. 2 and 3, it is noted that the case of uniform peripheral wall heat flux gives lower values of Nusselt number for given values of the free convection parameter and the number of sides. Yen [11], in a study of laminar forced convection through wedge-shaped passages, has also shown that the Nusselt numbers are lower for uniform peripheral wall heat flux compared to those of uniform peripheral wall temperature case. When Fig. 3 is compared with

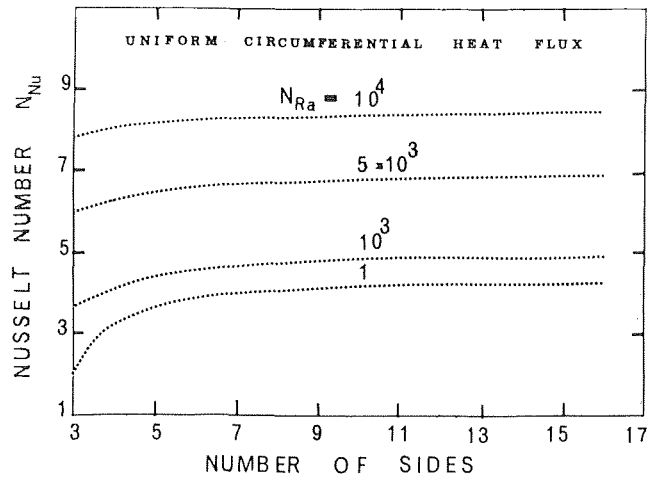

Fig. 5 Nusselt number against number of sides for various Rayleigh numbers under uniform circumferential heat flux

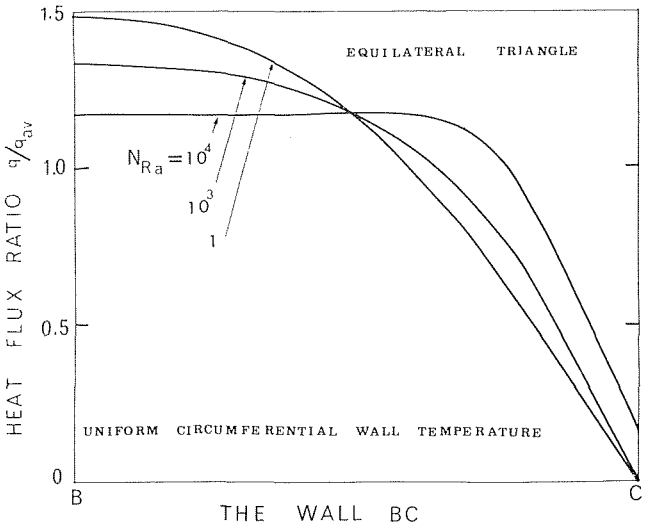

Fig. 6 Local wall heat flux ratio for equilateral triangle

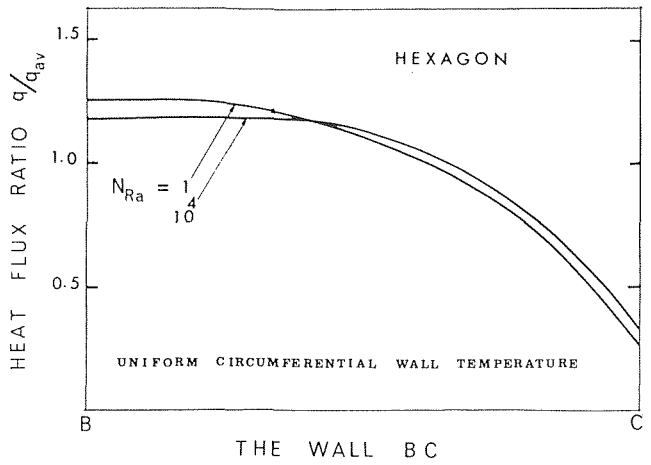

Fig. 7 Local wall heat flux ratio for hexagon

Fig. 5, it is observed that for a given value of the Rayleigh number, the influence of the increasing number of sides on the Nusselt number diminishes earlier for the case of uniform peripheral wall temperature compared to the case of uniform peripheral wall heat flux.

Local Heat Flux Ratio. The local heat flux distribution, according to equation (34), has been evaluated and, for two particular

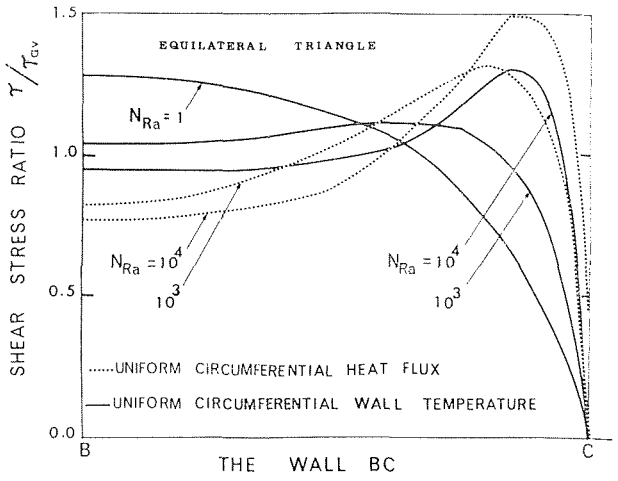

Fig. 8 Local shear stress ratio for equilateral triangle under (i) uniform circumferential heat flux; (ii) uniform circumferential wall temperature

geometries, is plotted in Figs. 6 and 7. Fig. 6 is for the equilateral triangle and shows that while at low values of the Rayleigh number the maximum value of local heat flux occurs at point B, at a high value of the Rayleigh number the heat flux becomes uniform over a substantial portion of the wall BC. Fig. 7 is for an hexagonal duct and shows that for this geometry, the local heat flux ratio is relatively less sensitive to the free convection effects.

It can be noted from both the Figs. 6 and 7 that the buoyancy effects increase the local heat flux ratio at the apex C, while they reduce the same at point B.

According to expectations, it has been observed that as the number of sides are increased, the differences in local heat flux ratio reduced, until for a circle they disappear completely.

Local Shear Stress Ratio. The local shear stress distribution has been evaluated from equation (35). Both the cases of uniform wall temperature and uniform wall heat flux have been analyzed. Fig. 8 presents, for an equilateral triangle, the local shear stress ratio for both the boundary conditions. This figure shows that while for low values of the Rayleigh number the shear stress ratio is maximum at point B, at high values of the buoyancy effects this maxima shifts toward the apex C. This rather unexpected result is borne out by calculations made from the exact solution given in [17]. Fig. 8 presents a comparison of shear stress ratios between the case of constant peripheral wall temperature and that of the constant peripheral wall heat flux. It is noted from this diagram that at high values of the buoyancy effects, the condition of uniform circumferential wall heat flux produces lower shear stress ratios at the point B, while it produces higher values of the same near the apex C.

As the number of sides are increased, the variations in local shear stress ratios are reduced, whether or not there are buoyancy effects present. This applies to both the circumferential boundary conditions under consideration. The differences in local values reduce very rapidly as the number of sides are increased from three.

Local Wall Temperature. For the case of uniform circumferential wall heat flux, the circumferential wall temperature difference ϕ has been studied. With or without buoyancy effects, the maximum wall temperature difference occurs at point B. As the number of sides are increased, the effect of buoyancy on local wall temperature diminishes, until for the circle it completely disappears. Local wall temperature distributions for four and eight-sided regular polygonal ducts are shown in Fig. 9.

Pressure-Drop Parameter. Pressure-drop parameter L, as a function of the Rayleigh number and number of sides, has been evaluated for the two wall boundary conditions. It is observed that when the number of sides is small and the Rayleigh number is high, the uniform circumferential heat flux condition results in

Table 5 Pressure-drop parameters L against Rayleigh numbers for various polygons for both the boundary conditions

N_{Ra}	PRESSURE DROP PARAMETER L											
	Uniform Circumferential Wall Temperature						Uniform Circumferential Heat Flux					
	Number of Sides						Number of Sides					
	3	4	6	8	16	Circle	3	4	6	8	16	Circle
1	26.75	28.50	30.04	30.17	31.98	32.06	27.03	28.56	30.06	30.17	32.00	32.06
100	34.53	35.26	36.16	36.86	37.16	37.69	53.39	41.90	38.07	36.87	37.32	37.69
500	63.10	61.03	59.81	59.81	59.72	59.63	129.02	94.67	68.73	62.94	60.15	59.63
1000	94.13	90.35	87.30	86.67	85.40	85.45	202.39	158.35	104.99	93.58	87.01	85.45
2000	146.80	142.01	136.97	135.57	133.36	132.81	347.16	278.30	171.04	149.73	136.29	132.81
5000	271.27	266.35	259.92	257.95	253.31	252.56	810.05	570.88	341.22	292.42	261.21	252.56
10000	437.32	429.78	423.25	421.70	414.98	413.91	1310.54	853.63	575.40	487.34	430.58	413.91

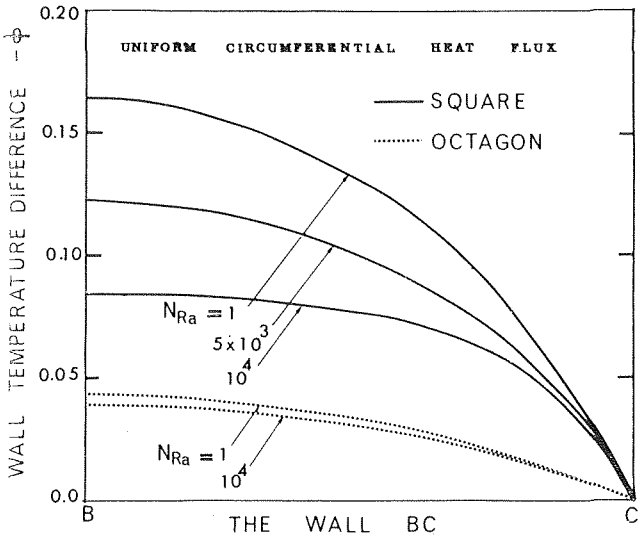

Fig. 9 Local wall temperature difference for square and octagonal ducts

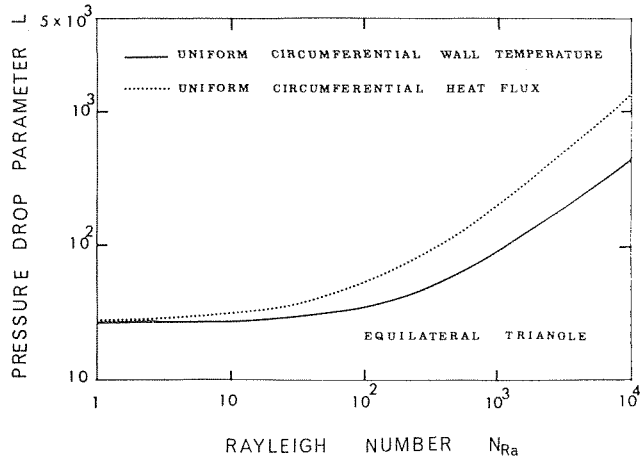

Fig. 10 Pressure drop parameter against Rayleigh number for equilateral triangle under (i) uniform circumferential heat flux; (ii) uniform circumferential wall temperature

higher values of the pressure-drop parameter compared to the case of uniform peripheral wall temperature. Table 5 lists some values of the pressure-drop parameter for a number of polygons under the two wall boundary conditions. Fig. 10 presents the pressure-drop behavior for an equilateral duct for the two cases, and clearly shows that the uniform wall heat flux condition results in higher pressure drops.

Conclusion

A solution by point-matching method in terms of a series containing Bessel functions has been obtained for the case of combined free and forced convection through vertical regular polygonal ducts. Two boundary conditions have been treated: Case 1—uniform circumferential wall temperature and Case 2—uniform circumferential heat flux. Case 1 results in higher Nusselt number values as compared to Case 2. In each case at higher values of Rayleigh number the influence of number of sides on Nusselt number diminishes.

Acknowledgment

Financial support of the National Research Council of Canada is gratefully acknowledged.

References

1 Elenbaas, W., "Dissipation of Heat by Free Convection," Parts I and II, Philips Research Report 3, N.V. Philips Gloeilampenfabrieken. Eindhoben, Netherlands, 1948, pp. 338–360, 450–465.

2 Bhattacharyya, A., "Effect of Buoyancy on Forced Convection Heat Transfer in Vertical Channels—A Literature Survey," AE-176 Aktiebolaget Atomenergii, Stockholm, Sweden, 1965.

3 Marco, S. M., and Han, L. S., "A Note on Limiting Laminar Nusselt Number in Ducts With Constant Temperature Gradient by Analogy to Thin-Plate Theory," Trans. ASME, Vol. 77, 1955, pp. 625–630.

4 Lu, P. C., "A Theoretical Investigation of Combined Free and Forced Convection Heat Generating Laminar Flow Inside Vertical Pipes With Prescribed Wall Temperatures," MS thesis Kansas State College, Manhattan, Kansas, 1959.

5 Clark, S. H., and Kays, W. M., "Laminar Flow Forced Convection in Rectangular Tubes," Trans. ASME, Vol. 75, 1953, pp. 859–866.

6 Eckert, E. R. G., Irvine, T. F., Jr., and Yen, J. T., "Local Laminar Heat Transfer in Wedge-Shaped Passages," Trans. ASME Vol. 80, 1958, pp. 1433–1438.

7 Tao, L. N., "On Same Laminar Forced Convection Problems," Journal of Heat Transfer, Trans. ASME, Series C, Vol. 83, 1961, pp. 466–472.

8 Schmidt, F. W., and Newell, M. E., "Heat Transfer in Fully Developed Laminar Flow Through Rectangular and Isosceles Triangular Ducts," *International Journal of Heat Mass Transfer*, Vol. 10, 1967, pp. 1121–1123.

9 Sparrow, E. M., and Haji-Sheikh, A., "Laminar Heat Transfer and Pressure Drop in Isosceles Triangular, Right Triangular and Circular Ducts," Journal of Heat Transfer, Trans. ASME, Series C, Vol. 87, No. 3, Aug. 1965, pp. 426–427.

10 Cheng, K. C., "Laminar Flow and Heat Transfer Characteristics in Regular Polygonal Ducts," *Proceedings of the Third International Heat Transfer Conference*, AIChE, Vol. 1, 1966, pp. 64–76.

11 Yen, J. T., "Each Solution of Laminar Heat Transfer in Wedge-Shaped Passages With Various Boundary Conditions," Wright Air Development Centre, Technical Report 57–224, July 1957.

12 Tao, L. N., "The Second Fundamental Problem in Heat Transfer of Laminar Forced Convection," *Journal of Applied Mechanics*, Vol. 29, TRANS. ASME, Vol. 84, Series E, 1962, pp. 415–419.

13 Tao, L. N., "On Combined Free and Forced Convection in Channels," JOURNAL OF HEAT TRANSFER, Trans. ASME, Series C Vol. 82, No. 2, May 1960, pp. 233–238.

14 Tao, L. N., "On Combined Free and Forced Convection in Circular and Sector Tubes," *Applied Scientific Research*, Section A, Vol. 9, No. 5, 1960, pp. 357–368.

15 Han, L. S., "Laminar Heat Transfer in Rectangular Channels," JOURNAL OF HEAT TRANSFER, TRANS. ASME, Series C, Vol. 81, No. 2, May 1959, pp. 121–128.

16 McLachlan, N. W., *Bessel Functions for Engineers*, Oxford, England, University Press, 1934.

17 Aggarwala, B. D., and Iqbal, M., "On Limiting Nusselt Number From Membrane Analogy for Combined Free and Forced Convection Through Vertical Ducts," *International Journal of Heat Mass Transfer* (in Press).

18 Sparrow, E. M., and Siegel, R., "A Variational Method for Fully Developed Laminar Heat Transfer in Ducts," JOURNAL OF HEAT TRANSFER, TRANS. ASME, Series C, Vol. 81, No. 2, May 1959, pp. 157–167.

19 Cheng, K. C., "Laminar Forced Convection in Regular Polygonal Ducts With Uniform Peripheral Heat Flux," JOURNAL OF HEAT TRANSFER, TRANS. ASME, Series C, Vol. 91, No. 1, Feb. 1969, pp. 156–157.

L. O. BILLIG
Research Specialist,
The Boeing Co.,
Seattle, Wash. Assoc. Mem. ASME

K. R. GALLE
Associate Professor of
Mechanical Engineering,
University of Washington,
Seattle, Wash.

A Numerical Method for Calculating Fully Developed Laminar Velocity Profiles From Temperature Profiles

It is noted that the velocity profile has a significant effect on the temperature profile that develops in a fluid flowing through a tube. A numerical method for retrieving the velocity profile from a temperature profile is given and the computer program written to implement the method is described. The method retrieved velocity profiles of reasonable accuracy from temperature profiles calculated from the Graetz solution and by Kays' numerical method.. The results of a study to estimate the effects of possible experimental errors from several possible sources on the calculated velocity profiles are included.

Introduction

When an isothermal fluid in fully developed steady laminar flow through a uniform tube encounters a change in tube-wall temperature, the temperature field that develops is a unique function of the velocity field, the thermal diffusivity of the fluid, and the wall temperature. The problem of calculating the temperature profiles that develop has been treated by many authors. Solutions are available for both Newtonian and non-Newtonian fluids, for a variety of boundary conditions. Fig. 1 shows several temperature profiles calculated by the numerical method of Kays [1][1] for a variety of different velocity profiles.

Fig. 1 demonstrates that velocity profiles have a significant effect on the temperature profiles. This suggests that the temperature fields that develop in flowing fluids may contain usable information about the velocity fields. By inference, then, they also contain information about the rheological properties of the fluid. If the temperature field is to yield usable information about rheological properties, however, there must first be a means of reconstructing the velocity field from temperature measurements.

This paper describes a numerical method of calculating the velocity profiles from temperature profiles that develop under conditions of steady, fully developed flow through a tube as just described. The key feature of the method developed herein is the construction of a numerical temperature grid independently of the velocity profile. A dimensionless group that is held constant is used in the construction of the grid. This group contains the local velocity as one of its factors. After the grid is complete, the temperatures in the final column of the grid are compared, one by one, to a physical temperature profile developed in fluid flowing through a tube. In this way a physical radius may be associated with each row of the grid. A one-step calculation then yields the corresponding fluid velocities.

The method was developed in the course of a search for a new method of studying the flow of a non-Newtonian fluid in a small tube. It has been programmed for a digital computer and has successfully retrieved parabolic velocity profiles from temperature profiles calculated from the classical Graetz solution [2]. It has also recovered the original velocity profile from a temperature profile calculated for a highly distorted non-Newtonian velocity profile by Kays' numerical method [1].

The Mathematical Model

The energy equation applicable to each point in a stream of incompressible fluid is

$$\rho c_p \frac{DT}{Dt} = \nabla \cdot (k \nabla T) + \mu \phi. \qquad (1)$$

Equation (1) may be expressed in cylindrical coordinates and the following assumptions made:

1 The system is axially symmetric.
2 Viscous dissipation is negligible.
3 Fluid properties are constant in the heated portion of the duct. Entrance values are used.
4 Transients have decayed.
5 There is negligible axial conduction in the fluid.

[1] Numbers in brackets designate References at end of paper.

Contributed by the Heat Transfer Division for publication (without presentation) in the JOURNAL OF HEAT TRANSFER. Manuscript received by the Heat Transfer Division, July 9, 1968; revised manuscript received, March 25, 1969. Paper No. 70-HT-C.

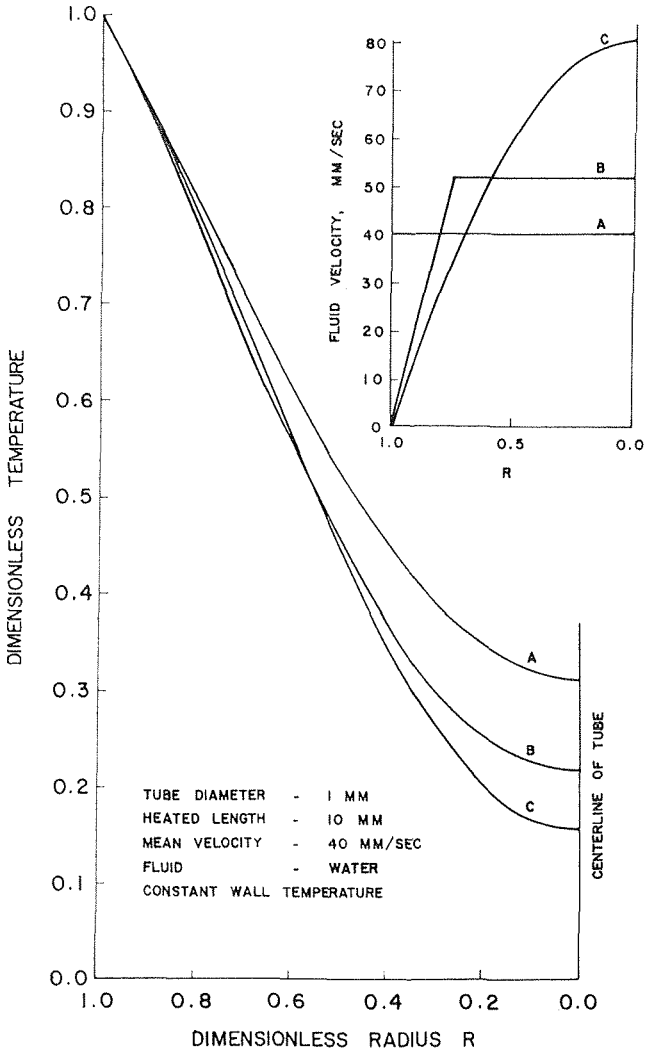

Fig. 1 Temperature profiles in fluid flowing through a tube as calculated by Kays' method [1] for the velocity profiles shown in the inset

6 The hydrodynamic velocity profile is fully developed at the entrance to the heated section of the duct and remains constant thereafter.

Under the foregoing assumptions, the energy equation reduces to the familiar form

$$u\frac{\partial T}{\partial x} = \frac{k}{\rho c_p}\frac{1}{r}\frac{\partial}{\partial r}\left(r\frac{\partial T}{\partial r}\right). \tag{2}$$

The thermal diffusivity $\alpha = k/\rho c_p$ and the dimensionless radius $R = r/r_0$ are introduced. A transformation $y = \ln R$, credited by Jakob [3] to Nessi and Nissolle [4], is made to transform the cylindrical coordinates of the tube to a semi-infinite Cartesian plane. The modified energy equation takes the form

$$u\frac{\partial T}{\partial x} = \frac{\alpha}{(r_0 R)^2}\frac{\partial^2 T}{\partial y^2} \tag{3}$$

where the velocity u is a function of R only, but where no specific form of the functional relationship is assumed. The symbol R is retained in equation (3) and subsequently for convenience in preference to the more cumbersome e^y.

The finite-difference form of equation (3) may be written as

$$u\frac{\Delta_x T}{\Delta x} = \frac{\alpha}{(r_0 R)^2}\frac{\Delta_y{}^2 T}{(\Delta y)^2}. \tag{3a}$$

Put

$$T_{m,n} = T(x_n, y_m)$$
$$\Delta_x T = T_{m,n+1} - T_{m,n}$$
$$\Delta_y T = T_{m+1,n} - T_{m,n}$$
$$\Delta_y{}^2 T = T_{m+1,n} - 2T_{m,n} + T_{m-1,n}$$
$$u_m = u(R_m).$$

In this notation, equation (3a) becomes

$$\frac{T_{m,n+1} - T_{m,n}}{\Delta x} = \frac{\alpha}{u_m (r_0 R_m)^2}\frac{T_{m+1,n} - 2T_{m,n} + T_{m-1,n}}{(\Delta y)^2}. \tag{3b}$$

If it were possible to measure all the temperatures used in equation (3b) it would be possible to solve immediately for the corresponding velocity, u_m. However, in considering possible experimental difficulties, we note first that

$$\left|\frac{\partial T}{\partial x}\right| \ll \left|\frac{\partial T}{\partial R}\right|.$$

(If that were not true, the assumption of negligible axial conduction would be untenable.) Hence the axial temperature gradient required in equation (3b) might be very hard to measure. Second, it appears possible to make many more temperature measurements in a radial traverse than could be made in an axial traverse. Data-smoothing techniques could be applied with more confidence to the radial temperature profile in such a case. In deference then to experimental difficulties we will derive a method of constructing a numerical temperature grid without knowing either the axial temperature gradient or the functional relationship between the fluid velocity, u_m, and the dimensionless radius R_m (or y_m). The final column of the numerical grid is then compared to a radial temperature profile so that a radius is associated with each index m. The corresponding velocity u_m will then be obtained from a one-step closed-form solution.

The task of constructing the temperature grid would be greatly simplified if there were a set of transformed radii $\{y_m\}$ such that equation (3b) could be written in the form

$$\Delta_x T = \frac{1}{P}(T_{m+1,n} - 2T_{m,n} + T_{m-1,n}) \tag{3c}$$

Nomenclature

c_p = constant-pressure specific heat
D/Dt = substantial derivative, $\partial/\partial T + U\cdot\nabla$
d = differential operator
k = thermal conductivity of the fluid
L = length of the heated portion of the duct
ln = natural logarithm
m, n = indexes in finite-difference equations
P = the dimensionless group $\dfrac{u(r_0 R\Delta y)^2}{\alpha\Delta x}$
R = dimensionless radius r/r_0
r = radial coordinate
r_0 = radius of tube
T = temperature
t = time
U = velocity vector
u = axial velocity
x = axial coordinate of tube
Y = a value of y between y_{m-1} and y_m
y = ln R
α = thermal diffusivity
Δ = finite difference
μ = viscosity
ρ = density
ϕ = dissipation function, also a dimensionless correction factor defined by equation (8)
∇ = vector differential operator
∂ = partial differential operator

where P is a constant chosen to satisfy stability requirements.[2] Comparison of equations (3*b*) and (3*c*) indicates that the constant P must be defined by the relation

$$\frac{1}{P} = \frac{\alpha \Delta x}{u_m (r_0 R_m \Delta y)^2}. \tag{4}$$

Since we wish $1/P$ to be constant, two observations must be made. First, there are two points in the flow field where equation (4) is singular; at the tube wall where the velocity is normally zero and at the center line where R is zero. Second, equations (3*b*) and (3*c*) are valid when Δy is a fixed quantity. Except for the special case in which $u_m R_m{}^2$ may be a constant, Δy must vary to satisfy equation (4). Hence equation (3*c*) must be corrected for the variation of Δy.

It is seen that there are three problems to be overcome before a relation such as equation (3*c*) can be applied to the computation of velocity profiles from temperature profiles; the stability problem, the problem of singularities, and the problem of variable Δy. It will be shown that (*a*) the stability problem has been solved by other authors, (*b*) the singular points can be avoided in the calculations, and (*c*) the introduction of unacceptable error by the variable Δy can be avoided by the use of a weighting factor on the temperatures.

Stability

Equation (3*b*) is similar in form to the finite-difference one-dimensional heat-conduction equation

$$T_{m,n+1} - T_{m,n} = \frac{\alpha \Delta t}{(\Delta x)^2} (T_{m+1,n} - 2T_{m,n} + T_{m-1,n}) \tag{5}$$

that Dusinberre [6] wrote (using the present notation)

$$T_{m,n+1} - T_{m,n} = \frac{1}{P} (T_{m+1,n} - 2T_{m,n} + T_{m-1,n}) \tag{5a}$$

where the modulus $P = (\Delta x)^2/\alpha \Delta t$.[3] Richtmyer [5] proved that the necessary and sufficient condition that the error in the numerical integration of equations of the form of (5) be bounded is that $P \geq 2$. The classical, graphical solution to the one-dimensional heat-conduction equation, published by Schmidt [6], used $P = 2$ so that equation (5*a*) reduces to

$$T_{m,n+1} = (T_{m+1,n} + T_{m-1,n})/2. \tag{6}$$

Dusinberre [7] recommended the use of $P = 3$, in which case equation (5*a*) becomes

$$T_{m,n+1} = (T_{m+1,n} + T_{m,n} + T_{m-1,n})/3. \tag{6a}$$

In the present study, a modification of equation (6*a*) was used successfully, where P was defined by equation (4). It was concluded that the stability criterion developed for one-dimensional conduction is also valid when applied to steady, axisymmetric, laminar flow.

Boundaries and Singularities

The points in the flow field where equations (3*c*) and (4) are singular may be avoided without great difficulty. Starting at the wall, $T_{1,n}$ is the wall temperature, which is one of the boundary conditions that must be given. The usual assumption in continuum fluid mechanics is that the fluid velocity is zero at a stationary, solid surface. With the wall temperature and the velocity at the wall known, the temperature computations may begin with $T_{2,n}$ for each $n > 1$.

At the second singularity, the center line of the duct, neither the temperature nor the velocity is known. It is known, however, that the temperature gradient, $\partial T/\partial R$, goes to zero. Both T and R are continuous and have continuous derivatives. Hence

$$\frac{\partial T}{\partial Y} = \frac{\partial T}{\partial R} \frac{dR}{dy} = R \frac{\partial T}{\partial R}.$$

Thus $\partial T/\partial y$ is the product of two quantities that go to zero independently as the center line is approached. For all practical purposes, therefore, the transformed temperature gradient $\partial T/\partial y$ may be set equal to zero for sufficiently small R. This was handled in the program by setting $T_{m+1,n} = T_{m,n}$ for m greater than some arbitrary integer, say, MY. By proper choice of MY, the center line may be approached as closely as desired. Thus the second singularity is avoided by staying a finite distance from the center line without incurring any significant penalty on accuracy.

Consequences of the Variability of Δy

It has been pointed out that, as u and R vary at different points in the flow field, Δy must also vary so that the product $u_m(r_0 R_m \Delta y)^2$ is held constant. This must be done to satisfy equation (4). The problem lies in the fact that the formulation of the second difference of temperature with respect to y, $\Delta_y{}^2 T$, is predicated on a constant Δy. A method of correction for the variation in Δy was developed and applied successfully. The development is given in the following.

Consider the computation of $T_{m,n+1}$, with values of Δy to either side of the node point (m, n) given by $\Delta y_1 = y_{m+1} - y_m$ and $\Delta y_2 = y_m - y_{m-1}$. Let y_{m-1}, y_m, and y_{m+1} be given. It is possible, without loss of generality and consistent with the requirement that $u_m(r_0 R_m \Delta y)^2$ be constant, to suppose that

$$|y_m - y_{m-1}| > |y_{m+1} - y_m|.$$

Obviously there exists some y, say $y = Y$, in the interval (y_{m-1}, y_m) such that

$$y_m - Y = y_{m+1} - y_m.$$

In the conventional formulation of the second difference of T with respect to y, e.g., as in equation (3*b*), the temperature $T_{Y,n}$ rather than $T_{m-1,n}$ should be used. That is

$$\frac{\Delta_y{}^2 T}{(\Delta y)^2} = \frac{T_{m+1,n} - 2T_{m,n} + T_{Y,n}}{(\Delta y)^2}$$

where $\Delta y = y_{m+1} - y_m$. Both T and its derivatives are assumed to be continuous. Therefore T must be piecewise linear over small intervals. Since T is linear over small intervals, it is possible to interpolate linearly between $T_{m-1,n}$ and $T_{m,n}$. On performing the interpolation, it is found that

$$T_{Y,n} = (1 - \phi_m) T_{m-1,n} + \phi_m T_{m,n} \tag{7}$$

where

$$\phi_m = 1 - \frac{y_{m+1} - y_m}{y_m - y_{m-1}}. \tag{8}$$

The quantities defined by equations (7) and (8) were used to write equation (6*a*) in the final form

$$T_{m,n+1} = [T_{m+1,n} + (\phi_m + 1) T_{m,n} + (1 - \phi_m) T_{m-1,n}]/3. \tag{6b}$$

We note parenthetically that higher-order interpolation could be used to obtain $T_{Y,n}$. In the cases run in this study, however, it was found that Δy tended to vary by a factor of about three between the maximum and minimum values in a field of 60–100 values. Linear interpolation was used therefore to save computer time.

[2] Richtmyer [5] defines a stable solution as one in which the error is bounded. He emphasizes, however, that the fact that the error is bounded does not, in any sense, mean that it is small.

[3] Jakob [3] credits the concept to Nessi and Nissolle [4] who introduced the expression $\alpha \Delta t/(\Delta x)^2 = K/2$ where K is chosen arbitrarily, numbers between $1/4$ and 1 being preferable in most cases. See p. 386 of reference [3].

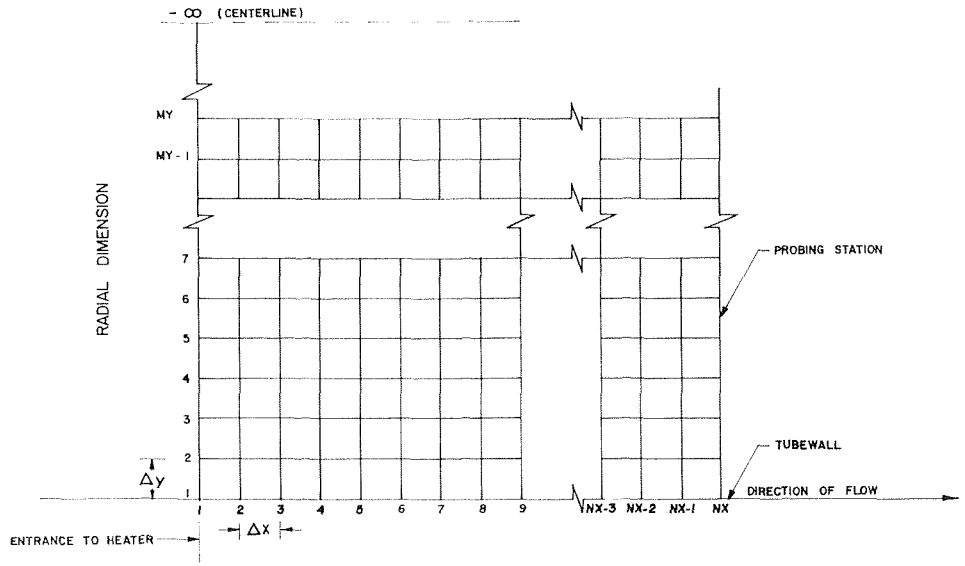

Fig. 2 The relationship between the numerical grid and the geometry of the heater. Numerical indexes are shown along the axes.

The Computational Scheme

A computer program was written to perform the calculations iteratively as described in the following.

The fluid temperature is assumed to be known and uniform when the fluid enters a short heated section of tube. The axial coordinate, x, is set equal to zero at the entrance to the heated section. Initial values for $\{\phi_m\}$ and Δx are chosen. Starting then at $x = 0$ and with the wall temperature known for $x > 0$, the temperature throughout the heated section is calculated. Computations based on equation (6*b*) are continued, filling column after column of the grid diagrammed in Fig. 2 and proceeding in the direction of increasing x (i.e., downstream) until $T_{MY,n}$ reaches the observed center-line temperature. The final result of these calculations is a one-dimensional matrix with MY elements of temperature, T_m. (Only the last column of figures in the grid in Fig. 2 is used.) The matrix exists in the transformed plane with each of the node points at an unknown distance from the edge of the plane, i.e., the tube wall.

The transformation back to cylindrical coordinates is made by comparing the numerical temperatures, T_m, to an experimental profile. Fig. 3 shows how this might be done graphically. For $m = 10$, T_m is the 10th element of the one-dimensional temperature matrix. For the temperature matrix to have physical significance, there must be a corresponding $T(R)$ in the physical system such that $T(R_m) = T_m$. Hence one could extend a line at constant m ($m = 10$ in the example of Fig. 3) to intercept the temperature curve of T_m, then extend the line across at constant temperature to intercept the curve of $T(R)$, then upward to locate the radius R_m on the upper abscissa. This is done for all the MY elements of the temperature matrix.

Two things are done in preparation for the second (and successive) iterations. A new value of Δx is calculated;[4]

$$\Delta x = L/N$$

where L is the length of the heated portion of the duct and N is the value of n when $T_{MY,n}$ reaches the observed (input) center-line temperature. Second, a new set $\{\phi_m\}$ is calculated using equation (8). Then the temperature field is reinitialized to the values at $x = 0$ and computations are resumed using equation (6*b*).

It was found that the program converged monotonically to stationary values of Δx and $\{\phi_m\}$ in about six iterations.

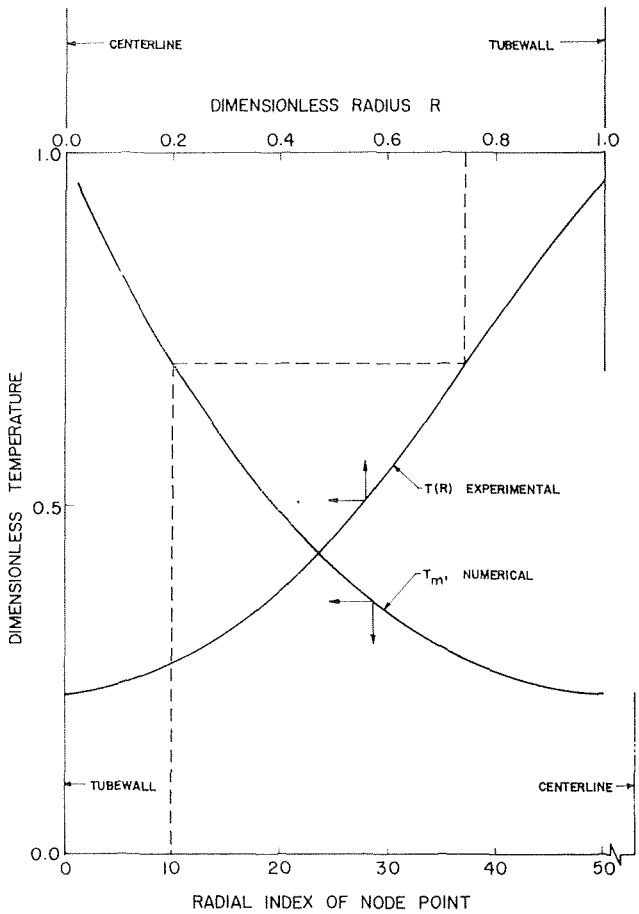

Fig. 3 Diagram illustrating the transformation from numerical coordinates to physical coordinates by comparing numerical and physical temperature profiles

[4] When the tube-wall temperature varies axially, Δx must be known in order that the tube-wall temperature be known at each step. It is seen from equation (4) that Δx affects the velocity as a scaling factor. If the actual center-line temperature is high, more steps must be taken in the x-direction for the calculated center-line temperature to reach an experimental center-line temperature; that is to say, Δx must be small. It follows that the calculated velocity will be smaller than it would be if the center-line temperature were low. Thus one of the reasons for forcing a match between the calculated and experimental center-line temperatures is to obtain a proper value for Δx.

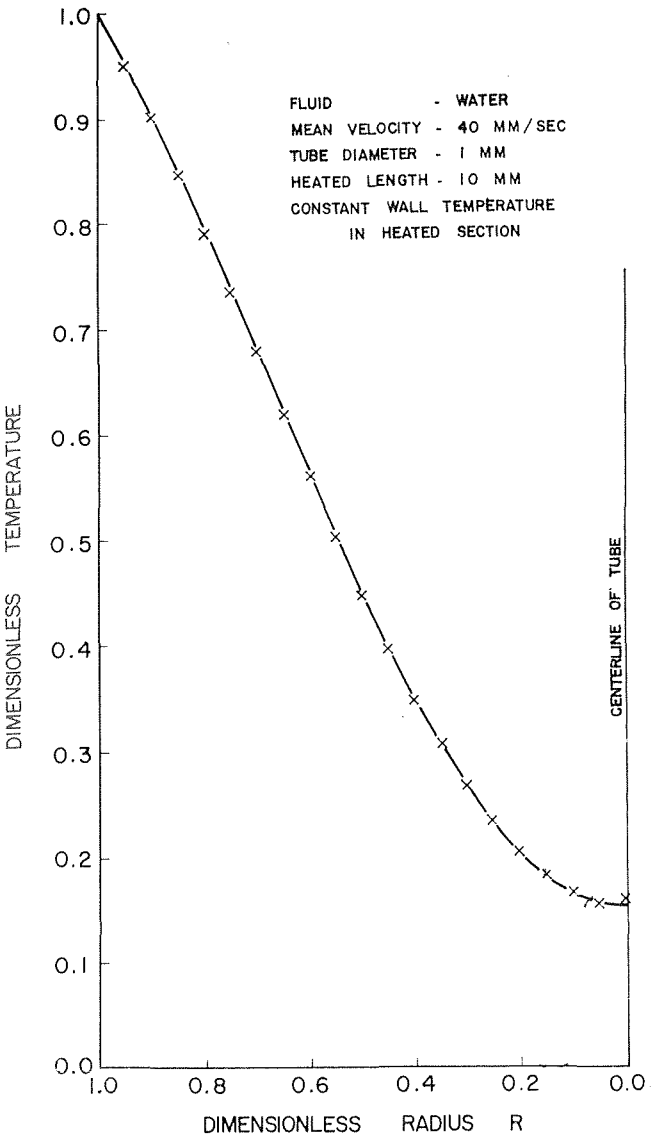

Fig. 4 Graetz temperature profile. The points calculated from the Graetz solution are indicated by the crosses. The solid line represents the profile calculated numerically by the method developed in this study.

After satisfactory convergence on Δx and ϕ_m is achieved, the velocities may be obtained by solving equation (4) for u:

$$u_m = \frac{\alpha P \Delta x}{(r_0 R_m \Delta y)^2} \tag{9}$$

or

$$u_m = \frac{\alpha P \Delta x}{\left[r_0 R_m \ln\left(\frac{R_m + 1}{R_m}\right)\right]^2} \tag{9a}$$

A more detailed discussion of the computer program is given in reference [8], which also contains a FORTRAN listing.

Test of the Numerical Method

The program was written so that the velocity profile can be calculated if a temperature profile is input or a temperature profile can be calculated if a velocity profile is input. The program was tested by comparing the results of a temperature-profile calculation to the classical Graetz solution. Fig. 4 shows a temperature profile calculated from the Graetz solution using eigenfunctions and derivatives published by Brown [9]. The temperature profile calculated by the Graetz solution is indicated by the crosses shown in the figure and the profile calculated numerically is indicated by the solid line. Fig. 5 shows points on a velocity profile calculated from the Graetz temperature profile in Fig. 4. The parabolic velocity profile assumed in the Graetz solution is indicated by the solid line in the figure.

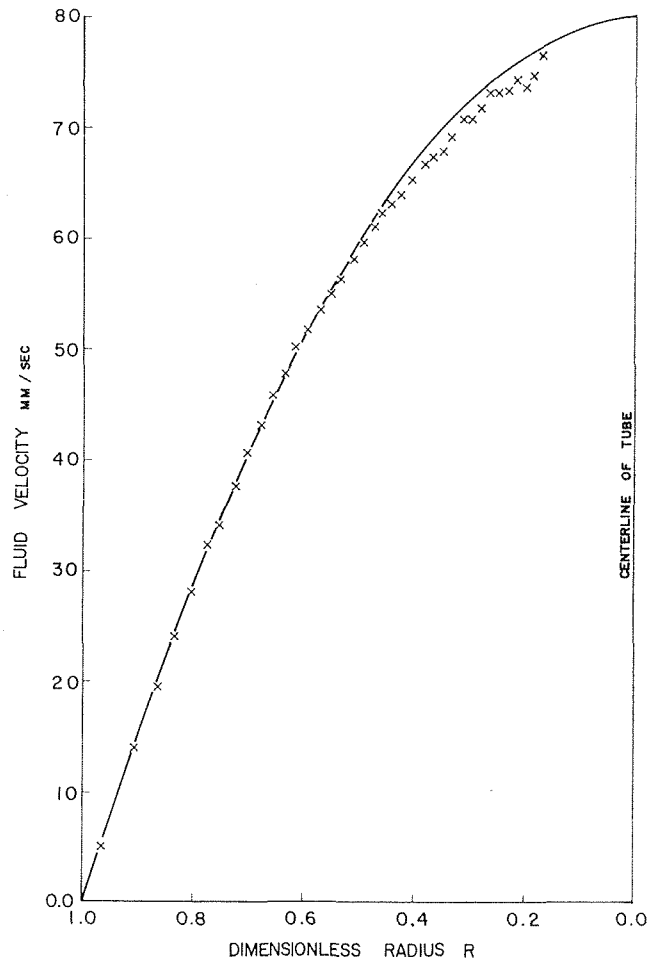

Fig. 5 Velocity profile calculated from the Graetz temperature profile. The calculated points are indicated by the crosses. The parabolic profile assumed in the Graetz solution is given by the solid line.

The numerical method was tested further by calculating a temperature profile for a highly distorted velocity profile by Kays' method. Then the method developed in this study was used to retrieve the velocity profile from the temperature profile. The assumed velocity profile and the results of the set of calculations are shown in Fig. 6.

From the results of the calculations just cited, it was concluded that the numerical method developed in this study would retrieve velocity profiles of reasonable accuracy from the temperature profiles developed in either Newtonian or non-Newtonian flow. There are undoubtedly many ways in which such information can be used. For example, if the velocity gradient at a tube wall is known and the axial pressure gradient is known (or can be measured), an apparent fluid viscosity at the tube wall may readily be calculated. Such explorations are, however, outside the scope of this paper.

Requirements on Data Accuracy

It is seen from Fig. 1 that large variations in the velocity profile produce relatively much smaller variations in temperature. It is clear that the determination of velocity profiles from temperature profiles imposes stringent requirements on the accuracy of the temperature data. Estimates have been made of the effects of

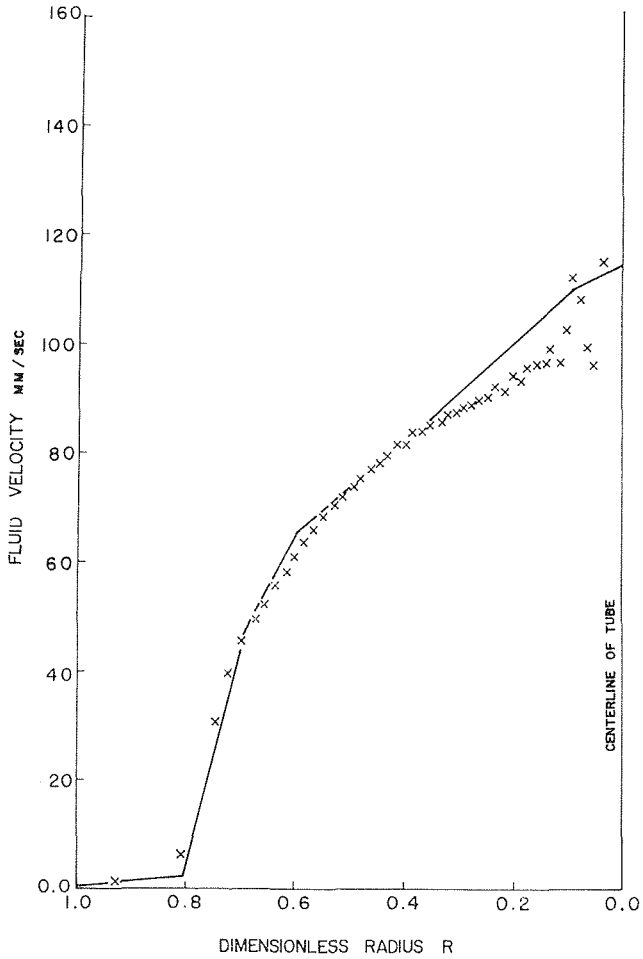

Fig. 6 Velocity profile calculated from a perturbed temperature profile. The temperature profile was calculated numerically by Kays' method for the velocity profile indicated by the solid line. The crosses represent the velocity profile retrieved from the temperature profile.

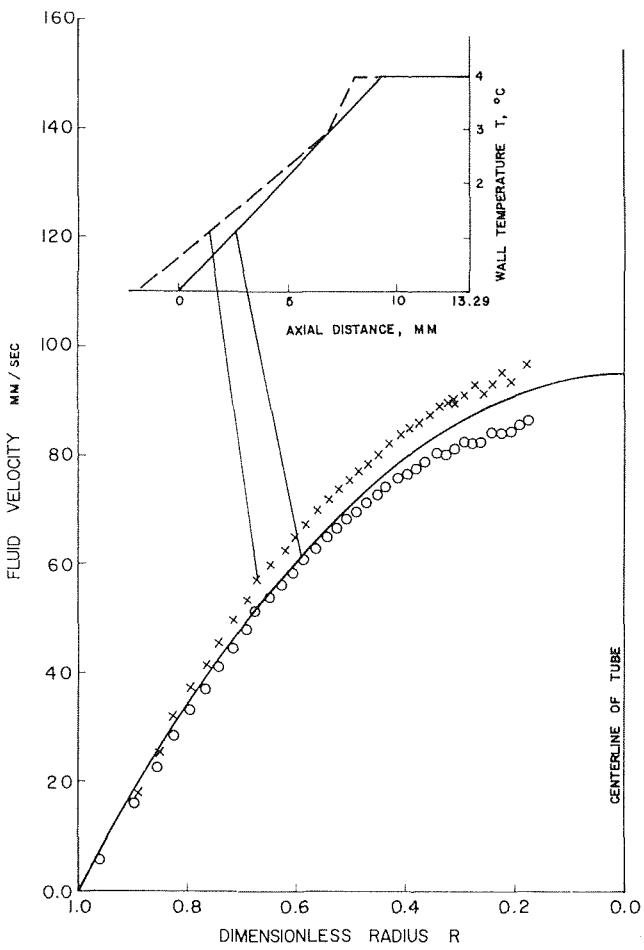

Fig. 7 The effect of errors in wall temperature on the velocity profile calculated from a temperature profile

errors in temperature measurements on the calculated velocity profiles. The errors considered were errors in temperature measurements as affected by sensor location, errors in radial temperature gradients, errors in wall temperature measurements, and the effect of variable thermal diffusivity. These studies are discussed next.

An estimate of the effect of small errors in temperature measurement on the calculated velocity may be made by assuming the errors to be small enough to linearize the equations. The ϕ_m's in equation (6*b*) will be assumed to be zero. Rather than perturb the temperature T_m that is associated with a radius R_m, assume that an error exists in the measurement of R_m. Standard techniques of differential calculus may be applied to equation (9) to obtain

$$\frac{1}{u_m}\frac{\partial u_m}{\partial R_m} = \frac{-2}{R_m} \tag{10}$$

According to equation (10), an error of 0.01 in the value of R_m would introduce an error in u_m of about 2 percent near the tube wall or an error of 4 percent at a point midway between the tube wall and the center line. As R_m approaches the center line, the error in u_m increases without limit.

An analysis similar to that just cited may be used to estimate the effect of an error in the radial temperature gradient. Assuming that the given temperature at R_m is correct, it has been shown [8] that

$$\frac{1}{u_m}\frac{\partial u_m}{\partial(\partial T/\partial R)} = \frac{2}{\partial T/\partial R} \tag{11}$$

Again, the effects of errors are least significant near the tube wall, where the temperature gradient is the greatest, and again the error in u_m increases without limit near the center line of the tube, where the temperature gradient goes to zero.

The greatest uncertainty in tube-wall temperature measurement would probably be at the junction between the heated and the unheated portions of the tube. The temperature differences to be measured are smaller there and the effects of axial conduction in the tube wall would cause greater uncertainty in regions of large axial temperature gradients. A study was made to assess the effect of error in wall-temperature measurement at the upstream end of the heater on the calculated velocity profile. Fig. 7 illustrates that study. A radial temperature profile was calculated by Kays' method for the parabolic velocity profile indicated by the solid line in the figure using the wall temperature indicated by the solid line in the inset. Then velocity profiles were calculated using the Kays' radial temperature profile and two wall temperature profiles; the original profile and a perturbed profile. The velocity profile calculated using the original wall temperature is indicated by the circled points in Fig. 7; that calculated using the perturbed wall temperature profile (indicated by the dashed line in the inset) is indicated by the crosses in the figure. Fig. 7 indicates that errors in wall temperature at the heater inlet would change the calculated velocity profile approximately by a scale factor. The form of the calculated profile is not modified significantly.

The possibility that the increase in thermal diffusivity with increasing temperature may modify the temperature profile was considered. According to data published by Eckert and Drake [10], the thermal diffusivity of water increases by about 0.3

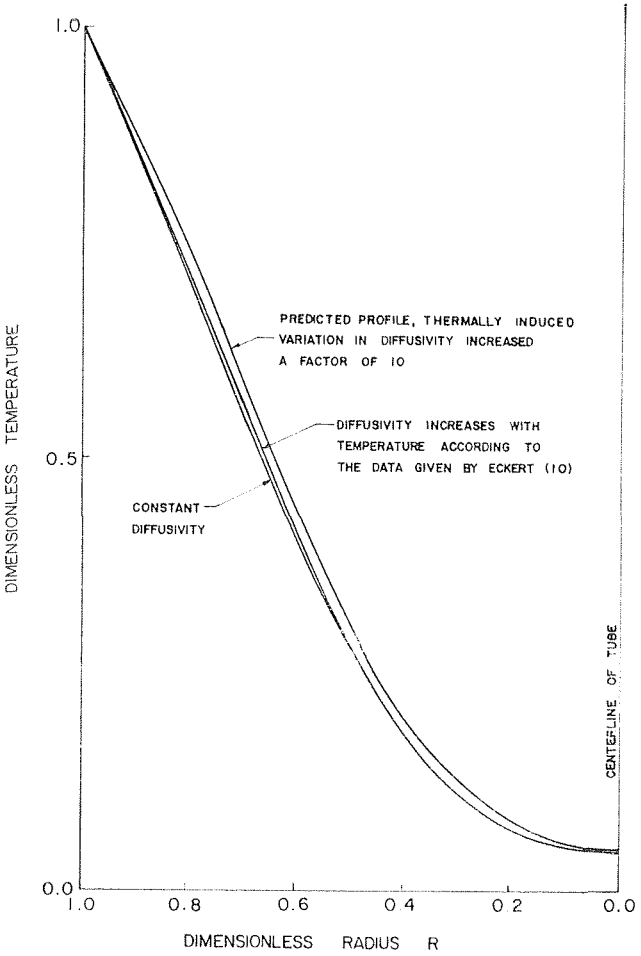

Fig. 8 Curves showing the result of including the change of thermal diffusivity with temperature on temperature profiles calculated by Kays' method

percent per degree Celsius near room temperature. The computer program written to calculate temperature profiles by Kays' method was modified to account for thermally induced changes in thermal diffusivity. The results of a set of computations, shown in Fig. 8, indicate that the effects of thermally induced changes in thermal diffusivity may be neglected for small temperature differences. (The use of large temperature differences is impractical in any case because the attendent viscosity changes could invalidate assumption 6, that the velocity profile remains constant.)

Conclusions

It has been shown that it is possible to calculate velocity profiles from the temperature profiles that develop in steady, fully developed, axisymmetric laminar flow. It is also possible, using the same assumption, to calculate the temperature profile, given any arbitrary, nonzero axisymmetric velocity profile. The new method has successfully retrieved parabolic velocity profiles from temperature profiles calculated from the Graetz solution. It has also retrieved highly distorted velocity profiles from temperature profiles calculated numerically by Kays' method. The new method of calculating temperature profiles has been tested against both the Graetz solution and Kays' numerical method. Acceptable agreement was obtained in each case.

A technique for using continuously varying grid sizes is inherent in the new numerical scheme. It is felt that there are many candidate applications for this differencing scheme and that it is a useful contribution to numerical science.

A study was made to estimate the effect of various experimental errors in temperature measurement on the calculated velocity profile. From this study it was concluded first that it will be difficult to measure velocities accurately near the center line of the tube by this method. A second conclusion is that accurate radial location of the temperatures is required to obtain good results. A third conclusion is that experimental apparatus should be designed to produce a steep temperature gradient, with the amount of heating at the center line just great enough to measure accurately. This means that, in order to measure low fluid velocities, the heater section should be as short as possible and still be consistent with the assumption of negligible axial conduction in the fluid.

It was found that assumed errors in tube-wall temperature measurement at the entrance to the heater section changed the calculated velocity profile approximately by a scale factor. The form of the velocity profile was not changed significantly. It was also found that, in water, at least, the effect of neglecting the change in thermal diffusivity with temperature had a very small effect on the calculated temperature profile. It appears then that the assumption of constant thermal diffusivity is justified.

Acknowledgment

This work was supported in part by National Institute of Health Grants Nos. HE 07293 and HTS 5147.

References

1 Kays, W. M., "Numerical Solutions for Laminar-Flow Heat Transfer in Circular Tubes," TRANS. ASME, Vol. 77, 1955, pp. 1265–1274.

2 Graetz, L., *Annals of Physik*, Vol. 18, 1883, p. 79. (Cited in [3].)

3 Jakob, M., *Heat Transfer*, Vol. 1, Wiley, New York, 1951.

4 Nessi, A., and Nissolle, L., "Methodes graphiques pour l'etude des installations de chaffage et des refrigeration en regime discontinu," Dunod, Paris, 1929. (Cited in [3].)

5 Richtmyer, R. D., "Difference Methods for Initial Value Problems," *Interscience Tracts in Pure and Applied Mathematics*, Vol. 4, Interscience Publishers, New York, 1957.

6 Schmidt, E., *Festschrift zum siebsigsten Geburtstag August Foeppls*, Julius Springer, Berlin, 1924.

7 Dusinberre, G. M., "Numerical Methods for Transient Heat Flow," TRANS. ASME, Vol. 67, 1945, pp. 703–712.

8 Billig, L. O., "Velocity Profiles in Flow Through Small Tubes," PhD dissertation in Mechanical Engineering, University of Washington, Seattle, 1967.

9 Brown, G. M., "Heat or Mass Transfer in a Fluid in Laminar Flow in a Circular or Flat Conduit," *AIChE* Journal, Vol. 6, 1960, pp. 179–183.

10 Eckert, E. R. G., and Drake, R. M., *Heat and Mass Transfer*, 2nd ed., McGraw-Hill, New York, 1959.

JI WU YANG
Assistant Professor, Department of Mechanical Engineering, State University of New York at Buffalo, Buffalo, N. Y. Assoc. Mem. ASME

Effect of Uniform Suction on Laminar Film Condensation on a Porous Vertical Wall

The problem of film condensation on a porous wall has been solved by a boundary layer treatment. A dimensionless suction velocity parameter β, which is proportional to the uniform suction velocity v_w and $^1/_4$th the power of longitudinal coordinate ($x^{1/4}$), is defined to characterize the process. The results are restricted to small values of β, as the solutions are given by power series expansion in β. The effects of uniform suction on heat transfer, condensation rate, film thickness, and velocity and temperature profiles are demonstrated through various examples. In general, uniform suction causes a substantial increase of heat transfer and condensation rate, especially at low subcooling and at high Prandtl numbers. The problem involves three governing parameters: subcooling, Prandtl number, and suction velocity. Comparison with the previous work of Jain and Bankoff is discussed.

Introduction

THE theory of gravity-induced laminar film condensation on a vertical wall has been studied for many years. The original analysis, as given by Nusselt in 1916, consisted of simple force and energy balances within the condensate film. The effects of inertia forces, energy convection, and interfacial shear were neglected. The pioneer work of Nusselt has been improved over the years by Bromley [1],[1] Rohsenow [2], and Chen [3], etc. These analyses were based on the integral equations of momentum and energy. In 1959, Sparrow and Gregg [4] reformulated the problem in terms of boundary layer theory. They introduced a similarity transformation which permitted an exact solution for the condensate, including both convection and inertia. This approach was further improved upon by Koh, Sparrow, and Hartnett [5], who included the interfacial shear and solved the combined boundary layer equations for the vapor and the condensate by a similarity transformation.

The foregoing analyses have been carried out under the condition that the vapor is condensed on a solid surface. No mass transfer occurs at the solid-liquid interface. The case in which the vapor condenses on a porous wall presents an interesting engineering problem. By maintaining a pressure difference across the porous plate, a portion of the condensate can be sucked out of the system, resulting in a thinner film on the wall. Since the heat transfer rate is governed by the film thickness, suction can therefore increase the heat transfer rate considerably. Further, sucking off a portion of the condensate from the liquid film may serve to control the film thickness and to prevent transition from laminar to turbulent flow, which is desirable in many engineering processes. Only two analyses of condensation on porous surfaces have been reported. Jain and Bankoff [6] considered condensation at a vertical wall and Frankel and Bankoff [7] studied condensation on horizontal tubes. The method employed by Bankoff, et al., is an extension of the perturbation method developed by Chen [3] based on the integral equations. The suction velocity was combined with the subcooling term to form a new perturbation parameter. The complete solution was obtained in terms of a double perturbation expansion. Their final results depend on the subcooling parameter, suction velocity, Prandtl number, and the longitudinal coordinate.

This paper presents a different analytical method for determining the effects of suction on heat transfer and flow characteristics. The condensate is treated as a boundary layer flow. The differential boundary layer equations are solved and the final results show that the subcooling, Prandtl number, and a dimensionless suction velocity defined in this paper are the governing parameters.

Analysis

A schematic diagram of the physical model and coordinate system is shown in Fig. 1. A porous vertical flat plate is maintained at constant temperature T_w. In contact with one side of this plate is a pure vapor at its saturation temperature T_s. The plate temperature is lower than the saturation temperature and therefore condensation occurs on the wall surface. Due to the pressure difference maintained across the wall, a portion of the condensate is sucked out through the wall. The suction velocity v_w is uniform along the wall. The remaining condensate forms a continuous laminar film flowing downstream.

The equations expressing conservation of mass, momentum, and energy for steady laminar flow in the liquid layer on a vertical wall are as follows [4]:

[1] Numbers in brackets designate References at end of paper.

Contributed by the Heat Transfer Division and presented at the Winter Annual Meeting, Los Angeles, Calif., November 16–20, 1969, of THE AMERICAN SOCIETY OF MECHANICAL ENGINEERS. Manuscript received by the Heat Transfer Division, May 14, 1969. Paper No. 69-WA/HT-14.

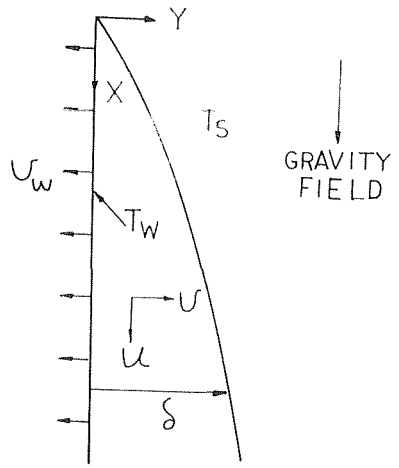

Fig. 1 Physical model and coordinates

$$\frac{\partial u}{\partial x} + \frac{\partial v}{\partial y} = 0 \tag{1}$$

$$u\frac{\partial u}{\partial x} + v\frac{\partial u}{\partial y} = \frac{g}{\rho}(\rho - \rho_v) + \nu\frac{\partial^2 u}{\partial x^2} \tag{2}$$

$$u\frac{\partial T}{\partial x} + v\frac{\partial T}{\partial y} = \alpha\frac{\partial^2 T}{\partial y^2} \tag{3}$$

The boundary conditions are:

$$u = 0, \qquad v = v_w, \qquad T = T_w \qquad \text{at } y = 0 \tag{4}$$

$$\frac{\partial u}{\partial y} = 0, \qquad T = T_s \qquad \text{at } y = \delta \tag{5}$$

The fluid properties and the suction velocity are assumed constant. The liquid-vapor interfacial shear is neglected in the present analysis. It has been shown that the effect of interfacial shear is negligible for Prandtl numbers greater than unity and is significant only for liquid-metal with large film thickness [5].

A stream function which satisfies the continuity equation is defined as

$$\psi = 4\nu c x^{3/4} f(\eta, \beta) - v_w x$$

where

$$\eta = cyx^{-1/4}$$
$$\beta = v_w x^{1/4}/c\nu \tag{6}$$
$$c = [g(\rho - \rho_v)/4\nu^2\rho]^{1/4}$$

Also, a dimensionless temperature is defined

$$\theta = (T_s - T)/(T_s - T_w)$$

It is noted that η and θ are the conventional similarity variables in laminar film condensation, C is a dimensionless constant, and β is the newly defined suction velocity parameter. The parameter β assumes negative values for suction, as v_w is in the negative direction according to Fig. 1. In terms of the new variables, the conservation equations (1–3) are expressed as follows

$$\frac{\partial^3 f}{\partial\eta^2} + 3f\frac{\partial^2 f}{\partial\eta^2} - 2\left(\frac{\partial f}{\partial\eta}\right)^2 + 1 = \beta\left(-\frac{\partial f}{\partial\beta}\frac{\partial^2 f}{\partial\eta^2} + \frac{\partial f}{\partial\eta}\frac{\partial^2 f}{\partial\beta\partial\eta} + \frac{\partial^2 f}{\partial\eta^2}\right) \tag{7}$$

$$\frac{\partial^2\theta}{\partial\eta^2} + 3\mathrm{Pr}f\frac{\partial\theta}{\partial\eta} + \beta\mathrm{Pr}\left(\frac{\partial f}{\partial\beta}\frac{\partial\theta}{\partial\eta} - \frac{\partial f}{\partial\eta}\frac{\partial\theta}{\partial\beta} - \frac{\partial\theta}{\partial\eta}\right) = 0 \tag{8}$$

When β is zero the foregoing equations reduce to those for a solid wall [5]. The boundary conditions are:

$$\frac{\partial f}{\partial\eta} = 0, \qquad \beta\frac{\partial f}{\partial\beta} + 3f = 0, \qquad \theta = 1 \qquad \text{at } \eta = 0$$
$$\frac{\partial^2 f}{\partial\eta^2} = 0, \qquad \theta = 0 \qquad \text{at } \eta = \eta_\delta \tag{9}$$

where the dimensionless film thickness is denoted as η_δ.

Since the solution is not similar for the present case of uniform suction, equations (7–8) are solved by a series expansion method. The reduced velocity and temperature variables are expanded in series:

$$f(\eta, \beta) = f_0(\eta) + \beta f_1(\eta) + \beta^2 f_2(\eta) + \cdots \tag{10}$$

$$\theta(\eta, \beta) = \theta_0(\eta) + \beta\theta_1(\eta) + \beta^2\theta_2(\eta) + \cdots \tag{11}$$

Substituting the series into equations (7–8) and equating like powers of β, yields the ordinary differential equations governing the functions $f_i(\eta)$ and $\theta_i(\eta)$. The results of the first four approximations are:

Zeroth approximation:

$$f_0''' + 3f_0f_0' - 2f_0'^2 + 1 = 0 \tag{12}$$

$$\theta_0'' + 3\mathrm{Pr}f_0\theta_0' = 0 \tag{13}$$

First approximation:

$$f_1''' + 3f_0f_1'' - 5f_0'f_1' + 4f_0''f_1 - f_0'' = 0 \tag{14}$$

$$\theta_1'' + \mathrm{Pr}(3f_0\theta_1' - f_0'\theta_1 + 4f_1\theta_0' - \theta_0') = 0 \tag{15}$$

Second approximation:

$$f_2''' + 3f_0f_2'' - 6f_0'f_2' + 5f_0''f_2'' - 3f_1'^2 + 4f_1f_1'' - f_1'' = 0 \tag{16}$$

$$\theta_2'' + \mathrm{Pr}(3f_0\theta_2' - 2f_0'\theta_2 + 4f_1\theta_1' + 5f_2\theta_0' - \theta_1' - f_1'\theta_1) = 0 \tag{17}$$

Nomenclature

C = $[g(\rho - \rho_v)/4\nu^2\rho]^{1/4}$, dimensionless parameter
c_p = heat capacity at constant pressure
f = dimensionless velocity variable, equation (6)
g = acceleration due to gravity
h = $q/(T_s - T_w)$, local heat transfer coefficient
h_{fg} = latent heat of condensation
k = thermal conductivity
$\dot{m}$ = condensation rate, equation (30)
Nu = hx/k, local Nusselt number
Pr = $c_p\mu/k$, Prandtl number
T = temperature
u = longitudinal velocity
v = normal velocity
x = coordinate measuring distance along wall from the leading edge
y = coordinate measuring distance normal to wall
α = thermal diffusivity
β = $v_w x^{1/4}/c\nu$, suction velocity parameter
δ = local film thickness
ζ = $c_p(T_s - T_w)$, subcooling parameter
η = $cyx^{-1/4}$, dimensionless variable
θ = $(T_s - T)/(T_s - T_w)$, dimensionless temperature
μ = viscosity
ν = kinematic viscosity
ρ = density
ψ = stream function, equation (6)

Subscripts

i = ith approximation (i = 0, 1, 2, ...)
s = saturation state
v = vapor
w = wall

Third approximation:

$$f_3''' + 3f_0f_3'' - 7f_0'f_3' + 6f_0''f_3 + 4f_1f_2'' + 5f_2f_1'' - 7f_1'f_2' - f_2'' = 0 \quad (18)$$

$$\theta_3'' + \Pr(3f_0\theta_3' - 3f_0'\theta_3 + 4f_1\theta_2' + 5f_2\theta_1' + 6f_3\theta_0' - 2f_1'\theta_2 - f_2'\theta_1 - \theta_2'') = 0 \quad (19)$$

The corresponding boundary values are found by applying the boundary conditions (9):
At $\eta = 0$

$$f_i = 0, \quad f_i' = 0 \quad (i = 0, 1, 2, \ldots\ldots)$$
$$\theta_0 = 1, \quad \theta_i = 0 \quad (i = 1, 2, \ldots\ldots) \quad (20)$$

at $\eta = \eta_\delta$

$$f_i'' = 0, \quad \theta_i = 0 \quad (i = 0, 1, 2, \ldots\ldots) \quad (21)$$

It now only remains to determine the film thickness η_δ. This is done by requiring that energy be conserved at the interface. Such an energy balance yields

$$k\left(\frac{\partial T}{\partial y}\right)_\delta - h_{fg}\left[\frac{d}{dx}\int_0^\delta \rho u dy - \rho v_w\right] = 0 \quad (22)$$

The first term in the foregoing equation is the heat conducted away into the liquid, while the second term represents the energy liberated as latent heat. Using the similarity variables and the series solutions, equation (22) yields the following expression:

$$\frac{c_p\Delta T}{h_{fg}\Pr} = -[-\beta/4 + f_0 + \beta f_1 + \beta^2 f_2 + \ldots\ldots]_{\eta_\delta} \Big/ [\theta_0'/3 + \beta\theta_1'/4 + \beta^2\theta_2'/5 + \beta^3\theta_3'/6 + \ldots\ldots]_{\eta_\delta} \quad (23)$$

Thus the film thickness is determined by the fluid properties (c_p, Pr, and h_{fg}), subcooling (ΔT), and the suction velocity (β). The present problem therefore involves these parameters.

For any preassigned values of Pr, β, and η_δ, the momentum and energy equations (12–19) can be solved simultaneously together with their boundary conditions (20–21). The value of the subcooling parameter ($c_p\Delta T/h_{fg}\Pr$) corresponding to the prescribed Pr, β, and η_δ is then computed from equation (23).

Discussion of Results

Heat Transfer. Once the boundary layer equations are solved, the heat transfer can be determined by the following equations:

$$\mathrm{Nu}/cx^{3/4} = -[\theta_0'(0) + \beta\theta_1'(0) + \beta^2\theta_2'(0) + \ldots\ldots] \quad (24)$$

where

$$\mathrm{Nu} = hx/k \quad (25)$$

$$h = k(\partial T/\partial y)_{y=0}/(T_s - T_w) \quad (26)$$

An alternate form which was used in reference [5] provides a more convenient representation for the Nusselt number:

$$\mathrm{Nu}\left[\frac{4\nu k(T_s - T_w)}{g(\rho - \rho_v)x^3h_{fg}}\right]^{1/4} = -\left[\frac{c_p(T_s - T_w)}{h_{fg}\Pr}\right][\theta_0'(0) + \beta\theta_1'(0) + \beta^2\theta_2'(0) + \ldots\ldots] \quad (27)$$

It is seen that there are two parameters governing the heat transfer: suction (β) and subcooling ($c_p\Delta T/h_{fg}\Pr$). Since suction reduces the film thickness it consequently results in an increase of heat transfer rate, as one expects. However, subcooling produces two opposing effects. It increases the film thickness and, in turn, results in a decrease of heat transfer. On the other hand, a larger thermal potential difference exists with subcooling and therefore yields a higher heat transfer rate. The net effect on heat transfer depends on the relative order of each effect and is demonstrated in Figs. 2 to 5 for four Prandtl numbers.

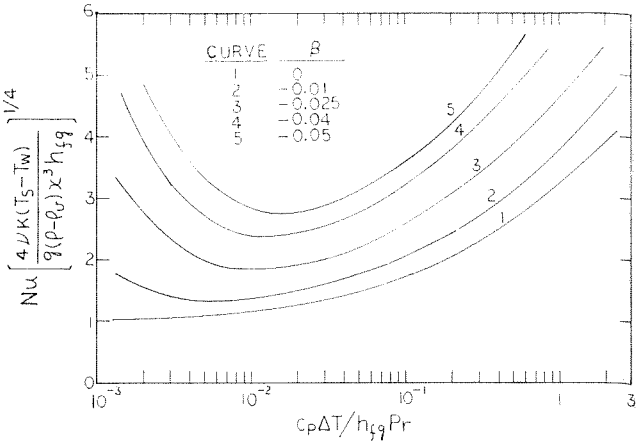

Fig. 2 Effect of uniform suction on heat transfer at Pr = 100

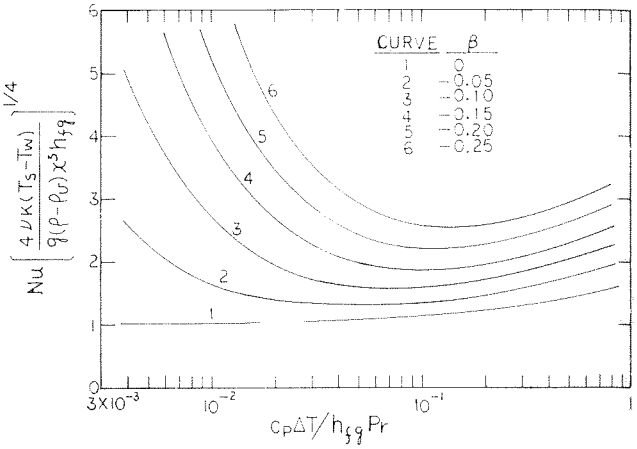

Fig. 3 Effect of uniform suction on heat transfer at Pr = 10

The effect on fluids with high Prandtl numbers is shown in Figs. 2 and 3 for Pr = 100 and 10, respectively. At smaller values of ($c_p\Delta T/h_{fg}\Pr$), heat transfer is reduced by subcooling and the reduction is enhanced by suction. Since the film is thin at low subcooling, the heat transfer is very sensitive to suction. For a given subcooling, considerable increase of heat transfer can be achieved by suction. For example, at ($c_p\Delta T/h_{fg}\Pr$) = 0.01 and $\beta = -0.05$, the increase of heat transfer is about 185 percent for Pr = 100 and 64 percent at Pr = 10. At larger values of ($c_p\Delta T/h_{fg}\Pr$), heat transfer is increased with subcooling. This is due to the fact that the rate of change of film thickness (thermal resistance) becomes slower at high subcooling. (See Fig. 9, to be discussed later.) Again, in this region suction produces a considerable gain of heat transfer. The minimum point of these Nusselt number curves represents a balance between the opposing effects due to subcooling and suction. It is at this minimum point that suction has the smallest effect on heat transfer.

The heat transfer results in fluids with low Prandtl numbers are shown in Figs. 4 and 5 for Pr = 1 and 0.03, respectively. The numerical solutions were restricted to small values of ($c_p\Delta T/h_{fg}$) (i.e., thin film), because the interfacial shear force was neglected in the present analysis. As seen in Figs. 4 and 5, subcooling results in a decrease of heat transfer for all cases. The rate of decrease of heat transfer is significantly higher with suction at small values of subcooling. A further increase of subcooling reduces the sensitivity of heat transfer to both subcooling and suction. No minimum point on the Nusselt number curves was obtained for Prandtl numbers less than unity.

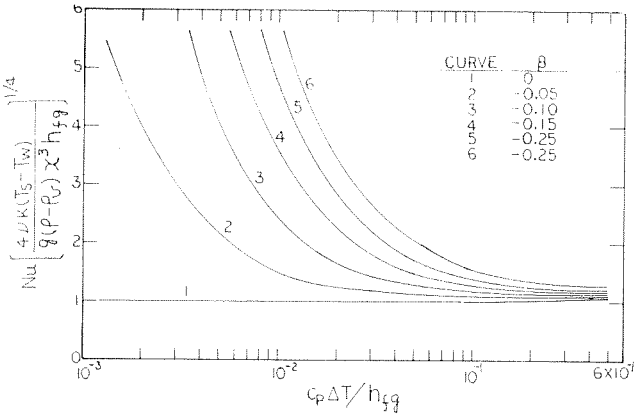

Fig. 4 Effect of uniform suction on heat transfer at Pr = 1

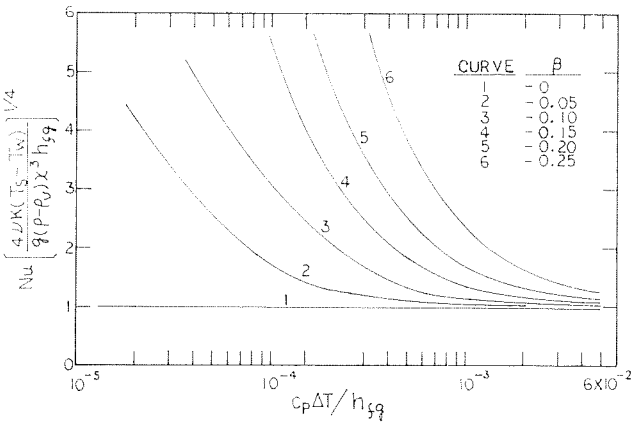

Fig. 5 Effect of uniform suction on heat transfer at Pr = 0.03

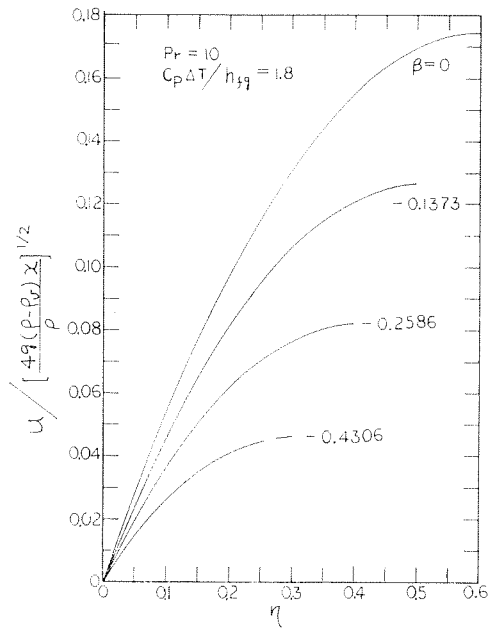

Fig. 6 Representative longitudinal velocity profiles at Pr = 10, $c_p\Delta T/h_{fg}$ = 1.8

Velocity and Temperature Profiles. The velocity and temperature profiles are of interest since they describe the detailed manner in which the flow and heat transfer are affected by suction. In terms of the new variables, the velocity components can be expressed as follows:

$$u/[4g(\rho - \rho_v)x/\rho]^{1/2} = f_0' + \beta f_1' + \beta^2 f_2' + \ldots . \quad (28)$$

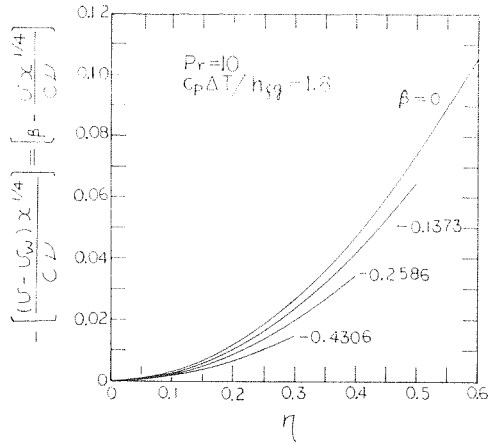

Fig. 7 Representative normal velocity profiles at Pr = 10, $c_p\Delta T/h_{fg}$ = 1.8

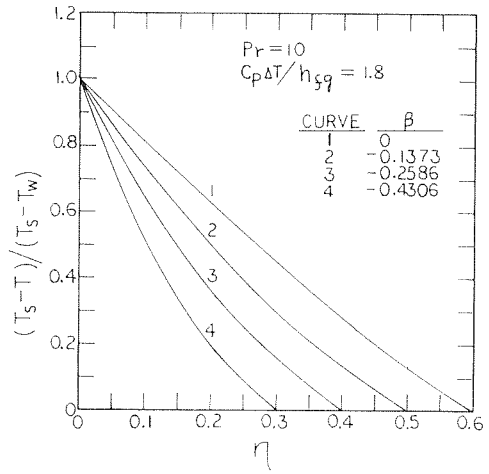

Fig. 8 Representative temperature profiles at Pr = 10, $c_p\Delta T/h_{fg}$ = 1.8

$$(v - v_w)/cvx^{-1/4} = (\eta f_0' - 3f_0) + \beta(\eta f_1' - 4f_1) + \beta^2(\eta f_2' - 5f_2) + \ldots . \quad (29)$$

Some representative profiles at Pr = 10, $c_p\Delta T/h_{fg}$ = 1.8 are shown in Figs. 6 to 8. The distribution of the longitudinal velocity, equation (28), is plotted in Fig. 6 for four suction velocities. The condensate velocity, and therefore the condensate flow rate in the film, is reduced by suction. The normal velocity distribution is more informative and is shown in Fig. 7. Contrary to the longitudinal velocity, the normal velocity is increased significantly by suction. For example, at $\eta = 0.3$, the normal velocity, $vx^{1/4}/cv$, is -0.2643 at $\beta = 0$ (solid wall) and is -0.4161 at $\beta = -0.4306$. The increase of the normal velocity contributes considerably to the convective heat transfer across the film, as indicated by the temperature profiles shown in Fig. 8. At $\beta = 0$ (solid wall), the temperature profile is nearly a straight line, implying that conduction dominates and convection plays a small role. With the increase of suction, the effect of convection is felt more strongly and the departure from the straight line profile is greater. The temperature gradient at the wall reveals that conduction through the wall also increases with suction as a result of the reduction in film thickness.

Film Thickness and Condensation Rate. Since the film thickness plays an important role in heat transfer, it is interesting to examine the change of the thickness due to suction and subcooling. Representative curves are shown in Fig. 9 for Pr = 10. For all cases, film thickness increases with subcooling and decreases with suction. The thickness strongly depends on suction at low subcooling and is relatively unaffected at high subcooling. This explains the heat transfer behavior discussed previously.

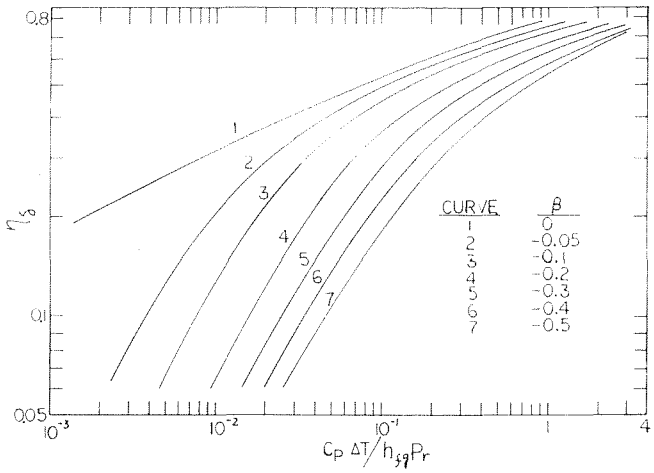

Fig. 9 Effect of uniform suction on film thickness at Pr = 10

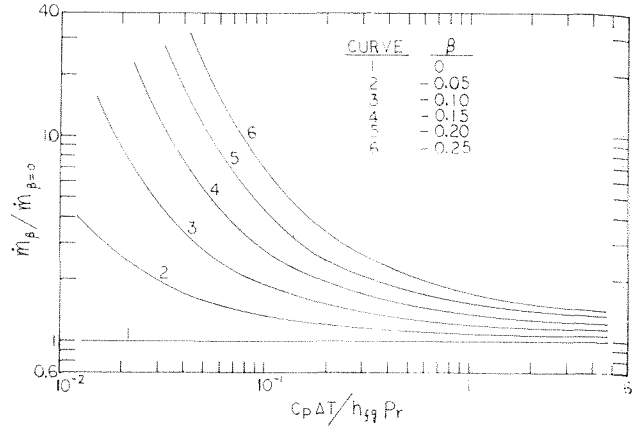

Fig. 10 Effect of uniform suction in total condensation rate at Pr = 10

The total condensation rate is readily obtained by applying the conservation of mass over a length x,

$$\dot{m}_\beta = \int_0^{\delta(x)} \rho u dy - \int_0^x \rho v_w dx \tag{30}$$

In terms of the dimensionless variables, this becomes

$$\dot{m}_\beta = 4\mu c x^{3/4}[f_0 + \beta f_1 + \beta^2 f_2 + \ldots\ldots \beta/4]_{\eta_\delta} \tag{31}$$

The effect of suction on the condensation rate is shown by the following expression:

$$\frac{\dot{m}_\beta}{\dot{m}_{\beta=0}} = [-\beta/4 f_0 + 1 + \beta f_1/f_0 + \beta^2 f_2/f_0 + \ldots\ldots]_{\eta_\delta} \tag{32}$$

Equation (32) is plotted in Fig. 10 for Pr = 10. The effect of suction on total condensation rate increases with suction and decreases with subcooling. The increase of total condensation rate with suction is expected, since suction provides an additional driving force for vapor moving toward the porous wall, which is essentially a mass sink. This effect is surprisingly large for a thin film and decreases rapidly as the film grows thicker.

Comparison With Previous Work

The only work on condensation along porous surface was reported by Jain and Bankoff in reference [6]. Jain and Bankoff solved the boundary layer equation in modified integral form by a perturbation method developed by Chen [3]. The method contained a double power perturbation series in α and ζ, defined as follows:

$$\alpha = v_w \left[\frac{\mu h_{fg} \rho^3 l}{g(\rho - \rho_v) K^3 (T_i - T_w)^3}\right]^{1/4} \tag{33}$$

$$\zeta = c(T_i - T_w)/h_{fg} \tag{34}$$

where l is an arbitrary length and T_i the interface temperature, which is the saturation temperature in this case. An alternate form of equation (33) is

$$\alpha = \beta(\mathrm{Pr}/\zeta)^{3/4} \tag{35}$$

It is known that the physical process of laminar film condensation on solid surface is governed by two parameters: the Prandtl number and the subcooling term, $c_p(T_s - T_w)/h_{fg}$. For a porous surface with uniform suction, the suction velocity is then included as an additional parameter, so that individual effect can be examined. However, in reference [6] the subcooling term, the Prandtl number, and the suction velocity are all contained in a single parameter α. It seems that the physical effect of suction cannot be adequately indicated by this parameter α. In the present work only the suction velocity is contained in the parameter β. The effect of suction can therefore be separated from the effects of subcooling and Prandtl number as shown in Figs. 2 to 10.

Since both α and ζ are used as the perturbation parameter in reference [6], their solutions are good only for small values of α and ζ. Their computations were performed over a range $0 < \alpha < 1$ and $10^{-5} < \zeta < 10^{-1}$. For the present work the subcooling term ζ is not a perturbation parameter and has no restriction on its range. The computations were extended to $\zeta = 300$, 10, and 0.6 for Pr = 100, 10, and 1 as shown in Figs. 2 to 4, respectively. Since the suction velocity β is still a perturbation parameter, the present results can be applied only to small values of β. The rapidity of convergence determines the upper limit of β. The computations covered the range $0 < \beta < 0.25$ for heat transfer and were extended to $\beta < 0.5$ for the representative curves of the velocity and temperature distributions and the film thickness. However, the applicability of β in this work is much broader than that of α in reference [6], as indicated in equation (35). Taking Pr = 1, $\zeta = 10^{-4}$, and $\beta = 0.25$, it gives $\alpha = 250$. This is 250 times higher than the upper limit of α in reference [6].

As a final remark, it is pointed out that the final results in reference [6] are given in terms of four parameters: Pr, α, ζ, and X, where $X = x/l$. In this work the dependence of the longitudinal coordinate x is implicitly contained in the suction velocity parameter β, equation (6). Therefore, the final results only depend on the three basic parameters: Pr, β, and ζ.

References

1 Bromley, L. A., "Effect of Heat Capacity of Condensation," *Industrial and Engineering Chemistry*, Vol. 44, 1952, p. 2966.

2 Rohsenow, W. M., "Heat Transfer and Temperature Distribution in Laminar Film Condensation," TRANS. ASME, Vol. 78, 1956, pp. 1645–1648.

3 Chen, M. M., "An Analytical Study of Laminar Film Condensation; Part I—Flat Plates," JOURNAL OF HEAT TRANSFER, TRANS. ASME, Series C, Vol. 83, No. 1, Feb. 1961, pp. 48–54.

4 Sparrow, E. M., and Gregg, J. L., "A Boundary-Layer Treatment of Laminar Film Condensation," JOURNAL OF HEAT TRANSFER, TRANS. ASME, Series C, Vol. 8, No. 1, Feb. 1959, pp. 13–18.

5 Koh, J. C. Y., Sparrow, E. M., and Hartnett, J. P., "The Two Phase Boundary Layer in Laminar Film Condensation," *International Journal of Heat and Mass Transfer*, Vol. 2, 1961, pp. 69–82.

6 Jain, K. C., and Bankoff, S. G., "Laminar Film Condensation on a Porous Vertical Wall With Uniform Suction Velocity," JOURNAL OF HEAT TRANSFER, TRANS. ASME, Series C, Vol. 86, No. 3, Aug. 1964, pp. 481–489.

7 Frankel, N. A., and Bankoff, S. G., "Laminar Film Condensation on a Porous Horizontal Tube With Uniform Suction Velocity," JOURNAL OF HEAT TRANSFER, TRANS. ASME, Series C, Vol. 87, No. 1, Feb. 1967, pp. 95–102.

R. R. BRANNON, JR.[1]
R. J. GOLDSTEIN
Professor.

Department of Mechanical Engineering,
University of Minnesota,
Minneapolis, Minn.

Emittance of Oxide Layers on a Metal Substrate

The variation of total normal emittance as a function of oxide thickness on a metal substrate is investigated experimentally for Al-Al_2O_3 and Cu-CuO systems. The measurements are made using a comparative black-body technique. Over the range of aluminum-oxide thicknesses investigated (1.2μ–86.4μ) the total normal emittance varies from 0.15–0.92 for a sample temperature of 96 deg C. With a copper-oxide thickness range from 1.2μ–5.6μ, the total normal emittance varies from 0.09–0.81 at 96 deg C. An analytical solution to the foregoing problem is formulated and the total normal emittance of the anodized aluminum samples is computed. Although the theoretical values are lower than the measured values, the effect of increasing oxide thickness on emittance is similar.

Introduction

THE VARIATION of emittance and solar absorptance of surface coatings has received considerable attention. Interest has been stimulated by applications to solar energy collectors and space vehicles. Research is being conducted to find a surface giving a high solar absorptance and low infrared emittance for solar heaters and the opposite—low solar absorptance and high infrared emittance for space radiators. There are of course many systems in which radiation heat transfer can play a key role. In some of these the surface is contaminated by an oxide layer whose thickness increases with time.

One of the earliest investigations of the variation of total normal emittance of a surface covered by oxide layers of different thicknesses was by Edwards and Taylor [1].[2] They investigated aluminum-aluminum oxide samples at 37.8 deg C with oxide thicknesses up to 10.9μ. They found that the emittance increased linearly with thickness of the oxide to about 2.03μ. Weaver [2], searching for a good space radiator, measured the total hemispherical emittance of aluminum oxide ranging to 25μ in thickness at a number of temperatures. Weaver found the emittance, in general, to increase with oxide thickness and to decrease with increasing temperatures. Hass, Ramsey, Triolo, and Albright [3] measured total normal emittance and total hemispherical emittance of aluminum-aluminum oxide systems at 20 deg C with oxide thicknesses to 2.5μ. They found the emittance to increase essentially linearly over this thickness range.

Hottel and Unger [4] determined the total emittance of various thicknesses of cupric oxide on shiny aluminum surfaces and Kokoropoulos, Salam, and Daniels [5] determined the total normal emittance of cupric oxide and cobalt oxide on shiny silver, nickel, and platinum substrates. Both studies found the total emittance to increase with increasing oxide thickness.

The present study includes the measurement of the dependence of total normal emittance on the thickness of oxide layers on a metal substrate for aluminum-aluminum oxide (Al-Al_2O_3) systems and copper-copper oxide (Cu-CuO) systems. The thickness of the Al_2O_3 layers range from 1.2–86.4μ while the thickness of the CuO layers range from 1.2–5.6μ.

Measurements are also reported for the dependence of total directional emittance on the thickness of oxide layers on a metal substrate for the Al-Al_2O_3 systems. In addition, theoretical calculations of total normal emittance of Al-Al_2O_3 systems are performed and compared to the experimental results.

Test Apparatus. The test apparatus, Fig. 1, is essentially the one described in detail in [6]. An abbreviated description is included herein to indicate possible sources of errors and to aid in the understanding of the present tests. The key element is the radiometer, in which radiant energy entering the aperture (a) is collected by a 12.70 cm dia gold surface mirror (b) and directed to a thermopile (c), which, in turn, is connected to a galvanometer (d). The test sample is held tightly against an electrically heated copper plate which is rigidly mounted in the back of the guard with a fixed sample holder (e) for total normal emittance measurements. For total directional emittance measurements, the sample is attached to a copper heater plate which is free to rotate about an axis as shown in (f). A radiation reference is provided by the black body (g). The black body and the test sample temperatures are controlled by varying the electrical power input to individual heaters. A double walled container, (e) or (f) has

[1] Presently, Engineering Research Division, E. I. Dupont de Nemours & Co., Wilmington, Del.

[2] Numbers in brackets designate References at end of paper.

Contributed by the Heat Transfer Division and presented at the Winter Annual Meeting, Los Angeles, Calif., November 16–20, 1969, of THE AMERICAN SOCIETY OF MECHANICAL ENGINEERS. Manuscript received by the Heat Transfer Division, January 2, 1969, revised manuscript received, June 12, 1969. Paper No. 69-WA/HT-4.

inner and outer walls coated with a black paint of high absorptivity. Cooled water flows through the double-wall creating a surrounding with well-defined temperature and radiation characteristics. A cylindrical opening in the guard permits the radiometer to view the test sample. In addition, an opening in a cylinder (3.18 cm in dia and 11.43 cm long) in the guard (h) acts as a black body at the surrounding guard temperature.

After steady-state conditions have been reached, the radiometer is sighted through the aperture (i) on the test surface and the two black bodies (g) and (h). The resulting galvanometer deflections are recorded. These readings in conjunction with the corresponding temperature measurements allow the calculation of the total directional emittance of the sample from the relation,

$$\epsilon_s = \frac{T_b^4 - T_g^4}{T_s^4 - T_g^4} \cdot \frac{\Delta_s - \Delta_g}{\Delta_b - \Delta_g} \tag{1}$$

A brief derivation (from [6]) of this equation seems appropriate here. The radiative energy flux leaving the black body at temperature T_b and arriving on a unit area of the thermopile is determined by the solid angle intercepted by the two diaphragms ahead of the thermopile and is designated as G_b.

$$G_b = F\sigma T_b^4 \tag{2}$$

Similar expressions may be written for the test sample at temperature T_s and small black body in the guard surface at temperature T_g and are designated as G_s and G_g, respectively.

$$G_s = F\sigma[\epsilon_s T_s^4 + \rho_s T_g^4] \tag{3}$$

$$G_g = F\sigma T_g^4 \tag{4}$$

With the assumption,

$$\epsilon_s = 1 - \rho_s \tag{5}$$

$$G_s = F\sigma[\epsilon_s(T_s^4 - T_g^4) + T_g^4] \tag{6}$$

Substracting equation (4) from equations (2) and (6) and combining the two resulting expressions,

$$\epsilon_s = \left(\frac{T_b^4 - T_g^4}{T_s^4 - T_g^4}\right)\left(\frac{G_s - G_g}{G_b - G_g}\right) \tag{7}$$

The radiation fluxes G can be related to the temperature of the thermopile when viewing the various surfaces. Assuming the radiation loss factor (from absorption in the air and at the gold mirror) and the extraneous heat losses and gains of the thermopile are the same during each reading,

$$\frac{G_s - G_g}{G_b - G_g} = \frac{T_{fs}^4 - T_{fg}^4}{T_{fb}^4 - T_{fg}^4} \cong \frac{4T_{fg}^3(T_{fs} - T_{fg})}{4T_{fg}^3(T_{fb} - T_{fg})} \tag{8}$$

The thermopile galvanometer reading Δ_j is proportional to the difference between the thermopile exposed surface temperature (T_f) and its rear surface temperature (T^*).

When the radiometer is sighted on the various surfaces, the readings are

$$\Delta_b = K(T_{fb} - T^*) \tag{9}$$

$$\Delta_s = K(T_{fs} - T^*) \tag{10}$$

$$\Delta_g = K(T_{fg} - T^*) \tag{11}$$

where K is a constant.

Nomenclature

A = defined in expression following equation (20)
B = defined in expression following equation (20)
D = defined in expression following equation (20)
d_1 = oxide film thickness
E = defined in expression following equation (20)
e = emissive power
$e_{b\lambda}$ = monochromatic emissive power of black body
F = shape factor determined by diaphragms ahead of thermopile
G_j = radiative energy flux arriving at thermopile when viewing j
g_1 = defined in expression following equation (20)
g_2 = defined in expression following equation (20)
h_1 = defined in expression following equation (20)
h_2 = defined in expression following equation (20)
i = radiation intensity emitted in a given direction
i_b = radiation intensity of a black body
$i_{b\lambda}$ = spectral radiation intensity of a black body
$i_{n\lambda}$ = spectral radiation intensity in normal direction
K = proportionality constant
k = absorption coefficient
n = index of refraction
$\tilde{n}$ = complex index of refraction $(n - ik)$
R = net monochromatic reflectance of multilayer system
r_{1p} = Fresnel reflection coefficient polarization parallel to plane of incidence at interface of media $0 - 1$
r_{1s} = Fresnel reflection coefficient polarization normal to plane of incidence at interface of media $0 - 1$
r_j = reflectance at interface of medium $j - 1$ to j
T_b = absolute temperature of reference black body
T_{fj} = absolute temperature of exposed surface of thermopile when viewing surface j
T_g = absolute temperature of water-cooled guard
T_s = absolute temperature of test sample
T^* = back (unexposed) side temperature of thermopile
t_{1p} = Fresnel transmission coefficient polarization parallel to plane of incidence at interface of media $0 - 1$
t_{1s} = Fresnel transmission coefficient polarization normal to plane of incidence at interface of media $0 - 1$
α_λ = monochromatic absorptance for incidence from a given direction
γ_1 = defined in expression following equation (20)
Δ_j = deflection of galvanometer produced by thermopile when viewing j
δ_1 = phase change in beam traversing the film, $2\pi n_1 d_1/\lambda$ for normal incidence
$\epsilon = \epsilon(\theta, \phi)$ = total directional emittance
ϵ_n = total normal emittance
$\epsilon_{n\lambda}$ = monochromatic normal emittance
ϵ_s = total directional emittance of test sample
ϵ_{th} = total hemispherical emittance of thermopile
ϵ_λ = monochromatic emittance in a given direction
θ = azimuthal angle
λ = wavelength in microns
μ_1 = defined in expression following equation (20)
ρ_s = total reflectance of test sample for diffuse incidence and reflection in a given direction
ρ_λ = monochromatic reflectance for incidence from a given direction
σ = Stefan-Boltzmann constant
ϕ = cone angle (to surface normal)
ϕ_0 = angle of incidence
ϕ_1 = angle of refraction

Subscripts

b = black body in general or reference black body in particular
g = guard or guard black body
n = direction normal to surface
s = test surface
0, 1, 2 = medium 0, 1, or 2, respectively
λ = wavelength or spectral quantity

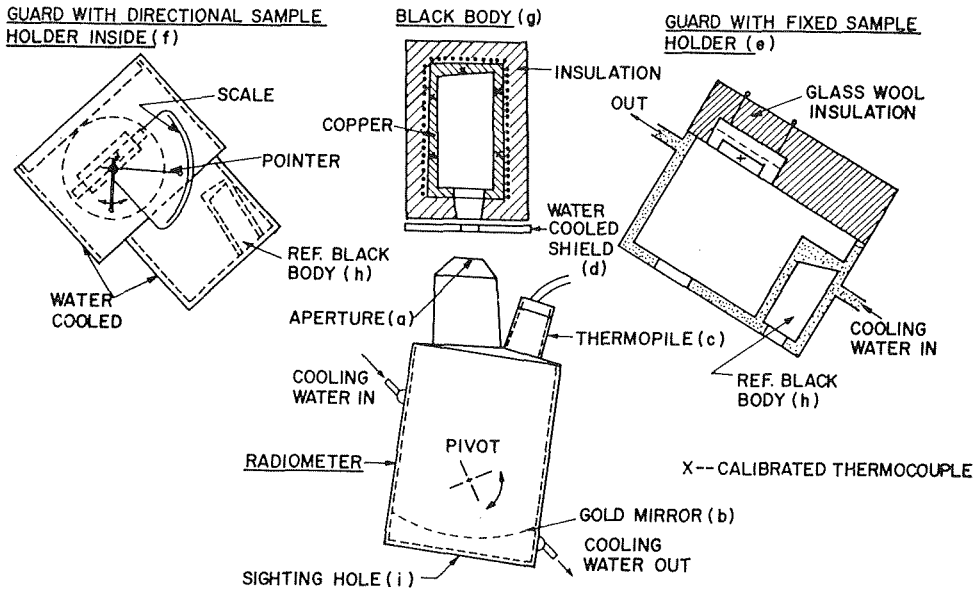

Fig. 1 Test apparatus—overall view

Substituting equations (9), (10), and (11) into equation (8) and combining with equation (7),

$$\epsilon_s = \frac{T_b^4 - T_g^4}{T_s^4 - T_g^4} \cdot \frac{\Delta_s - \Delta_g}{\Delta_b - \Delta_g} \tag{12}$$

The assumption $\epsilon_s = 1 - \rho_s$ requires that the sample does not have a net transmittance and strictly that the emittance does not depend on wavelength. Equation (6) is usually a good approximation even when the last condition is not fulfilled provided T_g is considerably smaller than T_s. A knowledge of the spectral variation of absorptance is required [7] to calculate the error when using equation (12) directly. The results of such a calculation are described later.

Theoretical Analysis. The theoretical analysis to determine the radiation properties of the oxide layer on a metal substrate is based on the Fresnel relations as presented by Heavens [8]. These relations give the reflection from and transmission through absorbing nonscattering (homogeneous) films with optically smooth surfaces in terms of the complex Fresnel coefficients. Heavens also presents an all-real-number expression for the reflection of an absorbing film on an absorbing substrate and it is this expression that is used in this study.

Fresnel derived expressions for the reflection and transmission of energy at a boundary separating two media (indicated by subscripts 0 and 1). These expressions for the amplitudes of the transmitted and reflected vectors for a nonabsorbing (transparent) isotropic medium are [8]

$$r_{1p} = \frac{n_0 \cos \phi_1 - n_1 \cos \phi_0}{n_0 \cos \phi_1 + n_1 \cos \phi_0} \tag{13}$$

$$t_{1p} = \frac{2n_0 \cos \phi_0}{n_0 \cos \phi_1 + n_1 \cos \phi_0} \tag{14}$$

$$r_{1s} = \frac{n_0 \cos \phi_0 - n_1 \cos \phi_1}{n_0 \cos \phi_0 + n_1 \cos \phi_1} \tag{15}$$

$$t_{1s} = \frac{2n_0 \cos \phi_0}{n_0 \cos \phi_0 + n_1 \cos \phi_1} \tag{16}$$

where r_{1p}, r_{1s} are the Fresnel reflection coefficients and t_{1p}, t_{1s} are the Fresnel transmission coefficients. The components of polarization are represented by p for the vector parallel to the plane of incidence and s for the vector normal to the plane of incidence.

Although the prime interest of the present study is the reflectance of a single absorbing layer on an absorbing substrate further insight to the physical process can be gained by next examining the terms in the expression for the reflectance of a nonabsorbing film bounded on both sides by nonabsorbing media. A beam incident on the film is divided into reflected and transmitted parts. Such division occurs each time the beam strikes an interface so that the transmitted and reflected beams are obtained by summing the multiply reflected and multiply transmitted elements. For the case of the single layer, the summation is easily effected and the net reflectance R of the system can be shown to be

$$R = \frac{r_1^2 + 2r_1r_2 \cos 2\delta_1 + r_2^2}{1 + 2r_1r_2 \cos 2\delta_1 + r_1^2r_2^2} \tag{17}$$

where equations similar to (13) or (15) could be used for r_1 and r_2.

Expressing R in terms of the refractive indexes, where the Fresnel coefficients reduce for normal incidence to

$$r_1 = \frac{n_0 - n_1}{n_0 + n_1} \qquad r_2 = \frac{n_1 - n_2}{n_1 + n_2} \tag{18}$$

gives

$$R_n = \frac{(n_0^2 + n_1^2)(n_1^2 + n_2^2) - 4n_0n_1^2n_2^2 + (n_0^2 - n_1^2)(n_1^2 - n_2^2) \cos 2\delta_1}{(n_0^2 + n_1^2)(n_1^2 + n_2^2) + 4n_0n_1^2n_2 + (n_0^2 - n_1^2)(n_1^2 - n_2^2) \cos 2\delta_1} \tag{19}$$

For nonabsorbing media this expression is readily evaluated. If the film or substrate or both are absorbing, the values of n_1 and n_2 need to be replaced by the complex index of refraction $\tilde{n} = n - ik$.

The system considered in this paper involves an absorbing oxide film on an absorbing substrate bounded by air as shown in Fig. 2. For this system, the net reflectance (cf, Heavens [8]) is

$$R_n = \frac{(g_1^2 + h_1^2)e^{2\mu_1} + (g_2^2 + h_2^2)e^{-2\mu_1} + A \cos 2\gamma_1 + B \sin 2\gamma_1}{e^{2\mu_1} + (g_1^2 + h_1^2)(g_2^2 + h_2^2)e^{-2\mu_1} + E \cos 2\gamma_1 + D \sin 2\gamma_1} \tag{20}$$

where

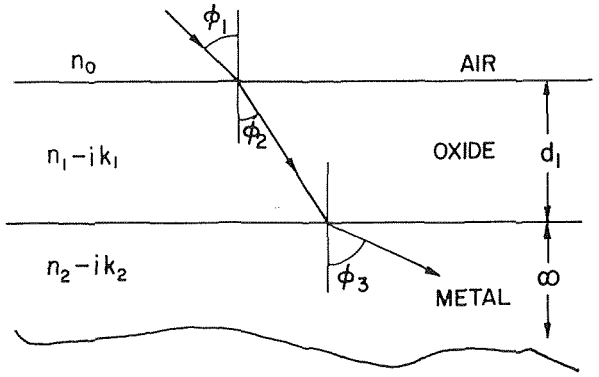

Fig. 2 Absorbing film on an absorbing substrate

$$g_1 = \frac{n_0^2 - n_1^2 - k_1^2}{(n_0 + n_1)^2 + k_1^2} \qquad h_1 = \frac{2n_0k_1}{(n_0 + n_1)^2 + k_1^2}$$

$$g_2 = \frac{n_1^2 - n_2^2 - k_1^2 - k_2^2}{(n_1 + n_2)^2 + (k_1 + k_2)^2} \qquad h_2 = \frac{2(n_1k_2 - n_2k_1)}{(n_1 + n_2)^2 + (k_1 + k_2)^2}$$

$$\mu_1 = \frac{2\pi k_1 d_1}{\lambda} \qquad \gamma_1 = \frac{2\pi n_1 d_1}{\lambda}$$

$$A = 2(g_1g_2 + h_1h_2) \qquad B = 2(g_1h_2 - g_2h_1)$$

$$E = 2(g_1g_2 - h_1h_2) \qquad D = 2(g_1h_2 + g_2h_1)$$

From conservation of energy, if there is no net transmission,

$$\rho_\lambda + \alpha_\lambda = 1 \tag{21}$$

The monochromatic absorptance (α_λ) and emittance (ϵ_λ) are related by Kirchhoff's law

$$\alpha_\lambda = \epsilon_\lambda \tag{22}$$

By combining equations (21) and (22),

$$\epsilon_\lambda = 1 - \rho_\lambda \tag{23}$$

Taking the monochromatic reflectance $\rho_\lambda = R$ one finds

$$\epsilon_\lambda = 1 - R \tag{24}$$

The monochromatic reflectance R_n can be calculated by substituting the monochromatic values of the optical constants n and k for each of the three media in equation (20). This equation was programmed and the values of R_n computed on a Control Data 6600 computer located at the University of Minnesota Computer Center. In the same program, the monochromatic emittance was computed from equation (24) and summed over the wavelength range 2μ–42μ to obtain total normal emittance for each oxide thickness.

The optical properties of aluminum oxide used in computing the monochromatic reflectance are given by Harris [9] and Harris and Piper [10]. The optical constants for aluminum were taken from Lenham and Treherne [11], who present values of n and k for a wavelength range of 2–22μ. The values of the optical constants for wavelength from 23–42μ were obtained by plotting the values of n and k from [11] versus wavelength and extrapolating the curves to 42μ.[3] The optical properties for both aluminum and aluminum oxide are shown in Table 1.

The directional emittance is defined as the ratio of the emitted intensity in a particular direction to the intensity from a black body at the same temperature. In general, for arbitrary surface conditions, the distribution of the emitted intensity i depends on the two angles θ and ϕ. The black-body intensity i_b is uniform. Then

$$\epsilon(\theta, \phi) = \frac{i(\theta, \phi)}{i_b} \tag{25}$$

For isotropy, which is assumed for the surfaces studied in this paper, there is no dependence on the angle θ and, correspondingly, $\epsilon = \epsilon(\phi)$. For the case of normal emittance, $\phi = 0$ deg and $\epsilon = \epsilon_n$.

$$\epsilon_n = \frac{i(0 \text{ deg})}{i_b} = \frac{i_n}{i_b} \tag{26}$$

The total normal emittance was computed from

$$\epsilon_n = \frac{\int_0^\infty i_{n\lambda} d\lambda}{\int_0^\infty i_{b\lambda} d\lambda} = \frac{\int_0^\infty \epsilon_{n\lambda} i_{b\lambda} d\lambda}{\frac{1}{\pi}\int_0^\infty e_{b\lambda} d\lambda} = \frac{\int_0^\infty \epsilon_{n\lambda} e_{b\lambda} d\lambda}{\sigma T_s^4} \tag{27}$$

At each wavelength λ, the product of $\epsilon_{n\lambda}$ and the black-body spectral energy density $e_{b\lambda}$ corresponding to the surface temperature T_s is formed. Planck's law is used to compute $e_{b\lambda}$ and $\epsilon_{n\lambda}$ has been determined from equation (24). The total normal emittance ϵ_n is then found by numerically integrating the term

Table 1 Optical properties of aluminum and aluminum oxide

Wavelength (μ)	Aluminum Oxide [9, 10] n	Aluminum Oxide [9, 10] k	Aluminum [11][a] n	Aluminum [11][a] k
2	1.57	0.00	2.30	16.5
3	1.52	0.00	4.41	24.2
4	1.50	0.00	5.78	25.95
5	1.49	0.00	7.10	33.02
6	1.43	0.00	8.83	38.96
7	1.37	0.003	11.04	44.29
8	1.29	0.009	13.92	48.53
9	1.26	0.027	15.71	53.73
10	1.31	0.088	20.18	57.33
11	1.48	0.33	21.89	58.65
12	1.65	0.66	22.35	62.12
13	1.70	1.03	23.51	66.28
14	1.70	1.19	24.79	73.58
15	1.75	1.50	24.27	81.17
16	1.88	1.45	25.24	88.53
17	1.95	1.35	28.69	92.64
18	2.05	1.30	29.08	96.15
19	2.08	1.25	29.41	98.31
20	2.10	1.20	30.18	100.15
21	2.13	1.15	30.58	103.80
22	2.20	1.10	31.40	110.55
23	2.30	1.05	31.80	114.30
24	2.34	1.03	32.20	118.50
25	2.38	1.00	32.60	123.50
26	2.40	0.97	33.00	128.00
27	2.45	0.95	33.40	132.70
28	2.47	0.93	33.70	137.40
29	2.48	0.91	34.00	141.80
30	2.50	0.90	34.30	146.30
31	2.53	0.87	34.60	150.80
32	2.55	0.83	35.00	155.50
33	2.60	0.80	35.20	160.00
34	2.60	0.77	35.50	164.50
35	2.55	0.75	35.70	169.20
36	2.50	0.73	35.90	173.60
37	2.50	0.72	36.20	178.00
38	2.50	0.70	36.30	182.80
39	2.50	0.67	36.50	187.00
40	2.50	0.65	36.80	191.50
41	2.45	0.63	37.00	196.20
42	2.45	0.63	37.20	201.00

[3] The extrapolation does not appear to critically affect the results. Calculations assuming n and k constant at wavelengths greater than 22μ (with the values they have at 22μ) do not yield significantly different reflections from those found using the extrapolated values.

[a] Values of n and k for wavelengths from 2μ–22μ were obtained from [11]. The values of n and k for 23μ–42μ were obtained by plotting the values of n and k from [11] versus wavelength and extrapolating the curves to 42μ.

$$\frac{\int_0^\infty \epsilon_{n\lambda} e_{b\lambda} d\lambda}{\sigma T_s^4}$$ over the wavelength range from 2μ–42μ.

Description and Preparation of Test Samples. The test samples used in this study were made from 99.9 percent pure copper (CDS No. 110; copper 99.9 percent min, oxygen about 0.04 percent) disks 0.95 cm thick and 5.08 cm in dia, and type 1100 alloy aluminum disks (99 percent + pure aluminum) 0.95 cm thick and 5.08 cm in dia. A 0.160-cm-dia thermocouple hole was drilled at midthickness through each sample to a depth of 2.54 cm after the samples were oxidized. Chromel-alumel thermocouple wires were installed using copper-oxide cement to hold them in place.

To minimize the effect of bare metal surface roughness and conditions on the emittance values of the oxidized samples, the surfaces of all samples were polished to a mirror-surface finish prior to oxidizing. Every effort was made to assure uniformity of surfaces.

The aluminum and copper disks were prepared in essentially the same way using the following procedure.

1 Disks were cut from round stock on a lathe and machined as smoothly as possible.

2 The tool marks were removed by polishing the surface with No. 600 wet or dry emery paper.

3 The copper surfaces were then polished to a mirror finish on a Buehler Polishing Assembly using water soluble red rouge.

4 The aluminum samples were polished to a mirror finish by hand rubbing them with buffing cloth and water soluble red rouge. The Buehler Polishing Assembly was not used as it tended to leave too many scratch marks on the soft aluminum.

5 The aluminum surface was finally polished with a commercial metal polish and buffed with a soft cloth.

6 The surfaces of the copper samples were oxidized (black cupric oxide, CuO) with the Ebonol "C" process. The time the samples remained in the bath ranged from $1^1/_2$ to 30 min and the oxide thickness varied from 1.2×10^{-4} cm to 5.6×10^{-4} cm (1.2–5.6μ).

7 The surfaces of the aluminum samples were anodized by a process referred to as hardcoating. The electrolyte solution is composed of 15 percent sulfuric acid by volume and is maintained at 0 deg C. Current density is approximately 0.031 amp per cm^2. The samples remained in the solution from $1^1/_4$ min to 1 hr and the oxide thickness varied from 1.2μ–86.4μ. The term hardcoat is used because the low-solution temperature and high-current density produces an oxide having greater dielectric strength and a denser structure than anodic coatings produced at higher temperatures and lower-current densities [12].

The sample properties arising from the anodizing process are associated intimately with the rate of growth of the coating and the solvent action of the electrolyte. These not only determine the thickness of the coating but also its porosity, mechanical properties, and chemical composition. Acid concentration, temperature, current density, voltage, and type of current influence these properties. However, the coating thickness, porosity or density, and transparency are the most critical parameters when anodized coatings are used for temperature control [2]. The amount of impurities and water vapor contained in the oxide will also have an effect on the emittance.

After the total emittance measurements were taken the thickness of each oxide layer was measured by sectioning the sample and examining the cross section with a microscope containing two parallel lines, the distance between which could be varied by a calibrated dial.

The CuO surfaces produced on those samples left in the bath less than 5 min were not uniform in appearance. Some areas of the surface appeared darker than others and there was something of a rainbow effect on those surfaces exposed $1^1/_2$ to 3 min. On the surfaces exposed 7 min or more the surface appeared uniform and was much blacker than the thinner surfaces. In contrast to the nonuniform appearance of the thinner copper-oxide coatings, all of the anodized aluminum surfaces exhibited a very uniform appearance. All of the coatings tested appeared diffuse to the eye and the oxide coatings were uniform and without pits.

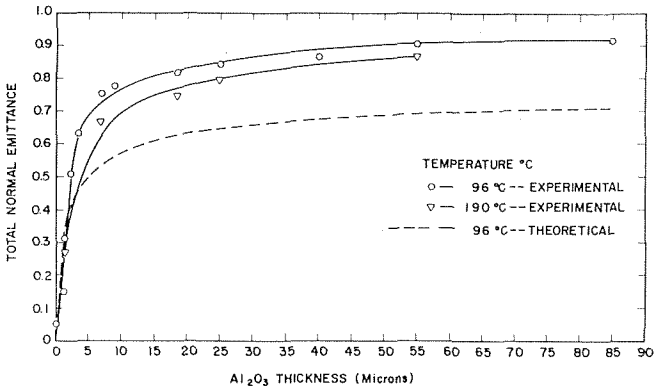

Fig. 3 Total normal emittance versus thickness of Al-Al_2O_3 system

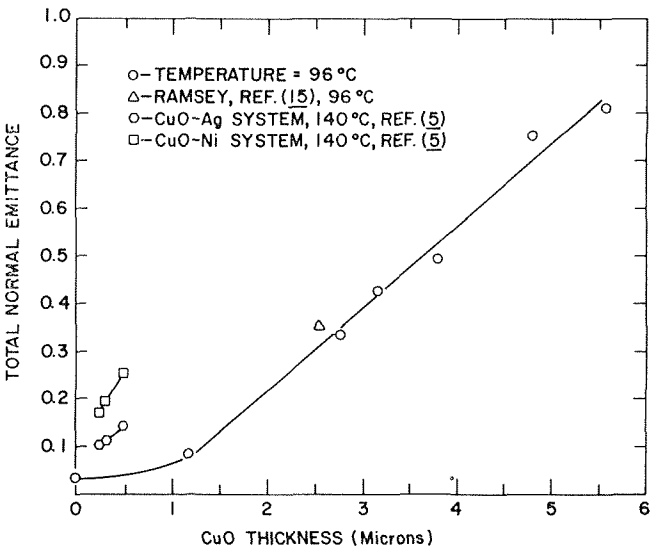

Fig. 4 Total normal emittance versus thickness of Cu-CuO system

Discussion of Results. The measured total normal emittance as a function of oxide thickness is shown in Fig. 3 for the Al-Al_2O_3 systems and Fig. 4 for the Cu-CuO systems. The results are tabulated in Tables 2 and 3 for the Al-Al_2O_3 systems and the Cu-CuO systems, respectively. In Fig. 5 the measured values of total normal emittance obtained in this study for the Al-Al_2O_3 system at 96 deg C are compared to earlier results obtained [1–3]. The differences observed in Fig. 5 between the results of the present study and those obtained by previous investigators can be at least partially attributed to the difference in temperatures at which various investigations were made and also due to the different anodizing processes used.

Table 2

Aluminum sample	Oxide thickness (μ)	Total normal emittance 96 deg C	190 deg C
Polished	0	0.06	
1	1.24	0.15	
2	1.47	0.31	0.27
3	2.44	0.51	
4	3.56	0.63	
5	7.11	0.76	0.67
6	9.14	0.78	
7	18.80	0.82	0.75
8	25.40	0.84	0.80
9	40.64	0.87	
10	55.88	0.91	0.87
11	86.36	0.92	

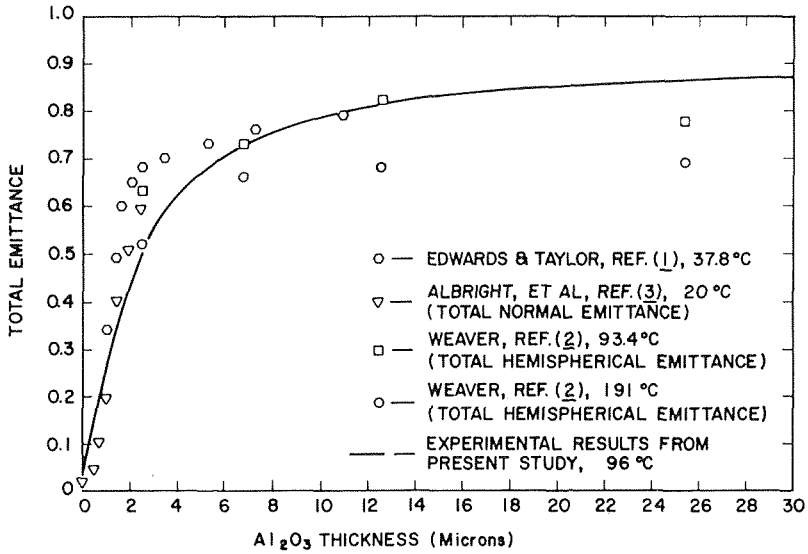

Fig. 5 Total emittance versus thickness of Al-Al_2O_3 system

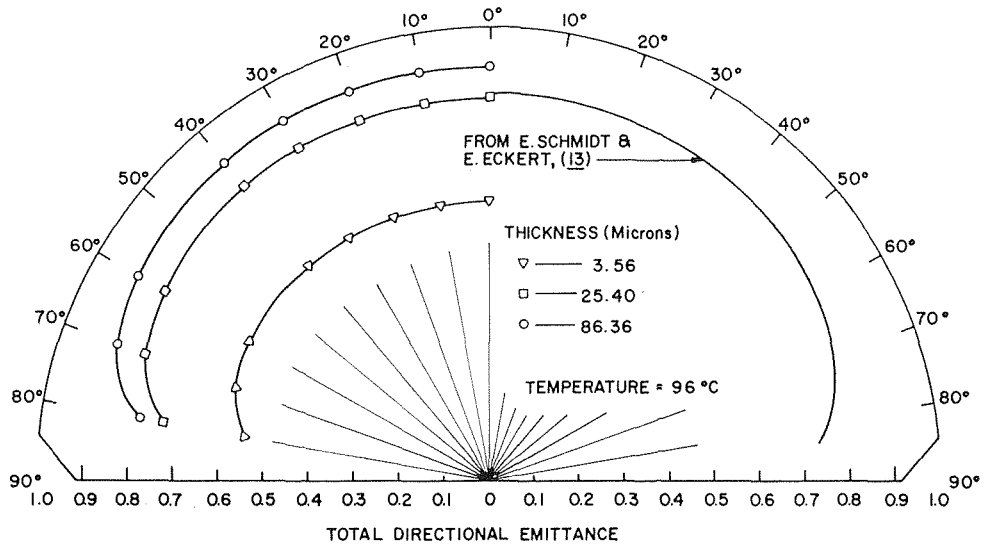

Fig. 6 Effect of coating thickness on total directional emittance of Al-Al_2O_3 system

Table 3

Copper sample	Oxide thickness (μ)	Total normal emittance 96 deg
Polished	0	0.04
1	1.19	0.09
2	2.79	0.33
3	3.18	0.42
4	3.81	0.49
5	4.83	0.75
6	5.59	0.81

The total normal emittance tends to decrease with increasing sample temperature. This is shown in Fig. 3 and also in Fig. 5. The decrease in total emittance as a function of increasing temperature is at least partially due to a shift of the black-body energy distribution curve to shorter wavelengths. The absorption coefficient of Al_2O_3 tends to decrease with decreasing wavelength, thereby making the oxide more transparent to radiation. Another factor might be the difference in the correction of the measurements required for the nongray surface at the two different temperatures. As mentioned in the description of the test apparatus the measurement error involved in assuming the surface is gray was calculated. Using the analysis of Edwards and Nelson [7] and the monochromatic absorptance data of Weaver [2], a maximum error of 6.8 percent (at about 8μ thickness—the smallest for which results are available) is found for the aluminum-oxide coated surface at 96 deg C. This would be smaller at higher temperature and at larger coating thickness. The correction is generally negative; that is, the measured values indicate a higher emittance than the true value. Because of the uncertainty of the spectral data no correction was made and the data were used directly.

It is noted from the results for the present investigation, Fig. 3, that the total normal emittance increases almost linearly as a function of oxide thickness up to about 3.6μ. Above this, the emittance shows only a gradual change with thickness. The last reported emittance value is only 0.77 percent higher than the previous value while the oxide thickness has increased by 35 percent.

The measurements of the total directional emittance for different oxide thicknesses on the aluminum indicate, Fig. 6, a variation similar to that reported by Schmidt and Eckert [13]. This result is also in qualitative agreement with the calculation of Francis and Love [14] who applied Fresnel's relations to the monochromatic reflectance of an absorbing layer on aluminum.

Little information was found concerning the variation of radia-

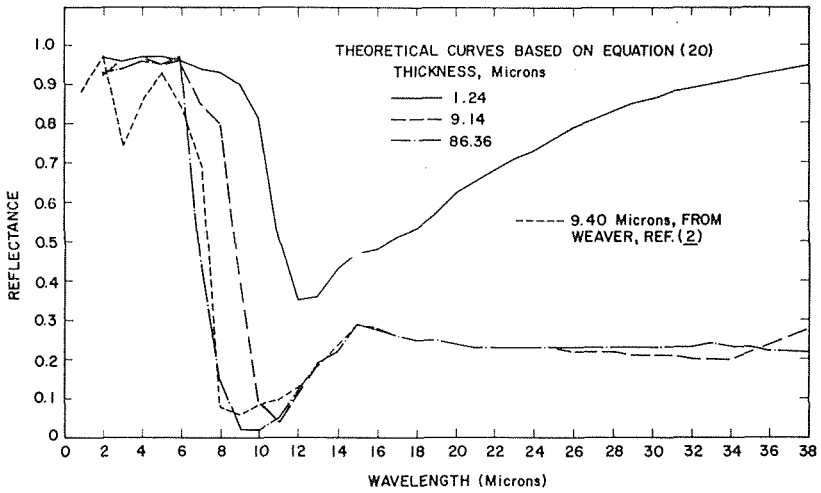

Fig. 7 Effect of coating thickness on reflectance of Al-Al_2O_3 system

tion properties of a copper-oxide on copper-substrate combination as a function of oxide thickness. The one measurement found was by Ramsey [15] who reported the total hemispherical emittance of a 2.54μ coating of CuO on a copper substrate to be 0.350 at 96 deg C, in good agreement with the present study. The results from reference [5] are shown in Fig. 4. Because of the different substrates used and their extremely thin CuO coatings, it is difficult to make a comparison with the present study. The present results, Fig. 4, for the Cu-CuO system indicate that the total emittance becomes almost linearly dependent on oxide thickness from 1–5 and $^1/_2$ microns. Since the oxide thickness of 5.6μ was the maximum that could be obtained using the Ebonol "C" process, it could not be determined at what thickness the emittance deviates from its linear dependence on thickness. An analytical treatment of the copper-copper oxide samples was not performed as insufficient data on the optical properties of CuO were found in the literature.

The analytical solution was performed to see how well the experimental results could be matched by a theoretical approach. It can be observed from Fig. 3 that the theoretical total normal emittance as a function of aluminum-oxide thickness follows the same general shape as the experimentally determined values. However, the theoretical results are approximately 30 percent lower than the experimental values for oxide thicknesses between 3.6μ–86.4μ. At the smaller thickness used the difference between the two values is less. The difference between the experimental and the analytical results is probably due to impurities in the aluminum-oxide layers which would cause increased scattering and absorption. The theoretical equations were derived assuming optically smooth surfaces and a homogeneous (no impurities which could cause scattering or increased absorption of radiant energy) oxide film. In this regard the use of sputtering and vacuum deposition are being examined as alternatives to produce uniform homogeneous coatings. The impurity content of the actual oxide would increase both the scattering and the absorption of radiant energy, thereby increasing the total emittance. Even so, the similarity in trend is an encouraging indication that, given a complete description of the surface layer, the radiation properties can be calculated.

In Fig. 7, the computed monochromatic values are compared with experimentally determined monochromatic reflectances obtained by Weaver [2]. The theoretical values show essentially the same trend as the experimental values through a wavelength of 15μ which is the longest wavelength reported by Weaver. The primary difference in the figure occurs at about 3μ. Here, the measured values show a sharp decrease in reflectance due to a strong absorption band. The analytical values do not show this dip since the data used for the optical properties (index of refraction, absorption coefficient) of aluminum oxide were obtained from measurements on thin aluminum-oxide films and indicated a value of zero for the absorption coefficient from 2μ–6μ wavelength. It should be noted that the correction for the nongray nature of the surface would be increased, at the condition studied, if this depression of the absorptance were not present at 3 microns.

Acknowledgment

Support under Project Themis during part of this study is gratefully acknowledged.

References

1 Edwards, J. D., and Taylor, C. S., "Some Reflection and Radiation Characteristics of Aluminum," *Heating, Piping, and Air Conditioning*, Vol. 11, 1939, p. 59.

2 Weaver, J. H., "Anodized Aluminum Coatings for Temperature Control of Space Vehicles," Air Force Systems Command, Technical Documentary Report No. ASD-TDR-62-918, Feb. 1963.

3 Albright, H. T., et al., "Solar Absorptance and Thermal Emittance of Aluminum Coated With Surface Films of Evaporated Aluminum Oxide," *Thermophysics and Temperature Control of Spacecraft and Entry Vehicles*, Vol. 18, *Progress in Astronautics and Aeronautics*, 1966, p. 47.

4 Hottel, H. C., and Unger, T. A., "The Properties of a Copper Oxide-Aluminum Selective Black Surface Absorber of Solar Energy," *Solar Energy*, Vol. III, No. 3, 1959, p. 10.

5 Daniels, F., Kokoropoulos, P., and Salam, E., "Selective Radiation Coatings-Preparation and High-Temperature Stability," *Solar Energy*, Vol. III, No. 4, 1959, pp. 7, 19.

6 Eckert, E. R. G., Hartnett, J. P., and Irvine, T. F., "Measurement of Total Emissivity of Porous Materials Used in Transpiration Cooling," *Jet Propulsion*, Vol. 26, 1956, p. 280.

7 Edwards, D. K., and Nelson, K. E., "Maximum Error in Total Emissivity Measurements Due to Nongrayness of Samples," *ARS Journal*, Vol. 31, 1961, p. 1021.

8 Heavens, O. S., *Optical Properties of Thin Solid Films*, Butterworths Scientific Publications, London, 1955, Chapter 4.

9 Harris, L., "Preparation and Infrared Properties of Aluminum Oxide Films," *Journal of the Optical Society of America*, Vol. 45, 1955, p. 27.

10 Harris, L., and Piper, J., "Transmittance and Reflectance of Aluminum-Oxide Films in the Far Infrared," *Journal of the Optical Society of America*, Vol. 52, 1962, p. 223.

11 Lenham, A. P., and Treherne, D. M., "Optical Constants of Single Crystals of Mg, Zn, Cd, Al, Ga, In, and White Sn," *Journal of the Optical Society of America*, Vol. 56, 1966, p. 752.

12 Vandenberg, R. V., "Characteristics of Hard Anodic Coatings on Aluminum," *Machine Design*, Vol. 34, 1962, p. 155.

13 Eckert, E., and Schmidt, E., "Über die Richtungsverteilung der Warmestrahlung von Oberflachen," *Forsch Gebiete Ingenieurw*, Vol. 6, 1935, p. 175.

14 Francis, J. E. and Love, T. J., "Radiant Heat Transfer Analysis of Isothermal Diathermanous Coatings on a Conductor," *AIAA Journal*, Vol. 4, 1966, p. 643.

15 Ramsey, J. W., "An Apparatus for the Calorimetric Measurement of the Total Hemispherical Emittance of Solid Surfaces," Master of Science thesis in Mechanical Engineering, University of Minnesota, 1965.

N. MALMUTH
M. KASCIC
H. F. MUELLER

North American Rockwell Corporation,
Los Angeles Division,
International Airport,
Los Angeles, Calif.

Asymptotic and Numerical Solutions for Nonlinear Conduction in Radiating Heat Shields

A two-point boundary value problem associated with nonlinear one-dimensional conduction in radiating heat shields and other applications is solved by perturbation and numerical methods. An exact numerical solution is compared with asymptotic results consisting of a previously developed weak conduction solution and its strong conduction counterpart, which is obtained in the present analysis. It is found that the strong conduction asymptotic applies over a much wider range of the radiation conduction parameter than the weak one. Typical calculations show that the maximum temperature of the heat shield is reduced by only nine percent, with a disproportionate increase in end temperature of 32 percent in increasing the radiation conduction parameter from zero to infinity. However, an important structural benefit is obtained by significant reduction in the temperature differences along the shield, with moderate increases in the radiation conduction parameter.

Introduction

In a previous paper [1],[1] the steady-state temperature distribution in a thin heat shield ($AODCPB$ in Fig. 1) is analyzed. The faces AB, BPC, and CD are considered insulated, and the thickness, δ, is assumed small enough compared to the total length, L, to validate the assumption of negligible transverse gradients. Furthermore, in the resulting one-dimensional problem, each surface element of AOD is assumed to be radiating to the surroundings whose temperature is assumed negligible compared to the shield's. Without significant loss of generality, constant material properties are stipulated along the shield, which is subject to a normalized arbitrary aerodynamic heat flux, $q(x)$, where x is the running arc length measured from the end, AB (see Fig. 1), and normalized with respect to L.

From an elementary heat balance applied to an element of the shield and the insulated end conditions, the following two-point boundary value problem is obtained for the normalized temperature T in terms of the aerodynamic heat flux, $q(x)$:

$$\epsilon T'' - T^4 + q(x) = 0 \tag{1a}$$

$$T'(0) = T'(1) = 0 \tag{1b}$$

where, with the thermal conductivity k, Stefan's constant σ, $\bar{T}$ = maximum conductionless temperature, and the emissivity $\bar{\epsilon}$, the parameter $\epsilon = \dfrac{\delta k}{\sigma \bar{\epsilon} L^2 \bar{T}^3}$ represents a measure of conductive relative to radiant flux. Other physical situations arising in astrophysics and illumination theory describable by a one-dimensional model similar to equations (1) are discussed in reference 1.

The approximation of small ϵ leads to a singular perturbation problem involving "boundary layers" in the vicinity of the ends $x = 0$ and 1. This problem was solved in [1]. However, for a typical q distribution, the fact that these layers were $O(\sqrt{\epsilon})$ in length and their mutual interaction involved a discrepancy in (1b) of $O(e)^{-1/\sqrt{\epsilon}}$ gave $\epsilon = 0.01$ as an approximate computational

[1] Numbers in brackets designate References at end of paper.

Contributed by the Heat Transfer Division for publication (without presentation) in the Journal of Heat Transfer. Manuscript received at ASME headquarters, January 12, 1970. Paper No. 70-HT-E.

Nomenclature

k = thermal conductivity [kcal/mh (deg)]
q = aerodynamic heat transfer distribution function normalized with respect to $\sigma\bar{\epsilon}\bar{T}^4 = \bar{q}$
$\bar{q}$ = maximum value of aerodynamic heat flux along shield [$k$cal/m^2h]
x = coordinate along shield normalized with respect to L
L = length of shield [m]
T = temperature normalized with respect to $\bar{T}$
$\bar{T}$ = maximum value of conductionless temperature along shield (grade)
$\epsilon = \dfrac{\delta k}{\sigma \bar{\epsilon} L^2 \bar{T}^3}$ conduction radiation ratio
$\bar{\epsilon}$ = surface emissivity
σ = Stefan-Boltzmann constant [$k$cal/ m^2h(deg)^4]
δ = thickness of shield [m] (see Fig. 1)

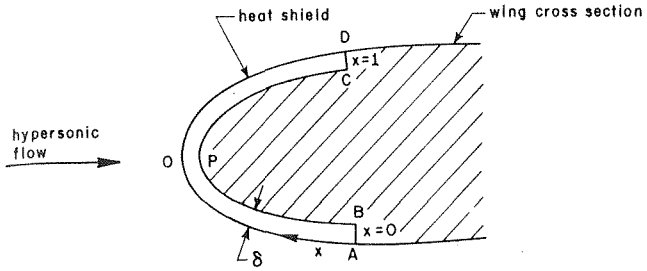

Fig. 1 Heat shield geometry

upper bound for the validity of the three-term expansion.

From a practical viewpoint, treatment of the complete ϵ range is of interest in many technical applications. Accordingly, an asymptotic expansion for the large conduction case, i.e., $\epsilon \to \infty$, will be given in this paper. It will be evident in what follows that three terms of the latter will provide good coverage down to values of ϵ near 0.1.

Further, a numerical solution valid nominally for $10^{-2} \leq \epsilon \leq \infty$ and capable of straightforward extension to smaller ϵ will also be discussed. Results from the latter will be compared with those obtained from the perturbation solutions of reference 1 and the present paper.

Analysis

By contrast to weak conduction, it can be shown that the asymptotic expansion for T about $\epsilon = \infty$ is regular, since it automatically satisfies the boundary conditions (1*b*) and is an infinitely differentiable function of ϵ [2]. Accordingly, the uniformly valid representation for T, on [0, 1], is asserted to be:

$$T(x;\epsilon) = \sum_{i=0}^{\infty} \epsilon^{-i} T_i(x) \text{ as } \epsilon \to \infty \tag{2}$$

Substitution of (2) into (1) gives:

$$T_0'' = 0 \tag{3a}$$

$$T_1'' - c_0 + q = 0 \tag{3b}$$

$$T_i'' = c_{i-1},\ i > 1 \tag{3c}$$

with

$$T_i'(0) = T_i'(1) = 0 \tag{4}$$

where

$$c_0 = T_0^4$$

$$c_m = \frac{1}{mT_0} \sum_{k=1}^{m} (5k - m) c_{m-k} T_k$$

To completely determine the solution, an additional condition is necessary. This is obtained from integration of (1*a*) over the interval, and corresponds to global energy conservation. For the linear problems involving the approximate quantities, this implies:

$$T_0^4 = \int_0^1 q dx \tag{5a}$$

$$\int_0^1 c_i dx = 0,\ i > 1 \tag{5b}$$

Equations (5) correspond to the orthogonality relation required for unique determination of the eigensolution corresponding to vanishing eigenvalue and conjunct occurring in similar Sturm-Liouville problems discussed in reference 3. There, the orthogonality constraint restricted the choice of excitation force, producing stable motions of a system in a resonant state.

By virtue of (5), the solution of (3) and (4) for an arbitrary $q(x)$ is:

$$T_0 = \left[\int_0^1 q(x) dx \right]^{1/4} \tag{6a}$$

$$T_1 = \int_0^x (x - t)[c_0 - q(t)] dt - 1/2 \times \int_0^1 (1 - t)^2 [c_0 - q(t)] dt \tag{6b}$$

$$T_i = P_i + \int_0^x (x - t) c_{i-1}(t) dt - 1/2 \int_0^1 (1 - t)^2 c_{i-1}(t) dt \tag{6c}$$

where

$$-P_i \equiv \frac{1}{4T_0^4} \sum_{k=1}^{i-1} (5k - i) \int_0^1 c_{i-k} T_k dx$$

For the particular q function used in reference [1][2] the values for the first three T_i's are:

$$T_0 = 0.90660600$$

$$T_1 = -0.005496692 - 0.15278896x + 0.15278876x^2 + 0.048634183 \sin \pi x - 0.003799546 \cos 2\pi x$$

$$T_2 = 0.04614323x - 0.0081919618x^2 - 0.075902522x^3 + 0.037951276x^4 - 0.014687851 \sin \pi x + 0.00028687203 \cos 2\pi x + 0.00049707397$$

Higher order coefficients could be generated from the recursive relations (6). The work is straightforward but tedious. However, as will be shown, if $0.1 \leq \epsilon \leq \infty$, only the indicated number of terms need be retained for satisfactory approximation of the numerical solution for the q function treated here.

The numerical solution was obtained by using Newton's method to find a zero of $T'(1)$ as a function of $T(0)$. These values were derived from successive solutions of the initial value problem for T based on a first guess for $T(0)$. The success of this scheme is implied by an existence and uniqueness proof that can be obtained with minor modifications of that given in [4] for a generalization of (1). For further generalizations, see [5].

Analytic continuation [6] was used to generate the numerical solutions. In this connection the required derivatives in the Taylor formula for T were easily found to an arbitrary order from differentiation of (1*a*). For the computations discussed subsequently, seven terms in the formula were used. Because (1*a*) is of second order, the error introduced by truncation is bounded by the first neglected term of the first derivative of the Taylor series, i.e., $\frac{h^7}{7!} |T^{(8)}(\eta)|$, where h is the step size and $0 \leq \eta \leq 1$. Thus, for $h \sim 0.01$, the error is $\leq |T^{(8)}(\eta)| \times .10^{-17}$. It is obvious from the preceding analyses that the first factor becomes large near $x = 0$ and 1 as $\epsilon \to 0$. For a fixed h, a computational lower bound for ϵ is thereby established.

For small ϵ, instabilities associated with the initial value formulation of singular perturbation problems such as (1) are well known [7], [8]. This difficulty was overcome in the present case by making $h/\sqrt{\epsilon} \ll 1$ and stepping from $x = 1/2$ to $x = 1$, using the condition $T'(1/2) = 0$, which is appropriate for q functions symmetrical about $x = 1/2$, such as the one considered in this analysis. Presumably, unsymmetrical q functions could

[2] $q = 0.37 + 0.48 \sin \pi x - 0.15 \cos 2\pi x$ on [0, 1].

also be handled by using an appropriate guess for $T'(1/2)$.

In the indicated nominal ranges, the following first guesses based on the asymptotic solutions were used:

$$T(1/2) \doteq 1 - 0.6662\epsilon + \ldots, 0.01 \leq \epsilon \leq 0.2 \tag{7a}$$

$$T(0) \doteq 0.906606 + \ldots, \epsilon \geq 0.2 \tag{7b}$$

The iterative process was terminated when $T'(1) \leq 10^{-7}$. To maintain this tolerance, double precision in the machine calculations was required.

Discussion

The results of the numerical solution calculated with the IBM 360–50 computer for the previously indicated q function are shown in Fig. 2. From subsequent considerations relating to the convergence of the procedure, as well as the truncation error estimate given previously, it is obvious that this method gives what may be termed, for all intents and purposes, the exact numerical solution of the problem. For these calculations, n, the number of uniformly spaced meshes was set equal to 100. This gave extremely accurate results in the range: $0.01 \leq \epsilon \leq \infty$. For $\epsilon < 0.01$, the large derivatives in the vicinity of $x = 0$ require a finer and perhaps nonuniform mesh spacing to keep the error term in (7) to within an acceptable tolerance.

From a practical standpoint, Fig. 2 shows that the maximum temperature of the heat shield is reduced by only 9 percent in increasing ϵ from 0 to ∞, with the disproportionate increase in the end temperature, $T(0)$, of 32 percent. However, an important structural benefit is obtained from the large reduction in the temperature differences along the shield with moderate increases in ϵ. Another interesting result is the proximity of the curves for $\epsilon = 1$ and $\epsilon = \infty$. This fact is probably responsible for the good agreement between the asymptotic about $\epsilon = \infty$ and the numerical solution for large excursions from $\epsilon = \infty$. Results for truncation at the second and third term of the asymptotic expansion, which are compared with the numerical solution in Fig. 3, clearly show this tendency. Moreover, for $\epsilon \sim 1$, the discrepancy between the numerical solution and the two-term asymptotic is at worst in the fourth significant figure and with three terms in the fifth. This improves considerably for $\epsilon \gg 1$. Fig. 3 also indicates good agreement between the asymptotics about $\epsilon = 0$ and the numerical solution for $\epsilon = 0.01$. The accuracy of both expansions truncated at three terms deteriorates in a "no man's land" of $0.01 \leq \epsilon \leq 0.1$. In this range the numerical solution provides the necessary coverage.

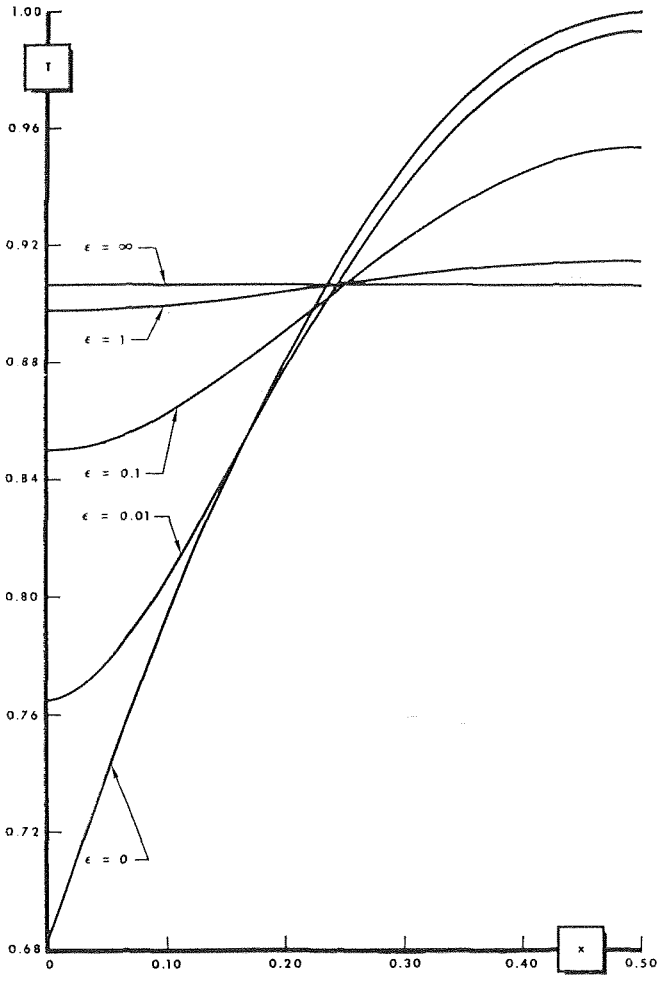

Fig. 2 Numerical solution for various ϵ values

It is of interest to assess to what extent the proximity of $T(x, \infty)$ and $T(x,\epsilon)$ for moderate values of ϵ, previously mentioned, applies to q functions other than the one treated here. One means of answering this question involves a study of the remainders for the truncated expansion (2). Inherent in this approach is the implicit assumption of rapid convergence of (2), even for significant excursions of ϵ from ∞. This conjecture is considered plausible based on the foregoing developments. A rigorous justification however is beyond the scope of the present analysis. As a motivation for such a corroboration, as well as providing insight into the present results and those for other q functions having similar properties to those of reference [1], we invoke the aforementioned assumption and obtain bounds on the second term evaluated at $x = 0$. Accordingly, we assert:

$$\epsilon|T(0, \infty) - T(0,\epsilon)| \doteq T_1(0)$$

Thus, we wish to show that $T_1(0) \ll 1$ for a general class of q's. For convenience, we consider q's symmetrical about $x = 1/2$. In addition, we further restrict our attention to cases where $q'(t) > 0$, $q''(t) < 0$ on $[0, 1/2]$[3] and $q'(0) > 2[1 - q(0)]$. Now $T_1' \geq 0$ inferred from (3*b*) implies T_1 is monotone increasing on $[0, 1/2]$. Equation (3*b*) implies that $T_1(1/2)$ is a maximum. Furthermore, (5*b*) implies that T_1 changes sign on $[0, 1/2]$, requiring that $T_1(0) < 0$. From (6*b*):

$$\sup|2T_1(0)| = \left|\inf \int_0^1 (1 - t)^2 q(t)dt - \sup \frac{c_0}{3}\right|$$

were, sup and inf signify least upper and greatest lower bounds, respectively. Now if $q(t) \geq \psi(t) \geq 0$ on [0,1], then $\int_0^1 (1 - t)^2 q(t)dt \geq \int_0^1 (1 - t)^2 \psi(t)dt \equiv I$. Selecting

$$\left.\begin{aligned} \psi &= 2(1 - q(0))t + q(0),\ 0 \leq t \leq \frac{1}{2} \\ &= -2(1 - q(0))t + 2 - q(0),\ \frac{1}{2} < t \leq 1 \end{aligned}\right\} \rightarrow \begin{aligned} \psi(0) &= \psi(1) = q(0) \\ \psi(1/2) &= 1 \end{aligned}$$

Thus,

$$I = \frac{9q(0) + 7}{48}$$

Noting that

$$c_0 < 2 \int_0^{1/2} [q'(0)t + q(0)]dt = \frac{q'(0)}{4} + q(0).$$

[3] Although the q function of reference 1 weakly violates the second of these inequalities, it can be represented to a good approximation by a function in this class.

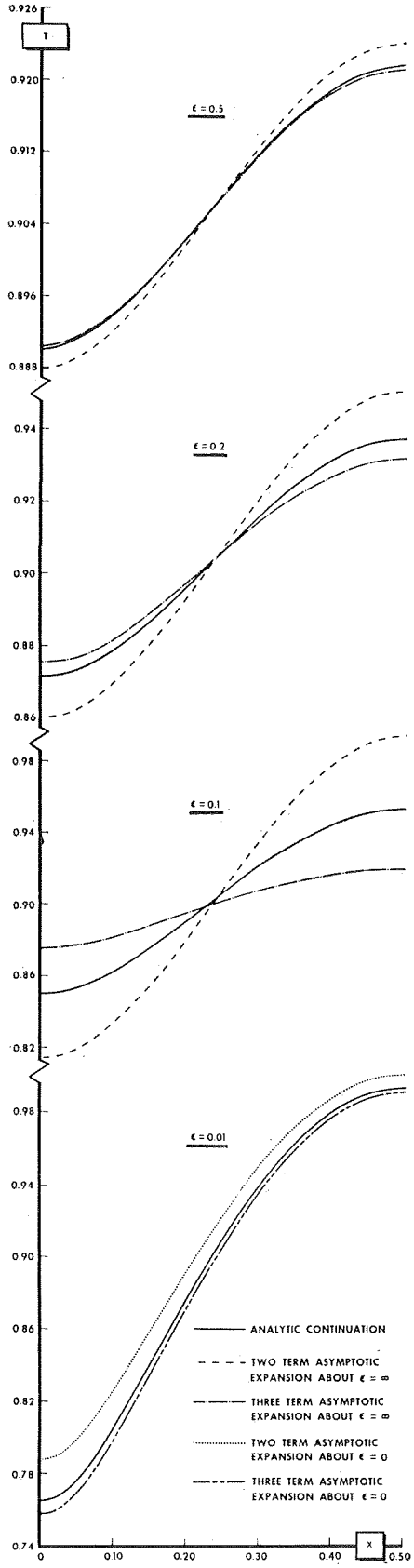

Fig. 3 Comparison of numerical and asymptotic solutions for various ϵ values

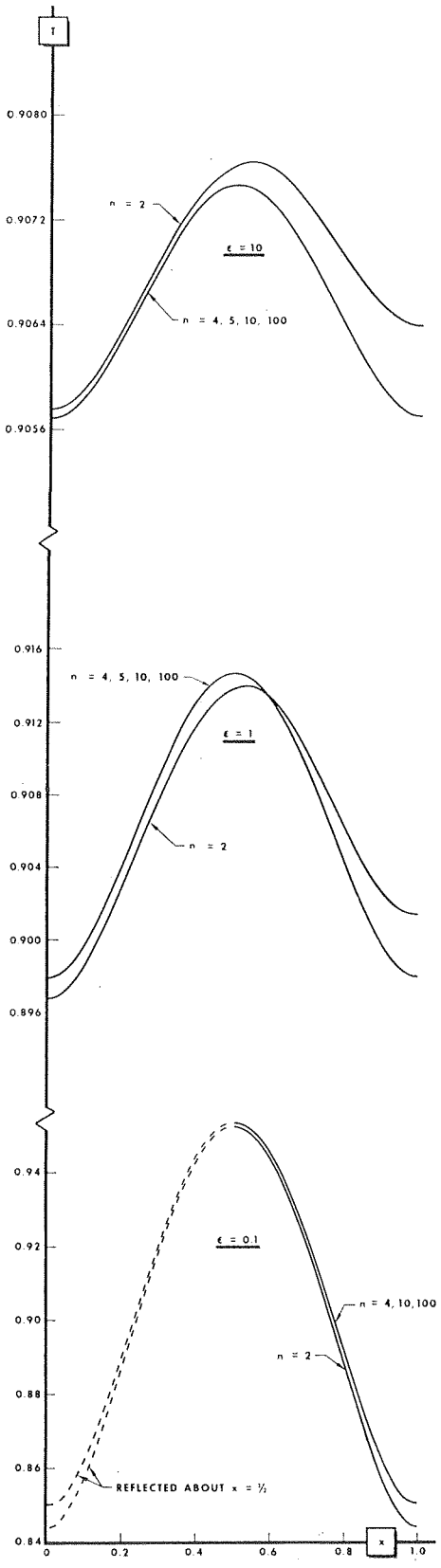

Fig. 4 Convergence of numerical solution with step size, n, for various values of ϵ

Since $q'(0) < 2(1 - q(0))$, it follows that,

$$|T_1(0)| \leq \frac{1 - q(0)}{96} \leq \frac{1}{96} = 0.0104$$

This bound is comparable in order of magnitude to $|T_1(0)|$ for the q of reference 1, whose value is 0.00929.

In Fig. 4, the convergence of the numerical solution with respect to mesh size is studied. It is obvious that over a wide range of ϵ, the convergence is extremely rapid, with ϵ having little or no effect. Presumably, analogous studies concerning the inclusion of more or less terms in the Taylor's formula would show similar trends by virtue of the previous truncation error estimate. Curves for $h = 1$ are not shown, since no real zeroes of $T''(1)$ as a function of $T(0)$ were obtainable for the cases indicated.

Acknowledgements

A portion of this research was sponsored by the Air Force Office of Scientific Research, Office of Aerospace Research, United States Air Force, under AFOSR contract number AF49-(638)-1477.

The authors wish to thank Messrs. Hector Rodriguez and Robert Lackaye, who programmed the solutions discussed here and performed the computations. They also are grateful to Mr. Walter Whitbeck for his helpful suggestions regarding the numerical solution and Mr. James Carey for his assistance in checking the analysis.

References

1 Mueller, H. F., and Malmuth, N. D., "Temperature Distribution in Radiating Heat Shields by the Method of Singular Perturbations," *International Journal of Heat Mass Transfer*, Vol. 8, 1965, pp. 915–920.

2 Coddington, E. A., and Levinson, N., *Theory of Ordinary Differential Equations*, McGraw-Hill, New York, 1955, pp. 22–32.

3 Courant, R., and Hilbert, D., *Methods of Mathematical Physics*, Vol. I, Interscience, New York, 1953, pp. 295, 354–358.

4 Henrici, P., *Discrete Variable Methods in Ordinary Differential Equations*, John Wiley and Sons, Inc., New York, 1962, pp. 347–348, 385.

5 Keller, H., *Numerical Methods for Two Point Boundary Value Problems*, Blaisdell, Waltham, Mass., 1968, pp. 7–21.

6 Davis, H., *Introduction to Nonlinear Differential and Integral Equations*, United States Atomic Energy Commission, Washington, 1960, pp. 247–266.

7 Murphy, W. D., "Numerical Analysis of Boundary Layer Problems in Ordinary Differential Equations," *Mathematics of Computation*, Vol. 21, 1967, pp. 583–596.

8 Pearson, C. E., "On a Differential Equation of Boundary Layer Type," *Journal of Mathematics and Physics*, Vol. 47, 1968, pp. 134–154.

G. E. MYERS
Associate Professor.
Mem. ASME

J. W. MITCHELL
Associate Professor.
Mem. ASME

Department of Mechanical Engineering,
The University of Wisconsin,
Madison, Wisc.

C. F. LINDEMAN, JR.
Aerospace Electronics Department,
General Electric Co.,
Utica, N. Y. Mem. ASME

The Transient Response of Heat Exchangers Having an Infinite Capacitance Rate Fluid

The transient response of heat exchangers to a step change in the temperature of the infinite capacitance rate fluid temperature is discussed. This work applies to condensers, evaporators, precoolers, and intercoolers. Analytical and finite difference methods are used to obtain solutions. The procedure for making useful hand calculations for the entire range of practical values of the parameters is presented.

Introduction

THE transient response of heat exchangers due to changes in the inlet temperatures of the fluids is useful for the dynamic control of power plants and air conditioning systems as well as many other applications. The general problem is quite complex in that it involves the solution of three simultaneous partial differential equations for temperatures as functions of time and position. Five parameters are involved which prohibit a graphical presentation in complete form. Consequently no general solution has yet been obtained. Solutions for a few special cases of technical interest are all that are available. The best compilation of these solutions can be found in *Compact Heat Exchangers* by Kays and London [1].[1]

In many heat exchanger applications the thermal capacitance rate of one fluid is much larger than that of the other fluid. Condensers, evaporators, intercoolers, and precoolers are such examples. These can be modeled by assuming one of the fluids has an infinite capacitance rate and consequently is always at a uniform temperature throughout the exchanger. In the transient analysis, the infinite capacitance rate fluid may be modeled as having a dwell time of zero. Restricting the problem to this special case eliminates one of the three differential equations and

Contributed by the Heat Transfer Division for publication (without presentation) in the JOURNAL OF HEAT TRANSFER. Manuscript received by the Heat Transfer Division, June 2, 1969. Paper No. 70-HT-B.

[1] Numbers in brackets designate References at end of paper.

Nomenclature

a = parameter defined by equation (18); dimensionless
A = parameter defined to be $R^*\bar{C}_w^*/N(1 + R^*)^2$; dimensionless
B = parameter defined to be $\bar{C}_w^*/(1 + R^*)$; dimensionless
$\bar{C}$ = fixed capacitance, product of mass and specific heat; Btu/F
$\bar{C}_w^*$ = ratio of wall capacitance to unstepped-fluid capacitance, $\bar{C}_w/\bar{C}_c$; dimensionless
I_0 = denotes a modified Bessel function of zero order; dimensionless
L = heat exchanger flow length; ft
N = parameter defined to be $\theta_{dc}/\bar{C}_c(R_c + R_h)$, equal to N_{tu}; dimensionless
R = fluid heat transfer resistance; hr-F/Btu
R^* = ratio of fluid heat transfer resistances, R_c/R_h; dimensionless
t = temperature relative to the initial temperature; F
T = magnitude of the step change in temperature of the infinite capacitance rate fluid; F
u = normalized relative temperature of the unstepped-fluid, t_c/T; dimensionless
u^* = ratio of the instantaneous outlet temperature of the unstepped-fluid to its steady-state value; dimensionless
U = parameter defined by equation (17); dimensionless
V = velocity of the unstepped-fluid, L/θ_{dc}; ft/hr
w = normalized wall temperature, t_w/T; dimensionless
x = length coordinate in flow direction; ft
x^* = normalized coordinate in flow direction, x/L; dimensionless
X = parameter defined by equation (14); dimensionless
Y = parameter defined by equation (15); dimensionless

(Continued on next page)

two of the five parameters. In addition, the solution will be valid for any flow arrangement.

An exact, analytical solution has been reported by Myers, Mitchell, and Norman [2] for step changes in the inlet temperature of the finite capacitance rate fluid. Thus, this problem has been completely solved analytically and the results presented in a manner useful to engineers. It is included in the Appendix for completeness and ready reference.

Rizika [3] has found the exact solution for a step change in the temperature of the infinite capacitance rate fluid. However, as reported by London, Biancardi, and Mitchell [4], the result is only readily usable for times less than one dwell time. Thus, it is useful only for cases with small wall capacitance. The electromechanical results of reference [4] cover only certain limited cases. An approximate solution for the response (for large wall capacitance) has been presented in [2] but the extent of the approximation is not well documented because an exact solution for comparison was not easily available.

The present paper discusses alternate approaches to the problem for intermediate and large values of wall capacitance. Graphs are presented for several special cases and the calculation procedure for any case of practical interest is outlined. The engineer will now be readily able to make hand calculations to obtain a solution for any set of parameters.

Analytical Development

Governing Equations. The governing partial differential equations for the case of a step change in the temperature of the infinite capacitance rate fluid may be obtained by writing energy balances on the wall and on the unstepped-fluid as discussed in [2]. For convenience, the cold fluid has been taken to be the finite capacitance rate fluid. The following equations result:

$$\bar{C}_w \frac{\partial t_w}{\partial \theta} + \frac{1}{R_h}[t_w - T1(\theta)] + \frac{1}{R_c}(t_w - t_c) = 0 \qquad (1)$$

$$\theta_{d_c}\bar{C}_c \frac{\partial t_c}{\partial \theta} + \bar{C}_c L \frac{\partial t_c}{\partial x} + \frac{\theta_{d_c}}{R_c}(t_c - t_w) = 0 \qquad (2)$$

In deriving these equations, it has been assumed that:

1 The fluid velocity is uniform across the flow passage (one-dimensional).

2 The heat transfer is one-dimensional (longitudinal conduction in the fluid and in the wall is assumed to be zero).

3 The conduction resistance through the wall is negligible.

4 The fluid capacitance, wall capacitance, thermal resistance, and flow rate are independent of temperature, time, and position.

5 The temperature of the infinite capacitance rate fluid is initially at 0 when it is suddenly stepped to a value T at zero time.

Because of the linearity and the homogeneity of these equations, it is entirely adequate to consider the initial condition for both t_w and t_c to be zero throughout the exchanger. Thus, t_w and t_c really represent temperature differences above the initial values of these temperatures. The initial and boundary conditions may then be written as follows:

$$t_c(x, 0) = 0 \qquad t_w(x, 0) = 0 \qquad t_c(0, \theta) = 0$$

The input to the problem is the term $T1(\theta)$ in equation (1) which represents the step change in the temperature of the infinite capacitance rate fluid.

These equations can be normalized by defining θ^*, x^*, $N = N_{tu}$, R^*, and $\bar{C}_w{}^*$ as in [1, 4]. Nondimensional temperatures, u and w, are defined by dividing t_c and t_w by the magnitude of the step change, T. In terms of these dimensionless groups, equations (1) and (2) become

$$\frac{R^*\bar{C}_w{}^*}{N(1 + R^*)}\frac{\partial w}{\partial \theta^*} + R^*[w - 1(\theta^*)] + (w - u) = 0 \qquad (3)$$

$$\frac{\partial u}{\partial \theta^*} + \frac{\partial u}{\partial x^*} + \frac{N(1 + R^*)}{R^*}(u - w) = 0 \qquad (4)$$

Equation (4) can next be used to obtain w in terms of u. This expression can then be substituted into equation (3) to eliminate w. Thus the two equations containing u and w can be transformed into one equation containing only u. The following result is obtained:

$$\frac{\partial^2 u}{\partial \theta^{*2}} + \frac{\partial^2 u}{\partial x^* \partial \theta^*} + \frac{N(1 + R^*)(1 + R^* + \bar{C}_w{}^*)}{R^*\bar{C}_w{}^*}\frac{\partial u}{\partial \theta^*} + \frac{N(1 + R^*)^2}{R^*\bar{C}_w{}^*}\frac{\partial u}{\partial x^*} + \frac{N^2(1 + R^*)^2}{R^*\bar{C}_w{}^*}[u - 1(\theta^*)] = 0 \qquad (5)$$

The initial and boundary conditions which are applicable to equation (5) are that

$$u(x^*, 0) = 0 \qquad u_{\theta^*}(x^*, 0) = 0 \qquad u(0, \theta^*) = 0$$

The initial condition of a zero time derivative replaces the initial condition for the wall temperature. It is obtained by recognizing that at $\theta^* = 0$, u, w, and u_{x^*} are all zero and consequently from equation (4), u_{θ^*} must also be zero at the start.

Examination of equation (5) shows it to be hyperbolic in nature. Solutions of this type of equation are sometimes facilitated if characteristic coordinates are used. Although previous investigations of this problem have not used this approach, it does offer some advantages and will be used here. The characteristic coordinates, ξ and η, for this problem are defined as follows

$$\xi = x^*$$

$$\eta = \theta^* - x^*$$

Nomenclature

Z = parameter defined by equation (19); dimensionless

$1(\ )$ = unit step function, zero for negative arguments and unity for positive arguments; dimensionless

ζ = characteristic variable defined as $(1 + R^*)\eta/\bar{C}_w{}^*$; dimensionless

ζ_1 = characteristic variable defined as $(1 + R^*)(\theta^* - 1)/\bar{C}_w{}^*$; dimensionless

η = characteristic variable defined as $\theta^* - x^*$; dimensionless

θ = time variable; hr

θ^* = normalized time variable, θ/θ_{d_c}; dimensionless

θ_{d_c} = dwell time of the cold or unstepped-fluid within the heat exchanger; hr

ξ = characteristic variable defined as x^*; dimensionless

$\phi_0[x, y]$ = function defined to be $e^{-y}\int_{\tau=0}^{x} e^{-\tau} I_0(2\sqrt{y\tau})d\tau$; dimensionless

Subscripts

c = denotes the cold or unstepped-fluid

h = denotes the hot or stepped-fluid

n = node index in the ξ-direction

w = denotes the wall condition or property

Superscripts

(ν) = node index in the η-direction

$*$ = denotes a nondimensional quantity

The resulting equation for $u(\xi, \eta)$ is

$$\frac{R^*\bar{C}_w^*}{N(1+R^*)^2}u_{\xi\eta} + \frac{\bar{C}_w^*}{(1+R^*)}u_\eta + u_\xi + N[u - 1(\xi+\eta)] = 0 \tag{6}$$

The boundary and initial conditions now become

$$u(\xi, -\xi) = 0 \qquad u_\eta(\xi, -\xi) = 0 \qquad u(0, \eta) = 0$$

The region of interest and the boundary conditions are shown in Fig. 1. Lines of constant time appear as diagonal lines at 45 degrees. The initial time line is the diagonal line passing through the origin. The exit of the exchanger is the vertical line at $\xi = 1$.

In the next section a finite difference solution to equation (6) is obtained. Then equation (6) is simplified by taking $\bar{C}_w \to \infty$ and an analytical solution is presented for this asymptotic case. Both of these solutions are facilitated by using the characteristic coordinate system.

Finite Difference Solution. The node arrangement for the finite difference formulation of this problem is the grid shown in Fig. 1. The finite difference approximations for u and its derivatives are given by

$$\left.\begin{aligned} u &\doteq u_n^{(\nu)} \\ u_\xi &\doteq \frac{u_n^{(\nu)} - u_{n-1}^{(\nu)}}{\Delta\xi} \\ u_\eta &\doteq \frac{u_n^{(\nu+1)} - u_n^{(\nu)}}{\Delta\eta} \\ u_{\xi\eta} &\doteq \frac{u_{n-1}^{(\nu)} + u_n^{(\nu+1)} - u_{n-1}^{(\nu+1)} - u_n^{(\nu)}}{\Delta\xi\Delta\eta} \end{aligned}\right\} \tag{7}$$

In selecting the relative grid spacing, $\Delta\eta/\Delta\xi$, it is important to be sure that any discontinuity in the fluid temperature moves through the heat exchanger at the proper speed. The proper speed in this case is the fluid velocity, $V = L/\theta_{d_c}$. In the original coordinate system (x, θ) this means that a discontinuity at position x should arrive at position $x + \Delta x$ after a time interval $\Delta\theta = \Delta x/V$. Therefore the time and distance intervals should be selected so that

$$\frac{\Delta\theta}{\Delta x} = \frac{1}{V} = \frac{\theta_{d_c}}{L}$$

In characteristic coordinates this means

$$\frac{\Delta\eta}{\Delta\xi} = \frac{\Delta\theta^*}{\Delta x^*} = \frac{\Delta\theta}{\theta_{d_c}}\frac{L}{\Delta x} = 1$$

Upon substituting equations (7), with $\Delta\xi = \Delta\eta$ into equation (6), the following expression is obtained:

$$u_n^{(\nu+1)} = \frac{[A + (B-1)\Delta\eta - N(\Delta\eta)^2]u_n^{(\nu)} + Au_{n-1}^{(\nu+1)} + [\Delta\eta - A]u_{n-1}^{(\nu)} + N(\Delta\eta)^2}{A + B\Delta\eta} \tag{8}$$

where

$$A = \frac{R^*\bar{C}_w^*}{N(1+R^*)^2} \quad \text{and} \quad B = \frac{\bar{C}_w^*}{1+R^*}$$

This expression is an explicit relation for calculating $u_n^{(\nu+1)}$ in terms of the three known values $u_n^{(\nu)}$, $u_{n-1}^{(\nu+1)}$, and $u_{n-1}^{(\nu)}$ which have already been calculated at previous times. The procedure starts by computing the value at node 1 on the first constant time line above $\theta^* = 0$ shown in Fig. 1. The computations continue diagonally along the constant time line, nodes 2, 3, 4, . . ., to the heat exchanger exit. Then the same steps are repeated beginning with node 1 along the next constant time line.

Fig. 2 presents the solution for the internal temperature distribution as a function of time for one typical case ($N = 3$, $R^* = 1$, and $\bar{C}_w^* = 1$). Observe the horizontal portions of the curves for $\theta^* < 1$. These describe the behavior of the fluid that was contained in the exchanger at the start of the transient. This fluid is always exposed to a uniform (but increasing) wall temperature and consequently the fluid temperature is also uniform. These horizontal portions have entirely left the heat exchanger at $\theta^* = 1$. This is consistent with the length of time required for the fluid to pass through the exchanger.

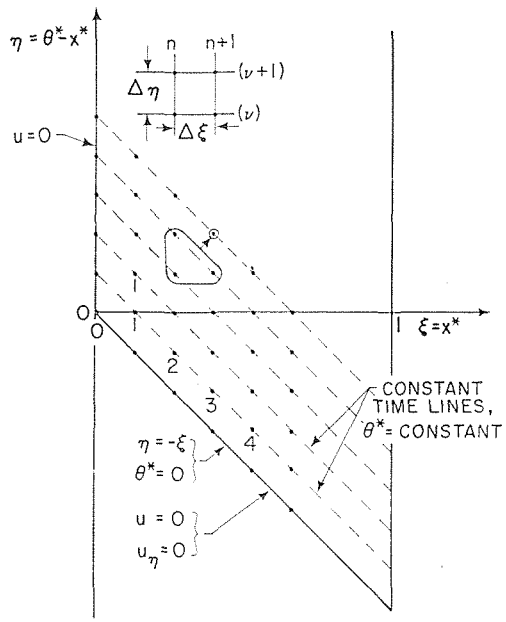

Fig. 1 Problem description in characteristic coordinates

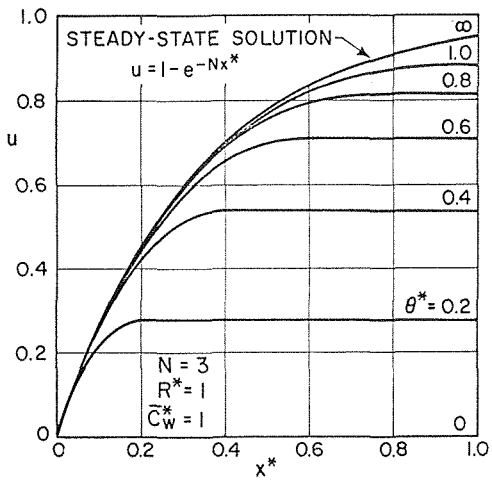

Fig. 2 Internal temperature distributions for $N = 3$, $R^* = 1$, and $\bar{C}_w^* = 1$

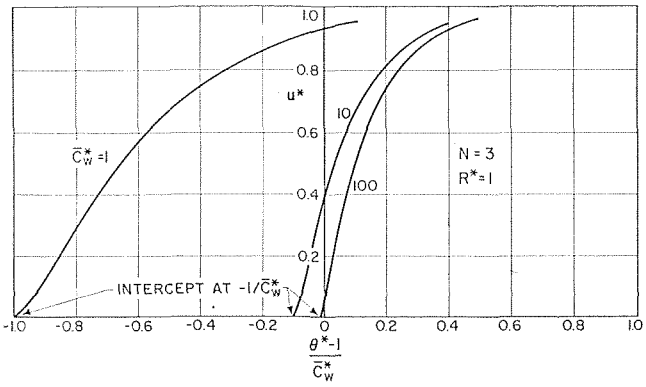

Fig. 3 Finite difference solution for $N = 3$ and $R^* = 1$

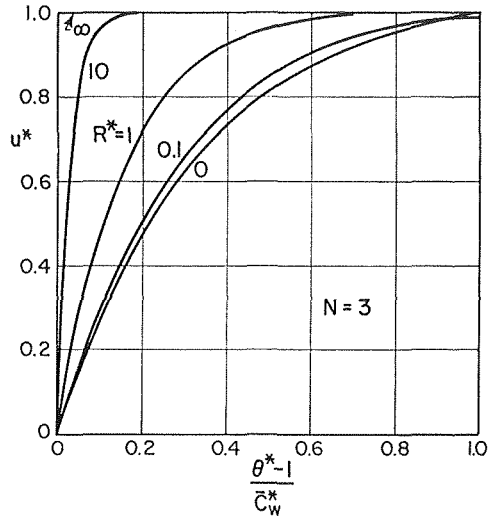

Fig. 4 Influence of R^* on the large wall capacitance solution

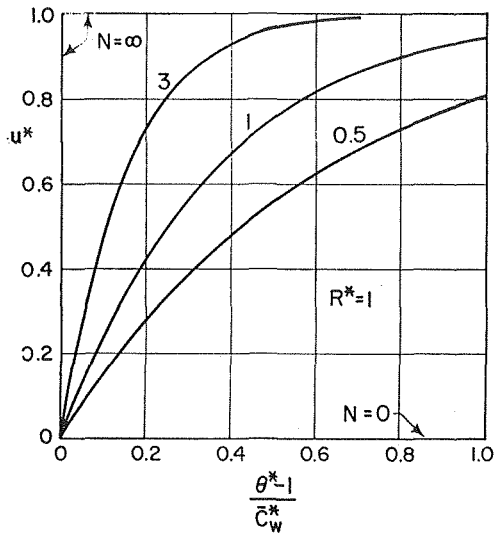

Fig. 5 Influence of N on the large wall capacitance solution

The horizontal portions of the solution for $\theta^* < 1$ correspond to the "easy-to-use" part of Rizika's exact analytical solution. This solution can be obtained by eliminating the x-derivatives from equation (5) and solving the resulting ordinary differential equation for u as a function of θ^*. The solution so obtained is valid as long as $\theta^* \leqq x^*$.

Equation (8) has been used to evaluate the solution to equation (6) for 27 combinations of N, R^*, and $\bar{C}_w{}^*$ to cover a large range of values for these parameters. A printout of the computer program used to determine the normalized exit response is available upon request. Fig. 3 shows solutions for three different values of wall capacitance for $N = 3$ and $R^* = 1$. In this figure the normalized exit response u^* is plotted as a function of $(\theta^* - 1)/\bar{C}_w{}^*$ for various values of $\bar{C}_w{}^*$.

The choice of $(\theta^* - 1)/\bar{C}_w{}^*$ for the abscissa has been made for two reasons. First, $\theta^* - 1$ appears naturally from the use of the characteristic coordinate $\eta = \theta^* - x^*$ when the solution is evaluated at $x^* = 1$. Second, the division by $\bar{C}_w{}^*$ is used to compress the abscissa for the intermediate and large values of wall capacitance which are of particular interest in this paper.

It can be observed from Fig. 3 that the transient is essentially complete by $(\theta^* - 1)/\bar{C}_w{}^* = 1$. This is substantiated by all of the other cases considered. This means that $\theta^* = 1 + \bar{C}_w{}^*$ is the nondimensional time required for the heat exchanger to respond. From this it is seen that the larger the wall capacitance the longer the response time.

As indicated in Fig. 3, the start of the transient is at $-1/\bar{C}_w{}^*$. Thus, as $\bar{C}_w{}^*$ increases, the starting point in this coordinate system approaches $(\theta^* - 1)/\bar{C}_w{}^* = 0$. This suggests that the large wall capacitance cases approach an asymptotic limiting solution as will be discussed in the next section.

Large Wall Capacitance Solution. When the unstepped-fluid is a gas, its capacitance is usually small relative to the wall capacitance. As reported by London [4] there are many cases of technical interest in which $\bar{C}_w{}^* > 100$. Thus, $\bar{C}_w{}^*$ is very large and for these cases it is possible to obtain a useful, asymptotic, analytical solution to equation (6).

To obtain this analytical solution, a new time variable is defined as

$$\zeta = \frac{1 + R^*}{\bar{C}_w{}^*}\,\eta$$

Then equation (6) simplifies to the following

$$\frac{R^*}{N(1 + R^*)}\,u_{\xi\zeta} + u_\zeta + u_\xi + N\left[u - 1\left(\xi + \frac{\bar{C}_w{}^*}{1 + R^*}\,\zeta\right)\right] = 0 \quad (9)$$

For large $\bar{C}_w{}^*$ (approaching infinity) the ξ in the argument f the unit step function can be neglected. The equation then reduces to

$$\frac{R^*}{N(1 + R^*)}\,u_{\xi\zeta} + u_\zeta + u_\xi + N[u - 1(\zeta)] = 0 \quad (10)$$

In obtaining equation (10) it should be noted that by definition of the unit step function,

$$1(\zeta) = 1\left(\frac{\bar{C}_w{}^*}{1 + R^*}\,\zeta\right)$$

since $\bar{C}_w{}^*/(1 + R^*)$ is always positive.

The three boundary and initial conditions become

$$u\left(\xi, -\frac{1 + R^*}{\bar{C}_w{}^*}\,\xi\right) = 0 \qquad \frac{1 + R^*}{\bar{C}_w{}^*}\,u_\zeta\left(\xi, -\frac{1 + R^*}{\bar{C}_w{}^*}\,\xi\right) = 0$$

$$u(0, \zeta) = 0$$

For $\bar{C}_w{}^* \to \infty$ the middle condition is automatically satisfied and the conditions reduce to the following:

$$u(\xi, 0) = 0 \qquad u(0, \zeta) = 0$$

The solution to equation (10) can be found using the Laplace transformation. The result is given as

$$u(\xi, \zeta) = 1 - e^{-N\zeta} - e^{-N\xi}\phi_0\left[\frac{N(1+R^*)}{R^*}\zeta, \frac{N}{R^*}\xi\right] + e^{-N\zeta}\phi_0\left[\frac{N}{R^*}\zeta, \frac{N(1+R^*)}{R^*}\xi\right] \quad (11)$$

where the function $\phi_0[x, y]$ has been tabulated by Brinkley, Edwards, and Smith [5].

The normalized exit response is then given by

$$u^* = \frac{1 - e^{-N\zeta_1} - e^{-N}\phi_0\left[\frac{N(1+R^*)}{R^*}\zeta_1, \frac{N}{R^*}\right] + e^{-N\zeta_1}\phi_0\left[\frac{N}{R^*}\zeta_1, \frac{N(1+R^*)}{R^*}\right]}{1 - e^{-N}} \quad (12)$$

where ζ_1 is equal to ζ evaluated at $x^* = 1$.

This solution has been evaluated and some of the results are presented in Figs. 4 and 5. Observe that the most natural coordinate, ζ_1, has been discarded in favor of $(\theta^* - 1)/\bar{C}_w^*$ in order to confine the effects of R^* to one parameter in Fig. 4. This is also consistent with the coordinate used in Fig. 3.

Fig. 4 shows that the effect of increasing R^* is to reduce the response time. It should also be observed that $R^* = 0.1$ to 10 covers practically the complete range of responses. Fig. 5 indicates that an increase in the value of $N = N_{tu}$ will also reduce the response time. These figures can also be used to obtain a qualitative idea of how the curves in Fig. 3 would shift for values of N and R^* other than the ones shown in Fig. 3.

Approximate Solution. As can be seen from Fig. 3, the response can be considered in three broad categories according to the magnitude of $\bar{C}_w^*$. For small $\bar{C}_w^*$ (e.g., $\bar{C}_w^* \leqq 1$) most of the response has been completed prior to $\theta^* = 1$. For $\theta^* \leqq 1$ Rizika's exact analytical solution [1, 4] can be evaluated. This solution is given by

$$u^* = \frac{1 - e^{-X}\left[Y \sinh \frac{X}{Y} + \cosh \frac{X}{Y}\right]}{1 - e^{-N}} \quad (13)$$

where

$$X = \frac{N(1+R^*)(1+R^*+\bar{C}_w^*)\theta^*}{2R^*\bar{C}_w^*} \quad (14)$$

and

$$Y = \left[1 - \frac{4R^*\bar{C}_w^*}{(1+R^*+\bar{C}_w^*)^2}\right]^{-1/2} \quad (15)$$

For large $\bar{C}_w^*$, which from Fig. 3 appears to be greater than 100, the analytical solution reported in the previous section may be successfully used. For intermediate values of $\bar{C}_w^*$ one can use Rizika's exact solution, as given by equation (13), up to $\theta^* = 1$, but for longer times equation (13) is not applicable and there is no easy way to evaluate the response. An approximate solution to help in these intermediate cases would be of value to the engineer.

One way to arrive at an approximate solution for $\theta^* > 1$ is to simply extend Rizika's exact solution beyond $\theta^* = 1$ in some reasonable manner. It is appropriate from the solution presented in Fig. 3 that u^* should be a function of $(\theta^* - 1)/\bar{C}_w^*$. A natural choice is to assume the following exponential form for the solution:

$$u^* = 1 - Ue^{-a(\theta^*-1)/\bar{C}_w^*} \quad (16)$$

where U and a are chosen so as to make both u^* and $\frac{du^*}{d\theta^*}$ agree with Rizika's exact solution at $\theta^* = 1$. This results in the following values for U and a:

$$U = 1 - \frac{1 - e^{-Z}\left[Y \sinh \frac{Z}{Y} + \cosh \frac{Z}{Y}\right]}{1 - e^{-N}} \quad (17)$$

and

$$a = \frac{1}{U}\frac{2N(1+R^*)\bar{C}_w^*}{(1+R^*+\bar{C}_w^*)}\frac{Ye^{-Z}\sinh \frac{Z}{Y}}{1 - e^{-N}} \quad (18)$$

with

$$Z = \frac{N(1+R^*)(1+R^*+\bar{C}_w^*)}{2R^*\bar{C}_w^*} \quad (19)$$

Although the expressions for U, a, Y, and Z are complicated functions of N, R^*, and $\bar{C}_w^*$, they can be readily calculated by hand.

A comparison of the approximate solution with the finite difference solution for all 27 cases shows that there is practically no difference between the two for $R^* \geqq 1$. For $R^* = 0.1$ the approximate solution falls off below the exact solution by as much as 10 percent of the full response. This is not a serious drawback however, since no practical case is expected to have an R^* less than one. The infinite capacitance rate fluid is expected to have the smallest heat transfer resistance as it is most likely to be either condensing or evaporating and consequently have a high heat transfer coefficient. Another possibility is either a precooler or intercooler in which the infinite capacitance rate fluid is a liquid and the other a gas. The liquid is expected to have the least resistance. Thus, the heat transfer resistance on the finite capacitance rate side would be greater than on the infinite capacitance rate side and consequently R^* would be greater than one.

All of the solutions obtained for $N = 3$ and $R^* = 1$ have been plotted in Fig. 6 for comparison. Observe how nicely the finite difference solutions approach the asymptotic solution for large wall capacitance. The approximate solution obtained by extending Rizika's solution can be seen in Fig. 6 only for $\bar{C}_w^* = 10$ because the $\bar{C}_w^* = 1$ and 100 cases cannot be distinguished from the corresponding finite difference solutions.

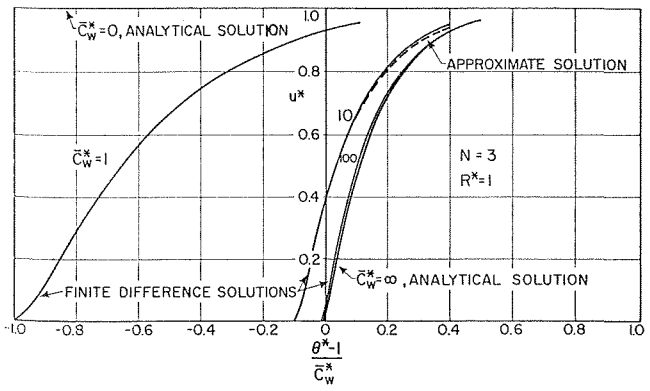

Fig. 6 Summary of solutions for $N = 3$ and $R^* = 1$

Calculation Recommendations

The following four solutions are now available for estimating the response of a heat exchanger to a step change in temperature of the infinite capacitance rate fluid:

1 Rizika's exact solution, equation (13)
2 Finite difference procedure, equation (8)
3 Large wall capacitance solution, equation (12)
4 Approximate solution, equation (16)

The engineer who wishes to make a calculation of such a response must choose between these solutions.

To select the appropriate solution it is recommended that the response at $\theta^* = 1$ given by Rizika's exact solution be computed first. If this value is above 0.9, most of the response has already occurred prior to $\theta^* = 1$ and Rizika's exact solution will give useful results (see Fig. 6 for example). If the value is less than 0.1 it would appear that the asymptotic solution for large wall capacitance would be a logical choice. For intermediate values one must either use the finite difference method or the approximate solution which extends Rizika's solution beyond $\theta^* = 1$. Since any practical case is expected to have $R^* > 1$, the approximate solution should be entirely adequate for these intermediate wall capacitance cases. It can also be used very nicely for large wall capacitance problems if a table of the ϕ_0-function is not available.

Discussion

Due to the number of parameters involved, it is not feasible to present complete curves to cover every case of interest. Consequently, only three figures have been selected, Figs. 4, 5, and 6, for comparison to the corresponding cases presented in [1, 4]. Additional cases may now be readily calculated using the methods discussed in this paper.

The effects of R^*, N, and $\bar{C}_w^*$ are the same as reported by previous investigators. The response is faster for larger R^*, larger N, and smaller $\bar{C}_w^*$. These effects can be observed from Figs. 4, 5, and 6, respectively.

It is interesting to note, based on Figs. 4 and 5, that for large wall capacitance cases the response requires about $(1 + \bar{C}_w^*)$ dwell times (i.e., $\theta^* = 1 + \bar{C}_w^*$). Thus, as the wall capacitance is increased, the significant time factor changes from the dwell time of the unstepped-fluid (for $\bar{C}_w^* = 0$) to $\bar{C}_w^*$ dwell times for large wall capacitance problems.

The electromechanical analog results of London [1, 4] agree reasonably well with the cases presented in this paper. It is felt, however, that the curves presented in this paper are better because of the relatively large number of nodes (100) used in the finite difference solution compared to the number of lumps (4) which London used. The present investigation suggests two improvements in London's presentation. First, the correlating time parameter should be $(\theta^* - 1)/\bar{C}_w^*$ which falls out naturally from the analysis in characteristic coordinates rather than $\theta^*/(1 + \bar{C}_w^*)$. Second, the implication that all responses for $\bar{C}_w^*$ greater than 5 are the same (see reference [4], Figs. 9 and 10) should probably be modified to $\bar{C}_w^* > 100$ as suggested by Fig. 6 in the present investigation.

Each of the 27 finite difference solutions was compared to Rizika's exact solution at $\xi = 1$ and $\eta = 0$. This is the largest value of θ^* for which Rizika's solution can be easily evaluated. In every case the agreement was to better than three decimal places. The solution shown in Fig. 6 for $\bar{C}_w^* = 1$ was also compared to Rizika's exact solution for shorter values of time. The finite difference solution exhibited more error at earlier times but was still within about one percent of full response. Thus, it is concluded that the finite difference solutions are as good as the exact solutions.

The effect of the choice of grid size on the response time is shown in Fig. 7. The calculated time to reach 95 percent of full response is plotted as a function of the number of nodes. This shows a significant change in the solution between 10 and 30 nodes but not much additional change in going to the 100 nodes used in this investigation. The typical solution required about 5 to 10 seconds on the UNIVAC 1108.

Application of finite difference methods to heat exchanger transients is not new, having been demonstrated by Dusinberre [6] in 1954. The special case considered by Dusinberre was very much over-simplified. Because he used a desk calculator, Dusinberre considered only 4 nodes. Fig. 7 indicates that one should definitely go beyond this number of nodes. The present investigation, covering a wide range of parameters and using a sufficient number of nodes, establishes confidence in this technique for heat exchanger transients.

Reference [2] presents an approximate integral solution to this problem for large values of wall capacitance. The present investigation shows that the results of [2] are about 5 percent high when compared to the infinite wall capacitance case of Fig. 6. This is remarkably good considering the simplicity of the solution obtained by the integral method and the assumptions involved. The results of [2] are no longer recommended for this problem however. Equation (16) presented in this paper gives far better results while retaining the ability to perform the calculations on the slide rule.

Conclusions

The conclusions of this investigation can be summarized as follows:

1 Useful solutions to the governing differential equations have been obtained using characteristic coordinates for both finite difference and analytical methods.

2 Several methods of calculating the transient response for any combination of N, R^*, and $\bar{C}_w^*$ have been presented and guidelines for which solution to use have been set forth. These are given as equations (8, 12, 13, and 16).

3 Successful sliderule calculations may now be made for any case of practical interest ($R^* \geq 1$) and for any wall capacitance using either equation (13) or equation (16).

APPENDIX

This appendix has been included to present the solution for the case in which the inlet temperature of the finite capacitance rate fluid is stepped instead of the infinite capacitance rate fluid. The

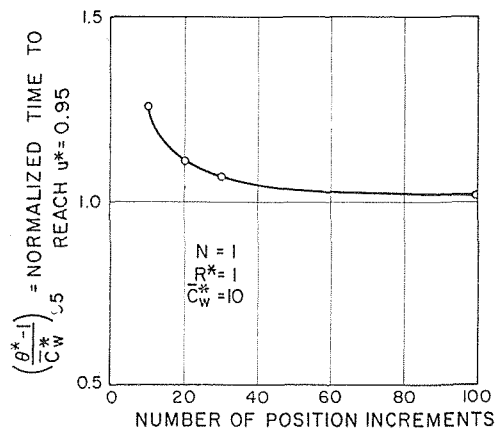

Fig. 7 Effect of node spacing on response time

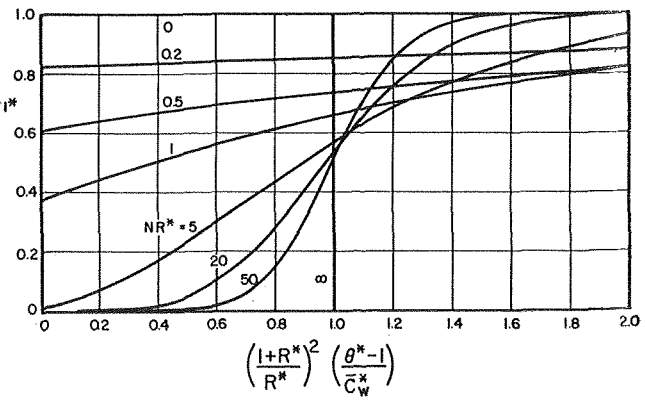

Fig. 8 Solution for a step change in the inlet temperature of the finite capacitance rate fluid

solution has been published in [2] and is re-presented here as

$$u^* = 1(\zeta_1)\{\phi_0[\zeta_1, NR^*] + e^{-NR^*}e^{-\zeta_1}I_0(2\sqrt{NR^*\zeta_1})\} \quad (20)$$

In arriving at this solution it was necessary to use different definitions of some of the nondimensional groups. These definitions are as follows:

$\bar{C}_h$ = fixed capacitance of the hot or stepped-fluid; Btu/F
$\bar{C}_w{}^*$ = ratio of wall capacitance to stepped-fluid capacitance, $\bar{C}_w/\bar{C}_h$; dimensionless
N = parameter defined to be $\theta_{dh}/\bar{C}_h(R_c + R_h)$, equal to N_{tu}; dimensionless
R^* = ratio of fluid heat transfer resistances, R_c/R_h; dimensionless
u^* = ratio of the instantaneous outlet temperature of the stepped-fluid to its steady-state value; dimensionless
ζ_1 = defined to be $N(1 + R^*)^2(\theta^* - 1)/R^*\bar{C}_w{}^*$; dimensionless
θ^* = normalized time variable, θ/θ_{dh}; dimensionless
θ_{dh} = dwell time of the hot or stepped-fluid; hr

The complete solution is presented in Fig. 8.

Acknowledgment

The University of Wisconsin Research Committee graciously donated the necessary computer time.

References

1 Kays, W. M., and London, A. L., *Compact Heat Exchangers*, McGraw-Hill, New York, N. Y., 1964, pp. 64–85.
2 Myers, G. E., Mitchell, J. W., and Norman, R. F., "The Transient Response of Crossflow Heat Exchangers, Evaporators, and Condensers," JOURNAL OF HEAT TRANSFER, TRANS. ASME, Series C, Vol. 89, No. 1, Feb. 1967, pp. 75–80.
3 Rizika, J. W., "Thermal Lags in Flowing Incompressible Fluid Systems Containing Heat Capacitors," TRANS. ASME, Vol. 78, 1956, pp. 1407–1413.
4 London, A. L., Biancardi, F. R., and Mitchell, J. W., "The Transient Response of Gas-Turbine-Plant Heat Exchangers—Regenerators, Intercoolers, Precoolers, and Ducting," TRANS. ASME, Vol. 81, 1959, pp. 433–448.
5 Brinkley, S. R., Edwards, H. E., and Smith, R. W., "Table of the Temperature Distribution Function for Heat Exchange Between a Fluid and a Porous Solid," U. S. Bureau of Mines, Pittsburgh, Pa., 1952.
6 Dusinberre, G. M., "Calculation of Transient Temperatures in Pipes and Heat Exchangers by Numerical Methods," TRANS. ASME, Vol. 76, 1954, pp. 421–426.

D. M. BENENSON
Professor.

A. A. CENKNER, JR.
Instructor.

Faculty of Engineering
and Applied Sciences,
State University of New York at Buffalo,
Buffalo, N. Y.

Effects of Velocity and Current on Temperature Distribution Within Crossflow (Blown) Electric Arcs

The effects of both velocity and current upon the temperature distribution within, and the cross-sectional shape of, steady-state 1.1 atm argon crossflow arcs have been determined experimentally. The tests were conducted over one range at constant current ($I = 60.3$ amp), $U = 0$, $41.8 \leq U_{cm/sec} \leq 127.0$ and another range at constant velocity ($U = 41.8$ cm/sec), $42.5 \leq I_{amp} \leq 80.8$. Forced convection (at constant arc current) exerts a profound influence upon the crossflow arc. At higher velocities, forced convection appears to completely penetrate the plasma. The effect of increasing current (at constant velocity) is to shield a central core region from the flow field. As a result of the effects of velocity, electrode design, interactions of the electrode jets, and slight misalignment of the jets, neither the isotherms nor the cross sections can be considered to be generally circular, even at the higher currents.

Introduction

The crossflow or blown arc is characterized by deflection generally in the direction of the main-stream flow. The extent of the deflection, the profile of the plasma, the cross-sectional shape, temperature distribution within the plasma, etc., depend upon many factors including the electrode material, electrode design, flow velocity, arc current, and geometry of the test facility. One consequence of the interaction of the gas-dynamic and electromagnetic aspects is that the plasma no longer is circularly symmetrical in cross section, although a mirror plane of symmetry in cross section may be found.

The deflection of the plasma with forced convection, together with the absence of circular symmetry in cross section, introduce an essential complexity into both the analytical and experimental studies of the blown arc configuration. Although such configurations have been employed in a wide variety of applications such as switch gear, arc heaters, space propulsion, and simulators, the difficulties associated with analytical and experimental investigations have resulted in a relative lack of quantitative information with respect to the detailed behavior.

Results of analytical studies should include the predictions of the arc profile, cross-sectional shape, and local temperature distribution as functions of arc current and main-stream velocity. Present analytical treatments of this configuration have treated the arc as a one-dimensional or quasi one-dimensional problem (e.g., survey of [1][1]). The particular formulations and assumptions imposed have generally neglected the azimuthal (or lateral) dependence of all variables (e.g., in cross section, the arc is assumed to be circular or quasi one-dimensional wedgelike). The results of recent quantitative experiments, at constant, low velocity and at low currents [2, 3], have shown the cross-sectional shape and local temperature distribution to depend significantly upon the azimuthal location. The results of [2 and 3] have indicated the analysis of the crossflow arc to be properly a three-dimensional, or at the simplest, a quasi two-dimensional problem.

The most detailed analysis presently available is found in [4 and 5]. Here a gaseous, quasi-neutral conductor in steady flow at low Mach number is considered. External magnetic fields are not applied; self-magnetic field is assumed to be negligible. The plasma is assumed to be circular or one-dimensional wedgelike in cross section. All quantities except electrical conductivity are assumed to be constant with temperature; the temperature dependence of electrical conductivity is represented by the linear-discontinuous model. The results of the analysis include:

1 The effect of curvature (in arc profile) increases the temperature gradient upstream of the center of the arc with respect to the gradients downstream of the center.

2 The maximum temperature occurs slightly upstream of the center of the arc. Along the mirror plane of symmetry in cross

Contributed by the Heat Transfer Division of The American Society of Mechanical Engineers and presented at the Winter Annual Meeting, Los Angeles, Calif., November 16–20, 1969. Manuscript received at ASME Heat Transfer Division, July 10, 1969. Paper No. 69-WA/HT-59.

[1] Numbers in brackets designate References at end of paper.

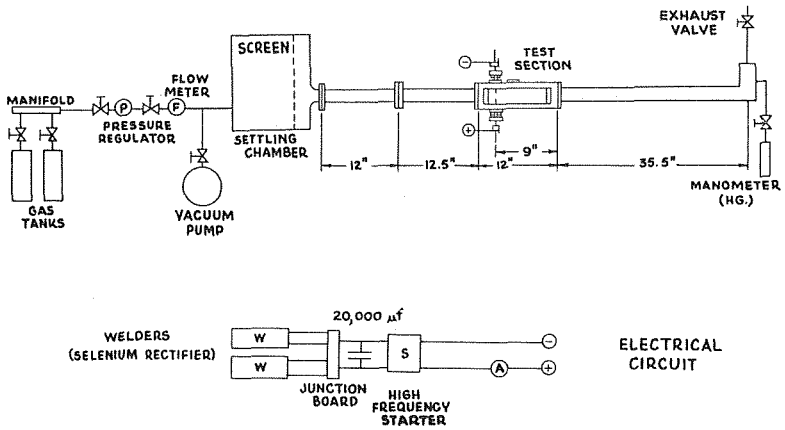

Fig. 1 Arc tunnel

section, the experiments of [2 and 3] are in qualitative agreement with the analytical predictions.

Analogous difficulties are introduced into the experimental investigations. The absence of circular symmetry in cross section requires the plasma to be observed at many different azimuthal positions. The resulting integrated intensity distributions of, say, arc radiation must be inverted to obtain the local distribution of emission coefficients from which the local temperatures are obtained. In [2 and 3], this was accomplished for the first time (the inversion method of [6 and 7] was employed), permitting the quantitative determination of local temperatures within the crossflow plasma. The experiments of [2 and 3] were conducted at constant, low main-stream velocity (U = 43.8 cm/sec), with current over the range $17.2 \leq I$ amp ≤ 34.1; the electrode spacing was maintained at 6.6 mm. The tests were conducted in argon at 1.1 atm.

The experimental results indicated the plasma cross section (a) was noncircular, with the major axis in the flow direction and (b) contained a central portion (a core), generally circular, well shielded from the main-stream flow, and an outer region, noncircular, in which convective interchange of energy occurred.

The experiments described herein extend the work of [2 and 3] to incorporate the effects of both main-stream velocity and (higher) arc current as parameters. Tests were conducted over the following ranges:

1 At constant current (I = 60.3 amp), U = 0, $41.8 \leq U$ cm/sec ≤ 127.0.

2 At constant velocity (U = 41.8 cm/sec), $42.5 \leq I_{\text{amp}} \leq 80.8$.

Electrode spacing was maintained constant, at 11.2 mm, for all tests. The experiments were conducted in argon at 1.1 atm. Local temperature distribution within the plasma was obtained in a horizontal plane about middistant between the electrodes (4.94 mm above the anode).

Reported herein are steady-state characteristics of the crossflow arc (including local temperature distribution, cross-sectional shape, and arc current and voltage). Operation under oscillatory modes [8], observed here at certain conditions, is not discussed.

The experiments have indicated a profound effect of velocity upon the local temperature distribution (and cross-sectional shape). As velocity was increased (with current maintained constant), the plasma cross section (and local temperature distribution) changed from that associated with a heated, blunt body to that of a heated, highly streamlined body. As current was increased, while maintaining a constant main-stream velocity, behavior somewhat similar to that found in [2 and 3] was observed. However, as a result of the higher current levels at which the present series of experiments were conducted, jet effects from the electrodes resulted in generally noncircular isotherms even within the core.

Experimental Facilities

Arc Tunnel and Accessories

The test facility was an open circuit tunnel consisting, basically, of the (bottled) gas supply and manifold, tunnel settling chamber, entrance flow passage, test section, and exit section, Fig. 1. The cross section of all flow passages were identical: $1^7/_8$ in. $\times$ $1^7/_8$ in. Appropriate meters and valves were installed to regulate the flow and pressure level.

The power supply consisted of two direct current (selenium rectifier) welders across which extensive capacitive filtering was employed to reduce the ripple to about ± 0.1 percent with a resistive load. To avoid touch starting of the arc, with the resultant contamination of the flow as well as possible damage to the electrodes, a high-frequency starter was employed, Fig. 1.

The test section, Fig. 2, was 12 in. long and could be located at several axial stations. The tests were conducted with the test section positioned as shown in Fig. 1. The test section was made of aluminum and suitably O-ringed and gasketed. The top and bottom walls were water-cooled. A 9-in. window was installed in one side wall; the window length was selected to permit viewing of the plasma over a wide range of azimuthal angles. A black anodized aluminum insert was inserted into the rear side wall. A viewing port was placed in the top wall for observation of the plasma from a rearwardlike direction.

Both electrodes were water-cooled. A 90-deg, conically tipped (OFHC) copper anode insert (0.250-in. base dia) and a tantalum cathode insert $^3/_4$-in. overall length were employed; a $^1/_4$-in. length of the cathode was 0.188-in. dia, while the remaining section was machined to a diameter of 0.080 in. with a 90-deg conical tip. A cylindrical notch (0.010-in. depth, 0.030-in. length) was machined in the smaller diameter section, 0.180 in. from the end. This notch was used as a reference for determination of spatial location. Both electrodes could be positioned continuously in the tunnel.

The arc tunnel arrangement is described in detail in [2, 3, and 9].

Optical System

Arrangement. The optical system employed, Fig. 3, permitted simultaneous observation of the plasma at 12 known azimuthal locations. The system was designed subject to the following constraints:

1 All 12 images must be in focus for any given camera setting.

2 Overall magnification to be as large as physical conditions permit (M = 0.46).

3 Images to be observed in a common horizontal plane containing the electrode center line.

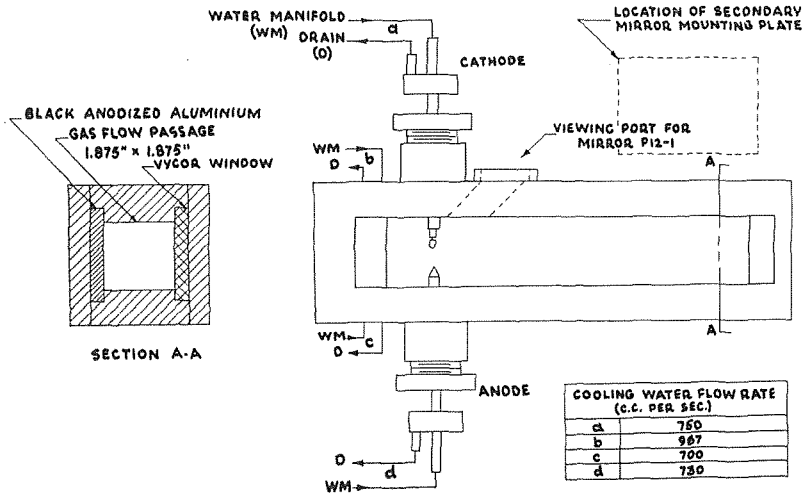

Fig. 2 Arc tunnel test section

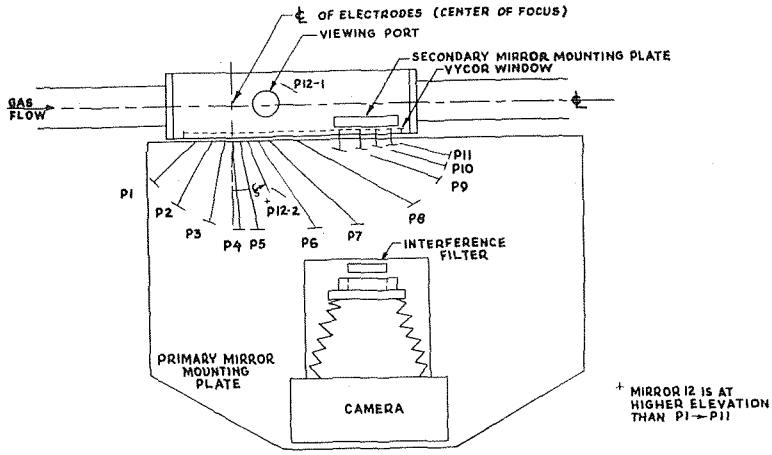

Fig. 3(a) Optical system—top view

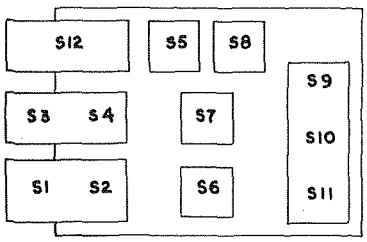

Fig. 3(b) Secondary mirrors

MIRROR NO.	ξ°	MIRROR NO.	ξ°
1	-45.5	7	46.4
2	-29.0	8	61.0
3	-10.3	9	70.5
4	3.9	10	73.5
5	19.0	11	76.4
6	34.5	12	90.0

Fig. 3(c) Azimuthal angles

4 Presence of field stops be minimized (this requirement resulted in a camera setting of f/32 for all data).

The optimal system contained three components:

1 Primary Mirrors. This set of 12 front surface mirrors was suitably aligned to view the plasma at known azimuthal angles (determined to within ±0.1 deg, Fig. 3(*c*)). Eleven of these mirrors were oriented in a common horizontal plane. The 12th mirror, which observed the arc from a rearwardlike position through the viewing port in the upper window, was not oriented in the same plane as the other mirrors; this mirror was used to determine the existence of the mirror plane of symmetry.

2 Secondary Mirrors. The function of these (front surface) mirrors was to compact the images of the plasma for placement upon a 4-in. × 5-in. negative.

3 Detector Arrangement. The grouping contained (*a*) the camera, (*b*) a narrow band optical interference filter (centered at about 4454 angstroms at normal (zero deg) incidence; 9.5 angstroms bandwidth).

Typical photographs of the plasma as viewed through the optical system are shown in Fig. 4. Below each image is seen the calibration data appropriate for the optics and film associated with that image.

The arrangement developed is, thus, approximately equivalent to the simultaneous use of 12 monochromators.

Calibration. Quantitative determination of the temperature distribution within the plasma resulted in the requirement of an absolute calibration of the optical system and film. Using a tungsten strip lamp, this calibration was performed for 11 optical paths (each optical path was designated by a number associated with a given primary mirror). Here the term optical path designates the sequence traversed by light during passage from the source to the film. This includes: emission from the source (calibration lamp or arc), transmission through test section window, reflection from primary and secondary mirrors, transmission through the filters and camera lens, and impingement upon the film.

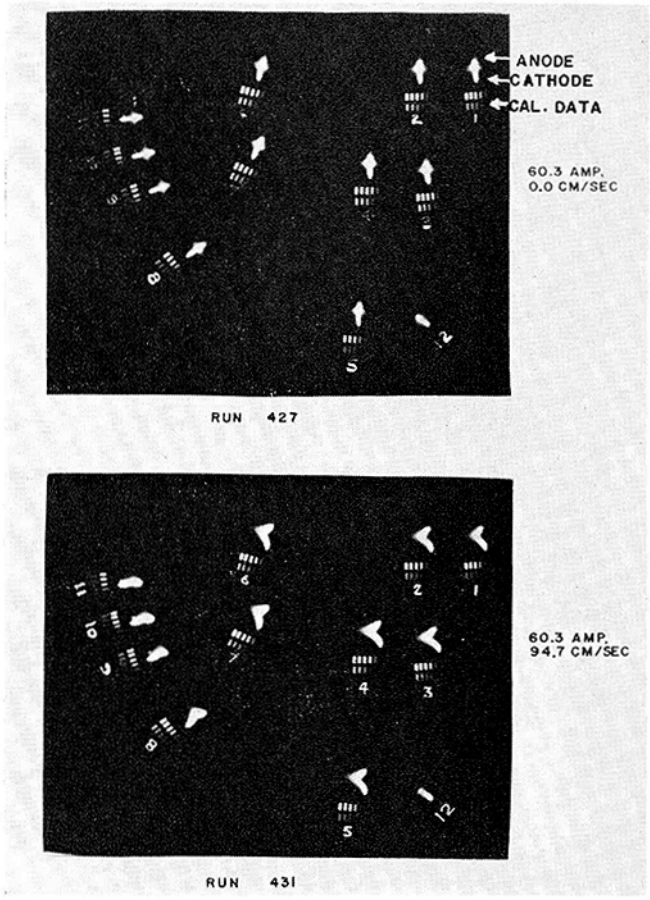

Fig. 4 Optical fields of 12 mirror systems as seen by camera

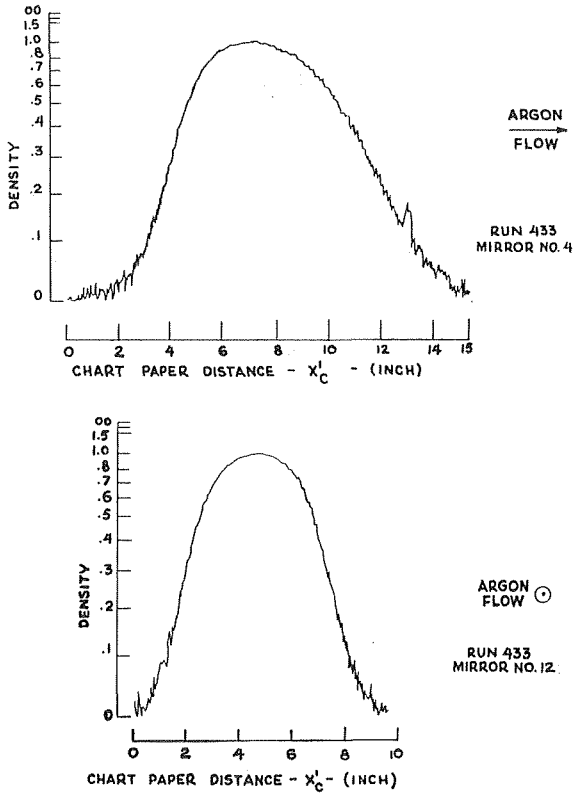

Fig. 5 Densitometer traces of arc

Ten calibration data points were placed on the film for each optical path. (Lens setting and exposure times were the same for both calibration and test data.) From reported spectral emissivities for tungsten [10] and from the known characteristics of the optical pyrometer used to measure brightness temperature [11], the calibration curve for each optical path was constructed. Scans with a microdensitometer were used to obtain the measured values of film density or darkening.

With the construction of the absolute calibration curve for each optical path, the absolute magnitude of any point in the integrated intensity distribution of arc radiation was determined through inversion of the calibration procedure.

Data Reduction. For each run, microdensitometer scans of the plasma, in conjunction with the calibration curve, yielded the absolute magnitude of the integrated intensity distribution. All scans were obtained in the same horizontal plane, 4.94 mm above the anode. The slit dimensions for the densitometer scans were 0.5 mm height by 10 microns width. Typical scans are shown in Fig. 5.

The local distribution of emission coefficients was obtained using the inversion method of [6]. The method required the plasma to contain a mirror plane of symmetry; the lower portion of Fig. 5 indicates this requirement was satisfied in the experiment. The procedure of [6] also required data input at equal increments of azimuthal angle; this was accomplished with the three-point interpolation method of [12].

With the emission coefficients now known, the local distribution of temperature was calculated using the simplified (frequency-independent) form of the Kramers-Unsold equation for continuum radiation. For the case of atmospheric (coaxial) argon plasmas, operated in the same current range as described herein, determination of temperatures according to continuum and line radiation were in agreement to within about ± 150 K for plasmas having center-line temperatures about 10,000 K [13, 14].

The results of the computations are presented in the form of (computer-plotted) isotherm distributions at each operating condition.

For atmospheric argon plasmas and for wavelengths in the range used (about 4454 angstroms), there is negligible self-absorption [13]. Further, as noted earlier, the plasma was observed to contain a mirror plane of symmetry in cross section. Under these conditions, it can be shown the local temperature distribution can be obtained by observation of the plasma through but one (90 deg) quadrant [2, 3]. Accordingly, the results reported herein were obtained using data from mirrors 4–12 only, Fig. 3.

Scans of the argon spectrum indicated the absence of strong argon lines over the range of incidence angles to the interference filter.

The optical system is described in detail in [2, 3, and 9].

Uncertainty in Arc Temperature

The accuracy of the optical pyrometer was about $\pm 1/2$ percent at about 1600 C and about $\pm 3/4$ percent at about 2100 C. Measurements were repeatable to within ± 1 percent. These sources of error result in an uncertainty of about ± 110 K in arc temperature.

The uncertainty in the absolute magnitude of the spectral emissivity of the tungsten ribbon calibration lamp is expected to not exceed ± 3 percent [15]. This yields an uncertainty in arc temperature of about ± 55 K.

Uncertainty in the characteristics of the narrow band optical interference filter were a maximum of ± 10 percent at a given angle of incidence. This results in an uncertainty of about ± 80 K in arc temperature.

Various factors in the inversion method may be selected over a range of values. Computer studies of the effects of variation of

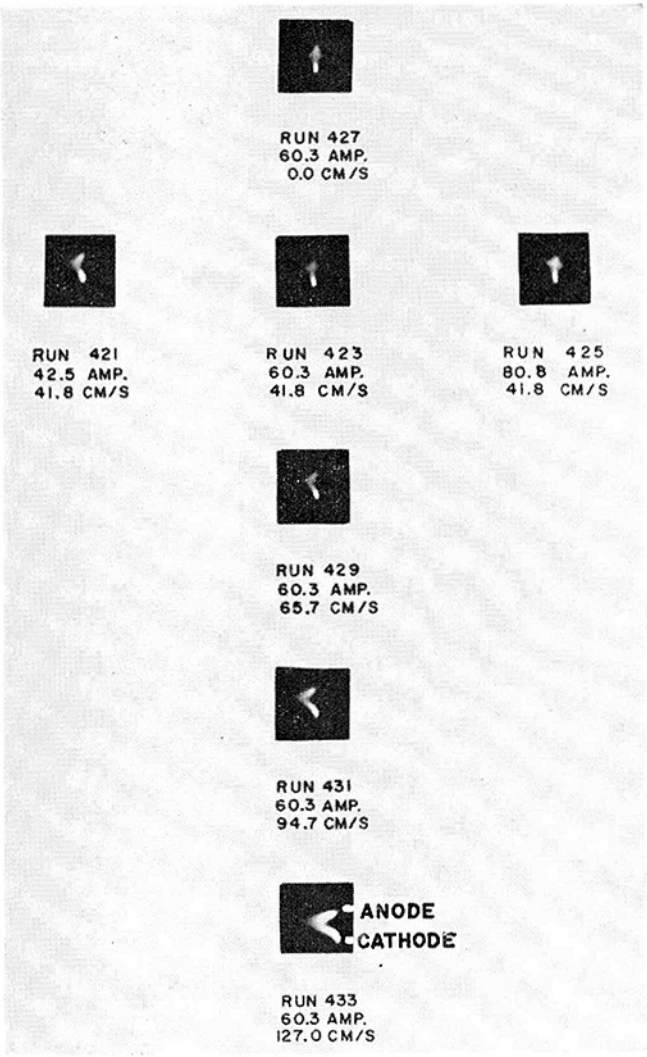

Fig. 6 Arc photographs through mirror system 4

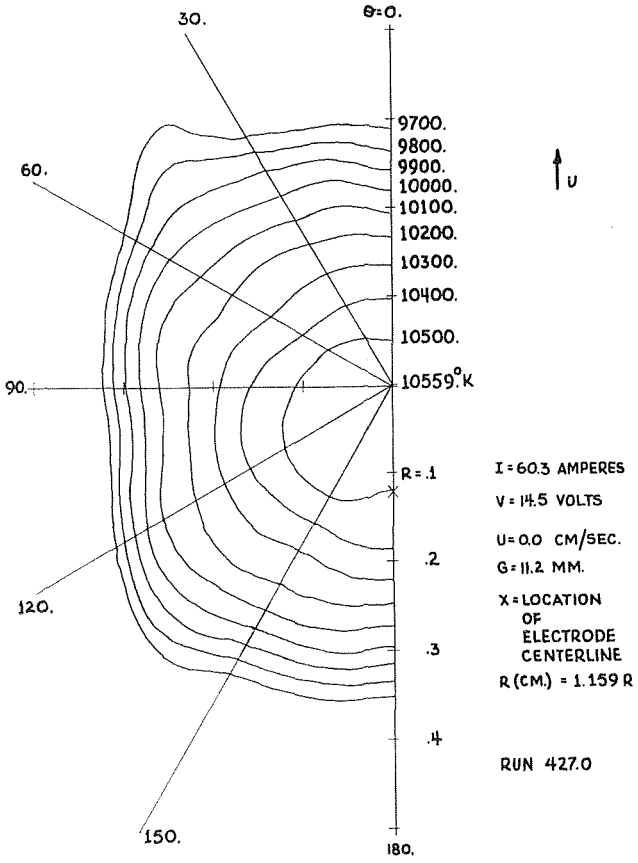

Fig. 7 Isotherm distribution

these factors [2, 3] indicate that these influence the resulting temperatures by a maximum of ±20 K.

The foregoing, together with uncertainties associated with application of the Kramers-Unsold equation, indicate that the temperatures are determined to within about ±400 K.

Discussion of Results

The experiments were conducted over the following ranges: (*a*) at constant current (I = 60.3 amp) $U = 0, 41.8 \leq U_{\text{cm/sec}} \leq 127.0$, and (*b*) at constant velocity (U = 41.8 cm/sec), $42.5 \leq I_{\text{amp}} \leq 80.8$. Electrode spacing was maintained constant, at 11.2 mm, for all tests. The experiments were conducted in argon at 1.1 atm. Local temperature distribution within the plasma was obtained in a horizontal plane about middistant between the electrodes (4.94 mm above the anode).

Views of the plasma, from nearly right angles to the flow (mirror 4, ξ = 3.9 deg (refer to Fig. 3)), are shown in Fig. 6 for each operating condition. The effects of forced convection (vertical column) and of arc current (horizontal row) can be seen qualitatively.

Consider convection at constant current. At zero flow, the configuration contains cusps on both upstream and downstream sides. These probably originate as a result of the jet effects due to the electrodes and become more pronounced as current is increased (for this configuration, cusps are not observed at relatively low currents—less than about 20 amp [2, 3]). The plasma does not appear quite symmetrical in the direction of flow (also refer to the upper portion of Fig. 4): A line connecting the ends of the cusps is inclined at an angle with respect to the horizontal. Since, in operation, the tip of the cathode is observed to melt and form a molten spherical layer upon which the plasma attaches, any slight misalignment of the attachment could produce the observed asymmetry.

The initial effect of forced convection (U = 41.8 cm/sec) is primarily to deflect the upstream cusp in the flow direction; relatively little deflection of the plasma as a whole is experienced. For all higher velocities, forced convection results in pronounced deflection of the plasma in the direction of flow.

Based upon the foregoing, it would be expected that (*a*) the isotherm distribution at zero speed would not be completely symmetrical, (*b*) at higher speeds, forced convection could significantly influence the temperature distribution within the plasma, and (*c*) at U = 41.8 cm/sec, a transition region could be found.

Consider the effects of arc current at constant main-stream velocity. As the current is increased the arc shape is seen to resemble more that found at zero speed. In effect, then, as the arc current is increased, the arc would be expected to become "stiffer" [5], less sensitive to forced convection. At 80.8 amp, both upstream and downstream facing cusps are found (in the presence of forced convection); a pronounced inclination of the line connecting the cusps is seen.

The influence of forced convection (at constant current) upon the isotherm distributions is shown in Figs. 7–11.

At zero speed, Fig. 7, the isotherms are approximately circular within a "core" (to about 10,200 K), and distinctly noncircular in the outer portion. The absence of extensive circular symmetry is probably the result of the jet effects noted earlier. At U = 41.8 cm/sec, Fig. 8, the plasma has undergone initial deflection;

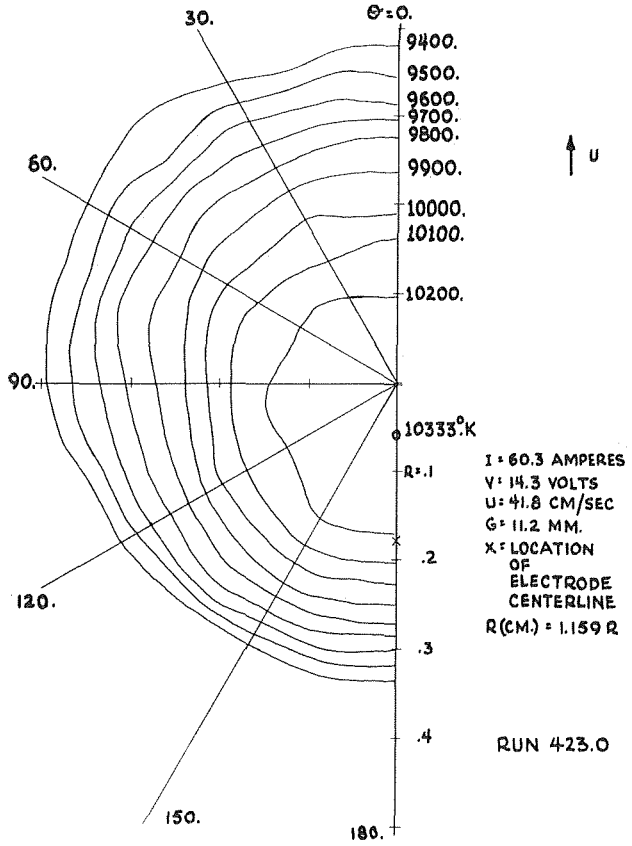

Fig. 8 Isotherm distribution

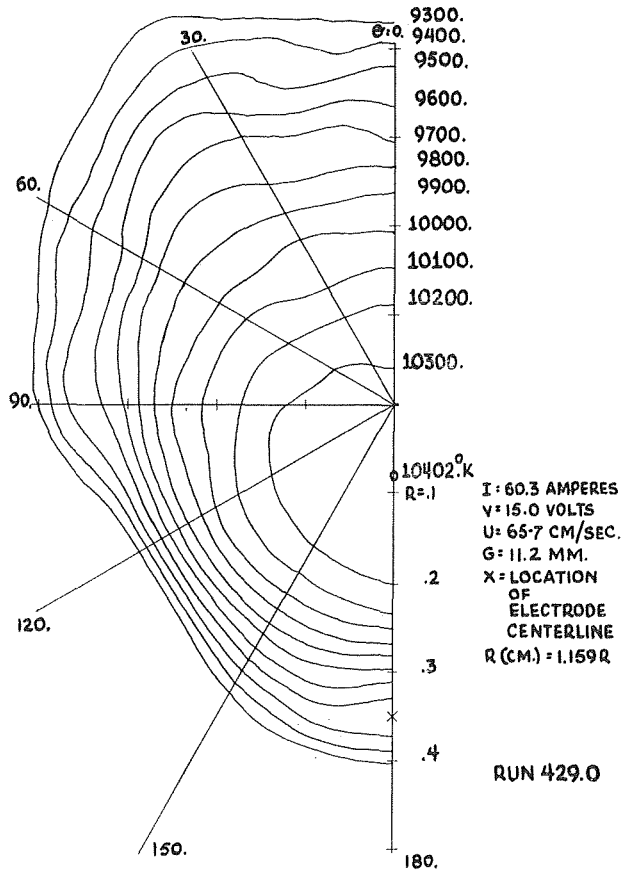

Fig. 9 Isotherm distribution

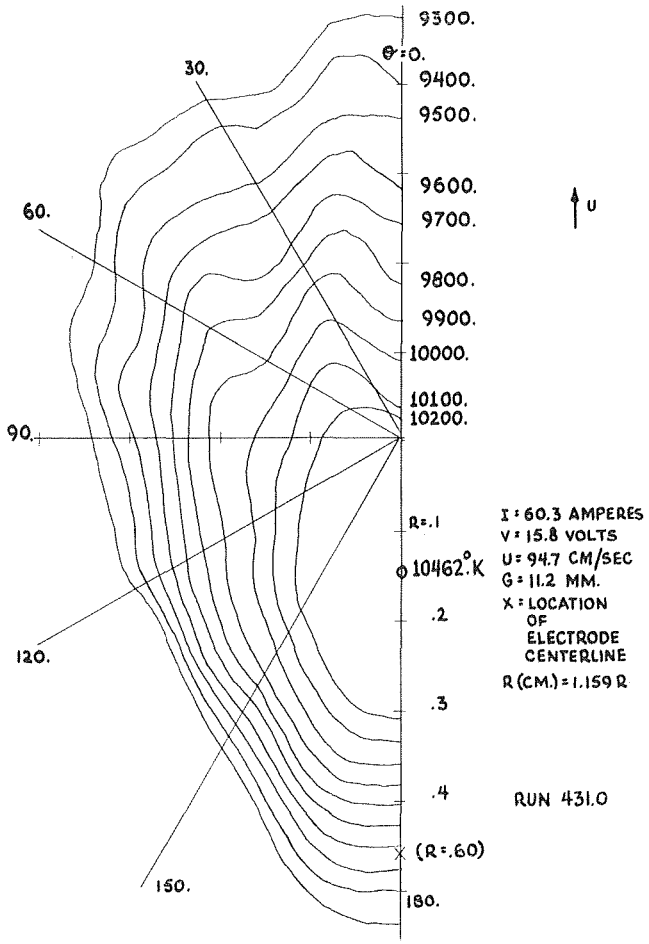

Fig. 10 Isotherm distribution

the upstream facing cusp has been forced downstream (refer also to Fig. 6). The isotherm distributions show the initial development of the characteristics observed with forced convection.

For all higher velocities, $U \geq 65.7$ cm/sec, Figs. 9–11, the effects of forced convection become more pronounced. Considering an isotherm to characterize the dimension of the plasma (e.g., $T = 9700$ K), the cross section is readily found to become increasingly elongated in the direction of flow and progressively shorter transverse to the flow ($\theta = 90$ deg) as the velocity is increased. The isotherms for $U = 65.7$ and 94.7 cm/sec, Figs. 9 and 10 become broader, or wider, along the downstream portion (90 deg $\leq \theta \leq 0$ deg); these suggest the case of flow in the wake of a heated body (e.g. [16]). Circular isotherms are present to a relatively small degree at $U = 65.7$ cm/sec (to 10,100 K). The isotherms at $U = 94.7$ cm/sec are noncircular in a core region. At the highest velocity tested, $U = 127.0$ cm/sec, all isotherms are highly elongated in the direction of flow.

Defining the center of the arc as the location, along the mirror plane of symmetry, midway between the intercepts of a characteristic isotherm (e.g., $T = 9700$ K), the temperature gradients upstream of the center are found to be greater than those downstream for all cases. For all finite velocities, the maximum temperature was located upstream of the center. Both results are in agreement with the analysis of [4 and 5]. Along the mirror plane symmetry it would be expected that azimuthal influences would be minimized (but not necessarily negligible). At the highest velocity, $U = 127.0$ cm/sec, the maximum gradients were transverse to the flow ($\theta = 90$ deg); at the lower velocities, the maximum gradients were in the range 120 deg $< \theta <$ 180 deg.

The results of these experiments indicated forced convection

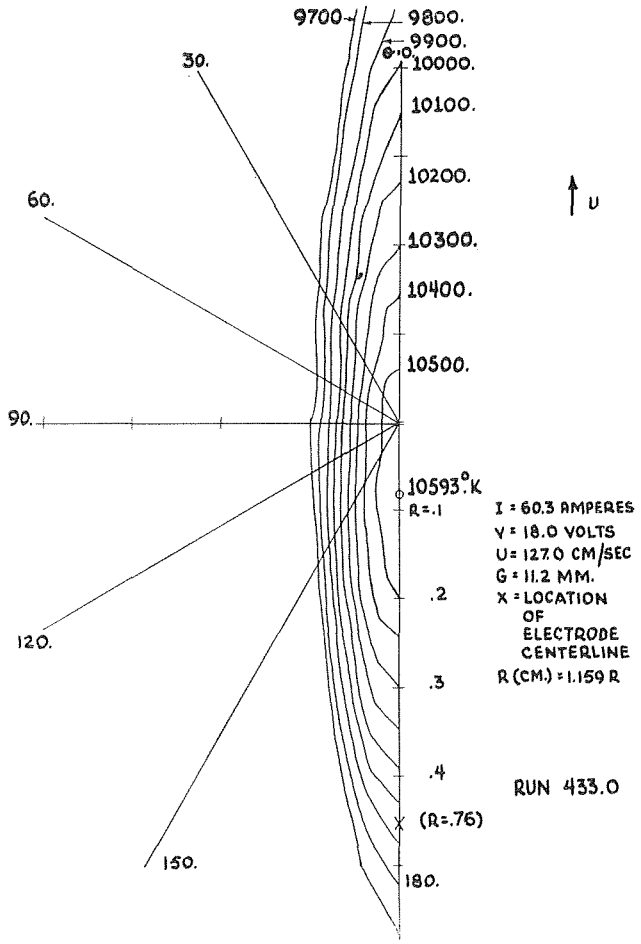

Fig. 11 Isotherm distribution

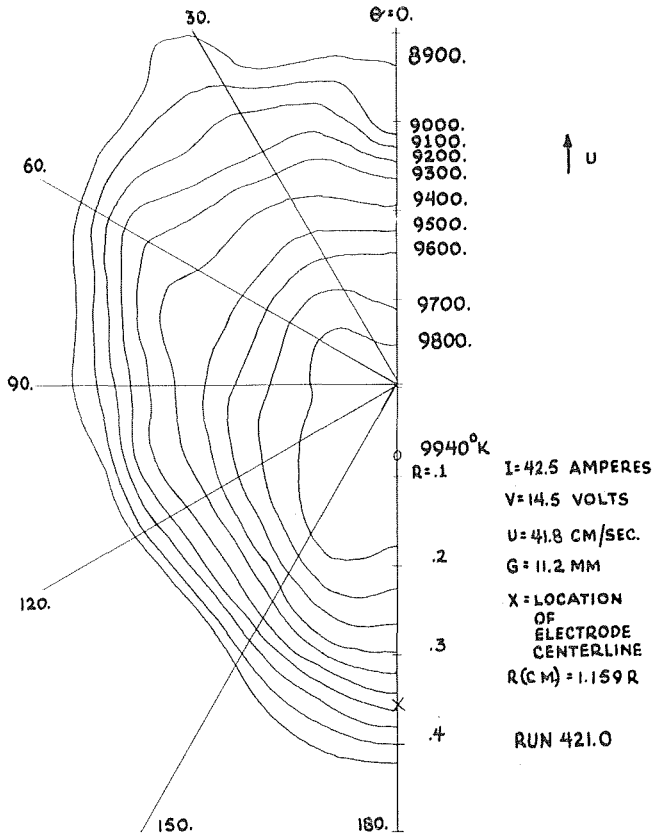

Fig. 12 Isotherm distribution

exerts profound influences upon the crossflow plasma; the effects include:

1 Change in the isotherm distributions from those associated with flow about a heated, blunt body to those about a heated, highly streamlined body. (The characteristic axial dimension increases and the characteristic transverse dimension decreases as velocity is increased.)

2 The isotherms generally become highly noncircular, with the major axis in the direction of flow. (Circular isotherms may be found over a relatively narrow range of conditions.)

3 Maximum values of the temperature gradients are not located along the mirror plane of symmetry; for high velocities, the maximum gradients are found in the transverse direction.

The effects of arc current (at constant velocity) upon the isotherm distributions are shown in Figs. 12, 8, and 13. The influence of convection is most pronounced at the lowest current, I = 42.5 amp, Fig. 12; the characteristics of the isotherm distribution are similar to those described earlier for U = 65.7 cm/sec, Fig. 9. As the current is increased, the arc is expected to become larger; this is observed upon consideration of a characteristic isotherm. The increased shielding of the plasma from the flow, as the current is increased, is also seen in Figs. 8 and 13 in the tendency for the isotherms to become more uniform upstream and downstream. It is important to note, however, that circular isotherms are not generally found at the highest current (I = 80.8 amp) probably as a result of the jet effects described earlier.

As a result of the combined influences of forced convection, jet effects, slight misalignments of the jets, electrode design, etc.,

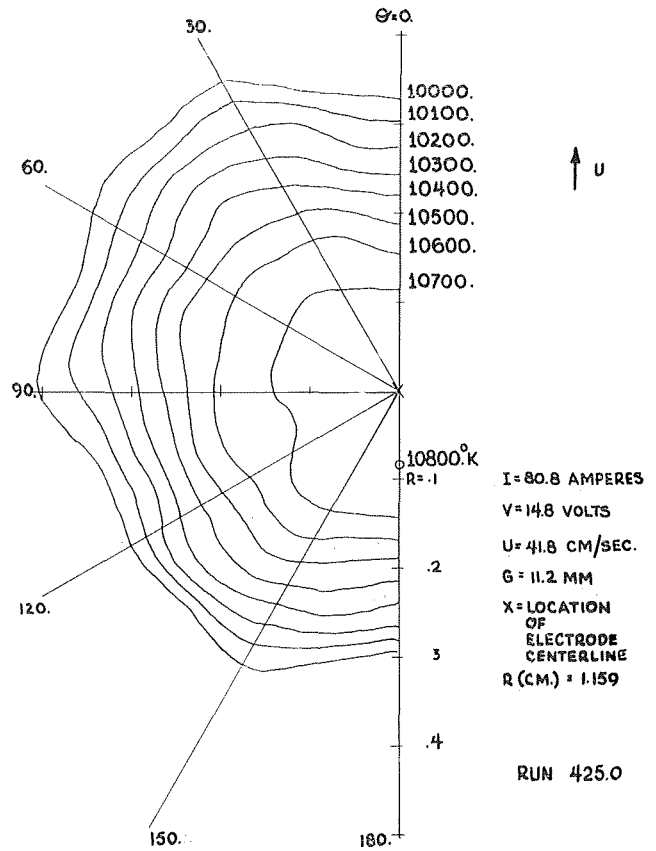

Fig. 13 Isotherm distribution

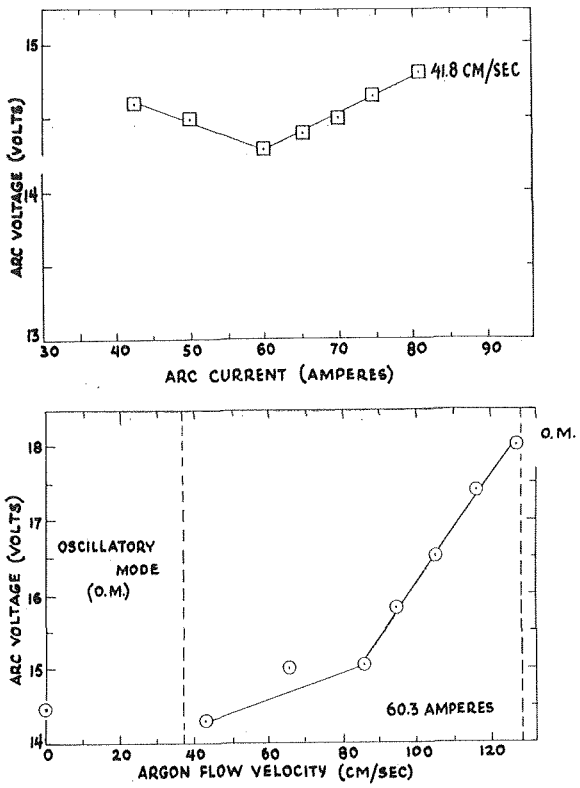

Fig. 14 Electrical arc characteristics

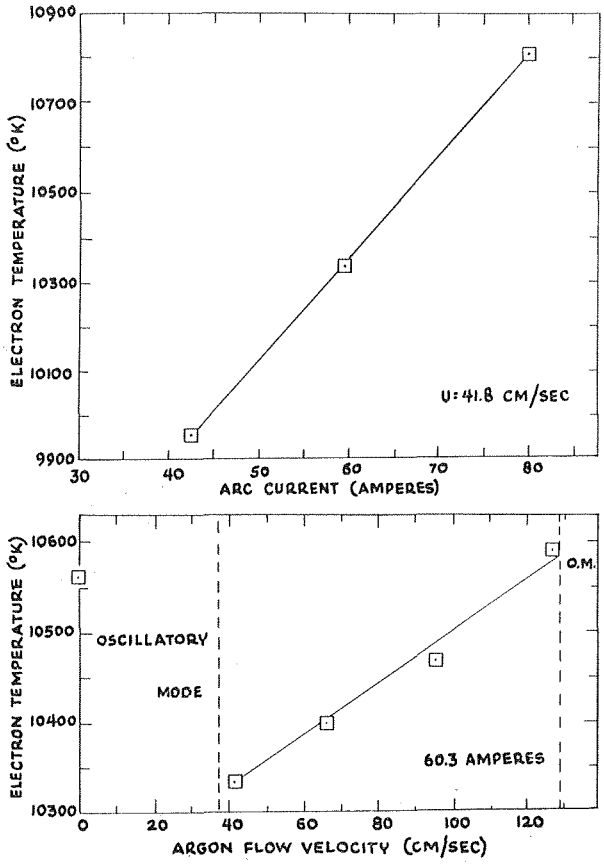

Fig. 15 Maximum electron temperature

noncircular isotherms may be expected to be present to a significant degree even at relatively high currents (for a given velocity).

A representative arc voltage-current characteristic (at constant velocity) is shown in the upper portion of Fig. 14; the variation observed is typical for such arc plasmas. Arc voltage as a function of velocity (at constant current) is shown in the lower portion of the figure. As a first approximation, the increase in voltage with velocity may be associated with the larger deflections of the plasma which occur as the velocity is increased. The relatively small changes in voltage observed at the lower velocities are consistent with the visual observations of the plasma, Fig. 6.

The maximum arc temperature as a function of current (at constant velocity) is shown in the upper portion of Fig. 15, and as a function of flow velocity (at constant current) in the lower portion of the figure. The increase in arc size with current, previously noted, and the observed increase in temperature with current are each consistent with analytical studies of coaxial plasma (e.g., [17]). The relation observed between arc current and velocity comes about as the result of the coupled interactions of the effects of plasma area, arc current and voltage, and velocity. Reduction of the cross-sectional area (and arc volume) would tend to increase arc temperatures (maintaining other parameters constant). Further, as the velocity is increased, convective interchange is increased (maintaining other parameters constant); this would compress the isotherms, effectively reducing the cross-sectional area, thus resulting in an increase of local temperatures. The relatively rapid decrease of the cross-sectional area (characterizing the plasma by an isotherm, e.g., $T = 9700$ K) with velocity (for $U \geq 65.7$ cm/sec) suggests that this is a primary factor in the observed increase of arc temperature in this regime. The relatively high temperature at zero speed probably is the result of the opposing influences of a somewhat large cross-sectional area (tendency to reduce temperatures) and the absence of through-flow (tendency to increase temperatures). The temperature at $U = 41.7$ cm/sec probably represents a transition condition.

Conclusions

The experiments have shown that forced convection (at constant arc current) exerts a profound influence upon the crossflow or blown arc. As the velocity is increased, the isotherm distributions and cross-sectional shapes change from those associated with the flow about a heated, blunt body to those about a heated, highly streamlined body. At high velocities, forced convection appears to completely penetrate the entire plasma, in the sense that none of the isotherms are circular in shape. The cross section is clearly noncircular, with the major axis in the direction of flow. As the velocity is increased, the major axis becomes elongated and the transverse dimension is reduced.

Although the effect of increasing current (at constant velocity) is to shield a central core region from the flow field, the isotherms (and cross sections) do not generally become circular at the higher currents; this comes about as a combination of the influences of the electrode jets, slight misalignments of the jets, electrode design, and velocity.

The experiments indicate clearly that future analytical studies of the crossflow arc must consider the azimuthal dependence of the parameters.

Acknowledgments

The authors wish to acknowledge the active interest of E. Soehngen and P. W. Schreiber, Aeronautical Research Laboratories, Wright-Patterson Air Force Base, and Dr. W. C. Roman, United Aircraft Research Laboratories; R. D. Anwyl, Eastman Kodak Company and the Company for providing guidance and films; L. Millholland, Jr., State University of New York at Buffalo for counsel and facilities for the photographic program;

Cornell Aeronautical Laboratory for providing a microdensitometer. A. J. Baker, State University of New York at Buffalo, contributed valuable assistance during many phases of the project. The research was partially supported by the United States Air Force Contract AF 33(615)-1797, the National Science Foundation Grant GK-1174, the Research Foundation of the State University of New York at Buffalo, and the Computing Center at the State University of New York at Buffalo. The Computing Center is partially supported by NIH Grant FR-00126 and NSF Grant GP-7318.

References

1 Meyers, T. W., and Roman, W. C., "Survey of Investigation of Electric Arc Interactions With Magnetic and Aerodynamic Fields," ARL 66-0184, 1966, Aerospace Research Laboratories, U. S. Air Force, Wright-Patterson Air Force Base, Ohio.

2 Benenson, D. M., Baker, A. J., and Cenkner, A. A., Jr., "Diagnostics on Steady-State Crossflow Arcs," *Transactions of the IEEE Power Apparatus and Systems*, Vol. PAS-88, 1969, pp. 513–521.

3 Benenson, D. M., Baker, A. J., and Cenkner, A. A., Jr., "Diagnostics on Steady-State Crossflow Arcs, I. Low Current," ARL 68-0109, 1968, Aerospace Research Laboratories, U. S. Air Force, Wright-Patterson Air Force Base, Ohio.

4 Thiene, P., "Convective Flexure of a Plasma Conductor," *Physics of Fluids*, Vol. 6, 1963, pp. 1319–1324.

5 Thiene, P., "Flexure of a Two-Dimensional Arc Under Forced Convection, AFOSR-TN-50-947, 1959, Air Force Office of Scientific Research.

6 Olsen, H. N., et al., "Investigation of the Interaction of an External Magnetic Field With an Electric Arc," ARL 66-0016, 1966, Aerospace Research Laboratories, U. S. Air Force, Wright-Patterson Air Force Base, Ohio.

7 Maldonado, C. D., and Olsen, H. N., "New Method for Obtaining Emission Coefficients From Emitted Spectral Intensities. Part II—Asymmetrical Sources," *Journal of the Optical Society of America*, Vol. 56, 1966, pp. 1305–1313.

8 Benenson, D. M., Naeher, C. H., and Gideon, J. B., "Oscillations of Electric Arcs in Argon Crossflow," *AIAA Journal*, Vol. 5, pp. 1517–1519.

9 Cenkner, A. A., "Steady-State Characteristics of a Crossflow Electric Arc," MS thesis, State University of New York at Buffalo, 1969.

10 Larrabee, R. D., "Spectral Emissivity of Tungsten," *Journal of the Optical Society of America*, Vol. 40, 1959, pp. 619–625.

11 "8620 Series Optical Pyrometer Manual, Double Adjustment Type," *Directions 77-1-0-3*, Issue 3, Leeds and Northrup Company, Philadelphia, Pa.

12 Duckworth, G. D., private communication.

13 Olsen, H. N., "The Electric Arc as a Light Source for Quantitative Spectroscopy," *Journal of Quantitative Spectroscopy and Radiative Transfer*, Vol. 3, 1966, pp. 305–333.

14 Gopalakrishna, K., "High Temperature Transport Properties of Argon Plasmas," Technical Report No. 29, 1967, Division of Engineering and Applied Physics, Harvard University.

15 Schreiber, P. W., private communication.

16 Schlichting, H., *Boundary Layer Theory*, McGraw-Hill, New York, 1960, pp. 319–326.

17 Prelewicz, D. A., and Benenson, D. M., "Nonsteady Concial Arcs in Fully Developed Plasma Flow," *AIAA Journal*, Vol. 5, 1967, pp. 1320–1324.

H. C. HOTTEL
Professor.

A. F. SAROFIM
Associate Professor.

I. A. VASALOS
Research Assistant.

W. H. DALZELL
Assistant Professor.

Department of Chemical Engineering,
Massachusetts Institute of Technology,
Cambridge, Mass.

Multiple Scatter: Comparison of Theory With Experiment

In the solution of the transport equation for scattering media it is usually assumed that the particles scatter independently, and that polarization effects may be neglected. The validity of these assumptions has been here tested by measurement of the bidirectional reflectance and transmittance of suspensions of monodisperse polystyrene spheres confined between two parallel glass slides, followed by comparison of the results with the values predicted from theory. For the range of conditions studied—particle diameters of 0.106 and 0.530μ, wavelengths of 0.436μ and 0.546μ, and optical thicknesses of 0.25–3000—the agreement between theory and experiment is excellent.

Introduction

Interest in problems as diverse as the transmission of solar radiation through the atmosphere and the oceans, the reflectance of pigmented surface coatings, and the conductance of powder or fibrous insulators has generated an enormous literature on multiple scatter through heterogeneous media. Most of this literature is devoted to the mathematics of solving the transport equation, or to a comparison of rigorous solutions with approximations such as the two-flux method rather than to an experimental determination of the range of applicability of available theory.

This paper presents complementary experimental and theoretical studies of the radiative properties of unidimensional suspensions of nonabsorbing but scattering spheres having perimeter-to-wavelength ratios in the range of practical interest and disposed in layers of thickness embracing both single-scatter and multiple-scatter phenomena. The transport equation used (see Appendix) does not include the effects of polarization, allowance for which would necessitate introduction of the Stokes parameters [1].[1] It is further assumed that the values of the absorption and scatter coefficients and of the phase function can be determined from the far-field single-scatter contributions of the individual particles within a unit volume—contributions given for spherical particles by the Mie equations [2]. This last assumption is justifiable when any volume dv large enough to contain many particles is still small compared to the system dimensions and when the particles within dv are far enough apart to act as independent scatterers. The objectives will be twofold; first, to test the validity of the assumptions regarding polarization effects and independent scatter and, second, to develop confidence in ability to predict the radiative properties of a well-defined scattering system entirely from theory. For the range of conditions over which the assumptions hold, the radiative properties of a scattering slab are defined entirely by the refractive indexes n_p and n_w of the particles and the dispersion medium, the perimeter-wavelength ratio $\pi d/\lambda$ where d is the particle diameter and λ is the wavelength (conventionally measured in vacuo), the number N_p of scattering particles per unit volume, the slab thickness L, and the refractive index variation at the boundaries of the slab.

Previous attempts to compare experiment with theory include those by Woodward [3] and Smart, et al. [4]. In both these studies, the bidirectional transmittance of latex particles was compared with values calculated using the Hartel approximation [5]. Good agreement between theory and experiment was obtained for optically thin systems, but the agreement became progressively worse as the optical thickness was increased. The lack of agreement at large optical thickness is due to error introduced by the Hartel approximation which, in the limit of an optically thick medium, predicts that the transmittance of a nonabsorbing, scattering slab approaches 0.5 rather than its true value of zero [6]. An additional uncertainty is introduced in Woodward's results by his neglect of the interface reflectance present in his experiments, a problem which was recognized by Smart, et al., and compensated for by a clever modification of their test cell. No reference will be made here to the semiempirical two-flux or Kubelka-Munk approximations since the effective scatter coef-

[1] Numbers in brackets designate References at end of paper.

Contributed by the Heat Transfer Division of The American Society of Mechanical Engineers and presented at the Winter Annual Meeting, Los Angeles, Calif., November 16–20, 1969. Manuscript received at ASME Headquarters, July 28, 1969. Paper No. 69-WA/HT-44.

ficients in these cannot be quantitatively related to the scatter cross section and phase function of a single particle but can only be determined experimentally.

Experimental Apparatus

Test Cell. The test cells were constructed from parallel standard microscope slides cemented with epoxy resin to a lucite frame. The cell faces were 5 cms sq, and the clearance between the inner glass surfaces was varied from 0.05–0.20 cms. The thickness of the slides was 0.15 cms.

Particle Suspensions. The particles studied were 0.106 and 0.530μ dia polystyrene latex suspensions produced by the Dow Chemical Company. The particle diameters, determined from electron micrographs, differed by 3–6 percent from the values supplied by the manufacturer. The suspensions were diluted with deionized millipore-filtered distilled water to the desired concentration range. The exact concentration was determined after a multiple-scatter run by evaporating under reduced pressure a known volume of the suspension and then weighing the residue.

Light Scattering Equipment. The bidirectional reflectance and transmittance were measured for the case of normal incidence only. The scattered radiation in this study is therefore independent of azimuthal angle, and its directional distribution can be obtained by a traverse in a single plane. The equipment consisted of (*a*) a mercury arc and optics to produce an unpolarized beam of 0.76-deg divergence and 0.12 cms image diameter at the sample cell, (*b*) an RCA 931A photomultiplier, and (*c*) optics to confine the received beam to 0.66-deg divergence angle. The state of polarization of the scattered radiation was measured by use of a Polaroid HN22 polarizer. The area viewed by the collector along the normal was 1.6 cms in diameter; it was made larger than the irradiated area in order to collect all the energy scattered in a given direction. Details of the equipment may be found in reference [7].

Mathematical Formulation

Determination of Scatter Coefficients. The Mie equations were used to evaluate the scatter cross section C_s and phase function for the different values of $\pi d/(\lambda/n_w)$, where (λ/n_w) is the wavelength in the aqueous dispersion medium, and for a refractive index ratio equal to n_p/n_w, that of polystyrene to that of water at the wavelength in question. (n's were interpolated from values in reference [8].) The scatter coefficient K_s was then equated to N_pC_s. Polystyrene is nonabsorbing in the visible, and the absorption coefficient is therefore zero. In order to simplify the solution of the transport equations the phase functions $p(\Theta)$ calculated from the far-field Mie equations were fitted by Legendre polynomial series, 6 and 14 terms being used for the 0.106μ and 0.530μ particles, respectively.

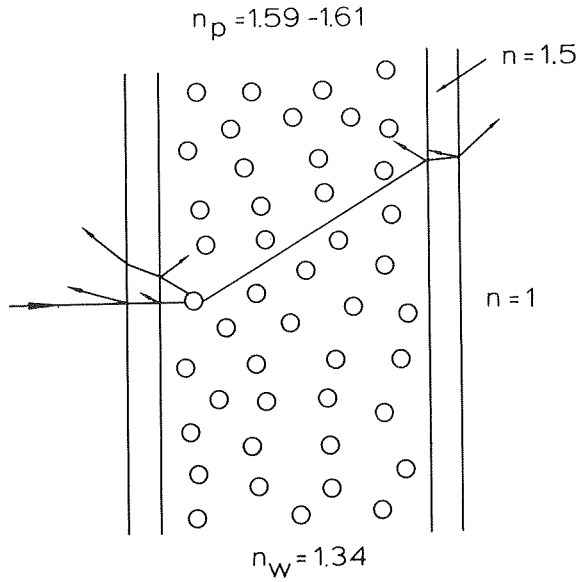

Fig. 1 Traces of contributions to reflectance and transmittance by beams that have been scattered once

Solution of Transport Equation. The transport equation was solved by the method of discrete ordinates (discrete conical sheets for polar symmetry) modified to allow for the double refraction and multiple reflection occurring at the glass interfaces of the test cell, Fig. 1.

General descriptions of the method are available in the literature [1, 9–11]; a summary of the method and a description of the treatment of the two-step change in refractive index at the boundaries are discussed in the Appendix. Based on the results [10] of an earlier study of the effect of number of ordinates on the accuracy of the calculated transmittances and reflectances, the scattered radiation from a volume element containing 0.106μ (0.530μ) particles was assumed to be concentrated into 20(40) discrete conical sheets.

Results and Discussion

Single Scatter. Previous investigators have observed discrepancies between the effective scattering diameters of particles and that observed in electron micrographs [12]. Single-scatter measurements were therefore performed to check the particle diameters in the particle suspensions as received. The measurements on optically thin suspensions of particles in a cylindrical

Nomenclature

a_k = weighting factor in Legendre polynomial series
C_s = scatter cross section of a particle
d = particle diameter
$i(\theta)$ = Mie scattering coefficients; $i_\perp(\theta)$, perpendicular component; $i_\parallel(\theta)$, parallel component
K_s = attenuation coefficient due to scatter
L = slab thickness
m = number of terms in Legendre polynomial series
n = refractive index of medium relative to vacuum, n_p = refractive index of particle, n_w = refractive index of aqueous phase of dispersion
N = number of abscissas used in integration formula
N_p = number of particles per unit volume
$p(\Theta)$ = phase function, normalized intensity distribution for single scatter
$P_k(\mu)$ = kth Legendre polynomial
PVC = percent volume concentration of particles
$\dot{Q}(\theta)$ = scatter energy flux at angle θ
R = hemispherical reflectance, R_D = diffuse component of hemispherical reflectance
T = hemispherical transmittance, T_D = diffuse component of hemispherical transmittance
v = volume
w_j = weighting factor in integration formula
θ = angle between scattered and incident beam, polar angle
Θ = angle between reference beam and inscattered beam
λ = wavelength measured in vacuo
ρ = reflectance of water-glass-air interface system, ρ_1 = reflectivity of water-glass interface, ρ_2 = reflectivity of glass-air interface
μ = cosine of polar angle
τ = optical depth in mean free paths, $\tau_1 \equiv K_sL$
Ω = solid angle

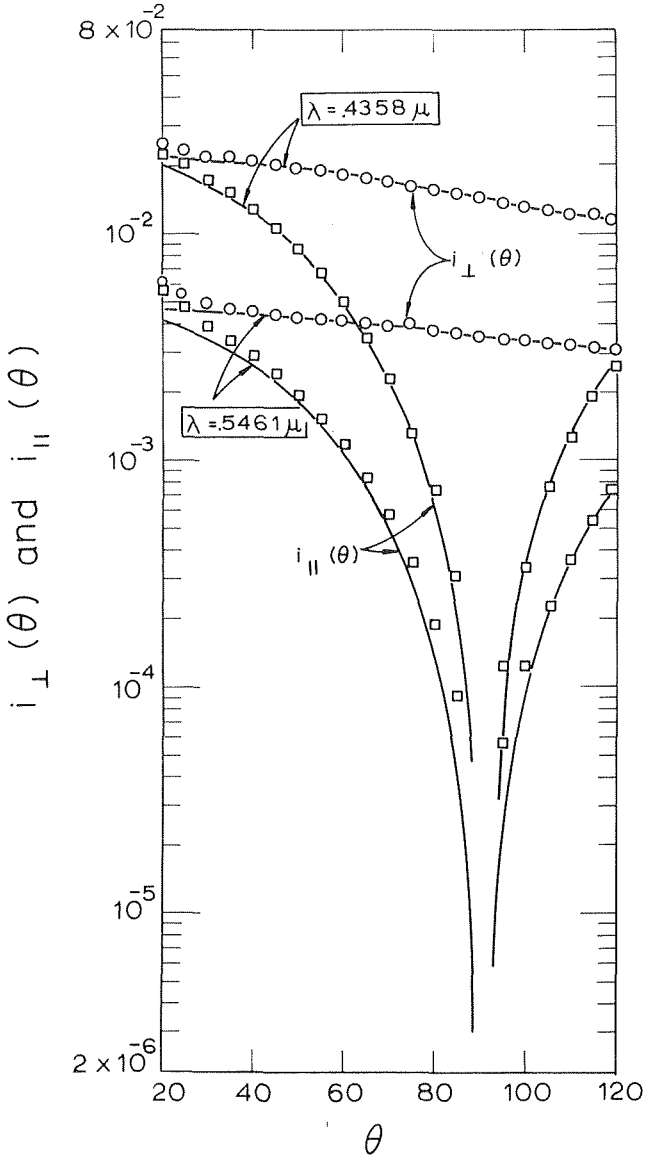

Fig. 2 Mie scattering coefficients, $i_\perp(\theta)$ and $i_\parallel(\theta)$, for 0.106μ dia spheres. Upper pair of curves, $\lambda = 0.436\mu$, $n_p/n_w = 1.19$, $\pi d/(\lambda/n_w) = 1.024$; lower pair, $\lambda = 0.546\mu$, $n_p/n_w = 1.20$, $\pi d/(\lambda/n_w) = 0.815$. Data points experimental results, solid lines theoretical.

cell were corrected [13] for reflectance at the cell walls and then used to calculate the Mie scattering coefficients, $i_\perp(\theta)$ and $i_\parallel(\theta)$. These are so defined that, for an incident beam of unit intensity and small divergence, the rate $\dot{Q}(\theta)$ at which energy is scattered into a small solid angle about θ, per unit solid angle of the incident and scattered beams, is given by

$$\dot{Q}(\theta) = (1/2)(\lambda/2\pi)^2[i_\perp(\theta) + i_\parallel(\theta)]$$

The values of $i_\perp(\theta)$ and $i_\parallel(\theta)$ calculated from the scatter measurements are compared with the predictions of the Mie equations in Figs. 2 and 3 for the two particle sizes ($d = 0.106$ and 0.530μ) and the two wavelengths ($\lambda = 0.436$ and 0.546μ) studied. The agreement between theory and experiment is considered to be good, the small discrepancies resulting from a combination of the following factors:

1 The spread in particle sizes.

2 The finite bandwidth of the monochromatic filter (65Å at half-peak transmission).

3 Finite source (0.76 deg) and collector (0.66 deg) angles.

4 Any difference in the effective diameter for scattering and that observed in electron micrographs.

5 Spurious scatter introduced by the apparatus, which becomes significant in the angular regions in which the scattered intensities are very low.

Estimation of the errors introduced by the different factors indicates that the spread in particle sizes (factor 1) is largely responsible in this study for the deviations between theory and experiment. (Failure to have adjusted the particle size from that reported by the supplier to that given by the electron microscope would have produced unacceptably large deviations.)

Multiple Scatter. Measurements were made of the directional distribution and state of polarization of scatter by nonabsorbing particles for perimeter-to-wavelength ratios of 0.81–5.1 and optical thickness $K_sL(\equiv\tau_1)$ of 0.25–3000; the fixed parameters were particle refractive index (1.59–1.61), refractive index of the dispersion phase (1.34), and the refractive index of the confining glass slides (1.5).

Polarization effects were found to be small, as illustrated in Fig. 4, in which the components of polarization of the bihemispherical transmittance and reflectance are presented for the case of normal incidence for two optical thicknesses. (An abscissa

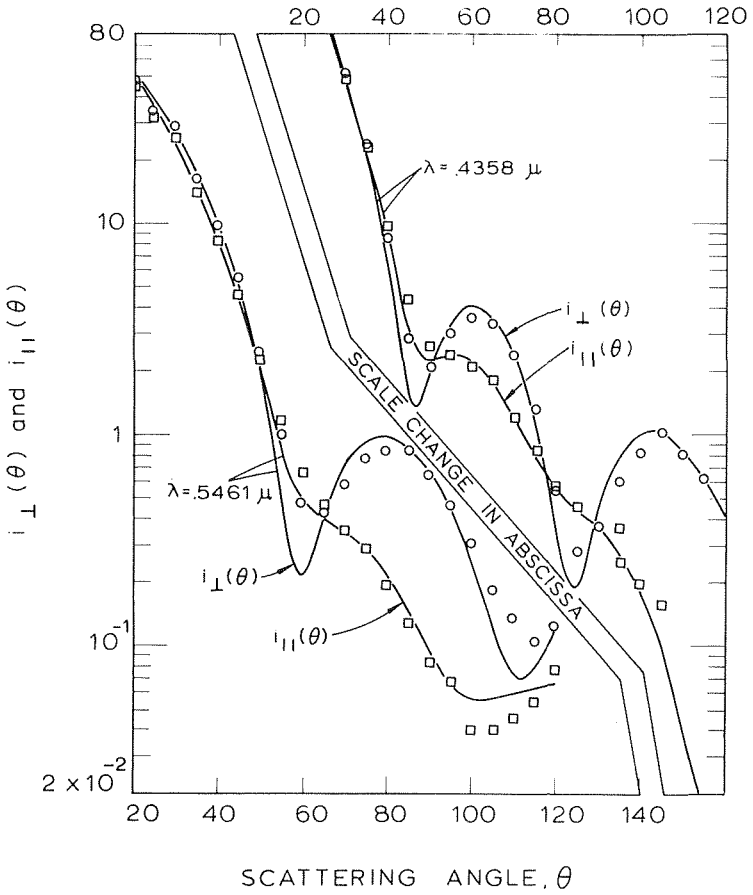

Fig. 3 Mie scattering coefficients, $i_\perp(\theta)$ and $i_\parallel(\theta)$, for 0.530μ dia spheres. Left pair of curves, $\lambda = 0.436\mu$, $n_p/n_w = 1.19$, $\pi d/(\lambda/n_w) = 5.12$; right pair, $\lambda = 0.546\mu$, $n_p/n_w = 1.20$, $\pi d/(\lambda/n_w) = 4.09$. Data points experimental results, solid lines theoretical.

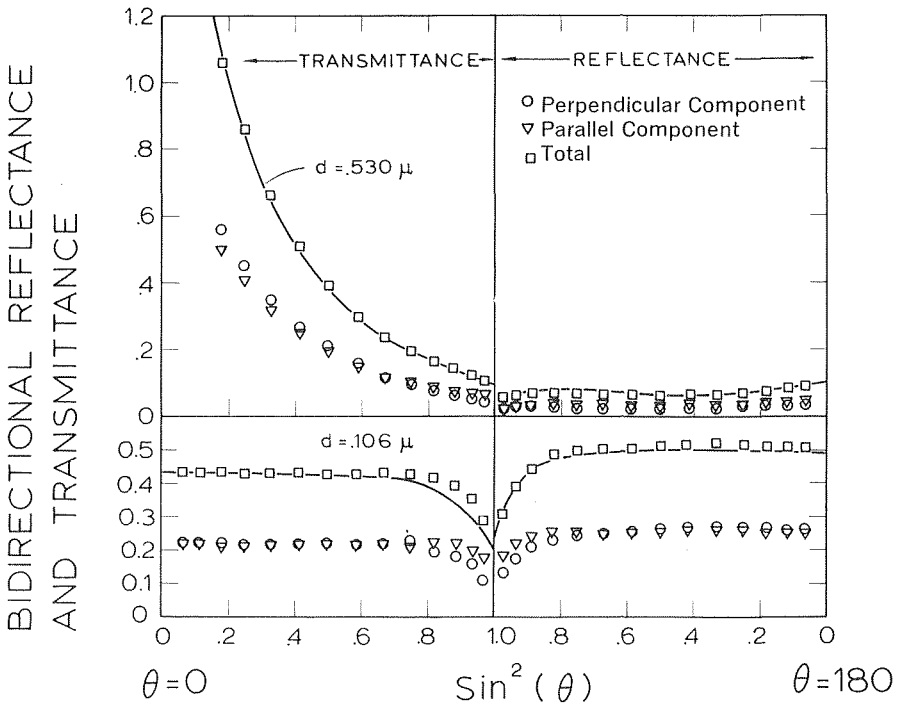

Fig. 4 Components of polarization of bidirectional reflectance and transmittance of polystyrene latex: $L = 0.147$ cms, $\lambda = 0.436\mu$. Bottom figure, particle diameter $d = 0.106\mu$, percent volume concentration (PVC) $= 3.48 \times 10^{-3}$, $\tau_1 = 2.80$. Top figure, $d = 0.530\mu$, PVC $= 1.40 \times 10^{-4}$, $\tau_1 = 1.091$. Data points experimental results, solid lines theoretical.

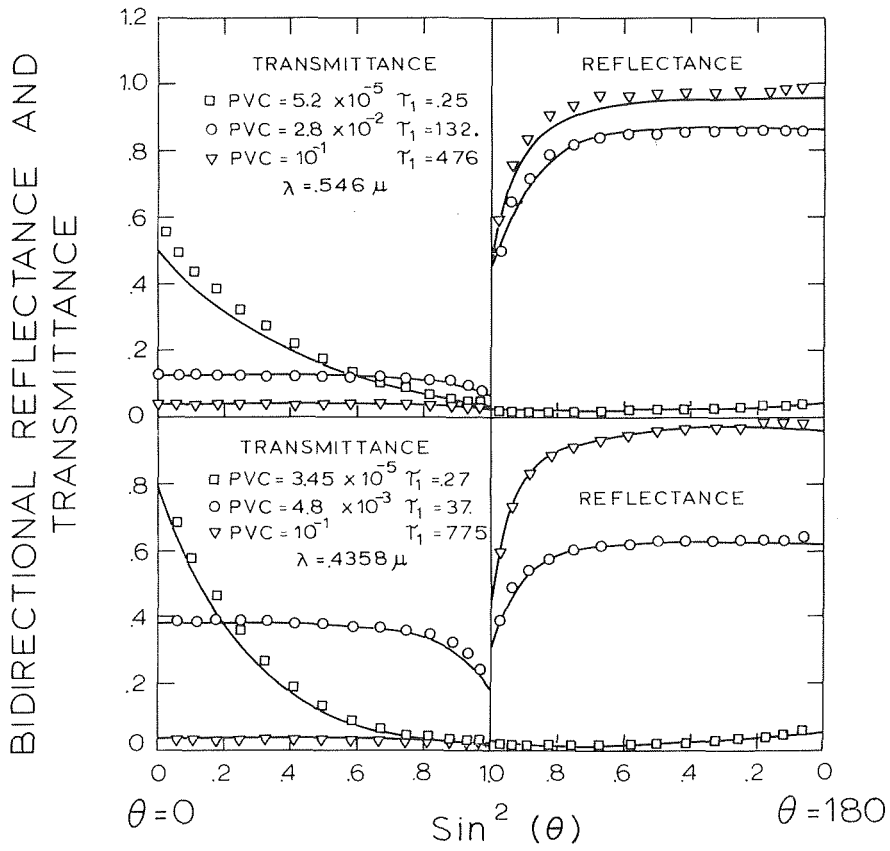

Fig. 5 Bidirectional reflectance and transmittance as a function of the percent volume concentration of 0.530μ polystyrene spheres, L = 0.147 cms. Data points experimental results, solid lines theoretical. Top family of curves, λ = 0.546μ, $\pi d/(\lambda/n_w)$ = 4.09. Bottom family, λ = 0.436μ, $\pi d/(\lambda/n_w)$ = 5.12.

of $\sin^2\theta$ is selected to give equal-area weightings to equal energy increments.) Theoretical values, containing *no* adjustable parameters but based on the assumptions that polarization effects may be ignored and that the particles scatter independently, are shown as solid lines; they can be seen to constitute an excellent representation of the experimental values. These results support the conclusion that polarization effects need not be included in the calculations of radiative transfer in the presence of multiple scatter.[2] The minimum distance of separation between particles here is evidently large enough to satisfy the criteria for independent scatter, which are tentatively suggested as clearances between particles exceeding 0.3 wavelengths [13] and clearance-to-diameter ratios exceeding 0.4 [13, 14]. The consequences of closer spacings between particles will appear in a later paper.

Additional evidence of the good agreement to be expected between calculated and measured values of the energy scatter is presented in Fig. 5 which includes results for two values of $\pi d/\lambda$ at each of three optical thicknesses. It is to be emphasized that the theoretical development here, unlike the two-flux method, contains no adjustable parameters.

A summary of the results of the integrated diffuse components of reflectance R_D and transmittance T_D (excluding the energy spikes along θ = 0 deg and 180 deg) is shown for a particle diameter of 0.530μ and a wavelength of 0.436μ in Fig. 6. The data points correspond to the measured values; nonscattered contributions to R and T are omitted from both measured and calculated values. The contribution T_D to the total transmittance is seen to go through a maximum at an optical density of about 3. Similar agreement between experiment and theory was obtained for the other particle size and wavelength studied but agreement would have been poor if allowance had not been made for suspension-glass and glass-air interfaces [10] which trap radiation scattered to angles of total internal reflection.

The foregoing generalizations on the relative unimportance of polarization effects in multiple-scatter problems were based on results that encompassed the entire range of optical thickness of interest and a $\pi d/\lambda$ range of 0.81–5.1. From consideration of the state of polarization for single scatter, it is expected that polarization effects will decrease with increasing particle size; consequently, the generalization of this study can be extended to larger particles but there is question as to their validity for $\pi d/\lambda$'s smaller than 0.81. In order to estimate the error in the limit of very small particles, the exact calculations by Coulson, et al. [16], on Rayleigh scatterers ($\pi d/\lambda < 0.3$) have been compared, for an optical thickness of one, normal incidence, and no reflection at the boundaries, with calculations in which polarization effects were neglected. Fig. 7 shows the differences between the bidirectional transmittance and reflectance obtained with (solid line) and without allowance (dashed line) for polarization; however, the mean transmittances and reflectances as given by the areas under the curves are essentially equal for the two cases. Thus, under the most extreme conditions, the differences between the approximate and more rigorous analysis is seen to be restricted to the directional distribution of the energy transferred and not to the total amount.

[2] Two polarization effects, however, are noticed in the results. The greater magnitude of the perpendicular than the parallel component, which is so noticeable when the optical thickness is vanishingly small (see Fig. 2), is still observable though small at an optical thickness of 1.09 (Fig. 4, top half) *if* observations are made at small angles θ. But at large angles ($\sin^2\theta = 1$; θ = 90 deg) the perpendicular component is exceeded by the parallel one because the boundary internal reflectance for the latter component is less.

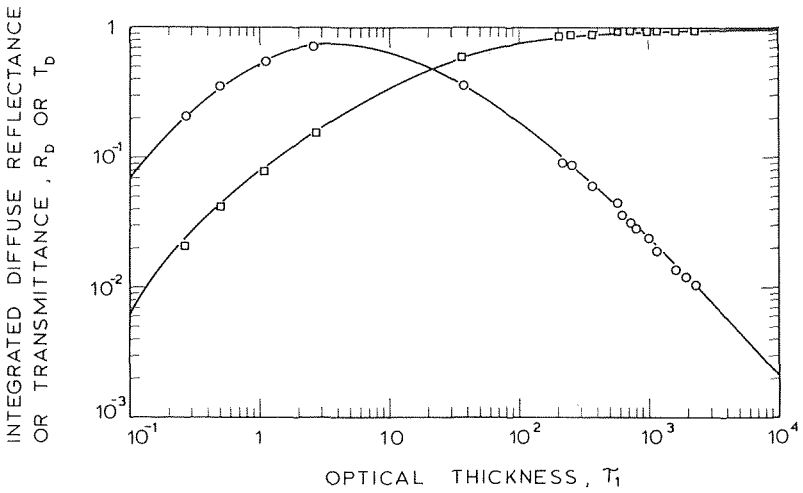

Fig. 6 Integrated diffuse reflectance (squares) and transmittance (circles) as a function of optical thickness. Data points experimental results, solid lines theoretical. $\pi d/(\lambda/n_w) = 5.12$.

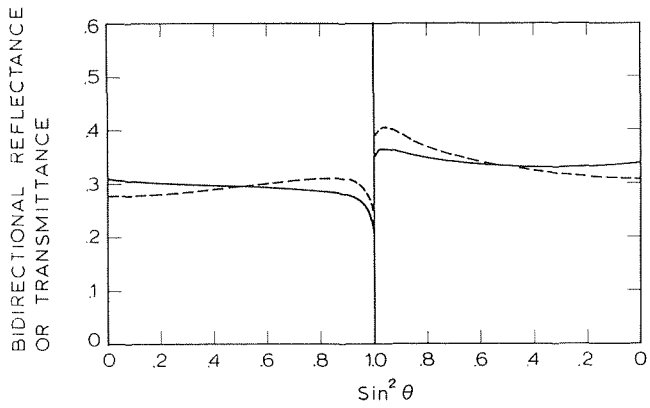

Fig. 7 Bidirectional transmittance and reflectance calculated with (solid line) and without (dashed line) allowance for polarization. Rayleigh scatter, $\tau_1 = 1.0$.

Conclusions

The radiative properties of particle suspensions in which the clearance between particles, assumed uniformly distributed, exceeds 0.3 wavelength and in which the ratio of clearance to diameter exceeds 0.4 may be calculated with confidence from theory. The Mie equations provide the single-scatter characteristics and the solution to the transport equation yields adequate allowance for multiple scatter. Polarization effects can generally be neglected.

Acknowledgment

Partial support for these studies by the National Science Foundation under Grant GK-220 and by the Godfrey L. Cabot Solar Energy Fund is gratefully acknowledged. The computations were performed in part at the M.I.T. Information Processing Center.

References

1 Chandrasekhar, S., *Radiative Transfer*, Oxford University Press, London, 1950.

2 Mie, G., "Beiträge zur Optik trüber Medien, speciell kolloidalen Metullösungen," *Ann. d. Physik*, Vol. 25, 1908, pp. 377–445.

3 Woodward, D. H., "Multiple Light Scattering by Spherical Dielectric Particles," *Journal of the Optical Society of America*, Vol. 54, 1964, pp. 1325–1331.

4 Smart, C., et al., "Experimental Study of Multiple Light Scattering," *Journal of the Optical Society of America*, Vol. 55, No. 8, 1965, pp. 947–955.

5 Hartel, W., "Zur Theorie der Lichtstreuung durch trübe Schichten, besonders Trübgläser," *Licht.*, Vol. 10, 1940, pp. 141–143 and 232–234.

6 Orchard, S. E., "Multiple Scattering by Spherical Dielectric Particles," *Journal of the Optical Society of America*, Vol. 55, No. 6, 1965, p. 737.

7 Fahimian, E. J., "Scattering of Radiation by Particle Layers," PhD thesis in Chemical Engineering, M.I.T., 1967.

8 *American Institute of Physics Handbook*, 1st ed., McGraw-Hill, New York, 1957.

9 Love, T. J., *Radiative Heat Transfer*, Merrill Publishing Co., Columbus, Ohio, 1968.

10 Hottel, H. C., et al., "Radiative Transfer in Anisotropically Scattering Media: Allowance for Fresnel Reflection at the Boundaries," JOURNAL OF HEAT TRANSFER, TRANS. ASME, Series C, Vol. 90, 1968, pp. 56–62.

11 Hottel, H. C., and Sarofim, A. F., *Radiative Transfer*, McGraw-Hill, New York, 1967.

12 Kratohvil, J. P., and Smart, C., "Absolute Angular Intensity Measurements on Mie Scatterers," *Journal of Colloid and Interface Science*, Vol. 20, 1965, pp. 875–892.

13 Vasalos, I. A., "Effect of Particle Separation on the Optical Properties of Dense Polystyrene Latices," PhD thesis in Chemical Engineering, M.I.T., 1969.

14 Churchill, S. W., Clark, G. C., and Sliepcevich, C. M., "Light Scattering by Very Dense Monodispersions of Latex Particles," *Discussions of the Faraday Society*, No. 30, 1960, 192 pp.

15 Sarofim, A. F., Hottel, H. C., and Fahimian, E. J., "Scattering of Radiation by Particle Layers," *AIAA Journal*, Vol. 6, 1965, pp. 2262–2266.

16 Coulson, K. L., Dave, J., and Sekera, Z., "Tables Related to Radiation Emerging From a Planetary Atmosphere With Rayleigh Scattering," University of California Press, Los Angeles, Calif., 1960.

APPENDIX

Formulation of Transport Equation and Boundary Conditions

The transport equation is formulated for the scattered radiation component only, with the contribution from the attenuated boundary-incident flux treated as an energy source term. On this basis and for the conditions of the present study—plane parallel dispersions, conservative scatter, normal incidence of primary beam, and interface reflection—the equation of transport takes the form

$$\mu \frac{dI(\tau, \mu)}{d\tau} = -I(\tau, \mu) + \frac{1}{2\pi} \int_{-1}^{1} I(\tau, \mu') \int_{2\pi} p(\Theta) d\psi d\mu'$$

(a) (b)

$$+ \frac{(1 - \rho)e^{-\tau}}{1 - \rho^2 e^{-2\tau_1}} \frac{p(\theta)}{4\pi}$$

(c)

$$+ \frac{\rho(1 - \rho)e^{-(2\tau_1 - \tau)}}{1 - \rho^2 e^{-2\tau_1}} \frac{p(180 - \theta)}{4\pi}$$

(d)

where $I(\tau, \mu)$ is the intensity of scattered radiation (i.e., exclusive of the transmitted component of the radiation incident on the boundaries) at an optical thickness τ and an angle θ with axis, $\mu = \cos\theta$, Θ is the angle between the reference beam and a secondary beam of intensity $I(\tau, \mu')$ that is partially scattered into the reference beam; ψ and μ' are the azimuthal angle and the cosine of the polar angle associated with the secondary beam; τ_1 is the optical thickness of the entire slab; ρ is the overall reflectance of the air-glass-water interface system, including multiple reflection within the glass slide. The term on the left-hand side of the equation is the rate of change in intensity with distance, those on the right represent (*a*) the attenuation due to scatter out of the reference beam, (*b*) the contribution, by scatter into the reference beam, from beams that have been scattered one or more times, (*c*) the scatter into the reference beam out of the attenuated components of the incident beam, including the multiply reflected components, that are directed along the positive x-axis, and (*d*) the scatter into the reference beam of the attenuated components of the incident beam that are directed along the negative x-axis. Replacement of the phase function by a m-term Legendre polynomial, integration over azimuthal angle, and division of the radiation field into conical streams in the directions μ_i yields N linear ordinary differential equations of the form

$$\mu_i \frac{dI(\tau, \mu_i)}{d\tau} = -I(\tau, \mu_i) + \frac{1}{N}\sum_{j=1}^{N} w_j I(\tau, \mu_j) \sum_{k=1}^{m} a_k P_k(\mu_i) P_k(\mu_j) + \frac{(1-\rho)e^{-\tau}}{1-\rho^2 e^{-2\tau_1}} \sum_{k=1}^{m} \frac{a_k P_k(\mu_i)}{4\pi} + \frac{\rho(1-\rho)e^{-(2\tau_1-\tau)}}{1-\rho^2 e^{-2\tau_1}} \sum_{k=1}^{m} \frac{a_k P_k(-\mu_i)}{4\pi}$$

where w_j represents the weighting function associated with a particular integration formula, and $P_k(\ )$ is the kth term in the Legendre polynomial series description of the phase function. The boundary conditions are given by

$$I(0, \mu_i) = \rho(\mu_i) I(0, -\mu_i)$$
$$I(\tau_1, -\mu_i) = \rho(\mu_i) I(\tau_1, \mu_i)$$

where $\rho(\mu_i)$ is the reflectance of the water-glass-air interface for the direction (μ_i) in question; $\rho(\mu_i)$ is unity for angles of total internal reflectance. The water-glass-air interface reflectance ρ can be expressed in terms of the reflectivities ρ_1 and ρ_2 of water-glass and air-glass interfaces.

$$\rho = \frac{\rho_1 + \rho_2 - 2\rho_1\rho_2}{1 - \rho_1\rho_2}$$

where ρ_1 and ρ_2 are obtained from Fresnel's equation:

$$\rho_1 \text{ or } \rho_2 = \frac{1}{2}\left\{\left[\frac{(n^2 - \sin^2\theta)^{1/2} - \cos\theta}{(n^2 - \sin^2\theta)^{1/2} + \cos\theta}\right]^2 + \left|\frac{n^2\cos\theta - (n^2 - \sin^2\theta)^{1/2}}{n^2\cos\theta + (n^2 - \sin^2\theta)^{1/2}}\right|^2\right\}$$

where for the water-glass interface n equals the ratio of refractive indexes of water and glass, and θ is the angle with the normal made by the beam in the water phase; and where for glass-air interface n equals the ratio of refractive indexes of glass and air, and θ is the angle made with the surface normal by the beam in the glass phase. The refraction of the beam across an interface is given by Snell's law

$$n_1 \sin\theta_1 = n_2 \sin\theta_2$$

The solution of the set of simultaneous equations with the foregoing set of boundary conditions introduces no difficulty in principle; special attention, however, must be taken to prevent roundoff errors from accumulating for the cases of large values of the number of ordinates N or the optical thickness τ.

The unscattered contributions T_u and R_u to the integrated system transmittance and reflectance are given by

$$T_u = \frac{(1-\rho)^2 e^{-\tau_1}}{1 - \rho^2 e^{-2\tau_1}}$$

and

$$R_u = \rho(1 + T_u e^{-\tau_1})$$

To these must be added T_D or R_D (see Fig. 6) to obtain the total transmittance or reflectance.

J. H. LIENHARD
Professor. Mem. ASME

KAUO-HWA SUN[2]
Research Assistant.

University of Kentucky,
Lexington, Ky.

Effects of Gravity and Size Upon Film Boiling From Horizontal Cylinders[1]

The vapor removal mechanism during film boiling on horizontal cylinders has been observed over an 81-fold variation of gravity and a tenfold variation of radius. These measurements are the basis for an assessment of prior predictions of wavelength. A significant low-gravity transition point in the vapor removal mechanism is identified and explained. "Best" formulas are recommended for the prediction of the wavelength and the minimum heat flux. These depend upon a single parameter which represents both size and gravity.

Introduction

THIS paper will report the first results of a NASA supported study of boiling under variable gravity. In it we shall present new data to test previously predicted bubble departure wavelengths during film boiling on horizontal cylinders. This data will embrace a much higher range of size and gravity than earlier data have. We shall also consider the minimum heat-flux prediction that depends upon this wavelength.

In 1963 Lienhard and Wong [1][3] developed expressions for the behavior of film boiling on horizontal cylinders. On the basis of an assumed interface configuration shown in Fig. 1(*a*) they showed that the frequency of bubble departure was the following real number,[4] $(i\omega)$:

$$(i\omega) = \left[kg \frac{\rho_f - \rho_g}{\rho_f + \rho_g} - \frac{\sigma k^3}{\rho_f + \rho_g} + \frac{\sigma k}{2(\rho_f + \rho_g)R^2} \right]^{1/2} \quad (1)$$

and they predicted that the dominant wavelength, λ_d, during film boiling could be obtained by maximizing this frequency. The result was:

$$\lambda_d = \frac{2\sqrt{3}\pi}{\sqrt{\dfrac{g(\rho_f - \rho_g)}{\sigma} + \dfrac{1}{2R^2}}} \quad (2)$$

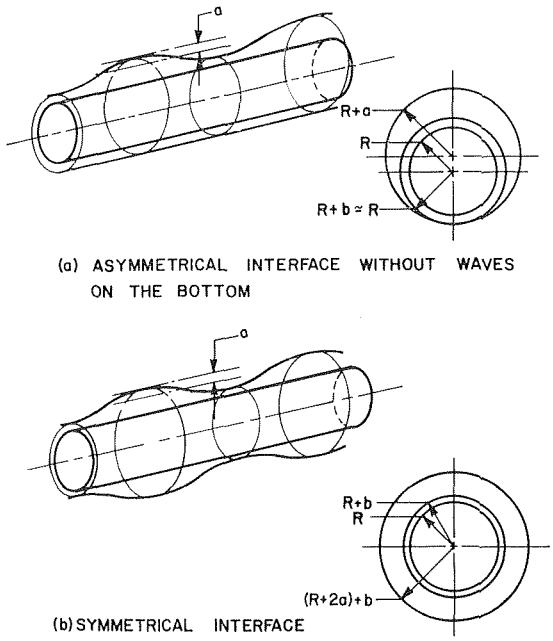

Fig. 1 Possible configurations of the liquid-vapor interface around horizontal cylindrical heaters during film boiling

Finally, they showed that by paraphrasing Zuber's [2] and Berenson's [3] arguments they could use equation (2) as the basis for a prediction of the minimum boiling heat flux, q_{min}.

$$q_{min} = (0.515)(0.09) \left\{ \sqrt{\frac{3}{2}} \frac{\rho_g h_{fg}}{R} \left[2g \frac{\rho_f - \rho_g}{\rho_f + \rho_g} + \frac{\sigma}{(\rho_f + \rho_g)R^2} \right]^{1/2} \left[\frac{g(\rho_f - \rho_g)}{\sigma} + \frac{1}{2R^2} \right]^{-3/4} \right\} \quad (3)$$

where the constant 0.515 was obtained experimentally using

---

[1] This work was supported under NASA Grant NGR/18-001-035.

[2] Present address: Research Assistant, Mechanical Engineering Department, University of California, Berkeley, Calif.

[3] Numbers in brackets designate References at end of paper.

[4] Explanations of symbols not defined in context will be found in the Nomenclature section.

Contributed by the Heat Transfer Division and presented at the Winter Annual Meeting, Los Angeles, Calif., November 16–20, 1969, of THE AMERICAN SOCIETY OF MECHANICAL ENGINEERS. Manuscript received by Heat Transfer Division, September 16, 1968; revised manuscript received June 9, 1969. Paper No. 69-WA/HT-12.

seven data points for isopropanol and the factor 0.09 is Berenson's constant.

The following transformations will put equations (1), (2), and (3) into convenient dimensionless form: We first introduce a dimensionless wavelength,

$$\Lambda \equiv \lambda_d/\lambda_{dF} \tag{4}$$

where λ_{dF} is Bellman's and Pennington's [4] value for a flat plate,

$$\lambda_{dF} = \frac{2\sqrt{3}\pi}{\sqrt{\dfrac{g(\rho_f - \rho_g)}{\sigma}}} \tag{5}$$

We next introduce a dimensionless frequency,

$$\Omega \equiv i\omega[\sigma/g^3(\rho_f - \rho_g)]^{1/4} \tag{6}$$

and we finally introduce a dimensionless radius,

$$R' \equiv R/[\sigma/g(\rho_f - \rho_g)]^{1/2} \tag{7}$$

In effect, R' compares heater radius with the wavelength, λ_{dF} and its numerical value is $2\sqrt{3}\pi$ when they are equal to one another. The square of R' is like a "Bond number" and it serves to compare the gravity forces removing bubbles from a heater with the surface forces that hold them on. Since such dimensionless groups as R' and R'^2 have been used by Lord Rayleigh and by Laplace before him, they practically have their roots in antiquity. We shall simply call R' the dimensionless radius and honor only its present application.

Under these transformations, equation (1) becomes

$$\Omega^2 = \frac{1}{\sqrt{3}\Lambda_{LW}}\left\{1 + \frac{1}{2R'^2} - \frac{1}{3\Lambda_{LW}^2}\right\}\left\{\frac{\rho_f - \rho_g}{\rho_f + \rho_g}\right\} \tag{1a}$$

where in the present applications $(\rho_f - \rho_g)/(\rho_f + \rho_g) \simeq 1$ in all cases. Equation (2) becomes

$$\Lambda_{LW} = \sqrt{\frac{R'^2}{R'^2 + 1/2}} \tag{2a}$$

where the subscript LW has been introduced to distinguish the Lienhard-Wong results from those of other authors we wish to consider. Equation (3) becomes

$$q_{min} = 0.515\, q_{min_F} f(R') \tag{3a}$$

where q_{min_F} is Berenson's flat plate value

$$q_{min_F} = 0.09\rho_g h_{fg}\left[\frac{\sigma g(\rho_f - \rho_g)}{(\rho_f + \rho_g)^2}\right]^{1/4} \tag{8}$$

and

$$f(R') = \left[\frac{18}{R'^2(2R'^2 + 1)}\right]^{1/4} \tag{9}$$

Data [1] in the range of dimensionless radius, R', from 0.017 to 0.25 showed that equation (2a) predicted wavelengths about 25 percent too low. In the discussion of [1], the authors pointed out that this could probably be improved by including b in the calculation. Two subsequent attempts were accordingly made to improve the accuracy of equation (2a). The first was by Siegel and Keshock [5] who assumed that the interface was shaped as shown in Fig. 1(b)[5] instead of Fig. 1(a), and who retained the minimum blanket thickness, b, in the equation. They obtained

$$\Lambda_{SK} = \sqrt{\frac{R'^2}{R'^2 + (1 + b/R)^{-2}}} \tag{10}$$

It is a simple matter to modify equation (2a) for a finite vapor blanket. We need only to increase R to $(R + b)$ in equation (2) and carry out the nondimensionalization. The result is

$$\Lambda_{LW} \quad \text{with} \quad \left(1 + \frac{b}{R}\right) = \sqrt{\frac{R'^2}{R'^2 + 1/[2(1 + b/R)^2]}} \tag{11}$$

While Siegel and Keshock did not evaluate b or make experimental comparisons, Baumeister and Hamill [6], succeeded in deriving an expression for b two years later. They used an assumption that the heat transfer must be maximum, subject to appropriate constraints, and their configurational assumption differed radically from those proposed in Fig. 1. Instead of taking the interface to be wavelike they imagined a sequence of spherical domes connected by annular passages. They obtained

$$\Lambda_{BH} = \frac{2}{\sqrt{3}\pi}\left\{\frac{\sqrt{1 + 6R'^2(1 + b/R)^2} - 1}{\sqrt{R'^2(1 + b/R)^2}}\right\} \tag{12}$$

Their analysis also permitted them to compute $(1 + b/R)$;

[5] This point might not be entirely clear in reference [5] which includes both the left-hand sketch in Fig. 1(a) along with the right-hand sketch in Fig. 1(b). The analysis in [5] is based on Fig. 1(b), however.

Nomenclature

a = amplitude of wave during film boiling

b = minimum thickness of vapor blanket during film boiling

c_v = constant volume specific heat of vapor

g = acceleration of a body in a force field

g_e = acceleration of a body in an earth-normal gravity field

h_{fg} = latent heat of vaporization

h_{fg}^+ = corrected latent heat; see equation (14)

$i = \sqrt{-1}$

k = thermal conductivity of vapor; or wave number, $2\pi/\lambda_d$ (identifiable by context)

M = molecular weight

p = pressure

p_c = critical pressure

p_r = reduced pressure, p/p_c

$\mathcal{P}$ = Parachor, $M\sigma^{1/4}/(\rho_f - \rho_g)$

q, q_{min} = heat flux; subscript min denotes the minimum boiling heat flux

q_{min_F} = Zuber's predicted minimum heat flux for a flat plate

$(q_{min})_r$ = reduced minimum heat fluxes, q_{min}/α

R = radius of a cylindrical heater

R' = dimensionless radius, $R/[\sigma/g(\rho_f - \rho_g)]^{1/2}$

R^0 = the ideal gas constant

T_c = critical temperature

ΔT = heater temperature minus saturation temperature

α = correlation factor, $g^{1/4}p_c(\mathcal{P}/M)(8Mp_c/3R^0T_c)^{3/4}$

$\Lambda, \Lambda_{BH}, \Lambda_{LW}, \Lambda_{SK}$ = dimensionless "most susceptible" wavelength, $\lambda_d/\lambda d_F$. Subscripts denote predictions by Baumeister-Hamill, Lienhard-Wong, and Siegel-Keshock, respectively

λ = observed wavelength during film boiling

λ_d = most susceptible wave-length during film boiling

λ_{dF} = λ_d for a flat plate, $(2\sqrt{3}\pi) \times \sqrt{\sigma/g(\rho_f - \rho_g)}$

ρ_f, ρ_g = saturated liquid and vapor densities, respectively

σ = surface tension

μ = viscosity of vapor

Ω = dimensionless frequency, $\omega i[\sigma/g^3(\rho_f - \rho_g)]^{1/4}$

ω = frequency of wave (imaginary for stable waves)

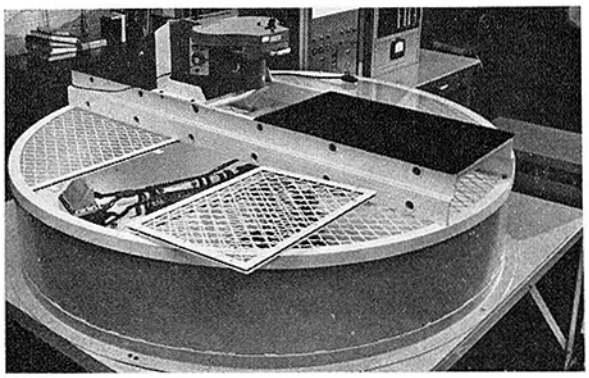

Fig. 2(a) University of Kentucky gravity boiling facility (showing test capsule in access doorway on left side)

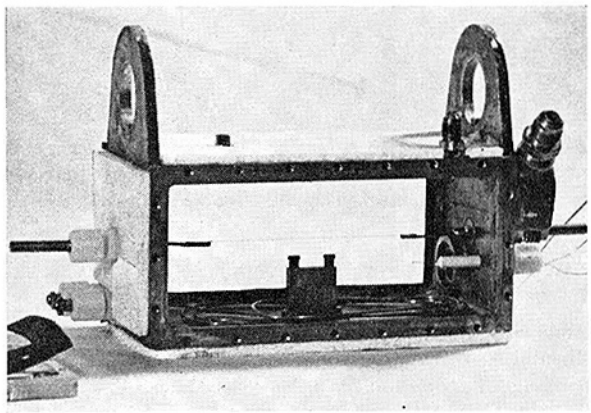

Fig. 2(b) Test capsule (showing test heater in center over 1-in. marker)

Fig. 2 Apparatus

$$(1 + b/R) = \exp\left\{3.65[k\mu\Delta T/R\rho_g\sigma h_{fg}{}^{+}]^{1/4}\right\} \qquad (13)$$

where $h_{fg}{}^{+}$ is a latent heat that includes a sensible heat correction

$$h_{fg}{}^{+} = \left[1 + \frac{0.34c_v\Delta T}{h_{fg}}\right]^2 h_{fg} \qquad (14)$$

Experimental observations of the film boiling process are now needed to facilitate a judgment of the preceding expressions for Λ, and to identify any limitations on these expressions. We shall return to the theory after having presented the results of such observations.

Experiment

Boiling was observed in saturated acetone, methanol, and isopropanol in both centrifuge and stationary tests. The centrifuge and the test capsule used are shown in Figs. 2(*a*) and 2(*b*), respectively. Full details of the experiments and a description of the apparatus are given in reference [7]. The data reported here were all observed on nichrome wires ranging from 32 to 12 gage in size mounted horizontally (i.e., perpendicular to the gravity field). Gravities, g, ranging between 1 and 81 times earth normal gravity, g_e, were imposed upon the wires and wavelengths were observed photographically.

About 233 data photographs—several for each data point—permitted us to measure wavelengths for over 50 conditions of gravity and radius. These wavelengths, although measurable with an accuracy of about 3 percent, exhibited wide variability. Although most of them were obtained in acetone, several observations in methanol and isopropanol were included to insure that other fluids obeyed the same governing equations.

The heat flux was arbitrarily regulated to some value well below the peak and hopefully not far above the minimum. We found that, although Lienhard and Wong observed no effect of heat flux upon λ in the range $q/q_{\min} \leq 4$, it was possible to distort the wave action and increase the merging of adjacent bubbles at higher heat fluxes. This is consistent with the studies of Nishikawa, et al. [8], who observed, not λ, but the *spacing of bubbles* leaving wires in water over an eightfold variation of q up to the vicinity of the peak heat flux, at $R' = 0.14$. They found that *bubble spacing* increased about twofold in this range.

Fig. 3 shows six typical photographs of film boiling under a variety of conditions, arranged in order of increasing R'. Let us consider what we see in each of these:

Fig. 3(a). Careful scrutiny of motion picture records in the R' range typified by this picture shows that the Taylor unstable wavelength briefly appears in the interface in the wake of departing bubbles. It is much shorter than the spacing between the bubbles on the wire and it very quickly merges into these bubbles. Since the bubbles must grow quite large by successive mergers before they have enough buoyancy to overcome the capillary forces that hold them to the wire, the bubble spacing is much larger than λ_d. We shall refer to this vapor removal process, which can be made out in Fig. 3(*a*), as the "bubble-merger" mechanism. Gravity exerts little influence on the interface, and Fig. 1(*b*) might possibly provide a more apt description of the interface than Fig. 1(*a*).

Fig. 3(b). The Lienhard-Wong description fits almost perfectly here. Transverse surface tension, axial surface tension, and gravity are all in good balance. Vapor removal is accomplished by the orderly growth of Taylor unstable waves and their subsequent collapse into departing bubbles. We shall subsequently refer to this as the "wave-collapse" mechanism of vapor removal.

Fig. 3(c). The radius is smaller than in 3(*b*) but g is larger and the resultant R' is somewhat higher than in 3(*b*). The heat flux is much higher than $q_{\min}$ and, while a wave pattern is clear, the wavelength varies along the length of the wire.

Fig. 3(d). The next value of R' is obtained by subjecting a small wire to a high g. The wave pattern is again clear and faithful to Fig. 1(*a*), but it exhibits almost 2 to 1 variability.

Fig. 3(e). For a value of R' almost equal to unity, the relative diminution of transverse surface tension results in a deterioration of the form of the wave pattern.

Fig. 3(f) The shaping effect of transverse surface tension is almost wholly lost in this case and our estimates of wavelength had to be made mainly from the spacing of departing bubbles.

The wavelength data are presented graphically in dimensionless forms in Figs. 4 and 5. A tabular presentation of the raw data is included in reference [7]. Fig. 4 also includes the low R' results from Lienhard's and Wong's stationary tests. The reader should remember as he scans Figs. 3, 4, and 5, that while Λ increases monotonically with R', λ does not. Fig. 3(*d*), for example, corresponds with a large Λ, even though λ is low at this high gravity.

On the basis of the photographic results, we find that the Lienhard-Wong description is quite valid in the range $0.12 \leq R' < 0.9$, but that it deteriorates in the range $0.07 < R' < 0.12$. For $R' \leq 0.07$, the bubble-merger mechanism is completely in control of vapor dynamics.

For $R' \geq 0.9$, the orderliness of the analytical model no longer exists in reality. Secondary wave motions and misalignment tend to disrupt the pattern. Fig. 1(*a*) appears to give only a reasonable first-order description of what is becoming an increasingly complicated phenomenon at larger R'. However, we were able to discern ragged waves up to $R' > 2.5$ and the Taylor theory still appears to account for the magnitude of these waves.

There is some evidence that the limiting value of λ_d as given by equation (2), namely, λ_{dF}, is approximately correct for even larger R'. Pomerantz [9] measured heat transfer coefficients during the film boiling of Freon-113 on $^3/_{16}$-in-dia tubes, under variable gravity. He also gave three ranges of *bubble spacings*

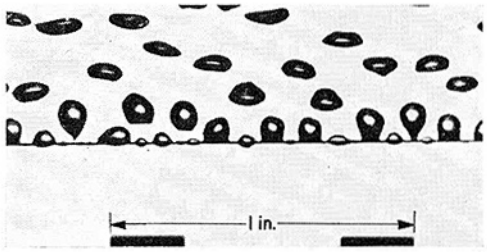

Fig. 3(a) $g = 1g_e$, $R = 0.0040$ in., acetone, $q = 51{,}800 \frac{\text{Btu}}{\text{ft}^2\text{hr}}$, $R' = 0.0642$

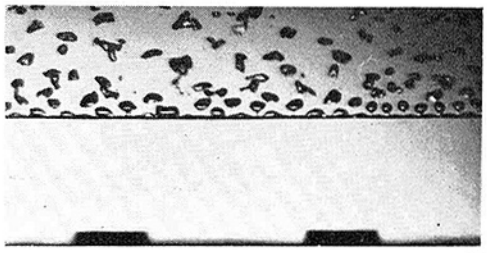

Fig. 3(d) $g = 38g_e$, $R = 0.0050$ in., acetone, $q = 99{,}000 \frac{\text{Btu}}{\text{ft}^2\text{hr}}$, $R' = 0.497$

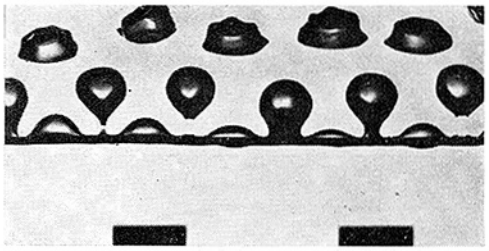

Fig. 3(b) $g = 1g_e$, $R = 0.0127$ in. acetone, $q = 41{,}200 \frac{\text{Btu}}{\text{ft}^2\text{hr}}$, $R' = 0.203$

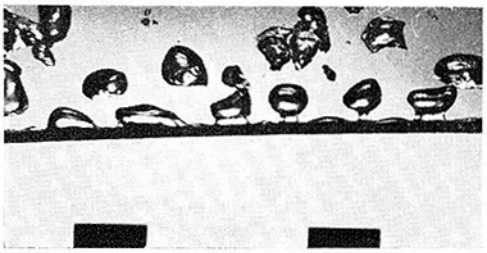

Fig. 3(e) $g = 8g_e$, $R = 0.0200$ in., acetone, $q = 40{,}600 \frac{\text{Btu}}{\text{ft}^2\text{hr}}$, $R' = 0.905$

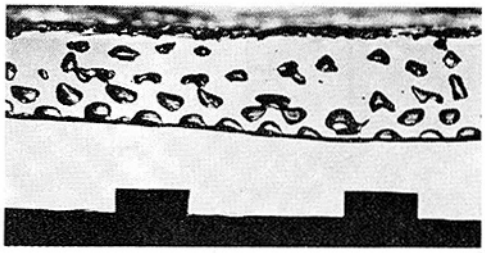

Fig. 3(c) $g = 10g_e$, $R = 0.0063$ in., methanol, $q = 132{,}000 \frac{\text{Btu}}{\text{ft}^2\text{hr}}$, $R' = 0.322$

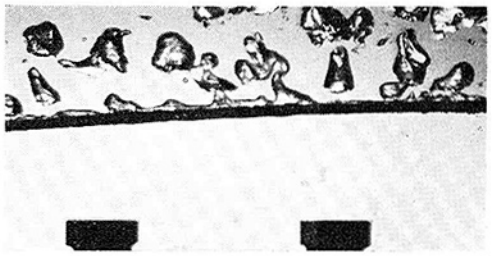

Fig. 3(f) $g = 26g_e$, $R = 0.0200$ in., acetone, $q = 60{,}000 \frac{\text{Btu}}{\text{ft}^2\text{hr}}$, $R' = 1.64$

Fig. 3 Vapor removal configuration for six typical cases of film boiling, in order of increasing R'

(which probably approximate Taylor wavelengths at his large R''s and relatively low heat fluxes). They reduce to

$$\Lambda(R' = 2.27) = 0.5 \text{ to } 2.32$$

$$\Lambda(R' = 4.55) = 0.59 \text{ to } 1.0$$

$$\Lambda(R' = 5.9) = 0.65 \text{ to } 1.18$$

All three of these values scatter widely about $\Lambda = 1$, or $\lambda_d = \lambda_{dF}$. He also claimed an average value of $\Lambda = 1.1$ for his bubble spacings, which is consistent with the trend of our wavelength data. The early photographic study of Westwater and Santangelo [10] provides one very clear photograph of methanol in film boiling on a horizontal tube from which we have obtained

$$\Lambda(R' = 3.03) = 0.80 \text{ to } 1.1$$

This also corroborates the trend at large R'. These results are all probably low by a small but unknown amount because of foreshortening, since the waves no longer align in the axial plane

Analysis of Wavelength Results

Let us first consider the three predictions of Λ: equation (2*a*) or (11), equation (10), and equation (12). We have evaluated $(1 + b/R)$ on the computer for acetone, using equation (13). Fortunately, this expression is only very weakly dependent upon ΔT in the ranges of interest. Thus we were able to assume $\Delta T \simeq 600$ deg F with the knowledge that an error of 2 or 3 hundred degrees would not seriously change the predicted value of $(1 + b/R)$. Since this computation is probably not very precise, it should only be viewed as indicative of the influence of b.

Fig. 6 shows Λ_{LW}, Λ_{SK}, and Λ_{BH} together for comparison. The contribution of the vapor blanket thickness is slight in this case, as illustrated by the slight difference between the Λ_{LW} curves including and neglecting b. The Λ_{SK} and Λ_{BH} curves both fall beneath the Λ_{LW} curves and, as we can see in Fig. 5, the data fall on and above Λ_{LW}.

Thus Λ_{SK} is probably based upon an erroneous description of the interface—at least in the range $R' \geq 0.07$. A more detailed discussion of λ in the range $R' < 0.07$ will be deferred until later in this paper. The fact that the Baumeister-Hamill result is so low probably reflects the comparative crudity of their model for the configuration. They solved a much more complete overall heat transfer problem and had to make stronger simplifying assumptions.

The broad variability of the wavelength data in Figs. 4 and 5 is explainable if we keep sight of the basic assumption underlying the prediction of both Λ_{LW} and Λ_{SK}. This is the supposition that λ is equal to λ_d, the wavelength for which the frequency, Ω, of oscillation is a maximum. Fig. 7 shows a plot of Ω against Λ, based upon equation (1*a*). This plot shows that the relationship is almost neutrally stable over a broad range of

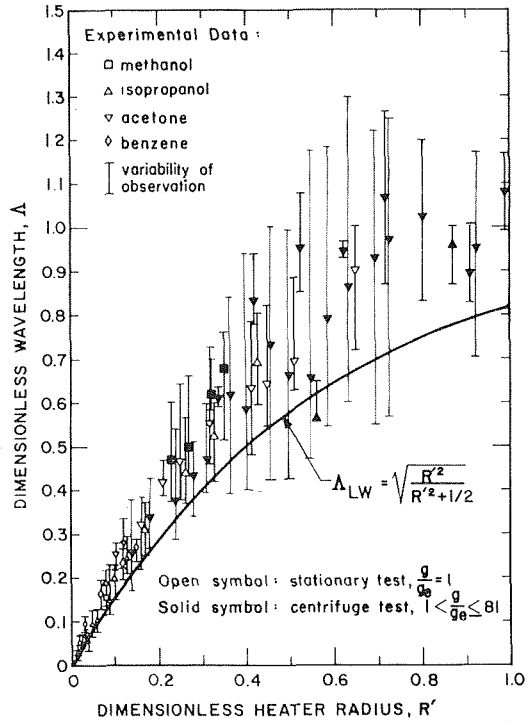

Fig. 4 Experimental wavelength on horizontal cylindrical heaters—low R' range

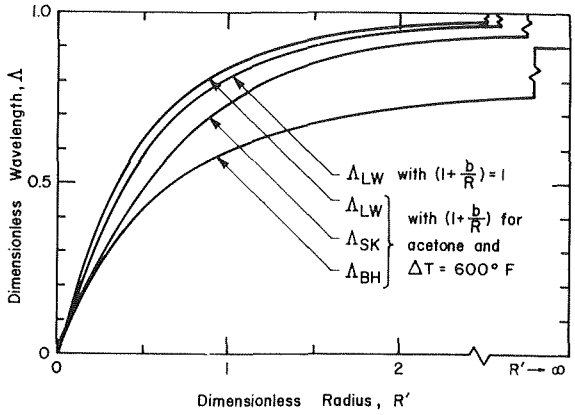

Fig. 6 Comparison of predicted Λ's

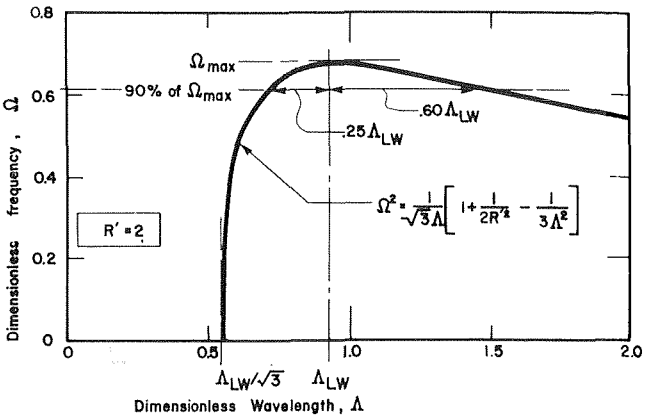

Fig. 7 Illustration of the variability of Λ in the vicinity of Ω_{max}

Λ. The narrow range of frequency, $\Omega \geq 0.9\ \Omega_{max}$, corresponds with $0.75\ \Lambda_{LW} \leq \Lambda \leq 1.60\ \Lambda_{LW}$.

The implication is that there is a broad band of frequencies favored almost equally with Ω_{max}. We should therefore *expect* to measure wavelengths in the range of, say, $0.75\ \Lambda_{LW}$ to $1.6\ \Lambda_{LW}$. The choice of 90 percent is of course arbitrary, but the use of this band in Fig. 5 appears to match the observed variability of data quite well.

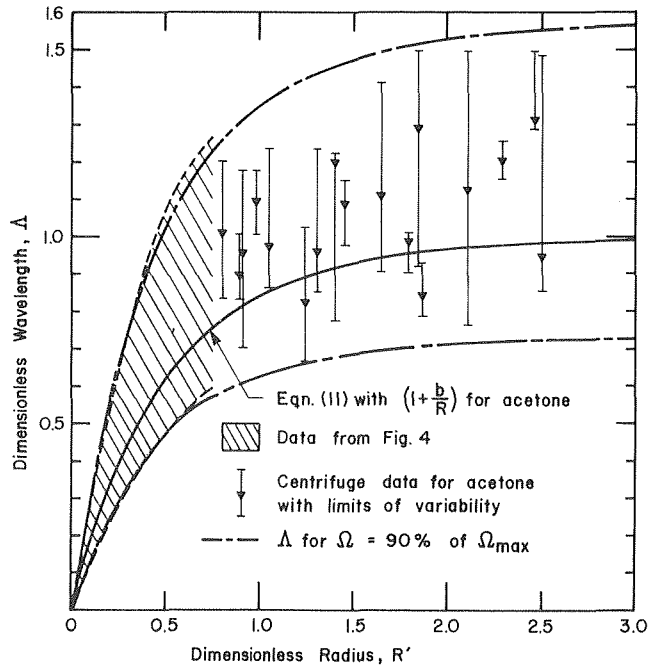

Fig. 5 Experimental wavelength on horizontal cylindrical heaters—high R' range

The Minimum Heat Flux

Equation (3*a*) can be put in the following dimensionless form using the corresponding-states correlation of Lienhard and Schrock[6] [11]:

$$\frac{q_{min}}{\alpha} = (q_{min})_r = 0.515(q_{min_F})_r f(R') \tag{15}$$

where $(q_{min_F})_r$ is a function of reduced pressure, $p_r = p/p_c$, only. The parameter α is a characteristic of the boiled liquid, and it has the following form[7]:

$$\alpha \equiv g^{1/4} p_c \frac{\mathcal{P}}{M}\left(\frac{8Mp_c}{3R^0T_c}\right)^{3/4} \tag{16}$$

We wish to use equation (15) as a correlation in the following form:

$$\frac{(q_{min})_r}{0.515\, f(R')} = (q_{min_F})_r \tag{15a}$$

This form of equation (3) should make it possible to check the equation by normalizing cylinder data for thermodynamically similar fluids onto a flat plate representation.

Before we do this, it is well to consider a serious experimental difficulty in obtaining q_{min} for horizontal cylinders. References

[6] The use of such correlations is treated at greater length in [7, 12–14].

[7] Some authors have inferred that the factor, 8/3, in α means that α is somehow tied to van der Waals' equation. This is not really the case since this constant could just as easily be eliminated for correlative purposes. With the factor of 8/3 included, one can multiply α by Berenson's constant, 0.09, to get a kind of van der Waals' q_{min_F}.

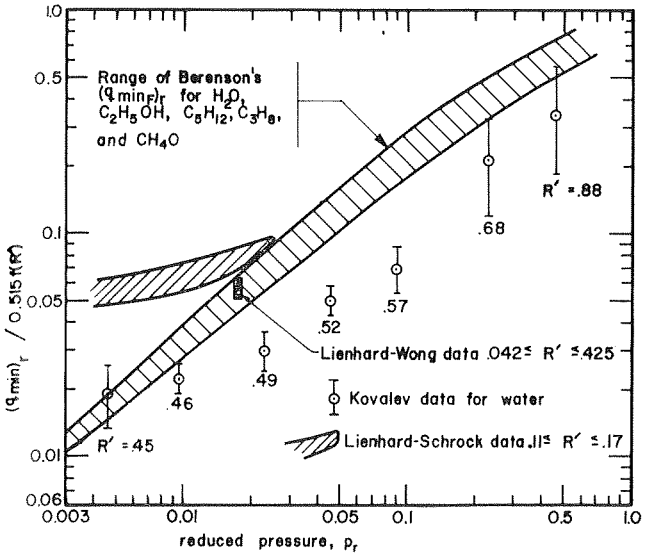

Fig. 8 Reduced minimum heat flux, normalized to flat plate values, as a function of reduced pressure

[1, 7, 11, 12] refer to the difficulties of eliminating end effects which cause the film-to-nucleate boiling transition to occur at heat fluxes above the true q_{min}. Very recently, Kovalev [15] devised an experimental trick for determining the true q_{min}. He bent the ends of his horizontal cylindrical heater 90 deg into the vertical position and led them out of the bath. In doing so, he completely removed the end effect problem and obtained what might be the most reliable q_{min} data in existence. The results are lower than other q_{min} data that have been reported at the same conditions.

Fig. 8 presents data for various horizontal cylinders from references [1, 11, 15]. These are compared with the Berenson-Zuber flat plate prediction for a variety of similar fluids. The Berenson equation would fall on a single line if the thermodynamic similarity of the fluids were perfect. The spread of the band occupied by these fluids gives a rough idea of the validity of the law of corresponding states in this application.

The data of Lienhard and Wong, for a single p_r but for a range of R', all fit onto a single point because they are all consistent with the function $f(R')$. The point in turn normalizes directly onto this curve because these are the data upon which the constant in the normalization was evaluated. The earlier data of Lienhard and Schrock were measured with somewhat less care given to avoiding end effects; hence they are higher.

A best curve through Kovalev's data, and consistent with equation (15*a*), would be given by equation (3) with the constant (0.515×0.09) reduced to about (0.332×0.09) or,

$$q_{min} = 0.332\, q_{min_F} f(R') \tag{17}$$

This expression would fall a little below the data in the low p_r range but serves very well for $p_r > 0.01$.

Unfortunately, Kovalev's experiments cast the same kind of ugly light upon q_{min} measurements that the early surface roughness experiments of Corty and Faust [16] cast upon nucleate boiling. The problem of making practical predictions becomes swamped by a capricious system variable in either case. Accurate predictions of q_{min} on horizontal cylinders cannot be made for practical configurations without knowing how vapor entrapment and cooling at the supports affect the transition. It is for this reason that we have not presented additional centrifuge data for yet another end mounting.

The Radius Range, $R' < 0.07$

A mechanism can be established for the transition that marks the smallest radius for which Taylor-unstable waves collapse and release bubbles. We have already noted, from photographs, that when $R' \leq 0.07$, bubble-mergers completely control vapor removal. An additional study of several photographs reveals that bubble departure takes place roughly as shown in Fig. 9. The radius, $\lambda/16$, shown in the sketch appears to be characteristic of this configuration.

This sharp corner can exist as long as it is not opposed by an equally strong countercurvature of the interface around the cylinder. But for small wires the countercurvature will prevent the corner from indenting inward and nipping off the bubble. At this point the departing bubble will have to spread out before it can depart, and merge with its neighbors if R is sufficiently small.

It is now possible to compare $\lambda/16$ with the radius of the wire at the *observed* transition from the wave-collapse mechanism to the bubble-merger mechanism.

$$R' \geq 0.07 \text{ for wave-collapse mechanism} \tag{18}$$

or

$$\frac{R}{\lambda_{d_F}} \geq \frac{0.07}{2\sqrt{3\pi}} = 0.00644$$

but

$$\left.\frac{\lambda_d}{\lambda_{d_F}}\right|_{R'=0.07} = \sqrt{\frac{0.07^2}{0.07^2 + 1/2}} = 0.0986$$

Therefore condition (18) takes the form

$$\frac{R}{\lambda_d} \geq \frac{0.00644}{0.0986} = \frac{1}{15.3}$$

which corresponds very well with photographic observations.

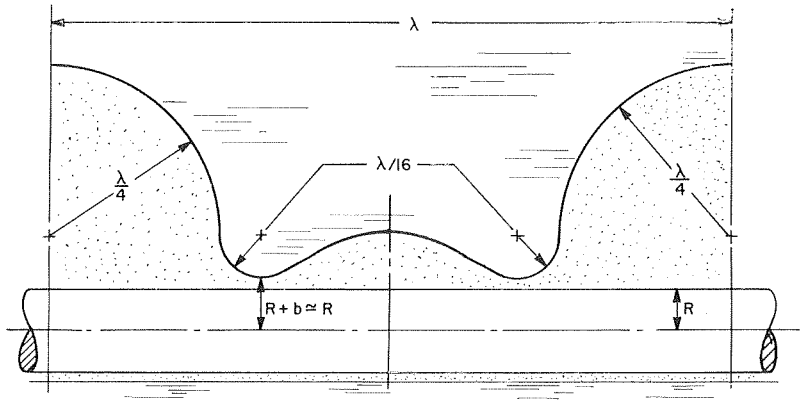

Fig. 9. Schematic representation of observed bubble departure configuration during film boiling

The problem of developing a description of vapor removal from small cylindrical heaters in film boiling at low gravity remains to be done. So too does the prediction of q_{min}. When they are accomplished such analyses will focus upon a force balance between surface tension and buoyancy. They will not be based upon considerations of Zuber's capillary waves.

Conclusions

1 The best prediction of Λ that we presently can make is

$$\Lambda = \sqrt{\frac{R'^2}{R'^2 + 1/2(1 + b/R)^2}} \tag{11}$$

where $(1 + b/R)$ can best be estimated at present using equation (13). The variability of actual data will be somewhat less than +60 percent and −25 percent because the wave motion approaches neutral stability over this range.

2 It is not relevant whether Λ is changed by varying, R, g, or the liquid being boiled. The single parameter, R', correctly accounts for all of these effects upon Λ.

3 Our best prediction of the absolute minimum q_{min} for horizontal cylinders is

$$q_{min} = 0.030 \left\{ \rho_g b_{fg} \sqrt[4]{\sigma g \frac{\rho_f - \rho_g}{(\rho_f + \rho_g)^2}} \right\} f(R')$$

The constant, 0.030, replaces Lienhard's and Wong's value which would be 0.0466 in this formulation The constant is extremely sensitive to end conditions on the cylinder and might rise to over twice this value for incautious mountings.

4 As R' drops below 0.07, conclusions 1 and 3 become increasingly inapplicable because the wave-collapse mechanism gives way to a bubble-merger mechanism.

References

1 Lienhard, J. H., and Wong, P. T. Y., "The Dominant Unstable Wavelength and Minimum Heat Flux During Film Boiling on a Horizontal Cylinder," JOURNAL OF HEAT TRANSFER, TRANS. ASME, Series C, Vol. 86, No. 2, May 1964, p. 220.

2 Zuber, N., "Hydrodynamic Aspects of Boiling Heat Transfer," AEC Report No. AECU-4439, Physics and Mathematics, June 1959.

3 Berenson, P. J., "Transition Boiling Heat Transfer From a Horizontal Surface," M. I. T., Heat Transfer Laboratory Technical Report No. 17, 1960.

4 Bellman, R., and Pennington, R. H., "Effects of Surface Tension and Viscosity on Taylor Instability," *Quarterly of Applied Mathematics*, Vol. 12, 1954, p. 151.

5 Siegel, R., and Keshock, E. G., "Nucleate and Film Boiling in Reduced Gravity From Horizontal and Vertical Wires," NASA TR R-216, Feb. 1965.

6 Baumeister, K. J., and Hamill, T. D., "Film Boiling From a Thin Wire as an Optimal Boundary-Value Process," ASME Paper 67-HT-62.

7 Lienhard, J. H., and Carter, W. M., "Gravity Boiling Studies —First Annual Report," TR No. 1-68-ME 1, College of Engineering, University of Kentucky, Lexington, Ky., 1968.

8 Nishikawa, K., Shimomura, R., Hatano, M., and Nagatomo, H., "Investigation of Surface Film Boiling Under Free Convection," *Bulletin of the JSME*, Vol. 10, No. 37, 1967, pp. 123–131.

9 Pomerantz, M. L., "Film Boiling on a Horizontal Tube in Increased Gravity Fields," JOURNAL OF HEAT TRANSFER, TRANS. ASME, Series C, Vol. 86, No. 2, May 1964, p. 213.

10 Westwater, J. W., and Santangelo, J. G., "Photographic Study of Boiling," *Industrial and Engineering Chemistry*, Vol. 47, 1955, p. 1605.

11 Lienhard, J. H., and Schrock, V. E., "The Effect of Pressure, Geometry, and the Equation of State Upon the Peak and Minimum Boiling Heat Flux," JOURNAL OF HEAT TRANSFER, TRANS. ASME, Series C, Vol. 85, No. 3, Aug. 1963, p. 261.

12 Lienhard, J. H., and Watanabe, K., "On Correlating the Peak and Minimum Boiling Heat Fluxes With Pressure and Heater Configuration," JOURNAL OF HEAT TRANSFER, TRANS. ASME, Series C, Vol. 88, No. 2, May 1966, p. 94.

13 Lienhard, J. H., "Interacting Effects of Geometry and Gravity Upon the Extreme Boiling Heat Fluxes," JOURNAL OF HEAT TRANSFER, TRANS. ASME, Series C, Vol. 90, No. 1, Feb. 1968, p. 180.

14 Borishansky, V. M., Novikov, I. I., and Kutateladze, S. S., "Use of Thermodynamic Similarity in Generalizing Experimental Data of Heat Transfer," International Heat Transfer Conference, University of Colorado, Boulder, Colo., 1961 Paper No. 56, p. 475 (see also discussion by Lienhard and Schrock, p. D-153).

15 Kovalev, S. A., "An Investigation of Minimum Heat Fluxes in Pool Boiling of Water," *International Journal of Heat and Mass Transfer*, Vol. 9, 1966, p. 1219.

16 Corty, C., and Faust, A., "Surface Variables in Nucleate Boiling," *Chemical Engineering Progress Symposium Series*, No. 17, 1955, pp. 1–12.

P. H. G. ALLEN
Department of Electrical Engineering,
Imperial College of Science
and Technology,
London, England

A. H. FINN[1]
Elliot Brothers Ltd.,
London, England

Profile Development With Mixed Convection in a High Prandtl Number Fluid

The paper deals with entry-length conditions for transformer oil in vertical laminar flow through a uniformly heated duct allowing for changes in density, viscosity, and thermal conductivity. The calculation method uses a fundamental property of high Prandtl number fluids and assumes a series of truncated temperature profiles. Calculated wall mean temperature rises have been verified experimentally for a simple case. Local and mean Nusselt numbers have been derived and an empirical correlation relating mean and limiting Nusselt numbers applied. The analysis includes evaluation of the free-convective component of pressure head which causes flow and distinguishes this from free-convective effects within the duct.

Introduction

USING the Clark and Kays [1][2] concept of limiting (or fully developed) conditions in a convecting duct with uniform wall heating, one can evaluate limiting velocity and temperature profiles for oil in laminar flow allowing for the effect of variable physical properties [2, 3]. Relatively complicated thermal systems may be analyzed [2, 4]. In practice, however, limiting conditions occur only (if at all) over small fractions of duct lengths. Thus a method for computing entry length conditions is needed. This is especially true for fluids with high Prandtl number, Pr, defined:

$$\mathrm{Pr} = \frac{\nu}{\alpha} \tag{1}$$

where ν and α are kinematic viscosity and thermal diffusivity, respectively. Both quantities are diffusion coefficients, ν for momentum and α for temperature. Momentum, zero at the duct walls, diffuses into the fluid to establish the velocity profile. Similarly, the temperature profile develops by the diffusion of thermal energy. Thus the fluid further from the wall travels further along the duct at its initial temperature before experiencing any temperature change. The Prandtl number therefore gives the relative rates at which the two profiles develop or, alternatively, the relative duct lengths (z) needed for the profiles to develop to a particular extent.

To allow for incomplete development, Clark and Kays [1] used a dimensionless correlation to relate calculations using limiting conditions to measured values on the air side of an air-to-water counterflow heat exchanger with short ducts. Air has nearly constant Pr of order 1 so profiles develop together. One object of the present work is to test the correlation method when Pr is much greater and varies throughout the duct. For transformer oil, it exceeds 470 at 20 deg C and falls to about 30 at 100 deg C. It is thus in order to assume fully developed velocity profiles coincident with partially developed temperature ones [5, pp. 119, 120]. Also, constant heat rate per unit of duct length gives, in an annulus, profiles of temperature θ having the same $(\partial\theta/\partial x)_0$ for all z. (The subscript gives the perpendicular distance x from the heated wall.) The present work tests a further simplification which was suggested, but not verified, previously [2], namely, that all partially developed temperature profiles are truncated versions of the fully developed one, developing outward from the wall and only changing shape where it meets fluid at its initial temperature.

Experimental results for oil in uniformly heated ducts are practically nonexistent. Kemeny and Somers [6] claimed uniform heating, but the extremely low thermal conductivity of oil relative to that of any solid metal tube makes the desired boundary condition unlikely. For this reason, the present work uses a novel design of heated surface. Other work, using transformer-type ducts [7, 8], is vitiated by the arbitrary nature of spot oil temperature measurements.

Equations Governing Fully Developed Laminar Flow Heat Transfer

General equations governing velocities u, v, and w (in the x, y, z-directions) in incompressible laminar fluid flow were derived by Navier [9]. The simplifying assumptions usually made when solving them are set out in Appendix 1. Using these, for limiting conditions in an infinitely wide duct (no y-direction changes),

$$\frac{\partial}{\partial x}\left(\mu \frac{\partial w}{\partial x}\right) = \frac{\partial p}{\partial z} \tag{2}$$

where μ is fluid dynamic viscosity and p is pressure causing

[1] Formerly, Department of Electrical Engineering, Imperial College of Science and Technology, London, England.

[2] Numbers in brackets designate References at end of paper.

Contributed by the Heat Transfer Division for publication (without presentation) in the JOURNAL OF HEAT TRANSFER. Manuscript received at ASME Headquarters, March 4, 1969; revised manuscript received, September 11, 1969. Paper No. 70-HT-A.

flow. The corresponding Fourier [10] equation is, neglecting $(\partial\theta/\partial z)^2$ compared with $(\partial\theta/\partial x)^2$,

$$\frac{\partial}{\partial x}\left(k\,\frac{\partial\theta}{\partial x}\right) = \rho c w\,\frac{\partial\theta}{\partial z} \tag{3}$$

where k, ρ, and c are fluid thermal conductivity, density, and specific heat, respectively.

These equations, or their cylindrical coordinate equivalents, have been solved by, e.g., Hallman [11], Hanratty, Rosen, and Kabel [12], Sidorov [13], Bodoia and Osterle [14], Yang [15], and Rao and Morris [16], and none of these allows for changes in both density and viscosity due to the temperature field, although McKillop [17] considered non-Newtonian viscosity. More significantly, they were solved analytically by Pigford [18] (for fluid density and inverse viscosity varying linearly with temperature) and numerically by Bradley and Entwistle [19] (for air with varying viscosity and density) with both constant wall temperature and uniform wall heating. Where density change is considered differences are evident. Usually, as in [12 and 19], the total pressure gradient is written as $\partial p/\partial z + g\rho$ (g is acceleration due to gravity), with p defined merely as "pressure," and ρ related to its value at an arbitrary datum temperature, e.g., duct wall in [11, 12, 16, 19], duct entry in [18]. An outstanding contribution by Lawrence and Chato [20] extends the solution to entry-length conditions with variable density and viscosity in a circular tube. In their momentum equation, local density has a duct-entry datum, but to evaluate their pressure parameter they integrated its arithmetic mean value ρ_m at distance z along the duct. This, they say, is because it was easily measured and because it has physical significance in a combined free-forced convection problem. This physical significance is explained in the next section. Their numerical method offers a complete alternative to the present analysis. However, its application is to simple duct sections; the present work establishes the accuracy of an entry-length calculation method which can then be applied to complex arbitrary geometries, in particular, those of power transformer cooling ducts.

Nature of Pressure Term

Before solving equation (2) for a vertical duct forming part of a closed system, the nature of $\partial p/\partial z$ must be clarified. Its local value for any x in the plane at z is, with upward flow,

$$\frac{\partial p}{\partial z} = \frac{\partial p_p}{\partial z} - g\rho \tag{4}$$

where p_p is the pressure due to pump action (if any). Wetherill [21] has shown that the natural convective pressure-causing flow, p_c, is given by

$$\begin{aligned} p_c &= gs \oint \theta\, dz \\ &= gs \text{ (area of height/temperature diagram)} \end{aligned} \tag{5}$$

where $s = d\rho/d\theta$ = const for transformer oil in the working range. It can be shown [3] that, in fact, it is the arithmetic mean temperature at z that must be integrated in (5). When this is taken as datum in each duct section, (4) becomes

$$\begin{aligned} \frac{\partial p}{\partial z} &= \frac{\partial p_p}{\partial z} - g(\rho - \rho_m) - g\rho_m \\ &= \frac{\partial p_p}{\partial z} - g\rho_m - gs(\theta - \theta_m) \end{aligned} \tag{6}$$

Here the first two terms combine to give the gradient of total pressure p' (pump and/or convective) causing flow, while the third gives the local distortion of the pressure gradient and, hence, of the velocity profile due to density changes. (The signs of g and the pressure gradients in relation to the positive z-direction must be borne in mind, e.g., in calculating forced flow downward in a heated tube.) Thus (2) becomes

$$\frac{\partial}{\partial x}\left(\mu\,\frac{\partial w}{\partial x}\right) = \frac{\partial p'}{\partial z} - gs(\theta - \theta_m) \tag{7}$$

Rearranging and allowing for temperature-dependent viscosity (3), (7) becomes

$$\frac{\partial^2 w}{\partial x^2} = \frac{1}{\mu}\left[\frac{\partial p'}{\partial z} - gs(\theta - \theta_m) - \frac{\partial w}{\partial x}\,\frac{\partial\theta}{\partial x}\,\frac{d\mu}{d\theta}\right] \tag{8}$$

while (3) becomes

$$\frac{\partial^2\theta}{\partial x^2} = \frac{1}{k}\left[\rho c w\,\frac{\partial\theta}{\partial z} - \left(\frac{\partial\theta}{\partial x}\right)^2\frac{dk}{d\theta}\right] \tag{9}$$

The forms of (8) and (9), applicable to rectangular and tubular ducts, have been given elsewhere [3] and are stated in Appendix 2. A dimensionless form of (8) has been given [22].

Temperature Profile Development

Consider oil at temperature θ_i and with mean velocity w_m entering a duct with one side dissipating heat at uniform thermal flux q_0. θ_i is uniform across the duct (see Fig. 1) so equals θ_b (defined in (10) below), which is thus independent of the geometry of the velocity profile.

The temperature of the oil in a hypothetical layer, thickness δx, close to the heated surface rises, giving a mean temperature gradient, $(\partial\theta/\partial x)_1 = q_0/k$, approximately, across it. Proceeding along the duct, the oil in this layer becomes hotter but, with q_0 constant, $(\partial\theta/\partial x)_1$ remains constant. As soon as θ_1, the temperature at $x = \delta x$, exceeds θ_i, heat flows into the adjacent layer, the flow rate increasing to a constant value q_1, giving $(\partial\theta/\partial x)_2 = q_1/k$, approximately in layer 2. Similarly, when $\theta_2 > \theta_i$, the heat flow extends to layer 3, and so on. During the process, the

Nomenclature

c = specific heat, of duct fluid
k = thermal conductivity, of duct fluid
s = slope of density/temperature graph, of duct fluid
u, v, w = velocities in x, y, z-directions, of duct fluid
α = thermal diffusivity, of duct fluid
μ = dynamic viscosity, of duct fluid
ν = kinematic viscosity, of duct fluid
ρ = density, of duct fluid
Pr = Prandtl number, of duct fluid
Gz = Graetz number, for heat transfer system
Nu = Nusselt number, for heat transfer system
Re = Reynolds number, for heat transfer systems
D_h = duct hydraulic diameter
g = acceleration due to gravity
p = local pressure-causing flow
p' = total pressure-causing flow
q = heat flux
x, y, z = Cartesian coordinates
X = duct x-direction dimension (thickness)
δx = small element of X
Δx = finite-difference element of X
Z = duct z-direction dimension (axial length)
Δz = finite-difference element of Z
θ = temperature
$\bar{\theta}_0, \bar{\theta}_b$ = integrated means with respect to z

Subscripts

b = bulk fluid
c = convective effect
f = limiting
i = duct entry
m = integrated mean
min = minimum value
p = pump effect
z = at axial distance z
0 = at $x = 0$ (duct heated wall)
$1, 2, 3 \ldots n$ = number of sequential increment Δx, Δz, or value at that number of increments

form of that portion of the temperature profile already developed is assumed not to change. Thus more of the ultimate profile appears above the θ_i level until, at some calculable value of z, its minimum temperature $\theta_{\min} \geq \theta_i$ and we have fully developed flow with uniform wall heating. Then all $\partial\theta/\partial z = \partial\theta_0/\partial z = \partial\theta_b/\partial z = \text{const}$ (θ_0 is the wall temperature). The final refinement is to let $\delta x \to 0$ so that the profile exhibits continuous curvature down to θ_i. For numerical calculation, δx is taken as a finite difference Δx.

Assuming the velocity profile corresponding to each stage in the development of the temperature profile to be itself fully developed, values of bulk fluid temperature θ_b are obtained, [5, pp. 104–105] for any z as

$$\theta_b = \frac{\int_0^X \theta w dx}{X w_m} \tag{10}$$

where X = duct thickness. For uniform wall heating, $\partial\theta_b/\partial z$ is the same for all z.

Calculation of Profiles

First, one must calculate the limiting temperature profile for a specified q_0 and w_m by simultaneous solution of (8) and (9). The boundary conditions are, for (8): $w = 0$ at $x = 0, X$; $\int_0^X w dx = X w_m$; for (9): $\theta = \theta_0$ at $x = 0$; $\partial\theta/\partial x = 0$ at $x = X$; $\partial\theta/\partial x = -q_0/k$ at $x = 0$. As a first approximation, θ_{0f} is chosen as likely to give $\theta_{\min}$ for the profile about equal to the specified θ_i. Next, a distance Δz_1 (initially unknown) is assumed necessary to establish the temperature gradient $(\partial\theta/\partial x)_1$ a distance Δx (here taken as $X/20$) from the duct wall. Using the truncated temperature profile thus formed and, initially, a parabolic velocity profile and the corresponding value of $\partial p'/\partial z$ at θ_i, the velocity profile is recalculated by finite-difference solution of (8). $\partial p'/\partial z$ is then adjusted until the velocity profile gives the specified w_m. This velocity profile, together with the original truncated temperature profile, is used in (10) to obtain θ_{b1} at Δz_1. Then, equating total heat input rate per unit duct width $(q_0 \Delta z_1)$ to axially convected thermal energy rate $(X \Delta z_1 \rho c w_m \partial\theta_b/\partial z)$, gives

$$\frac{\partial\theta_b}{\partial z} = \frac{q_0}{\rho c w_m X} = \text{const} \tag{11}$$

while

$$\Delta z_1 = \frac{\theta_{b1} - \theta_i}{\dfrac{\partial\theta_b}{\partial z}} \tag{12}$$

Conditions at Δz_1 along the heated duct are thus established and any required data, e.g., local Nusselt number, Nu_z, evaluated. Nu_z is defined

$$\mathrm{Nu}_z = \frac{q_0 D_h}{k(\theta_0 - \theta_b)_z} \tag{13}$$

where D_h is duct mean hydraulic diameter (here, $D_h = 2X$). The calculation is then repeated to give Δz_2, the distance needed for the temperature profile to diffuse $2\Delta x$, and so on, until every element of the fully developed profile is formed. It includes, of

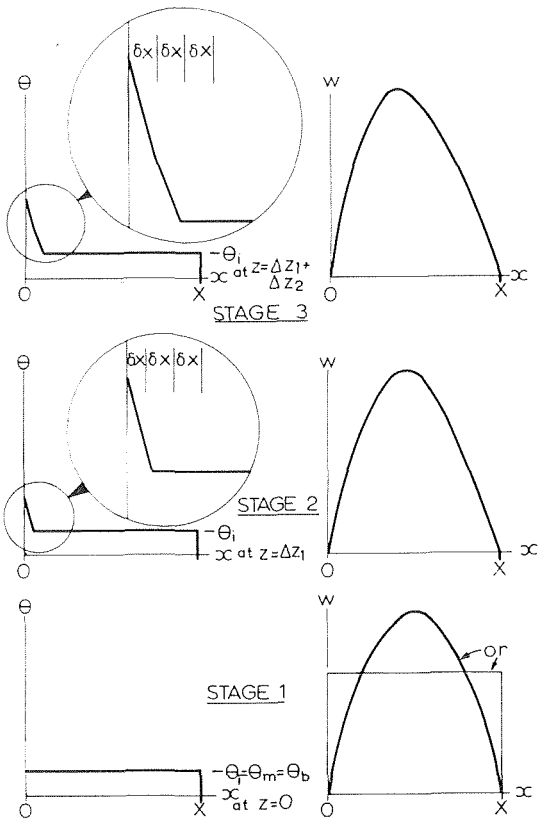

Fig. 1 First three stages in inlet length development

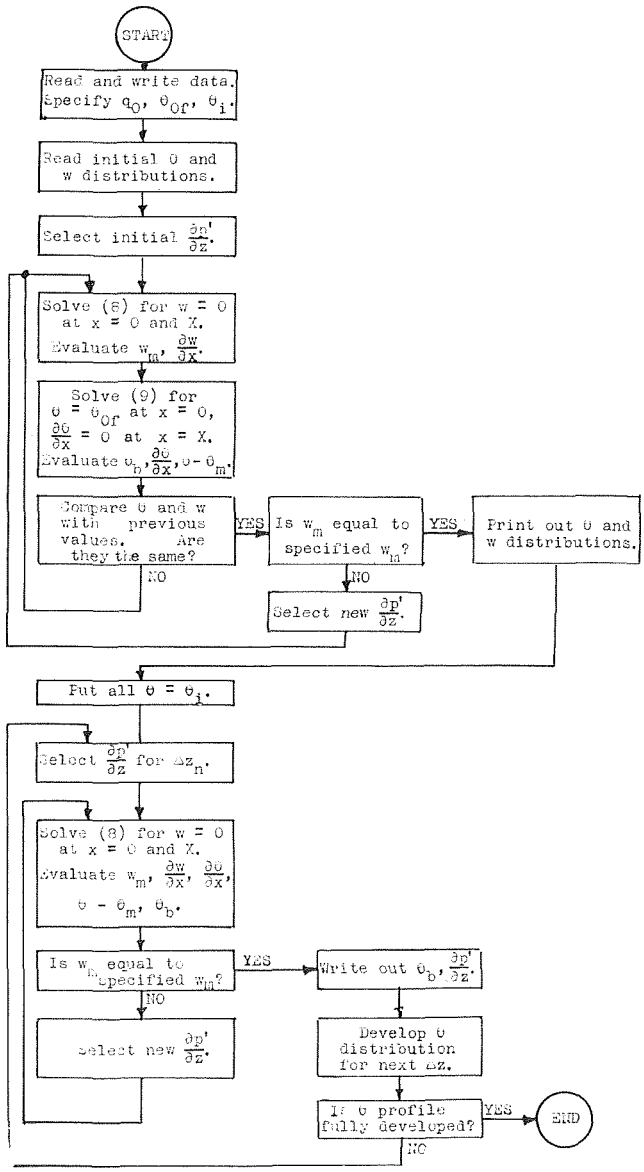

Fig. 2 Outline flow chart

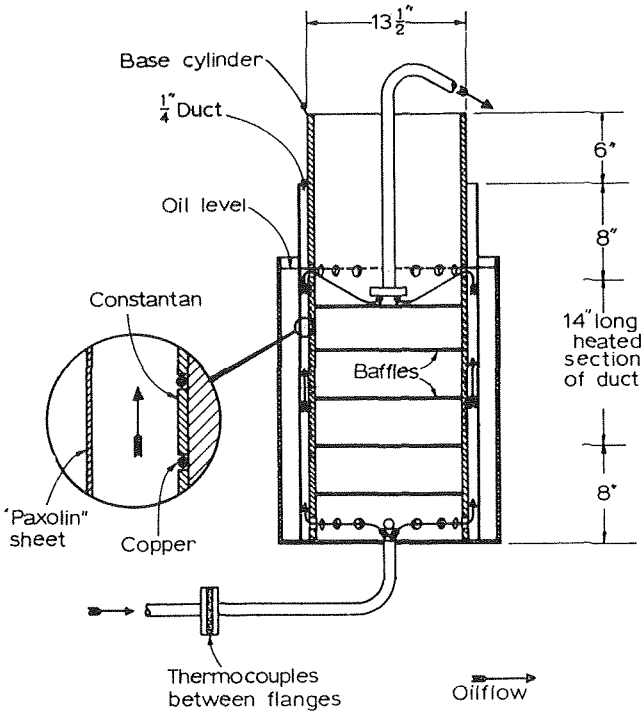

Fig. 3 Arrangement of test duct

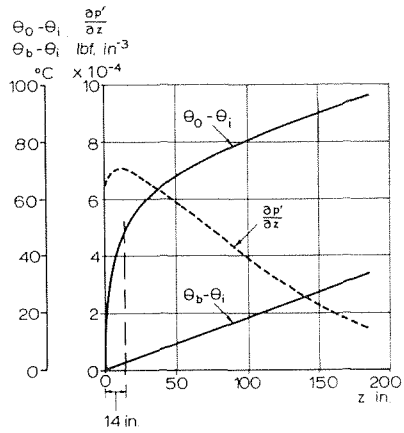

Fig. 4 Variation of θ_0, θ_b, and $\partial p'/\partial z$ along duct for $q_0 = 4.4w$ in.$^{-2}$, $w_m = 3.4$ in. sec^{-1}, $\theta_i = 57$ deg C

course, all cases where the actual duct length Z is less than Z_f, that necessary to establish limiting conditions.

Fig. 2 gives the outline flow chart for the calculation of fully developed and entry length conditions. The physical properties of the oil used[3] are given in detail elsewhere [23].

Experimental Arrangements

Fig. 3 shows the arrangement of the test duct. Its inner surface consists of a bakelized paper base cylinder, length 36 in. and with wall thickness ½ in. Around the outside of this, for a length of 14 in., is wound a constantan ribbon, 3/16 in. by 0.02-in. cross section, to form a helical winding. The electrical resistance of constantan changes negligibly with temperature so that the heat generated per unit length due to an electric current through the helix is invariant, although the temperature varies along it. The outer wall in the ¼-in. duct is formed by a sheet of "Paxolin." The duct-spacing arrangements are not shown in Fig. 3. They consist of 16 ¼-in-dia Paxolin rods placed over the helix (and over circumferential packing pieces of the same radial thickness above and below it). These are riveted to the cylinder at their lower ends and each is divided into two sections, doweled together. After wrapping the Paxolin sheet over them it was possible to withdraw them partially. In this way the wall is supported above and below the heat transfer surface which is itself unobstructed. Using a thin helix on a low thermal conductivity base minimizes the axial conductance of the heated surface compared with the solid tubes used in other reported work, e.g., [14]. As the cylinder diameter is very much larger than the duct radial thickness, curvature may be neglected and the duct considered as an infinitely wide one. By winding a 0.011-in-dia, Lewmex insulated, copper wire between the turns of the helix, the mean wall temperature, $\bar{\theta}_0$, is measured by change of electrical resistance.

Oil flows into the center of the bottom of the steel tank containing the duct assembly. It enters and leaves the duct through two sets of 1¼-in-dia holes in the base cylinder. Between these, horizontal baffles inside the cylinder prevent bypass flow and minimize inward heat transfer. Oil circulation is maintained by a d-c motor-driven gear pump and metered by a nutating disk meter. Oil cooling is by oil-to-water shell/tube heat exchanger. The oil inlet temperature is measured (and its uniformity across the flow section checked) by an array of thermocouples across the inlet pipe flange joint.

Results and Discussion

Temperature and velocity profiles were computed for the six combinations of q_0, w_m, and θ_i specified in Table 1. Typical calculated variations with z are given in Fig. 4 for θ_0, θ_b, and $\partial p'/\partial z$, and in Fig. 5 for Nu_z, Pr, and Reynolds number, Re, defined

$$\mathrm{Re} = \frac{D_h w_m}{\nu_b} \tag{14}$$

For each case, Table 1 gives:

1 Calculated values of Z_f and of θ_{0f} and Nu_f, duct wall temperature, and Nusselt number at Z_f.

2 Calculated mean duct wall temperature $\bar{\theta}_0$ for duct lengths (Z) of 5, 14, and 30 in.

3 Measured $\bar{\theta}_0$ for $Z = 14$ in.

Fig. 6 compares calculated and measured $\bar{\theta}_0$ for $Z = 14$ in.

Fig. 7 uses the Clark and Kays [1] method to correlate calculated values of Nu/Nu_f for the six specified heat transfer conditions in each of the three ducts. The abscissas are $\mathrm{Re}\,\mathrm{Pr}D_h/Z$, known as the Graetz number, Gz. Nu is defined [5, p. 123]

$$\mathrm{Nu} = \frac{q_0 D_h}{k(\bar{\theta}_0 - \bar{\theta}_b)} \tag{15}$$

[3] "Castrol" transformer oil to BS 148:1959, grade 2512.

Table 1 Principal results

Heat transfer conditions			Calculated duct wall mean temperature, $\bar{\theta}_0$(deg C) for duct length (Z):			Measured duct wall mean temperature for 14-in. duct, deg C	Fully developed conditions attained at		
q_0 w in.$^{-2}$	w_m in. sec^{-1}	θ_i deg C	5 in.	14 in.	30 in.		Z_f in.	θ_{0f} deg C	Nu_f
4.4	3.4	57	87	96	105	95	185	153	9.0
4.3	11.6	52	71	80	87	79	680	162	7.5
1.8	9.2	35	45	49	53	48	628	95	6.5
5.2	15.7	58	78	87	95	88	894	184	7.6
1.8	2.0	35	52	58	63	56	138	91	7.1
3.5	13.7	48	64	70	76	69	839	145	7.1

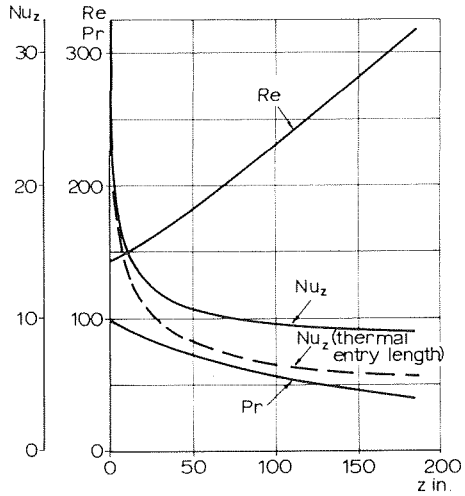

Fig. 5 Variation of local Nusselt, Prandtl, and Reynolds numbers along duct for $q_0 = 4.4$ w in.$^{-2}$, $w_m = 3.4$ in. sec^{-1}, $\theta_i = 57$ deg C

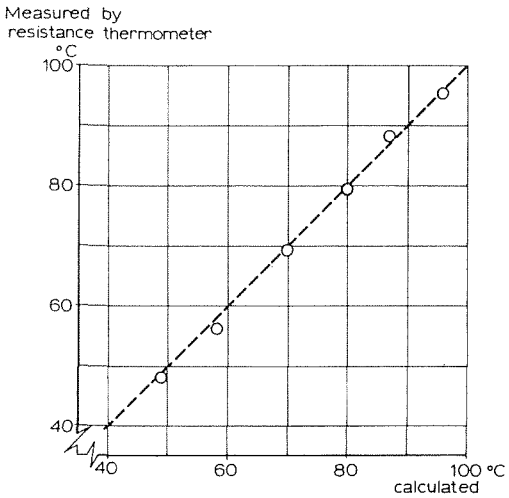

Fig. 6 Comparison of experimental and calculated wall mean temperatures

In the tests providing the data in Fig. 6, ratios of maximum to minimum q_0 and w_m, were about 3 and 8, respectively, while θ_i varied over a range of 20 deg C. Furthermore, the 14-in. heated length is never more than 10 percent, and usually less than 5 percent, of Z_f. Fig. 5 confirms that conditions are entirely entry-length ones. Nevertheless, there is excellent agreement between calculation and test, discrepancies being no greater than expected from uncertainty in oil physical properties (especially k). Having confirmed the accuracy of the calculation method, calculated values have been used to confirm the validity of the correlation method, Fig. 7. It should be noted that the Nu_f values in Table 1, which allow for variable ρ and μ, are very much higher than the constant property one of 5.38 [5, p. 117]. The flattening of the curve shows the diminishing returns of higher flow rates and/or shorter ducts within the laminar regime. Curiously, the correlation for these *mean* Nusselt numbers at varying physical properties agrees well with that quoted by Kays [5, p. 132] for *local* Nusselt number, Nu_z, at constant properties. This is explained qualitatively by the much higher absolute values of Nu_z with, compared to without, physical property change as z increases. For comparison, the curve for Nu_z [5, p. 132] calculated for thermal entry length only (i.e., no progressive velocity distortion) is shown dashed in Fig. 5.

The Gz range in Fig. 7 is well beyond that (Gz < 800) previously investigated. Mean curves for two earlier sets of results are added for comparison. One, from [1], is for a square cross-section duct; the other, from [2], is for the complex case of a high

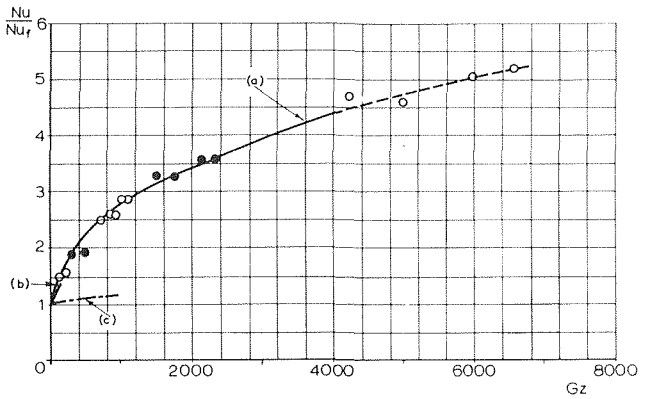

Fig. 7 Correlated results. Black circles are calculated results confirmed by test; hollow circles are calculated results. Curve (a) for Nu_z/Nu_f calculated for no physical property change [5]. Curve (b) for square section duct [1]; curve (c) for high voltage transformer duct [2].

voltage transformer duct with low thermal conductivity walls, not directly heated.

Qualitative evidence of the truncated form of developing temperature profiles is found in the measurements of Lawrence and Chato [20] and Stenkvist [24].

By considering fluid density changes both locally in each duct section and also around the complete flow path, the present work gives an insight into the mechanism of mixed convection. This is that the behavior of an element of fluid within the heated duct is unaffected by whether the overall pressure gradient causing its movement is due to a pump or to a convectively generated pressure head—or how much of it is due to one or to the other. Heat transfer performance is sensitive to velocity profile distortion which increases as local forces, due to changes in physical properties, increase relative to the overall pressure gradient [2]. This effect can be described as due to free convection; it results from physical property changes within the duct and not from the manner in which the pressure head causing flow is generated.

Conclusions

1 Equations governing limiting temperature and velocity distributions for laminar flow in a vertical, uniformly heated, duct are presented. They allow for changes in physical properties with temperature.

2 With a high Prandtl number fluid, the simplifying assumption of a temperature profile, in its limiting form, developing outward from the duct wall in the presence of an already fully developed velocity profile, gives accurate prediction of thermal performance with a simple duct geometry. It has proved equally successful in a much more complex system [25].

3 The Clark and Kays correlation method applies with high Prandtl number fluids in a unilaterally heated infinitely wide duct over a wide range of Graetz number.

4 The *pressure head generation mechanism of free convection* has been distinguished from its effect in improving heat transfer within a duct.

Acknowledgments

The work described formed part of a program of research into high voltage transformer winding cooling supported by the Science Research Council. The authors acknowledge the work of students T. J. Roper and A. Y. Rele on the overall design of the heat transfer circuit and annular heat exchanger, respectively, and of technician R. Gingell in their construction and assembly. Prof. W. M. Kays gave valuable advice. Facilities for numerical work were provided by Imperial College Computer Unit.

References

1 Clark, S. H., and Kays, W. M., "Laminar-Flow Forced Convection in Rectangular Tubes," TRANS. ASME, Vol. 75, 1953, p. 859.

2 Allen, P. H. G., and Allan, D. J., "Layer-Type Transformer-Winding Cooling Factors Derived From Analog Solution of the Governing Equations," *Proceedings, Institution of Electrical Engineers*, Vol. 110, 1963, p. 523.

3 Allen, P. H. G., "Laminar-Flow Heat Transfer With Physical Property Change," *Elektrotech. Obz.*, Vol. 57, 1968, p. 53.

4 Preiningerova, V., and Korinek, S., "Digital Computation of Heat Transfer in Layer-Type Transformer Windings," SNTL Technical Digest, Vol. 9, 1967, p. 683.

5 Kays, W. M., *Convective Heat and Mass Transfer*, McGraw-Hill, New York, 1966.

6 Kemeny, G. A., and Somers, E. V., "Combined Free and Forced-Convection Flow in Vertical Tubes—Experiments With Water and Oil," JOURNAL OF HEAT TRANSFER, TRANS. ASME, Series C, Vol. 84, 1962, p. 339.

7 Taylor, E. D., Berger, D., and Western, B. E., "An Experimental Approach to the Cooling of Transformer Coils by Natural Convection," *Proceedings, Institution of Electrical Engineers*, Series A, Vol. 105, 1958, p. 141.

8 Lobenstein, G., "Die Wärmeübergangszahl von Transformatorenöl in den Kühlkanälen hoher Zylinderspulen," *Deutsche Elektrotech*, Vol. 11, 1957, p. 481.

9 Navier, L. M. H., "Mémoire sur les lois du mouvement des Fluides," *Mém. Acad. r Sci. Inst. Fr.*, 2nd series, Vol. 6, 1823, p. 389.

10 Fourier, J., "Mémoire d'analyse sur le mouvement de la chaleur dans les fluides," *Mém. Acad. r. Sci. Inst. Fr.*, Vol. 12, 1833, p. 507.

11 Hallman, T. M., "Combined Forced and Free Laminar Heat Transfer in Vertical Tubes With Uniform Internal Heat Generation," TRANS. ASME, Vol. 78, 1956, p. 1831.

12 Hanratty, T. J., Rosen, E. M., and Kabel, R. L., "Effect of Heat Transfer on Flow Field at Low Reynolds Numbers in Vertical Tubes," *Industrial and Engineering Chemistry*, Vol. 50, 1958, p. 815.

13 Sidorov, E. A., "The Effect of Nonisothermicity on the Hydraulic Impedance in the Laminar Motion of Trickling Liquids in Tubes," *Soviet Physics-Technical Physics*, Vol. 3, 1958, p. 2480.

14 Bodoia, J. R., and Osterle, J. F., "The Development of Free Convection Between Heated Vertical Plates," JOURNAL OF HEAT TRANSFER, TRANS, ASME, Vol. 84, Series C, 1962, p. 40.

15 Yang, Kwang-Tzu, "Laminar Forced Convection of Liquids in Tubes With Variable Viscosity," ibid, p. 353.

16 Rao, T. L. S., and Morris, W. D., "Superimposed Laminar Forced and Free Convection Between Vertical Parallel Plates When One Plate Is Uniformly Heated and the Other Is Thermally Insulated," *Proceedings, Institution of Mechanical Engineers*, Vol. 182, Part 3H, 1967–1968, p. 374.

17 McKillop, A. A., "Heat Transfer for Laminar Flow of Non-Newtonian Fluids in Entrance Region of a Tube," *International Journal of Heat and Mass Transfer*, Vol. 7, 1964, p. 853.

18 Pigford, R. L., "Nonisothermal Flow and Heat Transfer Inside Vertical Tubes," *Chemical Engineering Progress, Symposium Series*, No. 17, Vol. 51, 1955, p. 79.

19 Bradley, D., and Entwistle, A. G., "Developed Laminar Flow Heat Transfer From Air for Variable Physical Properties," *International Journal of Heat and Mass Transfer*, Vol. 8, 1965, p. 621.

20 Lawrence, W. T., and Chato, J. C., "Heat-Transfer Effects on the Developing Laminar Flow Inside Vertical Tubes," JOURNAL OF HEAT TRANSFER, TRANS. ASME, Vol. 88, 1966, p. 214.

21 Wetherill, L., Discussion of "Hot-Spot Winding Temperatures in Self-Cooled Oil-Insulated Transformers," Vogel, F. J., and Narbutovskith, P., *Transactions of the American Institution of Electrical Engineers*, Vol. 61, 1942, p. 418.

22 Allen, P. H. G., Discussion of Papers 4, 34, and 40, Thermodynamics and Fluid Dynamics Convention, *Proceedings, Institution of Mechanical Engineers*, Vol. 182, Part 3H, 1967–1968, p. 413.

23 Allen, P. H. G., "Heat Transfer in Layer-Type Windings in High-Voltage Power Transformers," PhD thesis, University of London, England, 1960.

24 Stenkvist, E., "Temperature and Conditions of Oil Flow in Large Oil-Immersed Transformers," Technical Achievements of Asea Research, A.S.E.A., Vasteras, Sweden, 1946, p. 248.

25 Allen, P. H. G., and Finn, A. H., "Transformer Winding Thermal Design by Computer," Institution of Electrical Engineers Conference Publication 51, 1969, p. 589.

APPENDIX 1

Conventional Simplifying Assumptions

1 Conditions are steady-state ones.

2 Axial heat-conduction and momentum change are negligible.

3 Energy dissipation due to viscous effects is negligible.

4 Velocities and pressure gradients in directions perpendicular to the duct axis are negligible.

APPENDIX 2

Equations for Rectangular Ducts and Tubes

For a rectangular duct, (8) and (9) become

$$\frac{\partial^2 w}{\partial x^2} + \frac{\partial^2 w}{\partial y^2} = \frac{1}{\mu}\left[\frac{\partial p'}{\partial z} - gs(\theta - \theta_m) - \frac{d\mu}{d\theta}\left(\frac{\partial w}{\partial x}\frac{\partial \theta}{\partial x} + \frac{\partial w}{\partial y}\frac{\partial \theta}{\partial y}\right)\right] \quad (16)$$

$$\frac{\partial^2 \theta}{\partial x^2} + \frac{\partial^2 \theta}{\partial y^2} = \frac{1}{k}\left[\rho c w \frac{\partial \theta}{\partial z} - \frac{dk}{d\theta}\left(\left(\frac{\partial \theta}{\partial x}\right)^2 + \left(\frac{\partial \theta}{\partial y}\right)^2\right)\right] \quad (17)$$

For a circular tube, (8) and (9) become

$$\frac{\partial^2 w}{\partial r^2} + \frac{1}{r}\frac{\partial w}{\partial r} = \frac{1}{\mu}\left[\frac{\partial p'}{\partial z} - gs(\theta - \theta_m) - \frac{\partial w}{\partial r}\frac{\partial \theta}{\partial r}\frac{\partial \mu}{d\theta}\right] \quad (18)$$

$$\frac{\partial^2 \theta}{\partial r^2} + \frac{1}{r}\frac{\partial \theta}{\partial r} = \frac{1}{k}\left[\rho c w \frac{\partial \theta}{\partial z} - \left(\frac{\partial \theta}{\partial r}\right)^2 \frac{dk}{d\theta}\right] \quad (19)$$

For (16) and (18), boundary condition are $w = 0$ around duct walls, specified w_m or $\partial p'/\partial z$, while for (17) and (19) θ = const specified value around duct walls and, additionally, for (19)

$$\frac{\partial \theta}{\partial r} = -\frac{\text{duct wall heat flux}}{k} \text{ around duct walls:}$$

or

$$\frac{\partial \theta_b}{\partial z} = \frac{4(\text{duct wall heat flux})}{\rho c w_m D_h}$$

while for (17)

$$\frac{\partial \theta_b}{\partial z} = \frac{4(\text{duct wall mean heat flux})}{\rho c w_m D_h}$$

journal of heat transfer

discussion

Heat Transfer to Mercury Flowing in Line Through an Unbaffled Rod Bundle: Experimental Study of the Effect of Rod Displacement on Rod-Average Heat Transfer Coefficients[1]

G. McAreavey.[2] The authors have presented a rather interesting feature of heat transfer behavior in rod clusters. The phenomenon is of a particular importance for highly rated nuclear reactor fuel elements cooled by liquid metals, in which nonuniform rod spacing may arise from dimensional errors in support grids and thermal bowing between grids.

It is well known that the mean heat transfer coefficient increases with decreasing P/D, the rate of increase being greater the smaller the value of P/D. One might have expected, therefore, that for the displaced pin the heat transfer behavior, at least in the vicinity of the widest and narrowest gaps, would be very similar to that for pins with appropriate large and small P/D ratios, and that the average wall temperature would decrease, resulting in a higher, not lower average heat transfer coefficient. Clearly, this simple reasoning is complicated by the distortion of the heat flow lines shown by the authors in Fig. 4, but if the explanation lies in the lengthening of the heat flow paths, then one would expect to see an increase in wall temperature at every part of the circumference. Some typical plots of wall temperature would have made a valuable addition to the paper.

Secondly, it is difficult to understand why there should be no measurable change in the mean heat transfer coefficient of pin A when pin B is moved in the direction $p - q$. The minimum gap between pins A and B closes to half the extent that the gap between pins B and C closes, and the reduction in total coolant area available to pin A is $^5/_8$ the reduction for pin C. It is clear from consideration of Fig. 4 that the heat flow lines around pin A must also suffer some distortion. One would have expected, therefore, that the heat transfer coefficient for pin A would decrease to possibly half the extent of the decrease for pin C.

It would be useful to know to what extent the reported phenomenon is dependent on the achievement of fully developed flow, since this is rarely achieved in fuel elements with grid supports.

Finally, could any significant error in assessment of the average wall temperature arise from measurements at 40 deg intervals, bearing in mind that a sixth harmonic variation would be present, particularly for large displacements.

[1] By P. J. Hlavac, O. E. Dwyer, and M. A. Helfant, published in the November, 1969, issue of the JOURNAL OF HEAT TRANSFER, TRANS. ASME, Series C, Vol. 91, No. 4, pp. 568–580.

[2] Senior Engineer, Central Technical Services, United Kingdom Atomic Energy Authority, Reactor Group, Warrington, England.

Authors' Closure

First, let us look at the statement, "It is well known that the mean heat transfer coefficient increases with decreasing P/D, the rate of increase being greater the smaller the P/D ratio." Actually, this is only true for wide P/D ratios where there is a negligible amount of circumferential heat flow in the coolant stream. As the P/D ratio is lowered, the mean heat transfer coefficient goes through a rather sharp maximum at $P/D \approx 1.15$ for turbulent flow. This is caused by the introduction of circumferential heat flow in the coolant. As $P/D \rightarrow 1.00$, this circumferential heat flow becomes very appreciable with a corresponding decrease in the mean heat transfer coefficient.

Now, a very similar thing happens when a rod is moved off center, even for a P/D ratio as large as 1.75, except that the heat transfer in the coolant occurs over a circumferential distance that is much greater than that in the symmetrical case with the low P/D ratio. This is discussed on page 572 in the paper and illustrated in Fig. 4 on the page just preceding that. In the asymmetrical case, the heat flow through the greater distance causes the wall temperature to rise in that (those) portion(s) of the rod in relatively close proximity to another rod. It must be remembered that in turbulent-flow, liquid-metal heat transfer, the thermal resistance is not concentrated in a thin layer near the wall, as in the case of ordinary fluids.

It was further found that when a rod was moved toward a neighboring rod, its local heat transfer coefficient decreased at *all* points on its circumference—not just in that region facing the other rod. Again, this is believed to be due to the "pile up" of heat at the wide part of the coolant channel, caused by the circumferential heat flow from the narrow part of the channel. This is discussed in a second paper[3] from the same study which is scheduled for publication in the near future.

Referring to Mr. McAreavey's second point, the reduction in the coolant area for rod A is only about one-quarter that for rod C, but more importantly, the lost area is more expendable (i.e., the corner of the hexagon, not the side). The result is that there is very little circumferential heat flow around rod A, and therefore its mean heat transfer coefficient should not decrease appreciably, as rod B is moved toward C.

In liquid-metal heat transfer, particularly in the practical Peclet range, there is basically not a great deal of difference between fully developed turbulent-flow heat transfer and slug-flow heat transfer. For that reason, one would expect that the detrimental effects of rod displacement (or bowing) would be almost as bad in hydrodynamic entrance regions as in fully developed turbulent flow.

With a P/D ratio as large as 1.75, one would not expect to pick up a sixth harmonic variation in the circumferential temperature profile. Even as rod B was moved toward C, there was no significant effect of rod A on the circumferential temperature variation of rod B. Several surface-temperature profiles are presented in the paper by the authors.[3]

[3] Dwyer, O. E., Hlavac, P. J., and Helfant, M. A., to be published in the September, 1970, issue of *Nuclear Science Engineering*.